

WL-TR-95-2120



THREE-COMPONENT VELOCITY MEASUREMENTS DOWNSTREAM OF A BLUFF-BODY FLAMEHOLDER

CHARBEL N. RAFFOUL
ABDOLLAH S. NEJAD
RICHARD D. GOULD

OCTOBER 1995

FINAL REPORT FOR 06/01/93 TO 05/01/95

Approved for public release; distribution unlimited

19960731 100

AERO PROPULSION AND POWER DIRECTORATE
WRIGHT LABORATORY
AIR FORCE MATERIEL COMMAND
WRIGHT-PATTERSON AIR FORCE BASE, OH 45433-7251

NOTICE

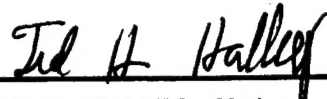
WHEN GOVERNMENT DRAWINGS, SPECIFICATIONS, OR OTHER DATA ARE USED FOR ANY PURPOSE OTHER THAN IN CONNECTION WITH A DEFINITELY GOVERNMENT-RELATED PROCUREMENT, THE UNITED STATES GOVERNMENT INCURS NO RESPONSIBILITY OR ANY OBLIGATION WHATSOEVER. THE FACT THAT THE GOVERNMENT MAY HAVE FORMULATED OR IN ANY WAY SUPPLIED THE SAID DRAWINGS, SPECIFICATIONS, OR OTHER DATA, IS NOT TO BE REGARDED BY IMPLICATION, OR OTHERWISE IN ANY MANNER CONSTRUED, AS LICENSING THE HOLDER, OR ANY OTHER PERSON OR CORPORATION; OR AS CONVEYING ANY RIGHTS OR PERMISSION TO MANUFACTURE, USE, OR SELL ANY PATENTED INVENTION THAT MAY IN ANY WAY BE RELATED THERETO.

THIS REPORT IS RELEASABLE TO THE NATIONAL TECHNICAL INFORMATION SERVICE (NTIS). AT NTIS, IT WILL BE AVAILABLE TO THE GENERAL PUBLIC, INCLUDING FOREIGN NATIONS.

THE TECHNICAL REPORT HAS BEEN REVIEWED AND IS APPROVED FOR PUBLICATION.



CHARBEL N. RAFFOUL
Program Monitor
Experimental Research Branch
Advanced Propulsion Division



TED H. HALLEY, Major USAF
Chief, WL/POPT
Experimental Research Branch
Advanced Propulsion Division



PARKER L. BUCKLEY
Deputy Chief, WL/POPT
Advanced Propulsion Division

IF YOUR ADDRESS HAS CHANGED, IF YOU WISH TO BE REMOVED FROM OUR MAILING LIST, OR IF THE ADDRESSEE IS NO LONGER EMPLOYED BY YOUR ORGANIZATION PLEASE NOTIFY WL/POPT, WPAFB OH 45433-7251 TO HELP MAINTAIN A CURRENT MAILING LIST.

Copies of this report should not be returned unless return is required by Security Consideration, contractual obligations, or notice on a specific document.

REPORT DOCUMENTATION PAGE

Form Approved
OMB No. 0704-0188

Public reporting burden for this collection of information is estimated to average 1 hour per response, including the time for reviewing instructions, searching existing data sources, gathering and maintaining the data needed, and completing and reviewing the collection of information. Send comments regarding this burden estimate or any other aspect of this collection of information, including suggestions for reducing this burden, to Washington Headquarters Services, Directorate for Information Operations and Reports, 1215 Jefferson Davis Highway, Suite 1204, Arlington, VA 22202-4302, and to the Office of Management and Budget, Paperwork Reduction Project (0704-0188), Washington, DC 20503.

1. AGENCY USE ONLY (Leave blank)	2. REPORT DATE	3. REPORT TYPE AND DATES COVERED	
	OCT. 95	FINAL 06/01/93 TO 05/01/95	
4. TITLE AND SUBTITLE		5. FUNDING NUMBERS	
THREE-COMPONENT VELOCITY MEASUREMENTS DOWNSTREAM OF A BLUFF-BODY FLAMEHOLDER		PE61102F PR 2308 TA S1 WU 01	
6. AUTHOR(S)		CHARBEL N. RAFFOUL ABDOLLAH S. NEJAD RICHARD D. GOULD	
7. PERFORMING ORGANIZATION NAME(S) AND ADDRESS(ES)		8. PERFORMING ORGANIZATION REPORT NUMBER	
EXPERIMENTAL RESEARCH BRANCH ADVANCED PROPULSION DIVISION 1950 FIFTH STREET WPAFB, OH, 45433-7251			
9. SPONSORING/MONITORING AGENCY NAME(S) AND ADDRESS(ES)		10. SPONSORING/MONITORING AGENCY REPORT NUMBER	
AERO PROPULSION AND POWER DIRECTORATE WRIGHT LABORATORY AIR FORCE MATERIEL COMMAND WRIGHT PATTERSON AFB OH 45433-7251		WL-TR-95-2120	
11. SUPPLEMENTARY NOTES Technical Monitor - Dr. A. S. Nejad (WL/POPT, WPAFB OH 45433-7251)			
12a. DISTRIBUTION/AVAILABILITY STATEMENT APPROVED FOR PUBLIC RELEASE; DISTRIBUTION IS UNLIMITED		12b. DISTRIBUTION CODE	
13. ABSTRACT (Maximum 200 words) In order to enhance fuel and air mixing for more efficient combustion, it has been suggested to use bodies that generate vortical and turbulent structures in their wake. The injected fuel from the surface of in-stream mounted fuel injectors will interact with the turbulent flow and thoroughly mix with the freestream air. Simple 2-d and 3-d bluff bodies have been the subject of experimental investigations for a number of years. However, the opportunity has never before existed for the full exploration of the flowfield downstream of such bodies. The introduction of laser Doppler velocimetry (LDV) must be credited for more accurate measurements in the area of fluid mechanics in general, and in particular in the recirculating and complex flows such as the case of this study. In order to establish a baseline frame of reference for future work employing bluff bodies with vortex generators, the flow characteristics around a 2-d bluff body were experimentally investigated in this effort. Three-component velocity measurements using LDV were made in the highly turbulent flow past a 2-d bluff body. The contribution of this study is unique as all three velocity components were simultaneously measured at each point without introducing disturbances to the flow. Vertical data profiles were obtained at 11 axial stations in the far-field and at 8 axial stations in the near-field. Spanwise (Z) profiles of the flowfield immediately downstream of the bluff body were also determined. The three orthogonal mean velocities (\bar{U} , \bar{V} , \bar{W}), the six Reynolds stresses (uu , vv , ww , uv , uw , vw) and all nine turbulent triple products (uuv , uvv , uvw , vuu , vvv , vww , wwu , wwv) were estimated. Comparisons between commonly used approximations for ww , uvw and vww (when the third component is not available) and the experimental measurements were made and are presented. Newly derived expressions for these parameters are suggested based on the direct measurements. The production, convection, and diffusion of turbulent kinetic energy (tke) were computed directly from the experimental data using numerical differencing. A balance of the tke equation in the flow was also performed, assuming the pressure fluctuations to be negligible. This allowed the identification of regions in this flowfield where tke is produced, convected, and diffused. Dissipation of tke was also obtained by balance.			
14. SUBJECT TERMS Flameholder, Bluff Body, Turbulent, Isothermal, Subsonic, Laser Doppler Velocimeter, Three-Component Velocity		15. NUMBER OF PAGES 216	
		16. PRICE CODE	
17. SECURITY CLASSIFICATION OF REPORT UNCLASSIFIED	18. SECURITY CLASSIFICATION OF THIS PAGE UNCLASSIFIED	19. SECURITY CLASSIFICATION OF ABSTRACT UNCLASSIFIED	20. LIMITATION OF ABSTRACT SAR

FOREWORD

This technical report reflects experimental research work which was performed at the Experimental Research Branch (WL/POPT) of the Advanced Propulsion Division (WL/POP), Wright Laboratory (WL), at Wright Patterson Air Force Base (WPAFB), Ohio. The test facility is located in Building 18c, Test Cell 18. The numerical results were reported by Spring, et al. of CFD Research Corporation (Huntsville, Al.) in WL-TR-95-2068, as a SBIR Phase-II final report.

The authors wish to acknowledge the assistance of Mr. S. Alan Spring for his assistance with computer software programming, the Computational Fluid Dynamic (CFD) results, and other related suggestions and discussions. Mr. Kevin Kirkendall was very helpful in the experimental setup and the data acquisition.

Also, part of this material was accepted by the University of Dayton as partial fulfillment of the requirements for the degree of Doctor of Philosophy in Mechanical Engineering for Dr. Charbel N. Raffoul.

TABLE OF CONTENTS

ABSTRACT.....	i
LIST OF ILLUSTRATIONS.....	vii
NOMENCLATURE.....	xi
CHAPTER	
1. INTRODUCTION.....	1
1.1 Problem Definition.....	1
1.2 The Present Research.....	3
1.3 Background.....	5
1.3.1 Bluff Body.....	5
1.3.2 Laser Doppler Velocimetry.....	8
1.3.3 Computational Fluid Dynamics.....	10
1.4 Outline.....	16
2. TURBULENCE MODELING.....	18
2.1 Introduction.....	18
2.2 Origin and Theory of Turbulence Modeling.....	19
3. EXPERIMENTAL APPARATUS.....	30
3.1 Facility.....	30
3.2 Bluff Body.....	31
3.3 Laser Doppler Velocimetry.....	33
3.3.1 Far-Field LDV System.....	36
3.3.2 Near-Field LDV System.....	38
3.4 Flow Seeders.....	40
3.4.1 Far-Field Seeding.....	41
3.4.2 Near-Field Seeding.....	42
3.5 Data Acquisition and Processing.....	42
3.6 Velocity Bias.....	45
3.7 Data Reduction Package.....	45
4. EXPERIMENTAL PROCEDURE.....	47
4.1 Introduction.....	47
4.2 Test Conditions.....	48

4.3 Sampling Method.....	49
4.4 Turbulence Statistics.....	50
4.5 Statistical Error Estimation.....	51
4.5.1 Uncertainty in the Means.....	51
4.5.2 Uncertainty in the Higher Order Moments.....	52
4.6 Measurement Errors.....	52
 5. FAR-FIELD EXPERIMENTAL RESULTS AND DISCUSSION.....	56
5.1 Introduction.....	56
5.2 Mean Velocity Data	
5.2.1 1-d LDV.....	57
5.2.2 3-d LDV.....	60
5.3 Vortex Shedding Frequency.....	75
5.4 Turbulent Normal and Shear Stresses.....	79
5.5 Turbulent Triple Products.....	86
5.6 Turbulent Kinetic Energy.....	96
 6. NEAR-FIELD EXPERIMENTAL RESULTS AND DISCUSSION.....	101
6.1 Introduction.....	101
6.2 Mean Velocity Data.....	102
6.3 Turbulent Stresses.....	110
6.3.1 Reynolds Stresses.....	110
6.3.2 Normal Stresses.....	110
6.4 Turbulent Kinetic Energy (TKE).....	118
6.5 Isotropy.....	118
6.6 ww Approximation.....	123
6.7 Turbulent Triple Products.....	125
6.8 uvw and vww Approximations.....	136
6.9 TKE Balance.....	139
6.9.1 TKE terms	146
6.9.2 Derivatives.....	149
 7. NUMERICAL RESULTS AND DISCUSSION.....	163
7.1 Introduction.....	163
7.2 Numerical Technique.....	163
7.3 Results and Discussion.....	166
 8. CONCLUSIONS.....	168
 BIBLIOGRAPHY.....	170

APPENDICES

APPENDIX A - LDV Data Reduction Equations.....	178
APPENDIX B - Mean Velocity Equations & Coordinate Transformation.....	180
APPENDIX C - LDV Definitions and Description of Components.....	184
APPENDIX D - Data Reduction Notes.....	187
APPENDIX E - Software File Output Format.....	190
APPENDIX F - TKE and Reynolds Stress Equations.....	191
APPENDIX G - Uncertainties: Uref, Means.....	195
APPENDIX H- Uncertainties in TKE, and TKE Terms.....	197

LIST OF ILLUSTRATIONS

Figure	Page
1. Experimental test facility.....	31
2. Bluff body schematic.....	32
3. Typical dual beam laser Doppler anemometer.....	34
4. Near-field LDV system configuration.....	39
5. Normalized mass flux variation from station to station based on measured mean axial velocities.....	49
6. Normalized mean axial velocity profiles; 1-d LDV.....	58
7. Normalized axial turbulence intensity profiles; 1-d LDV.....	59
8. Normalized mean axial velocity and turbulence intensity profiles.....	61
9. Normalized mean axial velocity and turbulence intensity profiles ; 1-d, & 3-d LDV.	62
10 Bluff-body near-field flow description.....	63
11. Normalized mean transverse velocity and turbulence intensity profiles.....	65
12. Normalized mean axial velocity PDF.....	66
13. Normalized mean transverse velocity PDF.....	66
14. Normalized mean spanwise velocity & turbulence intensity profiles at $x/H=1$	68
15. Axial, transverse, & spanwise turbulence intensity profiles at $x/H=1$	70
16. Normalized mean axial velocity profiles; 3-d LDV.....	71
17. Normalized axial turbulence intensity profiles; 3-d LDV.....	72
18. Normalized mean transverse velocity profiles; 3-d LDV.....	73
19. Normalized transverse turbulence intensity profiles; 3-d LDV.....	74
20. Normalized mean spanwise velocity profiles; 3-d LDV.....	76

21. Normalized spanwise turbulence intensity profiles; 3-d LDV.....	77
22. Frequency spectra at $x/H=-5$ & $x/H=2$	78
23. Normalized axial turbulent normal stresses.....	80
24. Normalized transverse turbulent normal stresses.....	81
25. Normalized spanwise turbulent normal stresses.....	82
26. Normalized \bar{uv} turbulent shear stresses.....	83
27. Normalized \bar{uw} turbulent shear stresses.....	84
28. Normalized \bar{vw} turbulent shear stresses.....	85
29. Normalized \bar{uuu} turbulent triple product distributions.....	87
30. Normalized \bar{vvv} turbulent triple product distributions.....	88
31. Normalized \bar{www} turbulent triple product distributions.....	89
32. Normalized \bar{vvv} turbulent triple product distributions.....	90
33. Normalized \bar{www} turbulent triple product distributions.....	91
34. Normalized \bar{vvv} turbulent triple product distributions.....	92
35. Normalized \bar{www} turbulent triple product distributions.....	93
36. Normalized \bar{uuw} turbulent triple product distributions.....	94
37. Normalized \bar{uvv} turbulent triple product distributions.....	95
38. Normalized turbulent kinetic energy.....	97
39. Axial mean normal stresses- Isotropy check.....	98
40. Transverse mean normal stresses- Isotropy check.....	99
41. Spanwise mean normal stresses- Isotropy check.....	100
42. Normalized mean axial velocity profiles; 3-d LDV.....	103
43. Normalized mean transverse velocity profiles; 3-d LDV.....	105

44. Normalized mean spanwise velocity profiles at $z/H=0$; 3-d LDV.....	106
45. Normalized mean spanwise velocity profiles at $y/H=0$; 3-d LDV.....	108
46. Normalized “1-d LDV” mean spanwise velocity profiles at $y/H=0$	109
47. Normalized \bar{uv} turbulent normal stress distributions.....	111
48. Normalized \bar{uw} turbulent shear stress distributions.....	112
49. Normalized \bar{vw} turbulent stress distributions.....	113
50. Normalized \bar{uu} turbulent stress distributions.....	114
51. Normalized \bar{vv} turbulent stress distributions.....	115
52. Normalized \bar{ww} turbulent stress distributions.....	116
53. Normalized turbulent kinetic energy.....	119
54. Axial mean normal stresses- Isotropy check.....	120
55. Transverse mean normal stresses- Isotropy check.....	121
56. Spanwise mean normal stresses- Isotropy check.....	122
57. Normalized turbulent kinetic energy-approximations.....	124
58. Normalized \bar{uuv} turbulent triple product distributions.....	126
59. Normalized \bar{uuw} turbulent triple product distributions.....	127
60. Normalized \bar{uvv} turbulent triple product distributions.....	128
61. Normalized \bar{vww} turbulent triple product distributions.....	129
62. Normalized \bar{uvw} turbulent triple product distributions.....	130
63. Normalized \bar{vww} turbulent triple product distributions.....	131
64. Normalized \bar{uuu} turbulent triple product distributions.....	132
65. Normalized \bar{vvv} turbulent triple product distributions.....	133
66. Normalized \bar{www} turbulent triple product distributions.....	134

67. Third moment \overline{uvw} of fluctuating velocity-approximations.....	137
68. Third moment \overline{vww} of fluctuating velocity-approximations.....	138
69a. TKE Balance at station $x/H=0.9$ (bubble location).....	141
69b. Convection term with error bars at station $x/H=0.9$	142
69c. Production term with error bars at station $x/H=0.9$	143
69d. Diffusion term with error bars at station $x/H=0.9$	144
69e. Dissipation term with error bars at station $x/H=0.9$	145
70. TKE Balance in the near-field.....	147
71. TKE Balance in the far-field.....	148
72. Production of TKE.....	150
73. Convection of TKE.....	151
74. Diffusion of TKE.....	152
75. Normalized mean axial velocity and velocity gradient distribution.....	154
76. Normalized mean transverse velocity and velocity gradient distributions.....	155
77. Normalized mean spanwise velocity and velocity gradient distributions.....	156
78. Normalized \overline{uv} turbulent stress and stress gradient distributions.....	157
79. Normalized \overline{uu} turbulent stress and stress gradient distributions.....	158
80. Normalized \overline{vv} turbulent stress and stress gradient distributions.....	159
81. Normalized \overline{ww} turbulent stress and stress gradient distributions.....	160
82. Two-dimensionality verification.....	162
83. Grid near bluff body used for CFD analyses.....	164

NOMENCLATURE

A	= area
f_d	= Doppler frequency
f	= vortex shedding frequency
H	= bluff body height
k	= turbulent kinetic energy, $k = (\overline{uu} + \overline{vv} + \overline{ww}) / 2$
l	= mixing length
\dot{m}	= mass flow rate
N	= number of LDV realizations
t	= time
U, V, W	= instantaneous velocities in the x-, y-, and z-dir., respectively
$\overline{U}, \overline{V}, \overline{W}$	= mean velocities in the x-, y-, and z-direction, respectively
u, v, w	= fluctuating velocity components
\overline{uu}	= axial normal stress
\overline{vv}	= transverse normal stress
\overline{ww}	= spanwise normal stress
\overline{uv}	= turbulent shear stress
\overline{uw}	= turbulent shear stress
\overline{vw}	= turbulent shear stress
$\overline{u_i u_j}$	= Reynolds stress tensor
\overline{uuu}	= axial turbulent triple-product
\overline{vvv}	= transverse turbulent triple-product
\overline{www}	= spanwise turbulent triple-product
\overline{vuu}	= mixed turbulent triple-product
$\overline{u_i u_j u_k}$	= triple velocity correlation
x	= axial coordinate
y	= transverse coordinate
z	= spanwise coordinate

Subscripts

ref = reference

Superscripts

$(\overline{\quad})$ = Overbar denotes “Ensemble-Averaged” (temporal mean)

Abbreviations

ASM	= Algebraic Stress Model
CARS	= coherent anti-stokes Raman spectroscopy
CFD	= Computational Fluid Dynamics
d, D	= Dimensional
DNS	= Direct Numerical Simulation
IFF	= Integral Fuel-Injector Flameholder
in	= inch
LDV	= laser Doppler velocimetry
LES	= Large Eddy Simulation
mm	= millimeter
NSE	= Navier Stokes Equations
PDF	= Probability Density Function
Re	= Reynolds number
RNG	= Renormalization Group
RSM	= Reynold Stress Model
s	= second
S	= Sample Variance
SNR	= Signal-to-Noise Ratio
St	= Strouhal number
TBD	= Time between Data
tke, TKE	= Turbulent Kinetic Energy

GREEK SYMBOLS

δ_{ij}	= Kronecker delta
ε	= dissipation rate of turbulent kinetic energy
λ	= laser beam wavelength
μ	= dynamic viscosity
μ_{eff}	= effective laminar and turbulent viscosities
μ_t	= turbulent viscosity
ρ	= density of the fluid
σ	= standard deviation
χ^2	= chi-square

CHAPTER 1

INTRODUCTION

1.1 Problem Definition

National interest in flight vehicles with Mach 4 to 6 flight capability has revitalized research interest in high-speed air breathing propulsion systems to power both manned and unmanned vehicles. With increasing flight speeds from high supersonic to low hypersonic velocities, the entire propulsion system will operate in a much more severe environment. As the operational limits of the gas turbine engine are reached, the aerodynamic conditions will become more favorable for operation of a subsonic-combustion ramjet propulsion system. Thermal management of propulsion and airframe components becomes a critical design factor beyond the Mach 6 flight regime. At these speeds, freestream air cannot be used for cooling as the ram air temperature will approach or exceed the material temperature limits of the propulsion system. Therefore, the future of high-speed flight depends to a large extent on the ability of the stored fuel to be used as a heat sink. The high temperature environment also places new and additional constraints on the combustion processes. For example, injection of fuel upstream of the flameholder is no longer a viable design option for mixing and flameholding, as the fuel would auto-ignite in the high-temperature inlet air and destroy the flameholder. As a solution to this problem, an alternative to a flameholder separate from the fuel injector, the Integral Fuel-Injector Flameholder (IFF), was studied by Hautman, et al. (1990). The IFF also serves as an in-stream fuel injector for enhanced mixing and could be used as a heat exchanger to various endothermic type fuels. It is a well-known fact that fuel-

air mixing is the critical factor which determines the combustion efficiency of the ramburner at many flight conditions. Previous research has also shown that the use of vortex generators attached to the base of the bluff body may further improve mixing and combustion efficiency much like lobed mixers used with turbofan engines (Spring et al., 1992).

The flowfield behind geometries such as bluff bodies has been the topic of many studies in the past. Davies and Beer (1971) summarize some previous experimental work concerning bluff bodies. It is also well established that the recirculation region downstream of such bodies enhances fuel-air mixing. This is due mainly to the increase in local turbulence levels in the recirculation region. It is also commonly known that turbulence is three-dimensional as well as rotational (Tennekes and Lumley, 1972). The flowfield downstream of bluff bodies placed in-stream is dominated by vortical structures, large and small, which gives the flow its turbulent characteristics.

An efficient and economical combustor design methodology requires numerical experimentation for identifying possible prototype candidates before fabrication and testing. Development of such Computational Fluid Dynamics (CFD) code requires a reliable database against which the predictions can be compared and validated. CFD combustion engineers will require a detailed database on: a) the combustor entrance conditions such as air temperature, pressure, velocity, and turbulence parameters distributions and their relationship to inlet operating conditions; b) fuel temperature, composition, and distribution profiles; and, c) location of the flameholders, and injection sites.

The flowfield in the regions immediately downstream of such bodies being three dimensional, requires a three-dimensional analysis. The introduction of laser Doppler

velocimetry (LDV) has allowed for the nonintrusive measurement of the instantaneous velocities and other turbulence parameters in complex turbulent flows. However, the use of LDV remained limited to single and two-dimensional studies due to the many complications involved in measuring the third component.

1.2 The Present Research

The present research offers a detailed study of the flowfield around a bluff body mounted in-stream in a subsonic isothermal flow. It also overcomes the difficulties in obtaining the three velocity components. A benchmark database is established for development and validation of computational codes. In order to establish a baseline frame of reference for future work employing bluff bodies with vortex generators, the flow characteristics of a cylindrical bluff body are experimentally investigated here. Three-component velocity measurements were made upstream, and in the highly turbulent flow downstream of the bluff body. The intense wake region is known to oscillate at a frequency coupled to the shedding frequency of the shear layers and contains large negative axial velocities. Although the flow behind bluff bodies has been under investigation for many years, the contribution of this study is unique as all three velocity components were simultaneously measured at each point without introducing disturbances to the flow. The three velocity components were measured directly using three orthogonal and overlapping probe volumes. This gives better accuracy than the more common method of obtaining the third velocity component as described by Meyers (1985) and Mehta (1990). This more common technique, which was not used here, uses an LDV system, which allows direct measurement of the U and V components, together with a second LDV system rotated at a

certain angle to allow the measurement of the U and the W components. Signals from the U component are combined with signals from the rotated component in an electronic double balanced mixer. A trigonometric adjustment of the difference frequency is then performed to yield the W-component measurement. However, if the W-velocity component is small compared to the other velocity components, large relative errors can result.

The three orthogonal mean velocity components ($\bar{U}, \bar{V}, \bar{W}$) were measured, producing profiles in the transverse and spanwise directions at 11 axial stations in the far-field and at 8 axial stations in the near-field behind the bluff body. Spanwise velocity measurements of the flowfield immediately downstream of the bluff body were also taken. All six Reynolds stresses, normal and shear ($\bar{uu}, \bar{vv}, \bar{ww}, \bar{uv}, \bar{uw}, \bar{vw}$), and all nine turbulent triple products ($\bar{uuu}, \bar{vvv}, \bar{www}, \bar{vuu}, \bar{vvv}, \bar{vww}, \bar{wuu}, \bar{wvv}, \bar{www}$) were also measured. Also, this report includes a statistical uncertainty analysis estimated for each of the first, second and third order moments using the *jackknife* method.

Comparisons between commonly used approximations, based on isotropic conditions, for \bar{ww} , \bar{uvw} and \bar{vww} (when the third component is not available) and the experimental measurements are made and presented. Newly derived expressions for these parameters are suggested using the direct measurements as reference. The production, convection, and diffusion of turbulent kinetic energy (TKE) are computed directly from the experimental data using numerical differencing. A balance of TKE in the flow is also performed to give an estimation of the dissipation of TKE. Regions in this flowfield where TKE is produced, convected, and diffused are identified. An uncertainty analysis was also estimated for each of the TKE terms. Since derivatives with respect to x and y are involved

in the TKE balance equation, first order derivatives of some of the important parameters are also reported here. Finally, comparisons between some recently developed numerical techniques and the experimental data are included.

1.3 Background

Simple 2-d and 3-d bluff bodies have been the subject of experimental investigations for a number of years (Fuji et al., 1978). Bluff-body flows exist in many places, such as the flows around flameholders in gas turbine and ramjet engines, and flows around buildings, bridges, and support structures. Researchers (Perry and Steiner, 1987; Mansingh and Oosthuizen, 1990) have found that the turbulence downstream of bluff bodies is created by a regular pattern of vortices shed from the trailing edge of the body, and that symmetric flow only exists as a time-average.

1.3.1 Bluff Body

Some examples of recent bluff-body studies include velocity measurements in the flowfield behind flat plates by Perry and Steiner (1987). They used a flying-hot-wire system for all measurements. The flat plates were placed normal or at an angle of attack with respect to the air flow at Reynolds numbers that ranged from 14×10^4 to 20×10^4 based on the projected height of the plate. Data were sampled every centimeter (cm) in the streamwise direction. They reported that the flow was clearly three-dimensional. The precise nature of the three-dimensionality was not stated. However, they suspected that it had to do with a periodic waviness of the vortex cores in the spanwise direction. They also concluded that the

mean-flow patterns of the bluff plates set normal to the freestream flow are not perfectly symmetrical, and are highly sensitive to the end conditions.

Okamoto (1981) conducted a study of air flow past a low aspect ratio hemispherical-cylinder mounted on the horizontal surface, in a wind tunnel with a 400x400-mm cross section at a flow Reynolds number of 4.74×10^4 , based on the diameter of the cylinder. By using a yaw head meter, the velocity vector was obtained. The time-mean velocity and static pressure were measured by pitot and static pressure tubes. Also, a constant temperature hot wire anemometer was used to measure the turbulence. Distributions in the turbulent shear flow region behind the hemispherical-cylinder were obtained. These measurements showed that the recirculation region behind the bluff body extended to $x/D = 2.4$. This recirculation zone length was much shorter than that of a two-dimensional fence ($x/D = 13.2$). This difference in recirculation zone length was attributed to the strong downwash behind the hemisphere-cylinder. A Strouhal number of 0.152, 0.225, and 0.222 was reported for a hemisphere-cylinder, a circular cylinder, and a sphere, respectively, for the same Reynolds number.

Mansingh and Oosthuizen (1990) studied the flowfield behind a rectangular cross-section cylinder. They determined that the spanwise base pressure measurements at mid-height showed considerable three-dimensional effects. They studied the effects of introducing a splitter plate in the center plane of the rectangular cylinder at various distances downstream. Their results indicated that splitter plates altered the manner of vortex formation in the wake causing a decrease in shedding frequency, an increase in base pressure, and a reduction in the overall drag by up to 50%. Their work was at low Reynolds

numbers, typically 0.35×10^3 and 1.15×10^3 , based on the height of the rectangular cylinder and the freestream velocity.

Durao, et al. (1988) have studied the flow around a square obstacle mounted in a water channel at a Reynolds number of 1.4×10^4 , based on the obstacle width and the upstream velocity. The purpose of their work was to study the nature of the fluctuations in the near-wake region of two-dimensional bodies. Their results showed that in the zone where the shear layer oscillates in a nearly periodic fashion, the turbulent energy associated with the random turbulent fluctuations is only about 40% of the total turbulent energy calculated using ensemble averaging. They also concluded that the steady-state numerical calculation of the separated flow behind two-dimensional bodies requires modeling of the periodic vortex-shedding motion.

Williamson (1989) studied the three-dimensional flowfield in the wake of a cylinder, mounted vertically in a water tunnel. Flow visualization was carried out by towing a cylinder through water in an xy towing tank, using fluorescent dyes washed off the cylinder surface. In the laminar vortex shedding regime ($Re_D < 180$), a discontinuity in the Strouhal-Reynolds number relationship is explained by a transition between different modes of oblique vortex shedding. Oblique shedding was shown to be caused by the end boundary conditions of the cylinders even for cylinders hundreds of diameters in length. They found that by manipulating the end conditions, parallel shedding can be induced which results in a continuous Strouhal curve.

Hautman and Rosfjord (1989) made measurements in a ramjet test combustor operating at realistic flight conditions. Velocity and turbulence intensity measurements were

made using a two-channel LDV system operated in the back-scatter mode. High-speed photography was used to study liquid injection and atomization. One of their objectives was to assess the variation of inlet turbulence on the flowfield downstream of a bluff body. Two types of turbulence modifiers were used to vary the upstream turbulence. Their measurements showed that there exists regions of high axial turbulent velocities downstream of the Integral Flameholder Fuel Injector (IFF) configurations. Their measurements were then used for the development of ramjet combustor design procedures.

The use of bodies that generate vortical and turbulent structures has been suggested to enhance fuel and air mixing (Spring, et al. 1992). It is believed that the injected fuel from the surface of the in-stream mounted fuel injector will follow the turbulent flow and more thoroughly mix with the freestream air. McCormick and Bennett (1993) performed a comprehensive and detailed experimental investigation of the vortical structure in the free shear layer downstream of a lobed mixer. They showed that a new vortex structure exists in addition to the known streamwise vortex array. This normal vortex sheds periodically from the trailing edge and plays a major role along with the streamwise vorticity in the enhanced mixing process.

1.3.2 Laser Doppler Velocimetry

In recent years, laser Doppler velocimetry (LDV) has become increasingly effective as a tool for non-intrusively measuring the instantaneous velocities at points in complex turbulent flows. This is because LDV is a reliable instrument for making instantaneous velocity measurements in highly turbulent flows and in flows with separation and recirculation regions. However, few simultaneous three-component measurements have been

reported to-date, due mainly to the increase in instrumentation and signal processing equipment required to make these measurements. In addition, optical access is required for all three components. Other difficulties include the ability to maintain a high coincident data validation rate so that temporal flow characteristics can be resolved. Also, the continuous drift (due to vibration and room air temperature fluctuations, etc.) of the three individual probe volumes necessitates adjustment for maintaining coincident three-component data.

Sjunnesson, et al. (1991) used a two-component LDV system to study the flowfield behind 2-d bluff bodies of various shapes at Reynolds numbers, based on the flameholder height, ranging from 2.8×10^4 to 8.4×10^4 for the isothermal and reacting flow conditions in air. Their study revealed that the recirculation zone was longer for the reacting flow case, that the flow recovered in a shorter distance in the isothermal case, and that the strong vortex shedding present in isothermal flows was not found in the reacting flow.

Geropp and Leder (1985) used a single component (LDV) to document the flowfield behind a 2-d wing body. They changed the angle of attack of an airfoil and a wedge, and showed that the length of the recirculating region in the wake increases for all bodies with increasing angle of attack. The suppression of vortex interaction was also obtained by placing a splitter plate at mid-height, downstream of the body, which resulted in a reduction in drag.

The turbulent wake behind a circular cylinder was studied by Absil (1988) using a two-color dual-beam laser Doppler anemometer (LDA). The Reynolds number based on the diameter of the cylinder was 1300. Mean velocities, turbulence intensities, Reynolds stresses, skewness and kurtosis factors, and other correlation functions were reported. His

measurements consisted mainly of stations in the far wake where no reverse flow existed. This was done on purpose to avoid the use of a Bragg cell in his LDA system. His data showed reasonable agreement with hot wire data taken previously. The investigation concluded by demonstrating that LDA is a powerful tool for measuring various turbulence quantities in turbulent flows.

Hosokawa, et al. (1993) studied the effects of flameholder geometries on the flowfield characteristics such as the recirculation zone size and vortex scale. They used a 1-d fiber-optic based laser Doppler velocimeter (FLDV) in an isothermal air flow behind two different versions of V-gutter shaped flameholders, with and without an extended base. They measured the axial mean and fluctuating velocities, and the frequency of the fluctuating flow. They found that the rectangular section of the extended flameholder played a role in the flow stratification, due to the uniform velocity profile over the extended surface. This also increased the fluctuating frequency and decreased the length of the recirculation zone.

Larousse, et al. (1991) used a two-dimensional LDV system to study the turbulent flow behavior behind 2-d and 3-d surface-mounted obstacles in a channel, where air flowed at a Reynolds number of 10^5 , based on the obstacle height. Major differences in the flow patterns, both upstream and downstream of the obstacles, were noted. A distinct unsteadiness of the upstream flowfield for three-dimensional obstacles led to increased values in the Reynolds shear stress.

1.3.3 Computational Fluid Dynamics

Durst and Rastogi (1977) used a one-component LDV system to study the flowfield behind a square obstacle in a two-dimensional water channel. The measurements were made

at a Reynolds number of 1.7×10^4 . Theoretical investigations were also made using finite difference calculation procedures for recirculating flows and boundary layers in order to solve the governing fluid flow equations. The turbulent viscosity was obtained from the solution of the two-equation $k-\epsilon$ turbulence model. For boundary layer regions, the three-equation $k-\epsilon-\bar{uv}$ turbulence model was also used. They found that the calculated longitudinal velocities did not compare well with those measured. They suggested that the $k-\epsilon$ turbulence model needs to be modified in order to obtain more accurate calculations in the separated flow regions.

Castro (1977) studied the numerical accuracy of finite difference techniques typically used for the calculation of elliptic type turbulent flows. The size of the truncation error term was investigated both analytically and by direct comparison between predictions and experiments. First, a classical turbulent shear flow was considered. For this flow, it was found that although the local numerical errors became large, the general features of the flow were well predicted. Next the flow over a backward-facing step and over a two-dimensional fence were considered. It was concluded that inadequate turbulence modeling was not the sole, or at least, not the major cause of discrepancies between predictions and experiments. It was further observed that common numerical methods with typical grid densities are often incapable of accurate predictions due to severe numerical errors in the regions of difficult geometry such as sharp corners.

Moss, et al. (1977) used pulsed-wire anemometry to measure mean velocities and Reynolds stresses in turbulent ($Re = 5 \times 10^4$) recirculating flow past a number of bluff bodies. The distributions of the Reynolds stresses were given for the recirculating zones and the

mixing layers. Measurements of the mean velocity and turbulence energy were compared with the predictions of a computer program based on a two-equation turbulence model.

Przulj and Younis (1993) performed a numerical simulation study of turbulent vortex shedding for flow over a square cylinder, at a Reynolds number of 250 based on the cylinder height. Their model captured the experimentally documented size of the recirculation zone. They showed that the prediction of turbulent vortex shedding is possible with a standard $k-\epsilon$ turbulence model. However, the model was found to lack sensitivity to the imposed mean-flow unsteadiness. They presented an assessment of important factors such as; a) discretization of convection terms; b) the use of the log-law for simulation of the near-wall regions; and c) the choice of turbulence model which influences the time-averaged simulations of turbulent vortex-shedding associated with bluff bodies. They suggested that suppression of vortex-shedding, which has often been associated with the use of $k-\epsilon$ turbulence modeling was due to inappropriate numerical discretization schemes. Turbulence models that have been developed for steady flow are shown to be inadequate for vortex-shedding applications. A simple modification was proposed for sensitizing the standard turbulence models for such flows. After modification of the ϵ -production term, the model accurately predicted the measured axial mean-flow and turbulence parameters. No transverse mean-flow velocities, or turbulent stresses were reported.

Martensson, et al. (1991) used different numerical simulation techniques to predict the flow behavior downstream of two different bluff-body geometries, mounted in-stream. The Reynolds numbers investigated were 4.5×10^4 and 8.7×10^4 , based on the bluff-body height. A triangular cross section geometry and a triangular cross section geometry with a

square cross section afterbody were studied. The bluff bodies were mounted with the apex of the triangular section facing the air flow. They reported results from a number of numerical experiments, using different grids, numerical schemes and flow conditions. The 3-d numerical results generally agreed better with experimental results than did the 2-d numerical results. There was a major improvement in matching the transverse turbulent fluctuating term, v' , as well as the Reynolds shear stress, $\overline{u'v'}$, with the experimental measurements, when using 3-d code. The spanwise velocities were not measured.

Kodali and Amano (1986) conducted a numerical study on the turbulent flowfield behind bluff bodies. They reported on an external flow over a disk and an internal flow past a cone. They compared two $k-\epsilon$ turbulence models, and two Algebraic Stress Models (ASM) where the only differences were the values of modeling constants. When compared with actual measurements, their results indicated that the ASM generally gave better predictions in the recirculating region than did the $k-\epsilon$ model. They also found that a modification to the ASM model gave a significant improvement of prediction.

Franke and Rodi (1991) calculated the vortex shedding behind a surface mounted square cylinder at a Reynolds number of 2.2×10^4 . Three variants of the $k-\epsilon$ eddy-viscosity model and two Reynolds-stress equation models were used to model the turbulence characteristics of the flow. The experimental data used were from Lyn (1989) who used a two-component LDV system, and from Durao, et al. (1988) for a Reynolds number of 1.4×10^4 . They found that the variations between the $k-\epsilon$ models and the Reynolds Stress models (RSM) were due to the near-wall treatments. They concluded that the RSM models

do a better job in predicting the length of the recirculation region and the level of total turbulence fluctuations.

More recently, numerical studies using various CFD techniques continued to be applied to simple bluff-body geometries. These studies have produced solutions using techniques varying in sophistication from steady-state algebraic stress models, to the dynamic subgrid-scale, Large-Eddy Simulations (LES) of Yang and Ferziger (1993).

Some early solutions modeled only half of the geometry, thus imposing symmetry on the flow. Time-averaged measurements indicated that the flowfield was symmetric with a steady pair of vortices downstream of the bluff body. However, detailed studies have shown that the instantaneous flowfield consists of a structured pattern of alternating large scale vortices. A symmetry plane enforced by the numerical model precludes the formation of the shed vortices, and thus requires the turbulence model to predict the proper turbulent fluctuations in the wake. Comparisons to experimental measurements have shown such predictions to be inadequate for bluff-body flowfields.

The LES technique is formulated and applied to a plane channel flow in which a two-dimensional obstacle is mounted to the tunnel-surface as reported by Yang and Ferziger (1993). The Reynolds number was 3.2×10^3 , based on the height of the obstacle. A Direct Numerical Simulation (DNS) was also conducted for comparison. They noticed that although the obstacle is two dimensional, the instantaneous separation and reattachment lines were found to be far from two dimensional. Secondary and tertiary unsteady flow regions were found near the bluff body. No comparisons with experimental measurements were made.

Werner and Wengle (1991) applied the LES technique to model the flow downstream of a 3-d bluff body (cube) mounted on the surface of a plate channel, at a Reynolds number of 5×10^4 . After comparison of their predicted results with the experimental data of Larousse, et al. (1991), they recommended that an improved spatial resolution immediately above the top face of the cube and near the two sides was necessary. In the case of the shear stress comparison, they concluded that second-order statistical moments (like \bar{uv}) were not sufficiently smooth in certain regions of the flow, such as just downstream of the bluff body, and at the reattachment region. This was attributed to the slowly converging second-order statistics in these particular flow regions.

The Renormalized Group (RNG) theory was applied by Choudhury, et al. (1993) to a selected number of separated turbulent flows, such as a backward-facing step and the periodic vortex shedding behind a circular cylinder. A substantial improvement over conventional turbulence models was realized, especially in predicting the mean flow quantities and in capturing the vortex shedding frequency, when the RNG k- ϵ model was used.

Also, Yakhot and Orszag (1992) reported excellent results for homogeneous shear flow and for flow over a backward-facing step. For the shear flow, the modified Reynolds stress transport model was also used. The modified eddy viscosity models gave the best results for the backward-facing step flow. In all cases no adjustments to the model turbulence constants were made.

1.4 Outline

The primary objective of this research was to perform an extensive experimental study of the flowfield downstream of a 2-d bluff body, mounted at mid-stream in a rectangular cross-section test section. The test conditions are atmospheric pressure and temperature. An experimental 3-d mapping of the flowfield in the near- and far-field regions downstream of as well as upstream of the bluff body is presented. The velocities were measured with a state-of-the-art 3-d LDV system. This allowed for nonintrusive pointwise measurements throughout the tunnel test section. The flowfield properties of interest include mean and fluctuating axial, transverse, and spanwise velocities, turbulent normal and Reynolds stresses and turbulent triple products. Comparisons of some of these measurements with CFD generated predictions are also presented.

Chapter 2 is a review of turbulence modeling and is presented primarily to show which turbulence parameters are of interest to turbulence modelers. This section is offered as guidance to the experimentalist so that useful turbulence measurements result.

The experimental apparatus, designed and used for this study, is described in detail in Chapter 3. The LDV system, flow system, the bluff-body geometry, and the test section design are presented in this chapter.

Chapter 4 describes the test procedure and summarizes the test run conditions. A discussion of measurement uncertainty and errors is also given here.

The far-field velocity measurements and turbulence parameters are presented in Chapter 5. The axial stations include two upstream and nine downstream locations.

The near-field velocity measurements and turbulence parameters are presented in Chapter 6. Also included are experimentally approximated expressions for \overline{ww} , \overline{vww} , and \overline{uvw} . A turbulent kinetic energy balance, used to estimate the turbulent dissipation rate, is also presented using the measurements made in the near-field region. A statistical uncertainty estimate for each of the TKE terms, at the recirculating bubble station location ($x/H=0.9$), is also presented. Spatial gradients of some important fluid parameters and a check of the two-dimensionality of the flow are also included.

Comparisons of the numerical predictions with experimental measurements are presented in Chapter 7.

Finally, conclusions and recommendations are given in Chapter 8.

CHAPTER 2

TURBULENCE MODELING

2.1 Introduction

Most flows occurring in the area of fluid mechanics and related applications are turbulent in nature. No specific definition can be given to such a phenomenon. However, turbulence is commonly described by its flow characteristics (Tennekes and Lumley, 1972). Turbulent flows are random and have unique characteristics; every turbulent flow is different. In general, turbulent flows exhibit large irregular spatial and temporal fluctuations in velocity, pressure, temperature, and vorticity. It is this irregularity of the flowfield that necessitates the usage of statistical averaging methods for the determination of turbulence parameters, a technique widely accepted in engineering. Because turbulent flows are so prevalent and interdisciplinary, there has been an increased interest in better understanding turbulent flow phenomena. In particular, Computational Fluid Dynamics (CFD) has surged as a new and very important methodology for predicting and better understanding the turbulent flow phenomena. One driving force for this activity in turbulence modeling is the recent development of high-speed digital computers, needed to solve the mathematical equations that attempt to model complex problems such as those encountered in turbulent flows. One of the underlying reasons for the interest of making the measurements reported in this study, is the validation of the computational approach (or numerical code) for predicting the mixing behind bluff-body flameholders. So far, most practical turbulence models fail to properly predict or capture the basic features of turbulent separated flows such as those

resulting from vortex shedding behind a bluff body. The nature of complex flows demand the solution to the nonlinear, rotational, three-dimensional and time-dependent flow equations. Some of the parameters of interest are the magnitude of the velocity vector, turbulence intensities, the Reynolds stresses, the vortex-shedding frequency and the length of the recirculation region. A brief description of turbulence modeling is presented next.

2.2 Origin and Theory of Turbulence Modeling

The subject of turbulence began to be better understood some 100 years ago, when Osborne Reynolds (1895) came-up with the idea of time-averaging the Navier-Stokes equations (NSE). Since turbulence is a continuum phenomenon, the time-dependent, three-dimensional NSE should give a sufficient description of the physics of turbulent flow. Consequently, statistical averaging methods using time-averaging must be used, which in turn lead to statistical correlations which must be determined in order for closure to take place. The dynamic behavior of laminar, as well as turbulent flows, for a Newtonian fluid in the absence of any external body forces is governed by the momentum transport balance, written in Cartesian-tensor notation as;

$$\frac{\partial(\rho U_i)}{\partial t} + \frac{\partial(\rho U_i U_j)}{\partial x_j} = -\frac{\partial P}{\partial x_i} + \frac{\partial}{\partial x_j} \left[\mu \left(\frac{\partial U_i}{\partial x_j} + \frac{\partial U_j}{\partial x_i} \right) \right] \quad (2.1)$$

The conservation of mass principle necessitates the use of the continuity equation as;

$$\frac{\partial}{\partial x_i} (\rho U_i) = 0 \quad (2.2)$$

Equation (2.2) together with the momentum transport balance (2.1) constitute the Navier-Stokes equations. These equations are given in rectangular coordinates here so as to be

useful for the current study. The instantaneous velocities U_i are then decomposed into a mean velocity \bar{U}_i , and velocity fluctuations u_i , such that;

$$U_i = \bar{U}_i + u_i \quad (2.3)$$

Where \bar{U}_i is interpreted as the time-averaged velocity, defined as;

$$\bar{U}_i = \frac{1}{2T} \int_{-T}^T U_i dt \quad (\text{as } T \rightarrow \infty) \quad (2.4)$$

(The mean value of a fluctuating quantity is zero by definition.)

These definitions are then substituted into the Navier-Stokes equations, and expanded giving the time-averaged momentum equations for turbulent flow also called the Reynolds averaged equations. The governing equation is given in tensor form as;

$$\frac{\partial(\rho \bar{U}_i)}{\partial t} + \frac{\partial(\rho \bar{U}_i \bar{U}_j)}{\partial x_j} = -\frac{\partial \bar{P}}{\partial x_i} + \frac{\partial}{\partial x_j} [\mu \left(\frac{\partial \bar{U}_i}{\partial x_j} + \frac{\partial \bar{U}_j}{\partial x_i} \right) - \rho \bar{u}_i \bar{u}_j] \quad (2.5)$$

This equation is identical to the NSE (2.1) except for the appearance of second-moment correlation involving the turbulent velocity fluctuation terms, $\rho \bar{u}_i \bar{u}_j$. Similar to the pressure and viscous stresses, these fluctuating inertia terms act on an element of the fluid and have the dimensions of shear stress (force/area). These are turbulent stresses induced into the flow because of turbulence. The additional stresses are identified after their originator, Reynolds, and are commonly known as the “apparent” or “turbulent” or “Reynolds” stresses. They add complexity to the problem by introducing six additional equations to the three-dimensional flow equations, which must be prescribed first in order to solve Equation (2.5) for the mean-flow parameters. Since we have more unknowns than we have equations, the objective of turbulence modeling is to define additional equations which relate these unknown Reynolds

stresses to the mean-flow parameters. Since, these equations cannot be determined a priori, this process is known as turbulence closure.

Turbulence modeling was initially formed on the mathematical derivation of the turbulent stresses using the same procedure used for laminar flows. The predominant assumption was that the effects of turbulence in the flowfield can be related to mean-flow parameters, such as the mean velocity gradient. Boussinesq (1877) was the first to propose the concept of an “apparent” or “turbulent” or “eddy” viscosity. In order to account for the presence of the Reynolds stresses in the turbulent momentum balance of Equation (2.5), it becomes necessary to model and evaluate these Reynolds stresses suitably. Boussinesq reasoned that the apparent turbulent shearing stresses act similar to viscous stresses and thus might be related to the local rate of mean strain through an apparent turbulent viscosity (see Hinze, 1975). He formulated the concept of an eddy-viscosity defined as follows;

$$-\rho \overline{u_i u_j} = \mu_t \left(\frac{\partial \overline{U}_i}{\partial x_j} + \frac{\partial \overline{U}_j}{\partial x_i} \right) \quad (2.6)$$

The proportionality factor, μ_t , is known as the “apparent turbulent coefficient of viscosity” or “eddy-viscosity” and is analogous to the constant of proportionality of the fluid’s laminar molecular viscosity, μ . The problem now is to find a suitable value or relation for determining μ_t . Boussinesq originally assumed a constant value of eddy-viscosity, μ_t . However, unlike laminar flows, turbulent flows are nonhomogeneous, and a single value for μ_t would imply homogeneity. The ‘turbulent viscosity’ of the fluid, μ_t , unlike the laminar viscosity which is a property of the fluid, is a flow-dependent variable since turbulence is a characteristic of the flow. Another problem lies in the mathematical contraction of Equation (2.6). If i is set to j and summed from $i = 1$ to 3 , the right-hand side is zero as required by

continuity, but the left-hand side is zero only if there is no turbulence. Therefore, to correct for this deficiency, Equation (2.6) is modified by an additional term as shown by;

$$-\rho \overline{u_i u_j} = \mu_t \left(\frac{\partial \overline{U}_i}{\partial x_j} + \frac{\partial \overline{U}_j}{\partial x_i} \right) - \frac{2}{3} \delta_{ij} k \quad (2.7)$$

Where k is the turbulent kinetic energy (TKE), and δ_{ij} is the Kronecker delta ($\delta_{ij} = 1$ if $i = j$ and $\delta_{ij} = 0$ if $i \neq j$).

Substitution of Equation (2.7) into Equation (2.5) yields;

$$\frac{\partial (\rho \overline{U}_i)}{\partial t} + \frac{\partial (\rho \overline{U}_i \overline{U}_j)}{\partial x_j} = -\frac{\partial \overline{P}}{\partial x_i} + \frac{\partial}{\partial x_j} [(\mu + \mu_t) \left(\frac{\partial \overline{U}_i}{\partial x_j} + \frac{\partial \overline{U}_j}{\partial x_i} \right)] \quad (2.8)$$

Equation (2.8) is also known as the "Boussinesq Effective Viscosity Model" since $(\mu + \mu_t)$ together constitute the effective laminar and turbulent viscosities, i.e., $\mu_{eff} = \mu + \mu_t$.

As mentioned earlier, the turbulent viscosity varies throughout the flowfield depending on the local flow conditions. It represents a measure of both eddy size and strength, and must therefore be modeled in terms of parameters which reflect these two quantities. The earliest attempt to develop an expression for turbulent viscosity that varies with position in the turbulent flow, was the so-called mixing-length hypothesis. This was first initiated by Taylor (1915), but is more often attributed to Prandtl (1925), some 10 years later. Prandtl, who discovered the boundary layer in 1904, now reasoned, partly on dimensional grounds, that the turbulent viscosity was proportional to the magnitude of the mean-strain rate, and to the square of a characteristic eddy-length scale. Since the mean strain rate has dimension $time^{-1}$, it can be thought of as a time scale. Therefore, if the mixing length is multiplied by this quantity, a

turbulent-velocity scale would result. The expression for turbulent viscosity derived from the mixing-length hypothesis, and written below as Equation (2.9), represents the product of a length scale and a velocity gradient. The eddy-viscosity, according to the mixing length hypothesis, is then prescribed as follows;

$$\mu_t = \rho l^2 \frac{\partial \bar{U}_i}{\partial x_j} \quad (2.9)$$

where, l , a linear dimension called the mixing length, is a characteristic of the flowfield, and is prescribed empirically. The shortcomings of this model include the difficulty in prescribing the mixing length for complicated flow geometries and the fact that μ_t vanishes in regions of zero mean velocity gradient. Another major drawback of this model is that it fails to take into account the processes associated with the transport of turbulence, thus isolating the eddy-viscosity at one particular point and making it unresponsive to changes in the flowfield at other locations. In other words, the mixing length must be known a priori everywhere in the flowfield in order to be used. Although in its general form, the mixing-length hypothesis is capable of producing adequate results for simple boundary-layer-type flows, it is unable to accurately predict flows with complex strain fields, such as those influenced by strong streamline curvature. Clearly, for complex flowfields such as those encountered behind 2-d and 3-d geometries, modifications are required to the mixing-length derivation before it can be used successfully.

Another approach to the turbulent viscosity dilemma was suggested by Kolmogorov in 1943 and later by Prandtl in 1945. The reasoning is that there exists a connection between turbulence parameters and the eddy-viscosity. They formulated a revised expression for the turbulent viscosity, known as the Prandtl-Kolmogorov turbulent-viscosity formula (1945);

$$\mu_t = \rho k^{1/2} l \quad (2.10)$$

The length scale, l , is now proportional to the size of the turbulent eddies, and must be prescribed explicitly. The turbulent viscosity is considered to be proportional to the square root of the TKE, k , which may be calculated throughout the flowfield, and easily interpreted physically. This is obtained from the solution of a related transport partial differential equation. A conservation equation for the TKE is derived by multiplying the i^{th} momentum equation by u_i and then summing from $i = 1$ to 3. The final form of the TKE conservation equation, in the fully turbulent regime, for flows with constant density in tensor notation is written as follows (see also Appendix F);

$$\frac{\partial k}{\partial t} + \bar{U}_j \frac{\partial k}{\partial x_j} = -\bar{u}_i \bar{u}_j \frac{\partial \bar{U}_i}{\partial x_j} - \frac{\partial}{\partial x_j} \left(\frac{\bar{u}_i^2 \bar{u}_j}{2} + \frac{\bar{p} \bar{u}_j}{\rho} \right) - v \frac{\partial k}{\partial x_j} - v \left(\frac{\partial \bar{u}_i}{\partial x_j} \right) \left(\frac{\partial \bar{u}_i}{\partial x_j} \right) \quad (2.11)$$

where the TKE is defined as; $k \equiv \frac{1}{2} (\bar{u}_i \bar{u}_i) \equiv \frac{1}{2} (\bar{u}^2 + \bar{v}^2 + \bar{w}^2)$, and $v = \mu / \rho$.

The general terms represented in Equation (2.11) describe the physical processes of turbulence. The first term on the right is the production term and represents the rate at which kinetic energy is generated and transferred to the turbulence. The second term on the right is known as the diffusion term and contains the triple velocity correlation terms known as the turbulent diffusion transport terms, the pressure diffusion terms resulting from pressure and velocity correlations, and the molecular diffusion terms. The third term on the right is the dissipation term and describes the rate at which turbulence is dissipated into heat or thermal energy. The first term on the left describes the unsteady behavior of TKE. The second term on the left is the convection term and describes the rate of convection of TKE. The terms on the left give the Eulerian derivative of TKE and describe its rate of change following a fluid

particle. For closure to take place, the production, dissipation, turbulent diffusion (triple products), and pressure-velocity correlation terms in the TKE equation have to be modeled, since they involve unknown correlations. This closure technique requires the use of approximations which are for the most part deductions and assumptions obtained when studying isolated or easily defined turbulent flows.

This alternate formulation for the turbulent viscosity, together with similar suggestions of other workers, is known collectively as "one-equation models." They are now distinguished from the models discussed previously, which are often referred to as "zero-equation models." Although this concept overcomes the problem of the eddy-viscosity going to zero as the mean velocity gradient vanishes, an a priori prescription for the length scale of turbulence, l , is still necessary, and therefore it has some of the same deficiencies as the mixing-length theory.

To reach a more universal model that overcomes this deficiency, "two-equation models" have been developed where the transport of the turbulence length scales are also accounted for. In addition to the Boussinesq approximation, and the TKE equation, a conservation equation for a variable that is a composite of k and l is solved. This constitutes a complete model of turbulence where no prior knowledge of turbulent structure is necessary. The differential equation for an independent solution for l is very awkward and not recommended. Many models have been developed in the past that used various possible combinations of k and l , such as the $k - \omega$ model of Kolmogorov; the $k - \varepsilon$ model of Chou (1945), Davidou (1961), and Harlow and Nakayama (1968); and the $k - kl$ model of Rotta (1968). However, the most popular of these two-equation models is the $k - \varepsilon$ model. The standard $k - \varepsilon$ model was well described by Jones and Launder (1972), but widely used in the form of Launder and Sharma (1974) who "retuned" the closure coefficients. The goal is to find

and solve a conservation equation for the dissipation rate, ε , with suitable closure approximations. For high Reynolds-number flows, ε is shown to be related to the turbulent length scale through;

$$\varepsilon \propto \frac{k^{3/2}}{l} \quad (2.12)$$

The turbulence closure problem is now resolved and the need to specify a length scale is overcome. The turbulent viscosity can then be obtained by dimensional arguments via;

$$\mu_t = \frac{C_\mu \rho k^2}{\varepsilon} \quad (2.13)$$

However, the TKE conservation equation and the much more complicated dissipation rate conservation equation contain several terms that are practically impossible to obtain, such as the pressure-velocity correlations terms, and the double and triple correlations of fluctuating velocity terms. These terms are generally labeled in a fashion similar to the TKE terms mentioned earlier, but in this case instead of k , they identify ε . Therefore, in order for closure to be possible, certain simplifying assumptions about these terms have to be made. For instance, measurements made in simple turbulent flows give the three “universal” constants, $C_{\varepsilon 1}$, $C_{\varepsilon 2}$, and C_μ . $C_{\varepsilon 2}$ is obtained from measurements of decaying turbulence similar to that found behind a grid in the absence of mean velocity gradients. Also, from experimental observations made in the near-wall region of a fully developed turbulent boundary layer, both convection and diffusion of TKE are very small and may be neglected, which means that turbulence generation is relatively in balance with turbulence dissipation. Under these conditions, the TKE for eddy viscosity reduces to the Prandtl's mixing-length formulation. This allows the approximation of the other two constants, $C_{\varepsilon 1}$, and C_μ .

The $k - \varepsilon$ turbulence model has proven to be useful for a large variety of flows including those where the streamlines do not curve significantly in shear regions, such as straight boundary layers, wakes and jets, where the shear-stresses dominate the coupling between the turbulence and mean-velocity fields. However, in curved flows, particularly when the normal-stresses contribute greatly to mean transport, such as in recirculating flow, the $k - \varepsilon$ model fares less well. Although the general features of the flow can sometimes be captured reasonably, the predicted turbulence quantities often show poor agreement with experimental measurements.

One of the major drawbacks of the two-equation turbulence models and for that matter any eddy-viscosity-based turbulence model is the implicit assumption of isotropic turbulence. That is, the models do not account for rotational or translational differences in the turbulent normal stresses. This is due to the turbulent pressure term which tends to overwhelm the velocity gradient terms in most flows and hence forces the three normal stresses to $2k/3$. In algebraic models, the turbulent viscosity is a local function while in the two-equation models it is a more complicated and more general function governed by two partial differential equations. The eddy-viscosity model simply relates the Reynolds stresses and the local mean velocity gradients or rates of mean strain via some empirically determined turbulent viscosity relationship.

It is well known that all shear flows and wall turbulence flows are anisotropic which raises doubts in the use of eddy-viscosity based turbulence models. To remedy this problem, Reynolds Stress Models (RSM) have been proposed. These models complete closure to the Reynolds equations without using the turbulent viscosity assumption. Like the two-equation models, the shortcoming of this modeling technique is the need to make assumptions

concerning the various terms to be evaluated, such as those encountered in the TKE transport equation. The terms that have been measured in this study include the nine third-order turbulent velocity correlations.

All the models mentioned above rely on assumptions and approximations for evaluation of high order correlations. Their success remains closely related to how well these terms are modeled and whether they are important in determining the transport of turbulence. Clearly, there still exists plenty of room for improvement and refinement.

Among the non-eddy viscosity based numerical computational methods available is the Algebraic Stress Model (ASM). This technique, first proposed by Rodi (1972), is sometimes considered simple, and yet still efficient to predict complex turbulent shear flows. With this method, the differential transport equations for the Reynolds stresses are replaced by a set of algebraic equations for Reynolds stresses assuming that the convection-diffusion term of the kinetic energy equation is proportional to that of the Reynolds-stress transport equations.

Of particular interest is the Renormalization Group (RNG) theory first applied to the $k-\epsilon$ turbulence model by Yakhot and Orszag in 1986, and later improved by Yakhot, et al. in 1992. The goal of the RNG theory is to systematically remove the smallest turbulent scales to a point where the remaining scales are resolvable. The constants used in the RNG $k-\epsilon$ model are derived from theory, removing much of the ad-hoc nature of the standard $k-\epsilon$ model, and represents the major functional difference between the models. Also, unlike the Reynolds Stress models which are based on Reynolds averaging, a technique that smoothes out some of the important features of turbulence, the RNG theory systematically removes the

smallest scales of turbulence to the point where the remaining scales are resolvable with currently available computer capabilities (Yakhot and Orszag, 1992).

Of all modeling techniques mentioned above, the two-equation eddy viscosity turbulence model remains the most widely used due to its simplicity and flexibility. Although it does not properly model the turbulence parameters in highly complex flows, it gives results good enough to allow the engineer to make certain decisions. Some recently modified versions of the $k - \epsilon$ model have given better results than the standard model as will be shown later in this study.

The current study shows a comparison between the experimental data and results from three numerical solutions; 1) a symmetric, steady-state $k - \epsilon$ solution; 2) a standard $k - \epsilon$, time-accurate solution; and 3) an RNG $k - \epsilon$, time-accurate solution. All solutions are two dimensional, and the mean velocities and Reynolds stresses are compared to the experimental measurements.

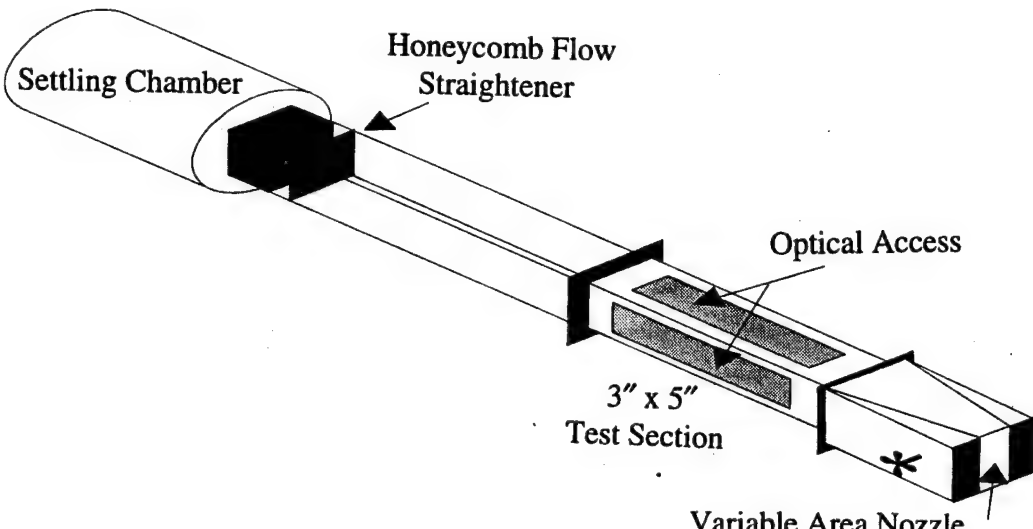
CHAPTER 3

EXPERIMENTAL APPARATUS

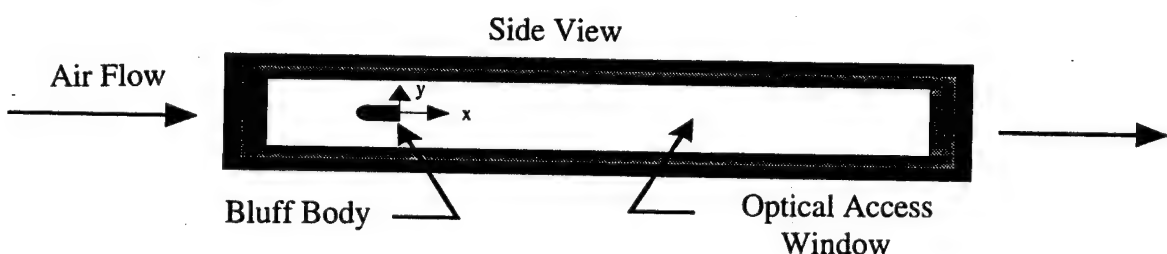
3.1 Facility

Schematics of the wind tunnel and the 2-d test section used for this study are shown in Figure 1. The test facility is located in Test Cell 18 at the Aero Propulsion and Power Directorate of Wright Laboratory, Ohio, and was designed and constructed to accommodate flow visualization and laser-based diagnostics. Full-view fused quartz windows on the top, bottom, and the two side walls, provide optical access to the 76.2-mm x 127-mm x 762-mm (3-in x 5-in x 30-in) test section. Air flow was supplied by a 7.5-horsepower radial fan blower followed by a 152.4-mm (6-in) diameter honeycomb flow straightening section and settling chamber. The flow straightener was placed close to the fan outlet to reduce the large scale turbulence produced by the fan. The air was further conditioned by passing through another set of honeycomb flow straighteners placed 304.8 mm (12 in) upstream of the test section entrance. Fine mesh screens were removed from this flow downstream of the straightening section because these became clogged with seed particles in an unpredictable and nonuniform fashion. Test section flow parameters, such as static pressure, and total temperature were monitored and recorded by a micro-computer based data acquisition system. For the present study, the inlet centerline reference velocity, U_{ref} , was monitored using a pitot/static tube, connected to a high resolution manometer, and located at $x/H=-24$ (12 inches upstream of the bluff body). The averaged inlet reference velocity was ~ 23.78 m/s

(78 ft/s), corresponding to a tunnel Mach number of 0.08 and a Reynolds number of 2.0×10^4 based on inlet flow conditions and the bluff-body height, H.



a) Flow Facility



b) Test Section

Figure 1. Experimental test facility.

3.2 Bluff Body

The shape of the bluff-body flameholder affects the flow stability characteristics through the influence on the size and shape of the wake region (Lefebvre, 1983). One of the primary functions of a flameholder is its ability to anchor the flame by creating a recirculation zone that enhances the mixing of the injected fuel and the incoming air. The recirculation zone is created when the static pressure in the central core, just downstream of

the bluff body, becomes low enough to create flow recirculation. The size of the recirculation zone can be increased by modifying the flameholder geometry. Increasing the recirculation zone length has a tendency to raise the maximum reverse mass flow and the rate of entrainment, albeit with some increase in pressure loss (Lefebvre, 1983). According to Fox & McDonald (1978), a hemispherical geometry, with the rounded head facing upstream, showed the lowest total (pressure and friction) drag coefficient, typically a C_d of 0.38. Therefore, a bluff body with a blunt nose geometry was selected for this study. A schematic of the bluff-body model and its orientation to the coordinate system is shown in Figure 2. The 25.4-mm (1-in.) long model consisted of: 1) a 6.35-mm (0.25-in) radius hemispherical nose, 2) a 15.875-mm (0.625-in) thick rectangular center section and, 3) a 3.175-mm (0.125-in) base/dump plate. This last section is interchangeable to allow for attachment of various vortex generator designs. The bluff-body height (H) was 12.7 mm (0.5 in), and spanned the entire test section giving a tunnel blockage of 16%.

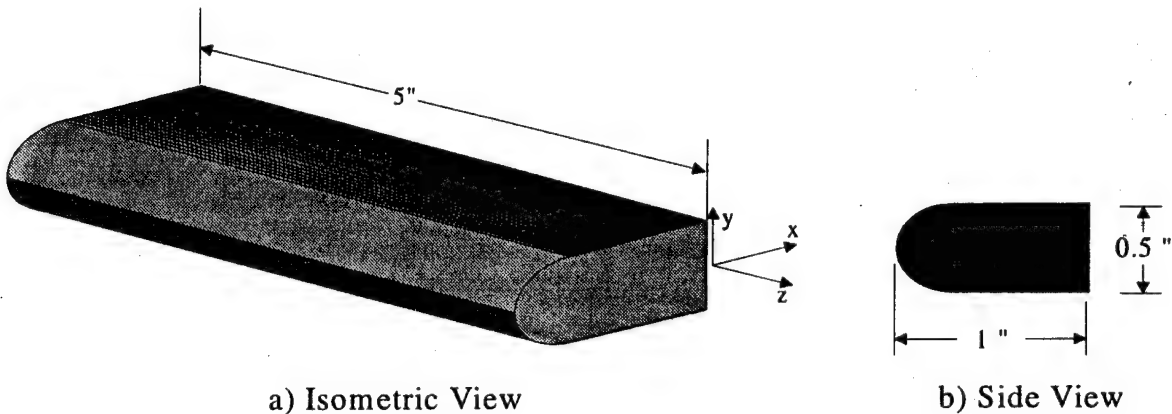


Figure 2. Bluff-body model schematic.

The model was mounted directly to the side wall windows as indicated in Figure 1b, in order to eliminate flow disturbing model supports (i.e. stings). The model was mounted

127 mm (4 inches) into the test section, downstream of the side window leading edge. Great care was taken to minimize the effect of the upstream influences on downstream flow behavior, since previous work had shown that the flow in the wake of a bluff body can be three-dimensional. This arrangement (see Figure 1b) provided the best optical access for probing the entire flowfield surrounding the bluff body. Care was taken to align the bluff body with respect to the laser Doppler velocimeter probe volume by running the laser beam along the edge of the bluff body.

3.3 Laser Doppler Velocimetry

Laser Doppler velocimetry (LDV) has been used for fluid flow measurement since the mid 1960's. Durst, et al. (1976) describes the theory and application of LDV at length. LDV is a nonintrusive instrument used to measure turbulent velocity fields without disturbing the flow, and where conventional techniques (i.e., hot wire) are not practical. Typical applications include turbulent boundary layers, vortices and wakes, such as the recirculation zone behind a bluff body or a backward-facing step. A single probe volume is created by crossing two polarized laser beams. At the crossing, the two beams constructively and destructively interfere to create fringes of light as shown in Figure 3. As seed particles in the flow pass through the probe volume, the scattered light from the fringes yield an amplitude modulated sinusoidal signal, called a Doppler burst. The frequency of the scattered light as the particle crosses bright and dark fringes is related to the particle velocity component perpendicular to the fringe direction by the following relation;

$$U(x, y, z) = \frac{f_d \lambda}{2 \sin(\phi / 2)} \quad (3.1)$$

Where λ is the laser beam wavelength, f_d the measured instantaneous Doppler frequency of the particle, and ϕ is the angle between the two laser beams being crossed to form the probe volume, also identified as the beam separation angle (see Appendix A).

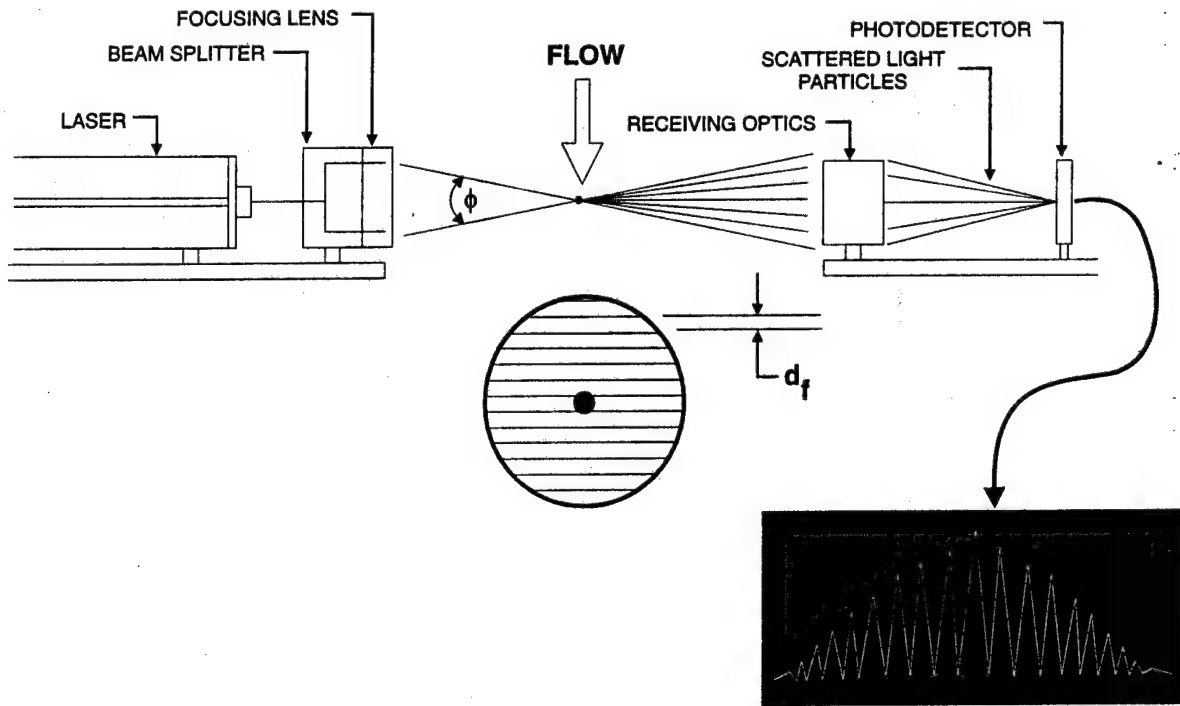


Figure 3. Typical dual beam laser Doppler anemometer

It is important to note that the velocity measured is the component perpendicular to the fringes in the probe volume. Two- and three-dimensional LDV systems are created by focusing additional pairs of laser beams of different colors at the same location, but at another orientation. By varying the orientation of the three sets of beams, three independent components of the same velocity vector can be measured simultaneously. The scattered light is collected by a lens and focused onto a pinhole aperture of a photomultiplier tube (PMT) (or photodetector), which transmits an electrical signal; a voltage modulated at the Doppler frequency that can be analyzed by a signal processor. The LDV signal processors amplify

and filter the signals from the photomultiplier, validate the Doppler frequency samples, and finally compute the Doppler period which is the reciprocal of the Doppler frequency. This integer number (in nanoseconds) is then transmitted to the computer. The Doppler frequency of the signal gives the velocity of the particle at the instance it passes through the probe volume. The particles arrive randomly at the measurement volume, and hence the output signal of an LDV used in a turbulent flow is a randomly-sampled signal.

Both one-component and three-component LDV system configurations were used in this study. The one-component system was used for validation of the three-component system as well as for mass-balance verification. The orientation of this system was such that the beams passed through the side windows of the test section, parallel to the top and bottom tunnel surfaces, and thus allowed for the measurement of the axial velocities at locations very close to the top and bottom tunnel walls. The far-field measurements were taken using two separate TSI fiber-optic probes based LDV systems. The three-component LDV system was mounted around the rectangular test section and was operated in the forward-scatter mode. Simultaneous measurements of axial (U), transverse (V), and spanwise (W) components of the velocity vector (see Appendix B) were made throughout the tunnel test section. In both the near- and the far-field measurements, the third component came from a second independent one Watt argon-ion laser. The optics were arranged to obtain a minimum beam waist diameter at the probe volume location. This gave the highest beam intensity. The transmitting and receiving optics were mounted on an xyz optical table capable of placing the measurement probe volume at various points throughout the tunnel test section with a resolution of ± 0.03 mm.

3.3.1 Far-Field LDV System

A three-component LDV system operating in the forward-scatter mode was mounted around the rectangular test section to make simultaneous measurements of the U, V, and W-velocity components. The optical system used in the experiments involved two separate fiber-optic based TSI Inc. laser Doppler systems. This allowed the laser beams to be oriented orthogonal to each other giving direct measurements of the three-orthogonal velocity components. A TSI Colorburst beam separator was used to separate the various wavelengths. The two most intense argon laser lines, the green ($\lambda=514.5$ nanometers) and the blue ($\lambda=488$ nanometers), were split into two beams of near equal intensity, frequency shifted, and directed via fiber-optic cables to a TSI model 9277 two-component fiber-optic probe. The transmitting optics included a 3.75x beam expander (for a full explanation of this term and other laser related terms, see Appendix C) and had a focal length of 450 mm. The orientation of this system was such that the beams passed through the side windows of the test section and thus allowed for the measurement of the axial and transverse (U,V) velocity components. In the other LDV system, the violet argon laser line ($\lambda=476.5$ nanometers) from a second argon laser was directed via fiber-optic cable to a TSI model 9274 one-component fiber-optic probe. This allowed the measurement of the spanwise velocity component (W). The orientation of this system was such that the beams were orthogonal to each other and thus passed through the top and bottom test section windows. In order to avoid directional ambiguity that would otherwise result from the highly turbulent recirculating flow, a 40-MHz frequency shift was applied to one beam in each of the three components. Both argon-ion lasers were operated at approximately one Watt for all measurements. The approximate

probe volume dimensions were 600- μm long and 80- μm diameter for the two-component system and 150- μm long and 100- μm diameter for the one-component system (see Appendix A). The fringe spacings for the green, the blue, and the violet were 1.738- μm , 1.827- μm , and 3.439- μm , respectively. The receiving optics consisted of a 120-mm lens focused onto a 0.25-mm diameter photomultiplier-tube aperture via an appropriate dichroic filter to selectively pass either the blue or green beams. Additionally, laser line filters were mounted to each photomultiplier tube. The violet signal was collected in the forward-scattered mode which was at ninety degrees with respect to the blue and the green axis in this system. A 476.5-nm laser line filter was used here to minimize signal cross-talk. Due to the requirement imposed by the processing electronics, that axial, transverse, and spanwise velocity components be obtained simultaneously, a great effort was made to ensure that the three separate probe volumes were coincident by passing all three through a 35- μm pinhole placed at 45 degrees to the violet and blue/green beam propagation directions. The effective measurement probe volume shape now becomes a sphere with a diameter equal to the beam waist with a cross-sectional area approximately equal to 0.008 mm², that of the violet beam. Although the effective probe volume size is reduced by the addition of the third component, the set-up had to be perfected in order to ensure that: 1.) all six beams passed through the pinhole, and 2.) that the beam's intensity was optimized as well as other factors which have to do with optimizing the data rate. These efforts are all responsible for producing the high quality, smooth and symmetric profiles that were observed in the resulting measurements of this study.

3.3.2 Near-Field LDV System

The system described above has a severe limitation insofar as it is geometrically impossible to obtain data in the near-wake region. It is physically impossible to get all three probe volume to coincide at a distance less than 12.7 mm (0.50 in) from the base of the bluff body, when at the center span location. Therefore, a different system setup was used in the near-field region. In this setup, the green and blue fringes were oriented at 90 degrees with respect to each other (i.e. orthogonal) and oriented at 45 and 135 degrees with respect to the horizontal axis of the test section. This allowed the measurements to be made to within 6.35 mm (0.25 in) of the trailing edge of the bluff body. The transformation equations discussed in Appendix B were used to recover the velocity components. The LDV used for this set of experiments was a conventional two-color, four-beam, back-scatter system (as shown in Figure 4). However, to achieve higher data rates and to increase the signal-to-noise ratio, the receiving optics were arranged in a forward-scatter configuration for this study. The LDV system included Bragg-cell modulators to allow a net frequency shift of 40 MHz in both the green and the blue beams. No beam expander was used in this system set-up. An 80-mm diameter, 181.5-mm focal length lens for transmitting, was used. The blue and the green lines of an argon-ion laser operating at one Watt were used in all measurements. The approximate measurement volume dimensions based on $1/e^2$ intensity points of the measuring volume were 600 μm in length and 80 μm in diameter (see Appendix A). Scattered light from the probe volume was separated with a dichroic filter so that approximately 80% of each color was passed to its respective photomultiplier tube. Narrow

bandpass filters are used to further reduce signal cross talk. The violet laser line was brought-in from the top similar to the far-field measurements case discussed earlier.

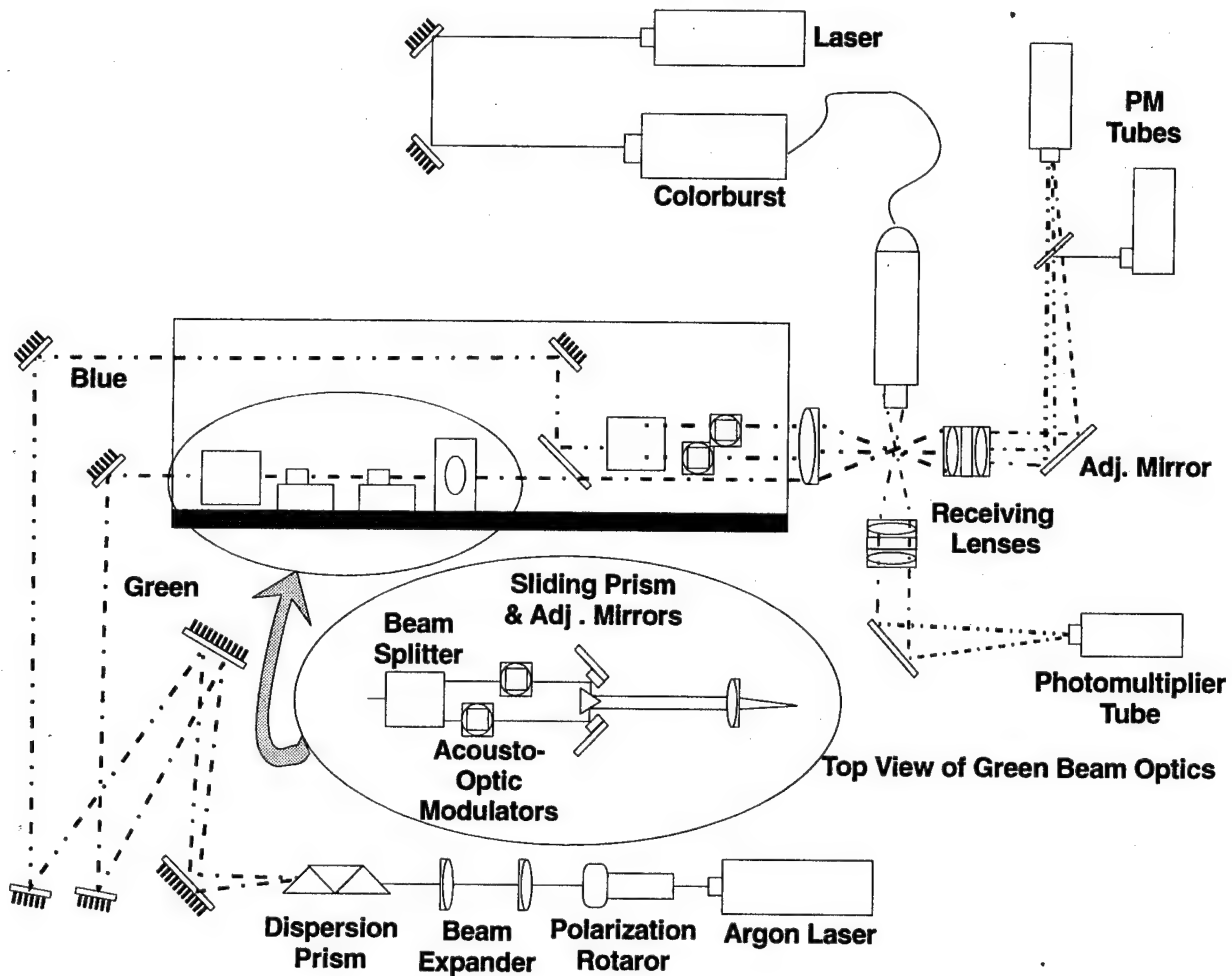


Figure 4. Near-field LDV setup.

For both LDV systems, in order to ensure spatial coincidence of the three probe volumes, a 35- μm pinhole was placed at 45-degrees at the focal point and all six beams were accurately co-located by forcing (steering) them to pass through the pinhole. The entire optical system was mounted on a three-axis traversing table, which allowed the probe volume to be positioned with a resolution of 0.03 mm (0.001 in). The origin (x,y,z=0) for all

LDV measurements was located on the transverse and spanwise centerline at the trailing edge of the flameholder as shown in Figures 1 and 2. Each LDV channel measured a velocity component for particles traveling through the probe volume.

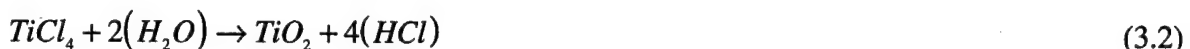
3.4 Flow Seeders

According to Jones, et al. (1990), seeding is the most difficult and often the most neglected aspect of laser velocimetry. Since particles in the flow are the source of the Doppler signal, seeding becomes an important factor in the performance of an LDV system. A classical dilemma arises due to the necessity to provide particles large enough to scatter sufficient light for good signal quality so as to be detected by the photodetector, yet small and light enough to closely follow curved flow streamlines even in fluid flow regimes having steep velocity gradients. Small seeding particles are also necessary in order to capture faithfully the turbulent fluctuations, and the higher order velocity correlations (Maurice, 1992). Any seeding solution represents a trade-off that must be made between signal quality and particle motion fidelity.

Two different flow seeders were used here, one for the far-field and one for the near-field measurements. In both cases, the seed particles were injected upstream of the settling chamber in order to ensure a uniform seed density at the inlet to the test section. This also provided seed densities sufficient to give data validation rates in excess of 10,000 per second for each channel (green, blue, violet beams) over most of the flowfield. The coincidence data rate, for both studies, varied between 1000/sec in the recirculation zone and 5000/sec in the freestream and the far-wake region of the bluff body.

3.4.1 Far-Field Seeding

For the far-field measurements, a chemical seeder developed by Craig, et al. (1984) which produced $\sim 1\text{-}\mu\text{m}$ diameter titanium dioxide particles, was used. The titanium dioxide (TiO_2) seed particles were generated by reacting titanium tetrachloride ($TiCl_4$) with moist air, according to the following chemical reaction;



The titanium dioxide seed particles produced here are the same as those commonly found in "toothpaste." However, the other product of this chemical reaction, is Hydrochloric acid, and is well known to be a health-hazard. Therefore, care was taken to ensure that small quantities of seed particles were generated and properly disposed of by venting the products through a roof-vent. The quantity was measured and controlled via an in-line rotometer. Titanium tetrachloride must be extremely well contained, because of the spontaneous reaction that takes place when placed in contact with moisture in the atmosphere.

The reaction chamber was designed using the specifications given by Nejad (1986). Craig, et al. (1986) measured the particle sizes generated by this device and found that they were fairly spherical and in the $0.2 - 1\text{ }\mu\text{m}$ diameter range. The reaction chamber was capable of supplying seed densities sufficient to give data validation rates ~ 5000 per second. Also, the (TiO_2) seed particles coated the test section windows very quickly, especially in the recirculation zone, and consequently reduced the data validation rate. The validation data rate dropped even further when the measurements were taken in the recirculation zone, where fewer seed particles are found and turbulence intensities are higher.

3.4.2 Near-Field Seeding

For the near-field measurements, a particle generator designed by Rabe and Sabroske (1994) was used. The reference gives a clear description of the seeder. The generator uses four Laskin nozzles submerged in liquid glycerin. Operational guidelines given in their work were followed. They measured the particle size distribution and found that they ranged from 0.5 to 1.0 μm in diameter.

In both the far- and near-field measurements, data acquisition was stopped and the test-section windows were cleaned when the data rate dropped below 1000 per second. Away from the bluff body and in the freestream, the coincident data rate appeared to remain relatively unchanged, at 5000 per second.

The smooth measured profiles indicate that the sample size of 5120 was sufficient to obtain good statistical estimates for the mean and higher order moments and that the flow was statistically steady. The smoothness was further demonstrated when the data were numerically differentiated in the axial and the transverse directions, using central differencing technique. The differentiated data was used in the turbulent kinetic energy equation, and the transport equation.

3.5 Data Acquisition and Processing

The data acquisition and processing system consisted of a three-channel IFA-750 Digital Burst Correlator and Analyzer by TSI, Inc. The IFA-750 signal processor allows for measurement of the Doppler frequencies of all three velocity components and ensures that the measurements are coincident to within a user-specified coincidence window. For multichannel operation, the signal processor ensures that all active channels produce a valid

data point within the coincidence window before data are accepted. Once the point is accepted, data are stored and then multiplexed into the computer via a data parallel interface.

The IFA-750 uses the signal-to-noise ratio (SNR) to distinguish the signal burst from the noise. It receives electrical signals from the photomultipliers, and extracts Doppler frequency information. The data are then analyzed using the Flow Information Display (FIND) software package which displays the turbulence statistics in real-time.

The Doppler signals produced by an LDV occur in short bursts, at random time intervals with typically 10 to 50 cycles in each burst. They are processed after passing through preset low and high-pass filters on each channel processor. There are three types of signals: 1.) A true Doppler signal whose frequency is proportional to the fluid velocity being measured, 2.) a pedestal, and 3.) wide-band noise.

The persistent wide-band background noise, the pedestal, and the fact that the Doppler signals occur at random intervals, all make processing the real signal a "challenging task". In order to extract the Doppler frequency, the Doppler signal has to be separated from the pedestal and the background noise has to be reduced as much as possible. This is done through the high-pass filter which eliminates the pedestal, while the low-pass filter reduces the amplitude of the wide-band or the background noise. Also, the signals occurring at random intervals in short bursts are detected by using a Burst Detector and Sampler. The burst detector is used to discriminate between the Doppler signal and the noise. When a signal exceeds a preset (SNR) level, a burst timer measures the length of the signal burst. Other steps follow to ensure that only good measurements are validated and sent to the computer. A more detailed discussion of how the IFA-750 extracts velocity information from Doppler signals, is available through publications such as the TSI manual (1992).

The TSI IFA-750 autocorrelator was used to process the LDV data, and extract Doppler frequencies. The system was set to operate in the coincidence mode, validate only a single measurement per burst, and to count at least eight fringes. The coincidence window was set to 20 μ sec throughout this study. This means that coincidence between measured velocity components (U, V, and W) has been defined to take place when all three laser velocimeter channels send a validated velocity measurement to the signal processor buffer within 20 μ sec of one another. It is considerably more difficult to obtain physically meaningful three-component data than two-component data. This is largely due to the difficulty in achieving and maintaining coincidence of the three probe volumes to obtain coincident three-component data. This difficulty caused a drop in the coincidence data rate by a factor of 3 to 9 less than the lowest of the three individual data rates was noted. The low and high-pass filters were set to 20 MHz and 100 MHz, respectively, on each of the three processors.

In the post-processing of an LDV data set, "bad" data points may be encountered and should be rejected. No matter how sophisticated the electronic circuitry of the autocorrelator is, there may be some validated points which are not "true" particle velocities, but rather a result of signal noise such as optical, electronic, or a combination of both. These points are called "outliers" or "spurious" since they often lie many standard deviations from the mean. Such points, though few in number, can have a significant effect on the magnitude of the calculated standard of deviation of the data set. Therefore, in this study, extreme outliers were removed first. Then the mean and standard deviation, σ , were calculated. All data lying outside a designated multiple of σ were then eliminated from the original data set. After that, the remaining data are considered as the 'true' data set, for which a new mean and a new

standard deviation are calculated. In addition to the frequency data, the time between data and the probe volume particle residence time were recorded. All sample sets included 5120 individual realizations for each velocity component. The data were filtered using a $\pm 3\sigma$ cut-off limit before final statistical parameters were calculated. In most cases, the signal-to-noise ratio was high and few samples were discarded. The statistical uncertainties of all measured parameters were also calculated using the *jackknife* method (see Benedict & Gould, 1996).

3.6 Velocity Bias

The problem of velocity bias in LDV measurements has been thoroughly examined since it was first recognized by McLaughlin and Tiederman (1973). Velocity bias arises from the fact that signal processors make discrete velocity measurements from individual realizations of seed particles passing through the probe volume. In a uniformly seeded flow, the number of particles per unit time passing through the measurement volume is proportional to the flow rate through that volume. Therefore, simple arithmetic averaging of an ensemble of realizations will produce a mean velocity biased towards values greater than the true temporal mean velocity. This effect is most pronounced in highly turbulent flows, and a number of different schemes have been proposed for its removal. No velocity bias corrections were used in the present study.

3.7 Data Reduction Package

An Intel 486-based PC data analysis system was used for data acquisition, evaluation, manipulation, and storage. In order to collect a realistic statistical sample, a minimum of 5120 realizations per channel were taken at each measurement location. The autocorrelator

time-stamps each velocity realization to allow for post-processing of the data. The data analysis software supplied by TSI, Flow Information Display (FIND), was found to be inadequate for this study for the following reasons; 1.) it did not allow control over angles between laser beams for the various components, 2.) it did not allow control over the Bragg shift direction, 3.) a point-to-point normalization of data was needed to accommodate the variations in the reference velocity, and 4.) it did not calculate statistical uncertainties.

In order to overcome these problems, a new data reduction computer program developed by Gould (1995), was used. This specialized software reads the standard TSI-750 generated output file that contains header information and the velocity and time information for each recorded velocity. User supplied information for the total temperature, pressure, differential pressure, and reference velocity at each point (x, y, z) are then read from an outside file. Advanced LDV data reduction techniques are then used to process, analyze, and prepare the data into a presentable format (a detailed derivation of data reduction equations is found in Appendix D). The angles are taken care of by using the coordinate transformation described in Appendix B. After extreme outliers are eliminated (if they exist), data are reduced once to determine σ , then again with user specified outlier criterion ($\pm 3\sigma$, in this study), and revised statistics are calculated. The reduced LDV data format is presented in Appendix E. The data reduction software output included the following: coordinates (x, y, z), reference velocity, normalized mean velocities, normalized turbulence intensities, normalized turbulent stresses, and normalized turbulent triple products. Also, the raw data from the LDV signal processor are stored and available for researchers who wish to obtain other information.

CHAPTER 4

EXPERIMENTAL PROCEDURE

4.1 Introduction

The mean flowfield parameters behind a bluff body mounted at mid-stream in a rectangular test section were measured using both a 1-d and 3-d laser Doppler velocimeter (LDV). A description of the experimental apparatus used to make these measurements was given in Chapter 3. This chapter describes the techniques used to obtain the following flowfield parameters:

- 1.) Mean axial, transverse, and spanwise velocities ($\bar{U}, \bar{V}, \bar{W}$).
- 2.) Mean axial, transverse, and spanwise rms turbulence levels (u, v, w).
- 3.) Mean spanwise velocities (\bar{W}) along the z-axis at $y=0$.
- 4.) Turbulent normal stresses ($\bar{uu}, \bar{vv}, \bar{ww}$).
- 5.) Reynolds stresses ($\bar{uv}, \bar{uw}, \bar{vw}$).
- 6.) Turbulent triple products ($\bar{uuu}, \bar{uuv}, \bar{uuw}, \bar{uvv}, \bar{uvw}, \bar{vvv}, \bar{vww}, \bar{www}$).

Also included in this chapter are parameter settings for the various LDV systems and flow system parameters, as well as the statistical uncertainty estimation techniques.

4.2 Test Conditions

As noted previously, the primary objective of this study was to provide an accurate, experimentally measured data set for the turbulent flow parameters behind a bluff body mounted in a rectangular test section. With this in mind, all flow conditions were carefully monitored and documented throughout the testing procedure. The flow conditions also included atmospheric temperature and pressure. The total temperature was sampled from thermocouples via an A/D converter board inserted in a personal computer to within ± 0.5 °F. The static pressure was also sampled via a pressure transducer to ± 0.01 psia. The pressure differential between static and total was constantly monitored using a highly sensitive manometer and was measured to within ± 0.025 inch-H₂O. The inlet velocity, U_{ref} , was then calculated for every measurement point at every station, with an uncertainty of ± 0.26 m/s (see Table 4.1 and Appendix G). The reference velocity changed slightly from one data point to another and from one day to another, depending upon the local atmospheric conditions. However, all parameters were normalized point-to-point by the measured reference velocity.

Table 4.1. U_{ref} Reading Variables Error.

data	uncertainty
T_t	± 0.5 °F
P_s	± 0.01 Psia
ΔP	± 0.025 in-H ₂ O
U_{ref}	± 0.26 m/s

4.3 Sampling Method

In all cases, 5120 individual realizations were accumulated for each velocity component at each measurement point to form turbulence statistics. The coincidence timing logic on the TSI IFA-750 master interface ensured that simultaneous (within 20 μ s) data were measured. As mentioned earlier, the velocity measurements presented in this study were not corrected for velocity bias. Mass flow rates based on integration of axial velocity measurements at all stations in the far-field were found to be within $\pm 2\%$ of the upstream profile at station $x/H = -5$ (Figure 5). These axial velocities were measured from top to bottom to include measurements in the boundary layers.

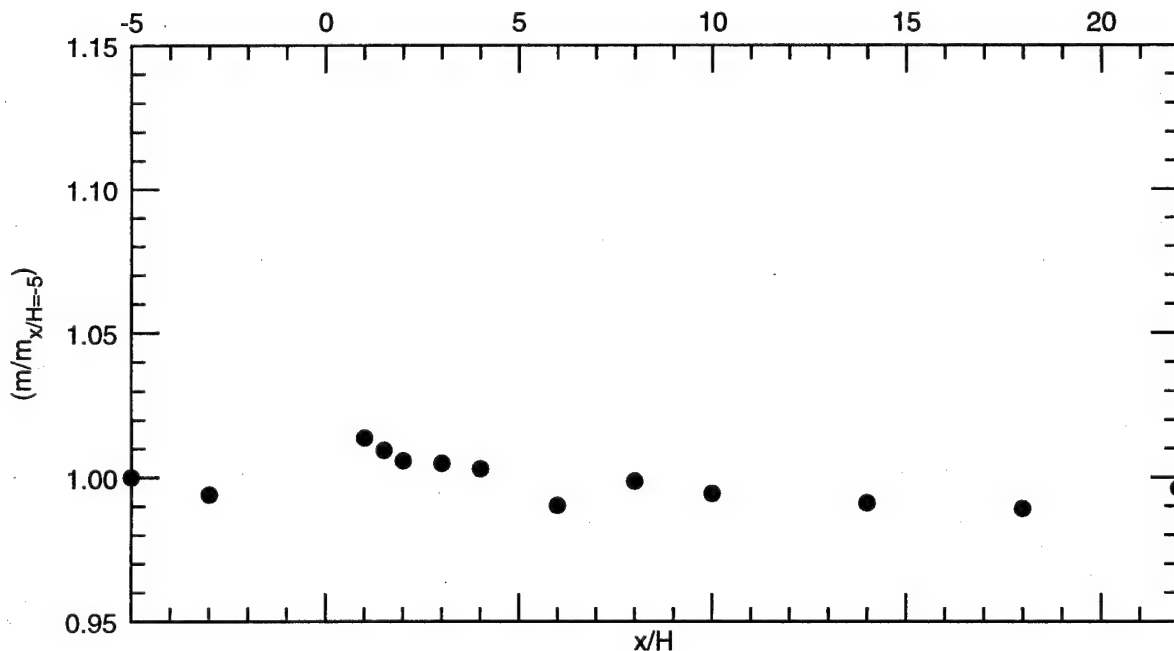


Figure 5. Normalized mass flux variation from station to station based on measured axial velocities.

4.4 Turbulence Statistics

The techniques used to obtain the following flowfield parameters are explained below. In computing the statistical parameters, all points lying far outside of the data set, are eliminated first. Then any point lying outside $\pm 3\sigma$ was discarded. On the average, the number of points that were eliminated was less than 50. Out of 5120, this number is considered on the high side, typically 20 outliers is an average theoretical number for a two-component LDV system. However, this is not an unreasonable number, since in this study, elimination or discrimination is based on three components of velocities, and if one component is eliminated, the two other corresponding components are also discarded. After the $\pm 3\sigma$ cutoff was applied to the 5120 realizations, the revised statistics were calculated. The mean, variance, cross-product and triple-product were then computed using the following equations (see also Appendix D);

$$\bar{U} = \frac{1}{N} \sum_{i=1}^N U_i \quad (4.1)$$

$$\bar{uu} = \frac{1}{N} \sum_{i=1}^N (U_i - \bar{U})^2 \quad (4.2)$$

$$\bar{uv} = \frac{1}{N} \sum_{i=1}^N (U_i - \bar{U})(V_i - \bar{V}) \quad (4.3)$$

$$\bar{uuu} = \frac{1}{N} \sum_{i=1}^N (U_i - \bar{U})^3 \quad (4.4)$$

where N is the number of actual samples in the revised data set.

4.5 Statistical Error Estimation

The irregularity of the turbulent flowfield necessitates the use of statistical averaging methods for the determination of turbulence parameters. Therefore a statistical uncertainty analysis is deemed necessary mainly because it is impossible to determine exactly any statistical quantity (random variable) using a finite sample size. This type of uncertainty is based on estimation and sampling theory. For instance, the standard deviation of a random distribution of mean values of a variable F is expressed as;

$$\sigma_{\bar{F}} = \sigma_F / \sqrt{N} \quad (4.5)$$

where “ σ “ is the standard deviation, and “ N ” is the number of actual samples in the revised data set.

For a normal distribution, a level of confidence can now be written for the measured values of \bar{F} by including an appropriate coefficient. For instance, for a 95% confidence interval ($\alpha/2=0.025$), the equation for ΔF is;

$$\Delta F = 1.96\sigma_F / \sqrt{N} \quad (4.6)$$

The equation states that the computed values of \bar{F} will not be in error from the true mean value by more than $\pm\Delta F$, 95% of the time.

4.5.1 Uncertainty in the Means

The uncertainty equations for the mean velocities are expressed as follows;

$$\Delta \bar{U} = \pm 1.96\sigma_u / \sqrt{N} \quad (4.7)$$

$$\Delta \bar{V} = \pm 1.96\sigma_v / \sqrt{N} \quad (4.8)$$

$$\Delta \bar{W} = \pm 1.96\sigma_w / \sqrt{N} \quad (4.9)$$

Using these equations, for a 95% confidence (Snyder, et al. 984), the maximum absolute expected error, for the axial velocity, was found to be 1.17% at station $x/H=0.5$, where the axial turbulence intensity level was 42%. The maximum absolute expected error for the transverse velocity was found to be 1.92% at station $x/H=0.9$, where the turbulence intensity level was 70%. As for the spanwise velocity, the maximum absolute expected error was found to be 0.95% at station $x/H=0.5$, where the turbulence intensity level was 34% (see Appendix G).

4.5.2 Uncertainty in the Higher Order Moments

In this study, the *jackknife* resampling method described by Benedict & Gould (1996) was used to calculate the uncertainties of higher order statistics such as the 2nd and 3rd order moments. These terms included the six turbulent stresses, and all nine turbulent triple products. All uncertainties are represented by error bars in the experimental data profiles. Also, these uncertainties were used to estimate the uncertainty error in the TKE terms (see section 6.9).

4.6 Measurement Errors

When using LDV as a tool to perform experimental measurements, several sources of errors might result. These errors usually result from optical misalignment, such as the alignment of the optical table and the test section, signal processing, refractive index variations of the gas medium and of the windows, probe volume effects, particle seeding effects, and the data sampling method used. However, most of these errors can be reduced to

an insignificant level or even eliminated. For instance, in this study the angle between the test section and the optics table was measured and found to be less than 0.03 degree.

There are various sources of biasing error that can effect the accuracy of LDV measurements made in highly turbulent flows. These are signal bias, fringe bias, and velocity bias. Signal bias (also called directional bias) occurs mainly in recirculating flows such as the flow studied here. Particles traveling in the opposite direction to the main flow cannot be discriminated from particles flowing at the same velocity in the main direction by the photodetector, since they both scatter light the same way. However, frequency shifting imposes a fixed frequency on the fringes, typically 40 MHz, which modifies the photodetector output so that information from turbulent and reversing flows can be evaluated accurately. Now, the fringes move so that a zero velocity particle will produce a Doppler frequency equal to the shift frequency. Fringe bias occurs when seed particles traverse the fringes of the probe volume at large angles of incidence and generate an incomplete number of fringe crossings required to allow signal validation by the processor. This reduces the signal validation of low velocity particles which leads to a bias towards an incorrectly high value of mean velocity. However, this type of bias error can also be eliminated by appropriate frequency shifting (Roesler et al., 1980). Velocity bias occurs because the velocity data are obtained as the seed particles randomly pass through the probe volume. Naturally this passage of particles takes place at unequal time intervals. Due to the fluctuating nature of turbulent flow, there will be more particles per unit time passing through the probe volume during time intervals when the velocity is high. This leads to a bias towards high mean velocity as calculated by simple ensemble averaging of the data. The

magnitude of this error frequently outweighs most of the other errors listed above (Gould et al., 1986).

The techniques currently used for eliminating velocity bias error include the 1-d and 2-d corrections of McLaughlin and Tiederman (1973), and the time between validated data method of Barnett and Bentley (1974). These techniques can be used for bias correction after the data are acquired. Velocity bias correction can also be done during data acquisition. Experimental sampling techniques have also been proposed, such as the equal time interval sampling technique first proposed by Stevenson, et al. (1982). However, this method requires a relatively high data rate on the order of three times the passage frequency of the turbulent microscales as concluded by Gould, et al. (1986). It was found that the highest passage frequency of the turbulent microscales in a turbulent flow behind an axisymmetric sudden expansion was approximately 2000 Hz. Therefore, for equal interval sampling to work for such a geometry, the data validation rate must be greater than 6000 Hz. After examination of post facto bias correction schemes, Gould et al. (1986) concluded that these schemes were ineffective and could introduce larger errors than the original uncorrected data contained.

The coincident data rate in this study varied from 5000 per second in the freestream, to 1000 per second behind the bluff body, in the recirculation zone, for a clean window. Gould, et al. (1986) found that equal interval sampling becomes less effective as the data validation rate dropped, to the point where no bias elimination takes place as the data rate approaches 500 Hz.

In this study, the results are believed to be slightly biased in most of the high turbulence regions, especially in the recirculation region. However, the mass balance

variation from station to station shows that this bias error in the regions where biasing is possible, accounts for a global mass flow error of less than 2%. Local errors in the mean velocities are probably larger than this. In fact, Gould, et al. (1986) gave a rule of thumb which gives the error in mean velocity due to biasing $\sim 1/3$ the turbulence intensity.

Other possible error sources which may effect an LDV measurement by reducing the signal to noise ratio, are those caused by dirty windows, non-flat windows, non-homogeneous windows, and impurities and small chips in the window material. These error sources change the optical path length which can deviate the incoming laser beams. The beams also tend to diverge and lose spatial coherence (Baker et al., 1974), causing a drift in the beam's coincidence, and reducing the effective size of the probe volume. Among other causes, the signal-to-noise ratio decreases as a result of the improper beam crossing. The high quality quartz windows (originally used for Schlieren measurement) used in this study and the continuous cleaning of the windows, after every three data points (in the recirculation region) helped to maintain the data rate at the maximum values attainable.

CHAPTER 5

FAR-FIELD EXPERIMENTAL RESULTS AND DISCUSSIONS

5.1 Introduction

In order to map the flowfield throughout the tunnel, the velocity measurements were made in two separate sets: the “far-field” and the “near-field”. The near-field experimental measurements are comprised of locations between $x/H=0.25$ and 1.2 and are presented in Chapter 6. The far-field measurements included stations from 5 base heights ($x/H=-5$) upstream to 22 base heights ($x/H=22$) downstream of the bluff body. The bluff-body dump plane, i.e., the trailing edge, was assigned station $x=0$. Negative x -values refer to measurement stations upstream of the bluff body. Care was taken to maintain a symmetric flowfield; measurements were taken across the entire vertical (i.e. transverse coordinate) tunnel cross section to verify that the flow was symmetric. All measurements are normalized with respect to the reference velocity measured at the same instance, and the bluff-body height, $H=12.7$ mm (0.5 in). The three-component LDV system provided the axial, transverse, and spanwise mean and fluctuating components of the velocity field together with the normal and Reynolds-shear stresses, and the higher order turbulent triple products. The results of the far-field measurements are presented next.

Two separate sets of measurements are presented in this section. The LDV beam configuration of the three-component LDV system was such that wall-to-wall measurements of the three velocity components was not possible. For this reason, it became necessary to make two separate sets of velocity distribution measurements. First, using the LDV system

in a single component configuration, wall-to-wall (top to bottom) measurements of the axial velocity distribution (U) were made at stations $x/H = -5, -3, 1, 1.5, 2, 3, 4, 6, 8, 10, 14, 18$, and 22 . The single component measurements were used for two purposes: 1.) to validate the three-component measurements and, 2.) to check for conservation of mass. The mass flow rate was obtained by numerically integrating the axial velocity profiles at various stations across the tunnel. The mass flow rates, shown in figure 5, were found to be within $\pm 2\%$ of the upstream profile obtained at $x/H = -5$. Three-component LDV measurements were made at the same axial stations listed above. However, measurements were limited to the central 5.58 cm (2.2 in) portion of the flowfield in the vertical (transverse) direction ($-2.2 \leq y/H \leq 2.2$).

5.2 Mean Velocity Data

5.2.1 1-D LDV

Figures 6 and 7 show the evolution of the axial mean velocity and turbulence intensity distributions at all measured stations, as measured with the single component LDV. The vertical bars in the following figures denote the statistical uncertainty. The measurements show a relatively flat upstream velocity profile representative of fully developed channel flow at $x/H = -5$. Nearer to the bluff body, at $x/H = -3$ the incoming velocity distribution was affected by the presence of the flameholder and shows a slight velocity deficit in the center. Downstream of the bluff body, highly turbulent regions clearly identify the wake and show the extent of mixing and the flow recovery. However, this recovery was very slow and even at the last measurement station, $x/H = 22$, the presence of the bluff body was still evident in the wake.

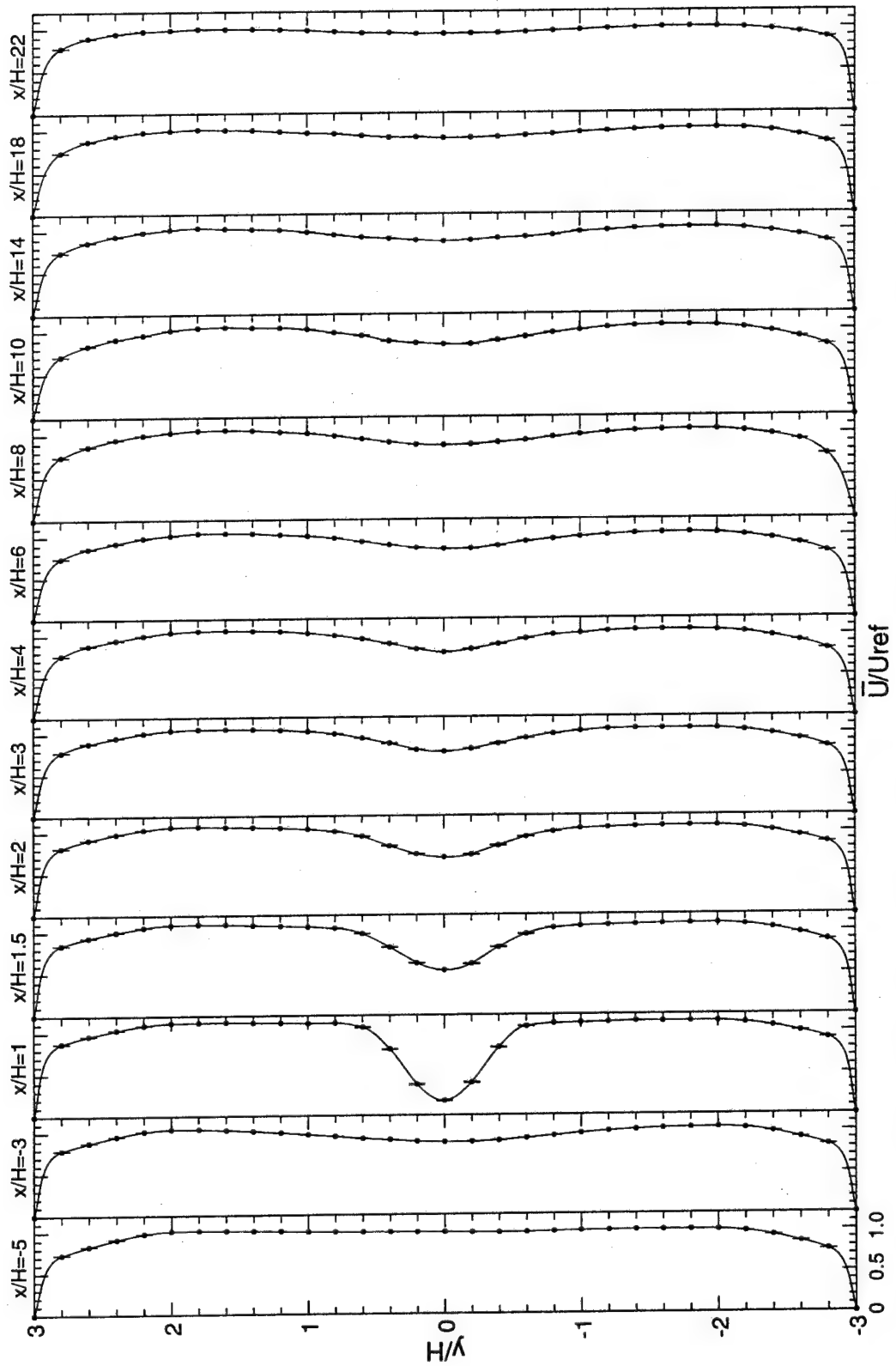


Figure 6. Normalized mean axial velocity profiles; 1-d LDV.

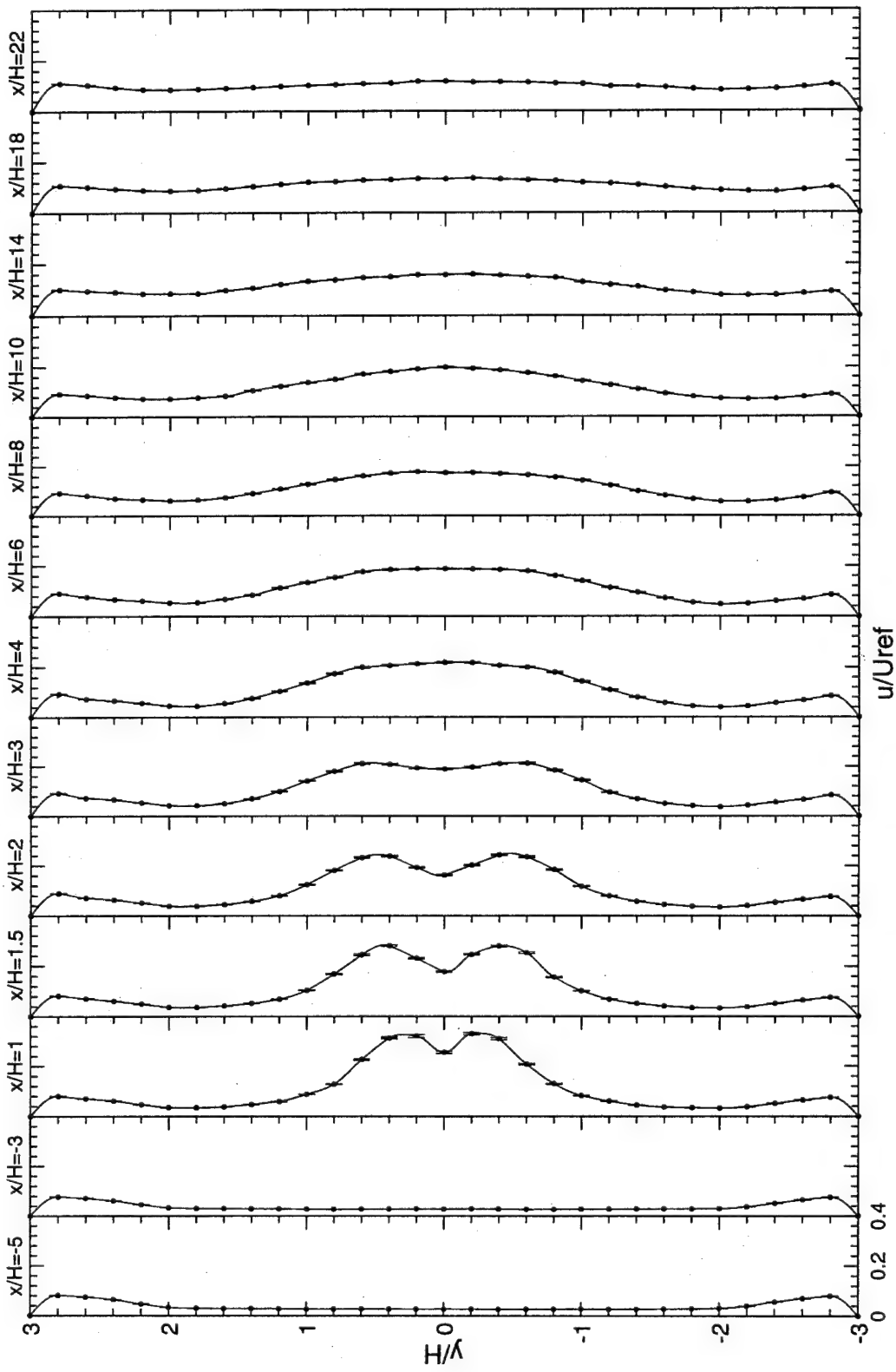


Figure 7. Normalized axial turbulence intensity profiles; 1-d LDV.

Figure 8 shows the distribution of the axial velocities and the turbulence intensities at the two upstream locations. Upstream of the bluff body, $x/H=-5$, the flow exhibits a flat velocity profile typical of fully developed channel flow and a uniform 3% turbulence intensity distribution in the center region increasing to a maximum of 8% within the wind tunnel wall boundary layer. At these low levels of turbulence one does not expect to encounter velocity bias (Gould et al., 1986). Measurements at $x/H=-3$ show the upstream influence of the bluff body on the incoming flow, typical of subsonic flow conditions. The central velocity deficit results from the stagnation point on the front of the bluff body. However, no change was noticed in the turbulence level. The measurements at $x/H=-5$ were used as the initial conditions in the numerical studies.

5.2.2 3-D LDV

Axial mean velocity and turbulence intensity distributions measured at $x/H=1$ with the one and three-component LDV systems are compared in Figure 9. This is the most demanding measurement station in the far-field, where the turbulence intensity is the highest and the measurements are taken within the unsteady recirculating wake behind the bluff body. The general agreement between the two measurement systems at all stations was also excellent. However, the slight discrepancy, between the two profiles shown in Figure 9, may be due to: 1.) differences in atmospheric relative humidity (see Appendix G) between the time when the two profiles were taken (winter vs. summer); and 2.) the change in the bluff-body geometry, which varied slightly during the course of the research, due to surface erosion caused by the seeding material. Three-component velocity measurements, closer to the bluff body than $x/H=1$, are presented in the near-field measurements, in Chapter 6.

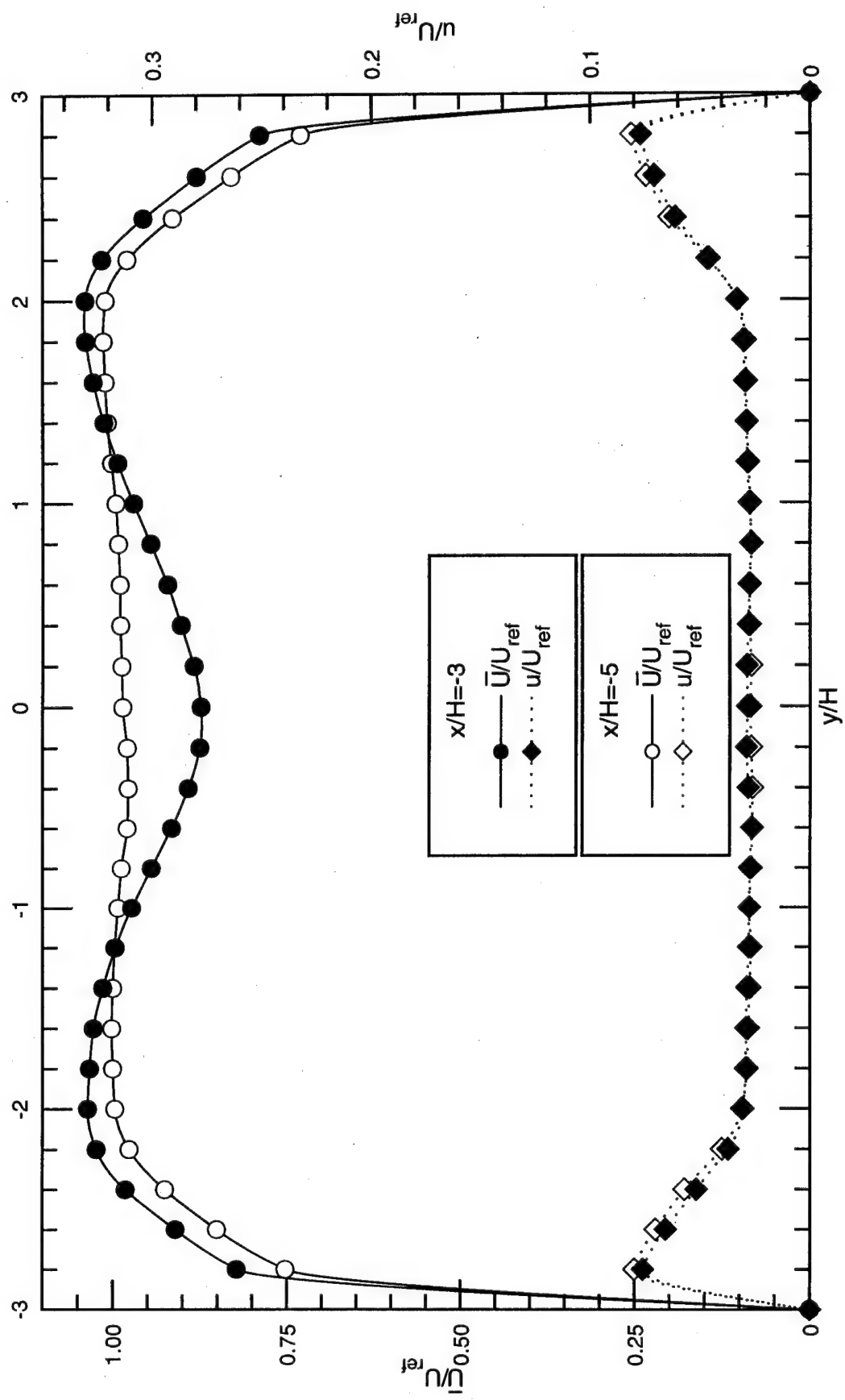


Figure 8. Normalized mean axial velocity and turbulence intensity profiles.

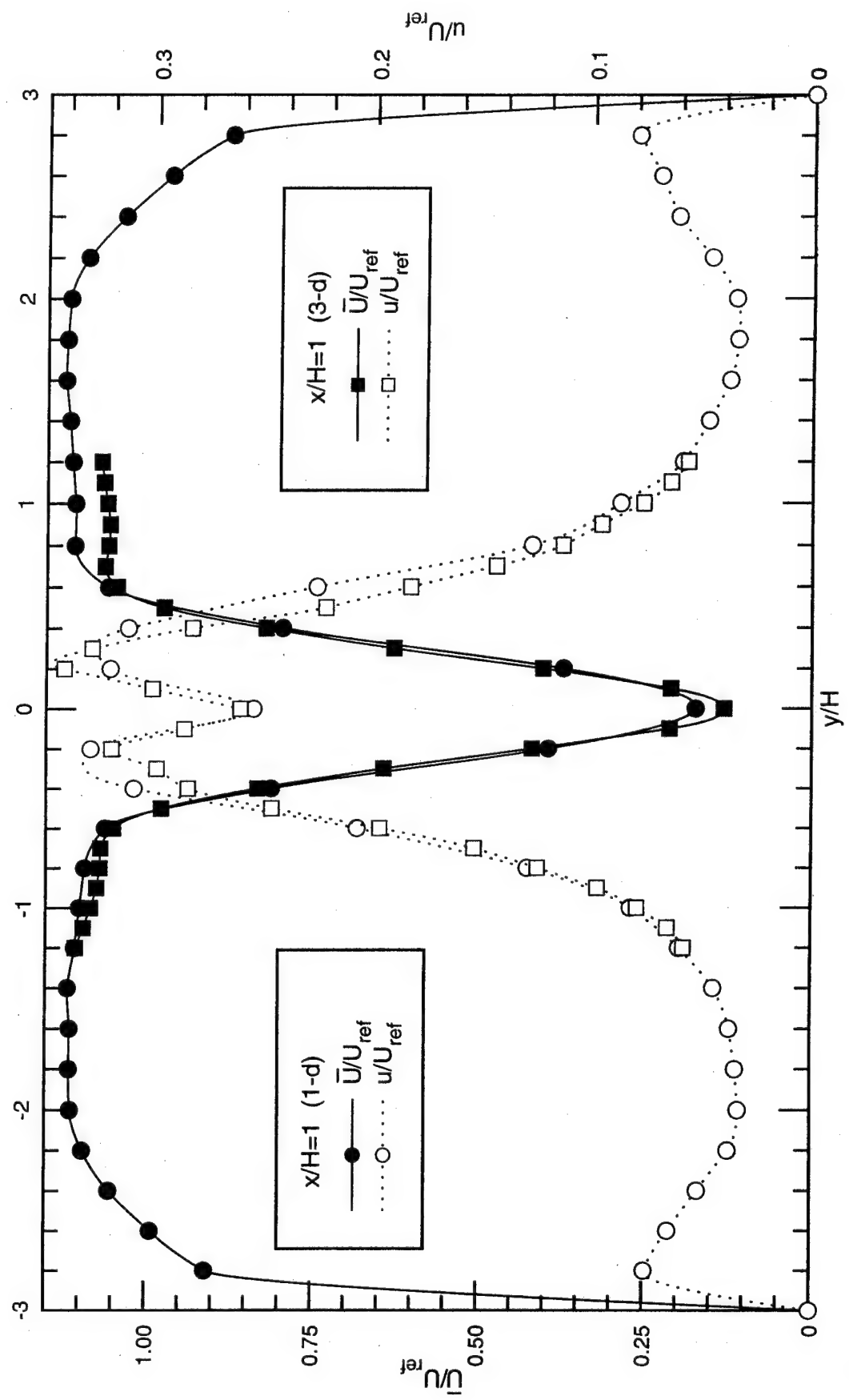


Figure 9. Normalized mean axial velocity and turbulence intensity profiles; 1-d, 3-d LDV.

Measurements at $x/H=1$ showed a large velocity deficit in the center of the wake. Because this measurement location is just downstream of the stagnation point (see Figure 10), no negative mean velocities were realized. The near-field measurements will show that the recirculation bubble extended only to $x/H=0.90$.

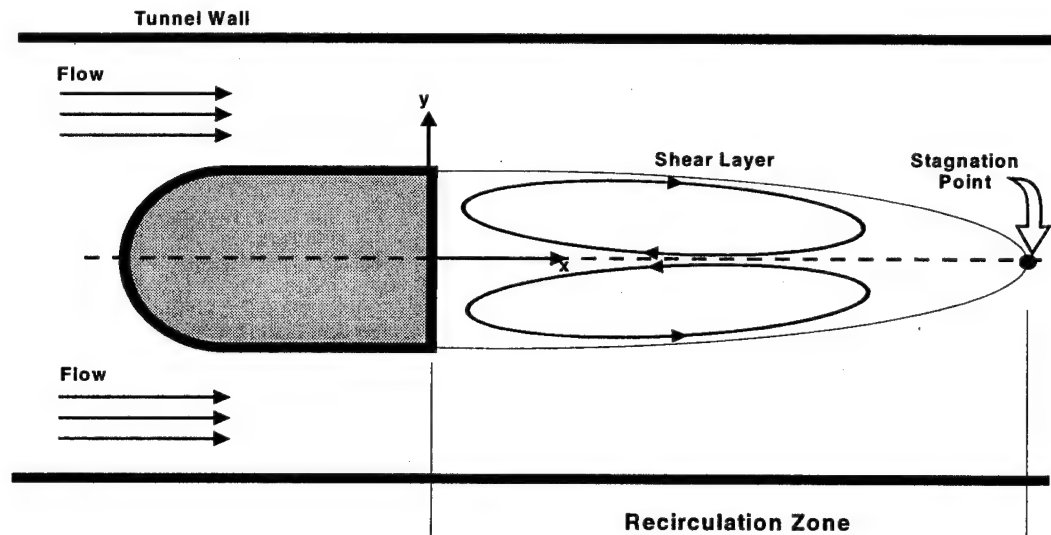


Figure 10. Bluff-body near-field flow description.

In Figure 9, the velocity distribution revealed two symmetric shear layers, each with a thickness of $0.6H$. The resulting wake at this station was 20% wider than the bluff-body height. The maximum turbulence level was realized within the shear layers, roughly at $y/H=\pm 0.2$, where the mean velocity gradient was the largest. As anticipated, downstream of $x/H=\pm 0.2$, turbulence production dropped as the velocity gradient decreased and the flow became more uniformly distributed. Although the measurements closer to the centerline, $-0.2 < y/H < 0.2$, showed velocity gradients of the same magnitude, the turbulence intensity dropped. Before offering an explanation for this behavior, the distribution of the transverse velocity and turbulence field are examined.

Transverse mean velocity and turbulence intensity profiles for station $x/H=1$ are shown in Figure 11. The effect of the bluff body becomes readily observable in this figure, where the flow rapidly turns from both sides toward the centerline to fill the low pressure region behind the bluff body. The turbulence intensity reaches its maximum level, $v/U_{ref}=0.75$, at the centerline, $y/H=0.0$, corresponding to the location with the highest mean velocity gradient. Interestingly, the regions of maximum turbulence production in the axial and transverse directions do not correspond spatially. The following is provided as a possible explanation. It is well established that this configuration results in periodic shedding of vortices from the upper and lower separation points. Time-averaged estimates of the rms turbulence fluctuations obtained with an LDV system result from the superposition of small scale turbulence and large scale fluctuations due to the passage of the periodic vortices through the probe volume. In standard configuration, the LDV instrument is incapable of differentiating between these two sources of turbulence. Assuming that the flowfield is spatially and temporally symmetric, the passage of the upper and lower vortices skew the axial velocity probability density function (PDF) in a symmetrically similar fashion at the centerline $y/H=0$, as shown by the histogram in Figure 12. However, away from the centerline, this contribution is dissimilar, i.e., different regions of the upper and lower vortices pass through the probe volume and result in compilation of skewed velocity PDFs and this longer moment arm relative to the mean. Hence, a higher axial turbulence intensity is measured away from the center as shown in Figure 9. In contrast, the contributions of periodic vortex shedding from the upper and lower separation points to the transverse velocity PDFs are directional. For example, the time-averaged value of the transverse

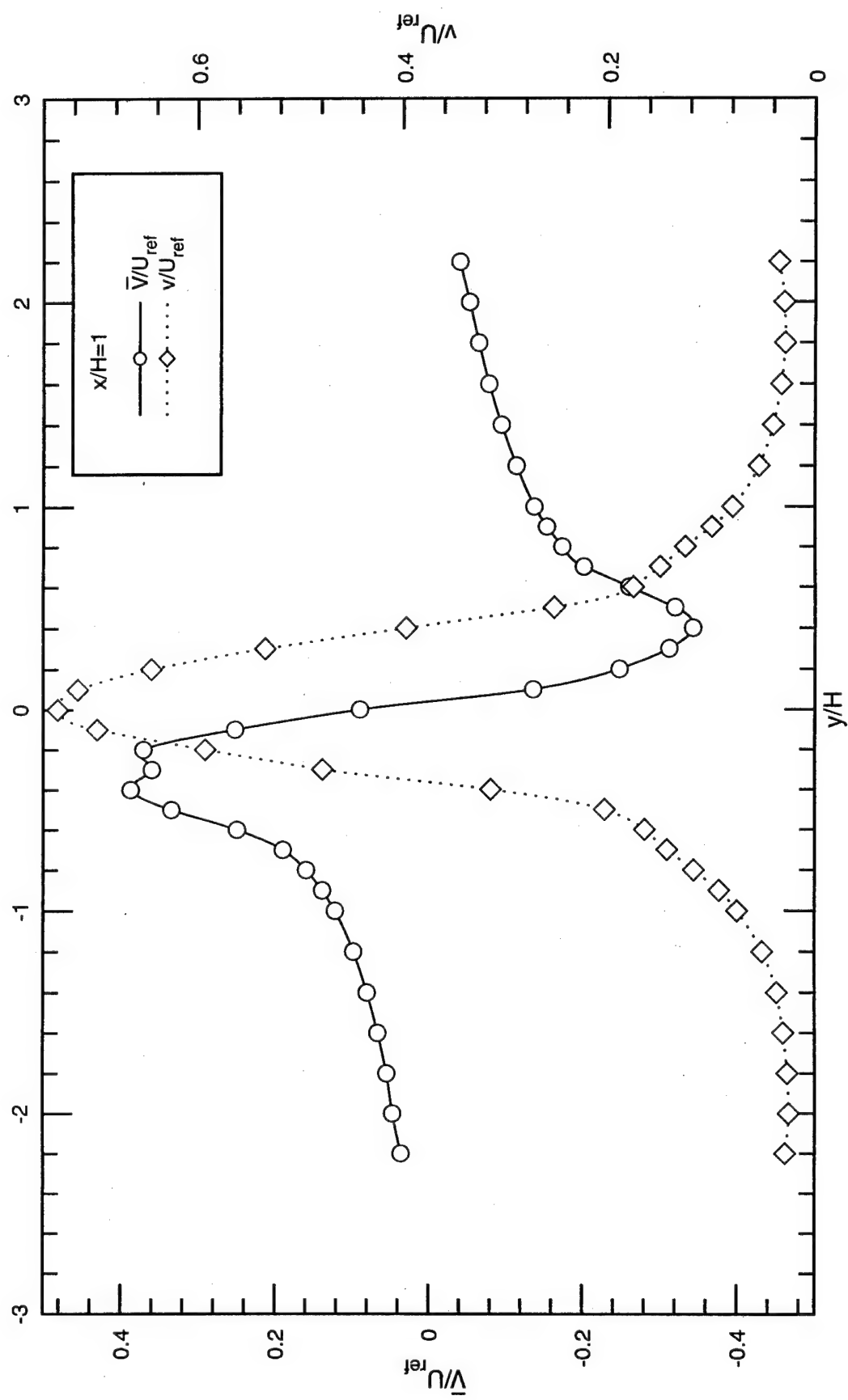


Figure 11. Normalized mean transverse velocity & turbulence intensity profiles.

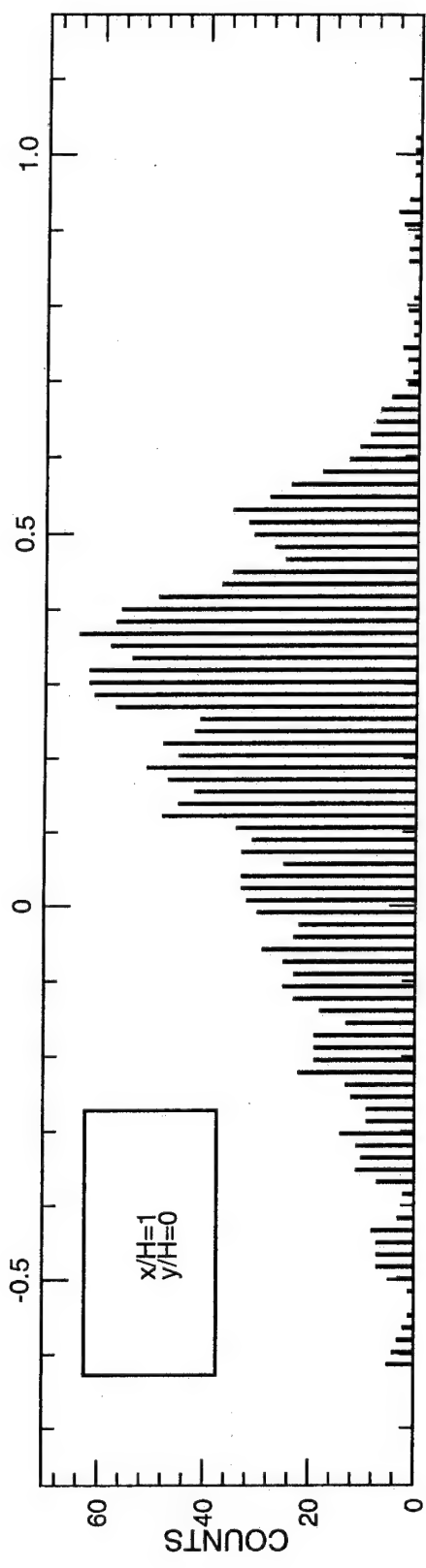


Figure 12. Normalized mean axial velocity PDF.

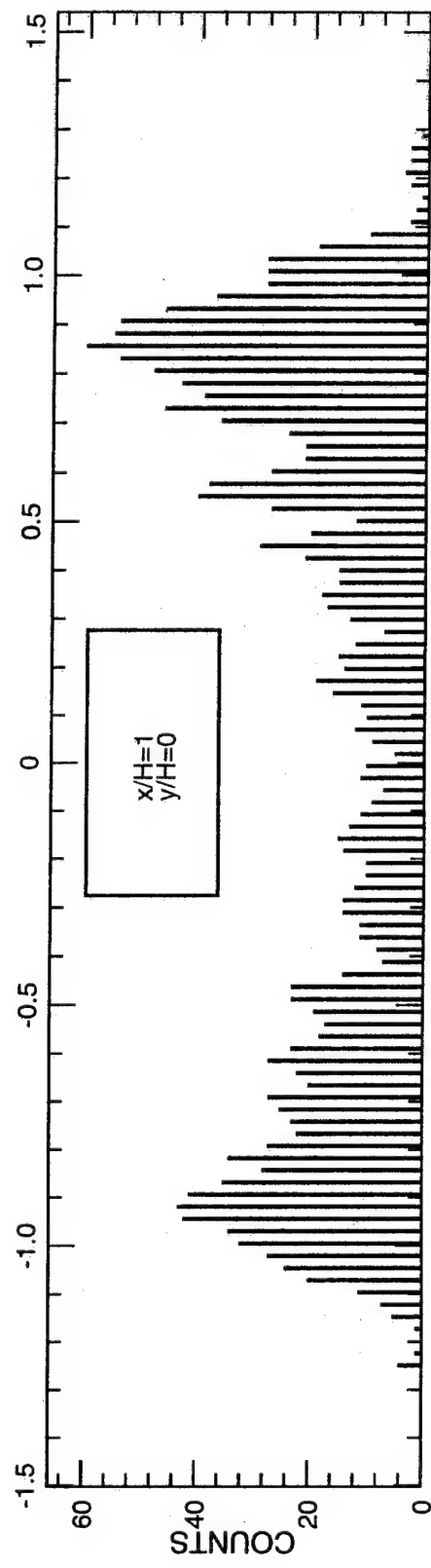


Figure 13. Normalized mean transverse velocity PDF.

velocity at the $y/H=0$ is negligible, i.e., $\bar{V}=0$. Therefore, the passage of a vortex shed from the upper corner of the bluff body skews the velocity PDF to show a negative (lower) mean velocity and conversely, a vortex shed from the lower corner skews the velocity PDF to show a positive (higher) mean velocity. Over time, the combined effect results in a much wider bi-modal velocity PDF, as shown in Figure 13, and a higher estimated value of turbulence intensity regardless of the measurement location, y/H . The trend of lower axial turbulence intensity at $y/H=0$ as compared to the levels in the shear layers is preserved out to station $x/H=3$. Downstream of $x/H=3$, the upper and lower shear layers do not show individual characteristics and have merged to form a single highly turbulent region (Figure 7). The need for mixing augmenters is clearly evident. For example, 27.94 cm (11 inches) downstream of the bluff body, at $x/H=22$, the shear layers have only grown to 4 times the bluff-body thickness and occupy roughly 67% of the tunnel cross sectional area. However, one must remember that this study is taking place in a confined flow.

Due to the two-dimensional nature of the bluff body, the spanwise velocity distributions (W) show negligible values throughout most of the measurement domain. However, the spanwise velocity distribution at $x/H=1$, shown in Figure 14, suggests that the flowfield immediately downstream of the bluff body is three-dimensional. After investigating the flowfield in the spanwise direction, it was deduced that the small positive w -component velocity value at $y/H=0$ could be due to a boundary layer asymmetry. It is believed that the combined effects of side wall boundary layers and the pressure field behind the bluff body drive the flow away from the walls and towards the center of the flameholder resulting in the formation of two pairs (upper and lower) of counter rotating spanwise

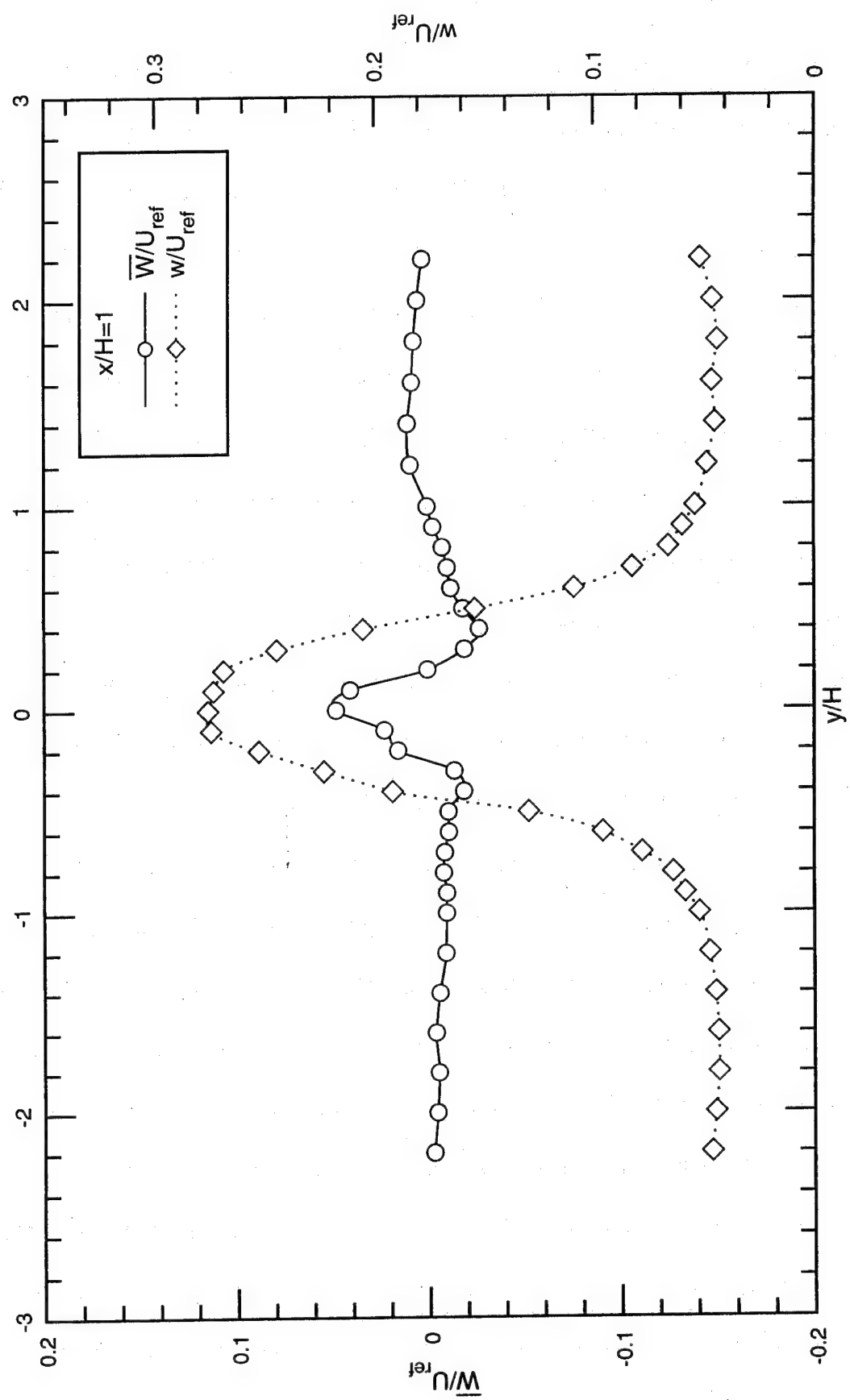


Figure 14. Normalized mean spanwise velocity & turbulence intensity profiles at $x/H=1$.

vortices. The peak value of turbulence intensity is believed to be due to the unsteady lateral motion of the vortex pairs.

Figure 15 shows a comparison between the three measured normalized turbulence intensities at $x/H=1$. Peak values of axial normalized turbulence intensity (i.e. the square root of the turbulent normal stress, normalized by the reference velocity) occur at $x/H=1$, in the shear layers and reach a value of 31% of the freestream mean velocity. This value is slightly above that obtained behind a backward-facing step (25%), as reported by Gould, et al. (1990). It is noteworthy that the peak transverse normalized turbulence intensity is 77%, approximately 2.5 times the value of the peak axial normalized turbulence intensity (33%), and 2.75 times that of the spanwise turbulence intensity (28%). Axial mean velocity and turbulence intensity profiles obtained with the three-component LDV system are shown in Figures 16 and 17, respectively. There exists a very close match to the measurements obtained with the single component LDV system.

Distribution of the transverse mean velocities and turbulence intensity profiles at all measured stations are presented in Figures 18 and 19, respectively. Negative values of y/H correspond to measurement locations below the bluff-body centerline. At $x/H=-5$, the inlet velocity profile shows negligible transverse velocity magnitude, however, at $x/H=-3$, there is a distinct transverse velocity distribution. Note that negative values of transverse velocity show that the flow has begun to turn downward and conversely the positive values indicate an upward turning of the flow around the bluff body. The flow rapidly turns to fill the low pressure wake region immediately downstream of the bluff body. The peak values of the transverse velocities are located inside the recirculation zone bound by the upper and lower

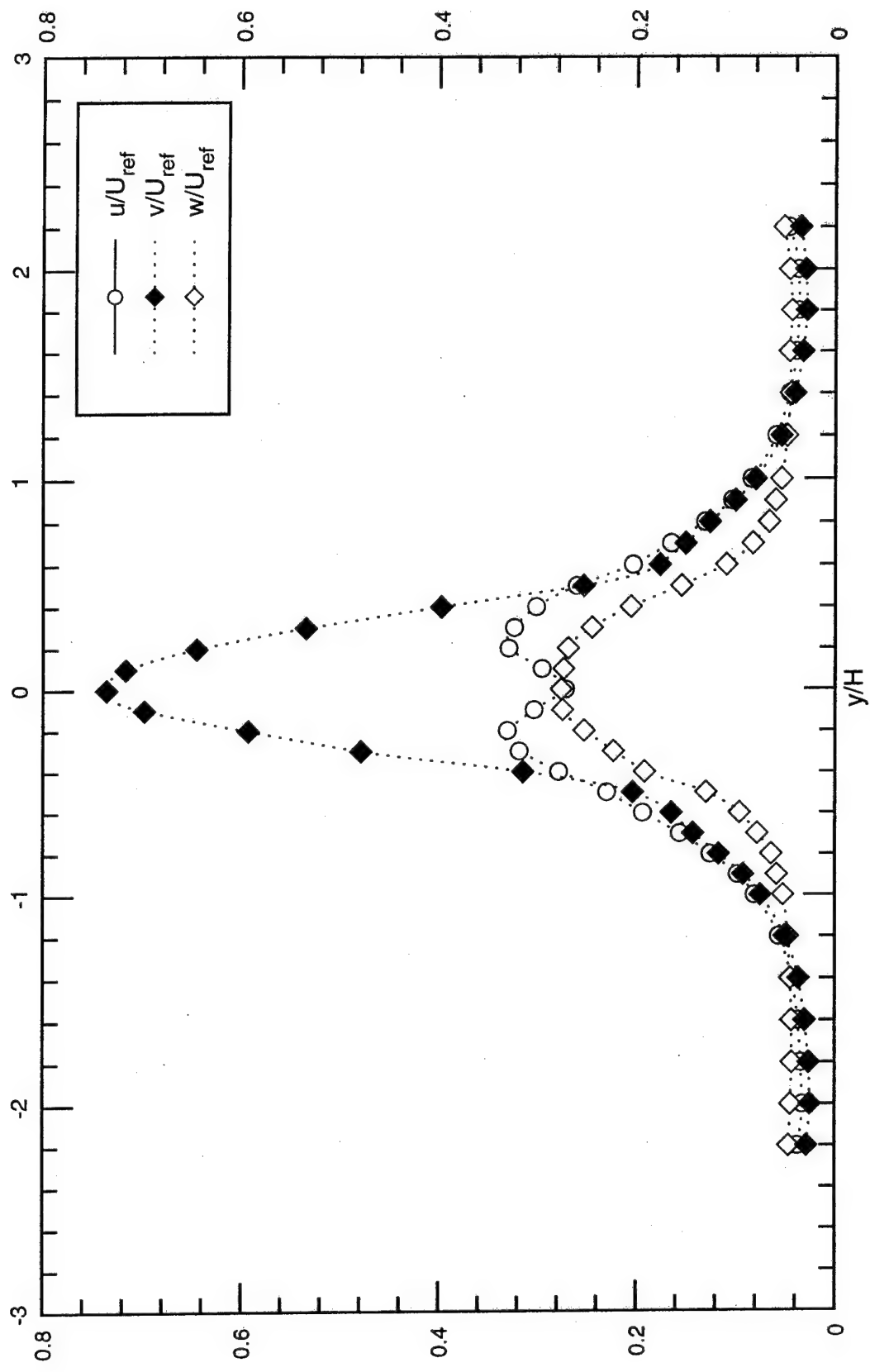


Figure 15. Axial, transverse & spanwise turbulence intensity profiles at $x/H=1$.

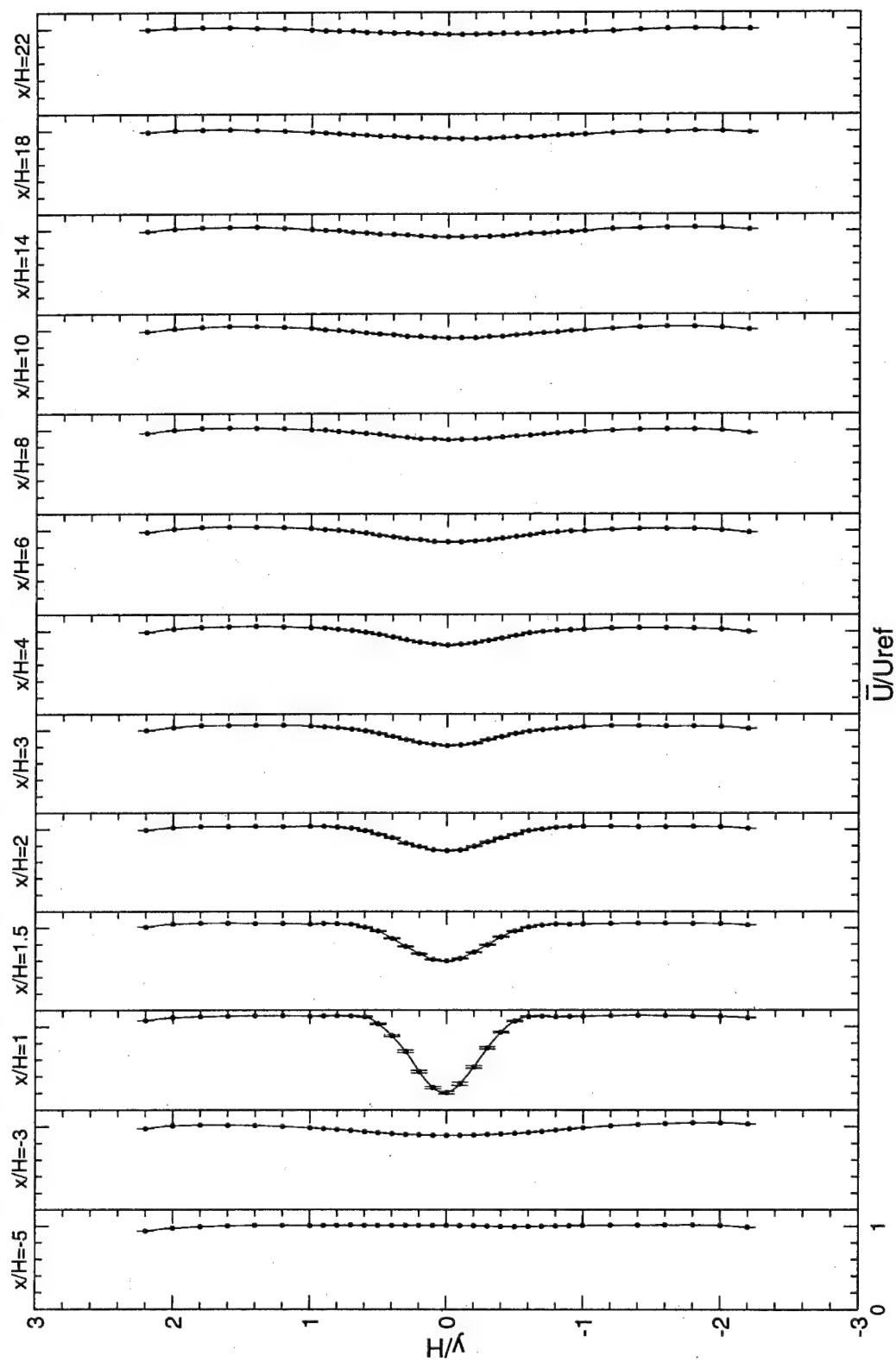


Figure 16. Normalized mean axial velocity profiles; 3-d LDV.

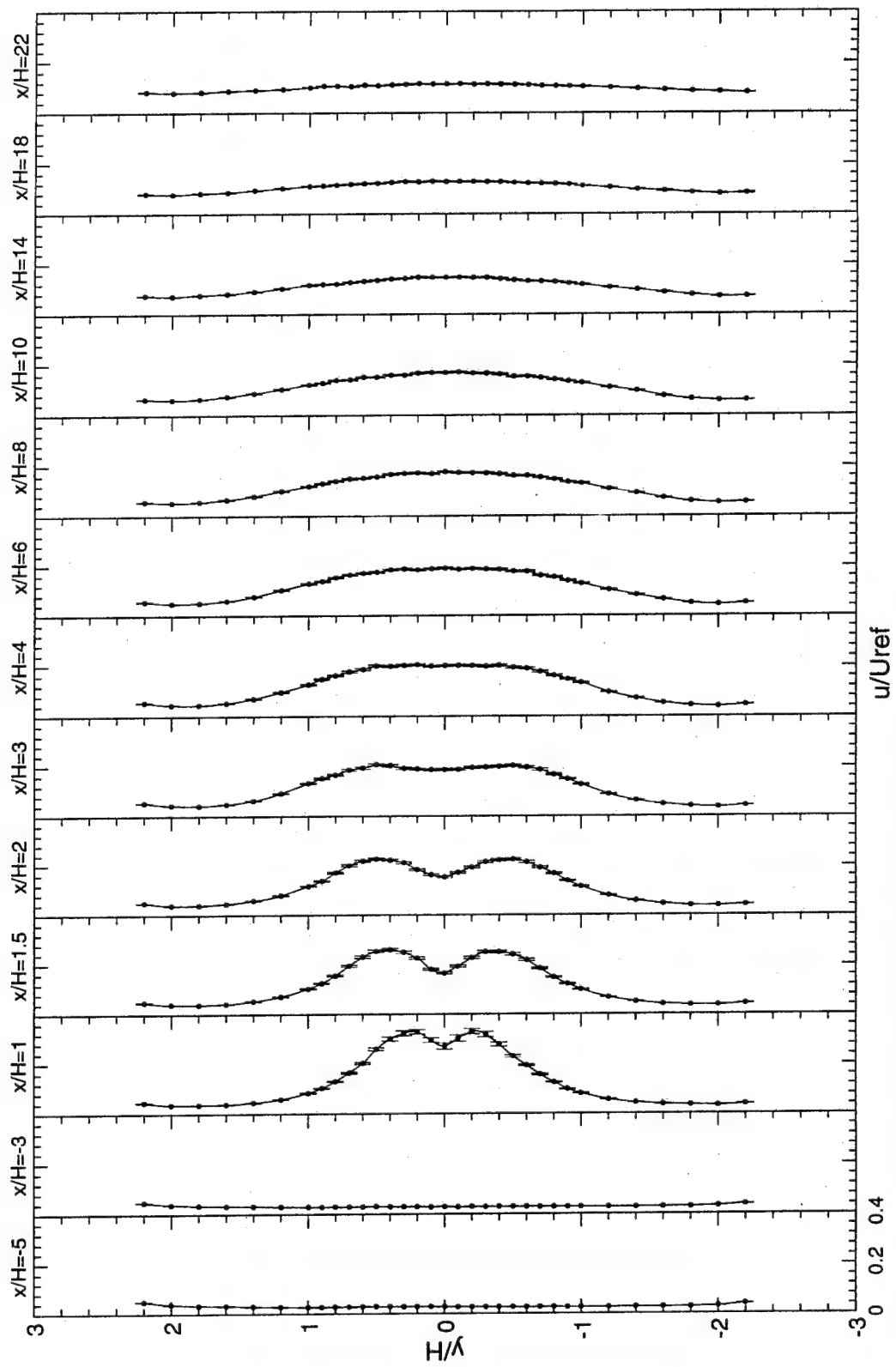


Figure 17. Normalized axial turbulence intensity profiles; 3-d LDV.

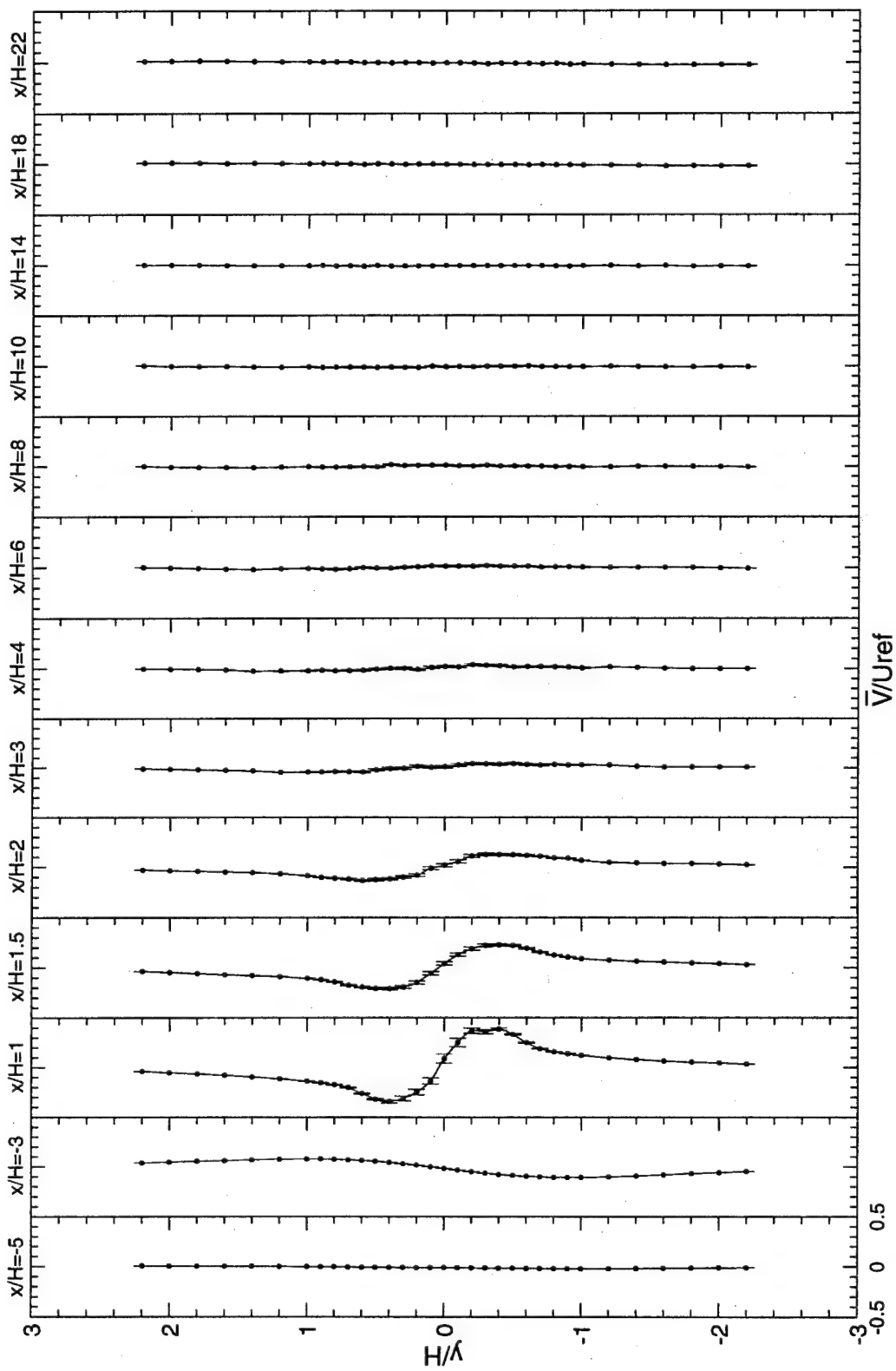


Figure 18. Normalized mean transverse velocity profiles; 3-d LDV.

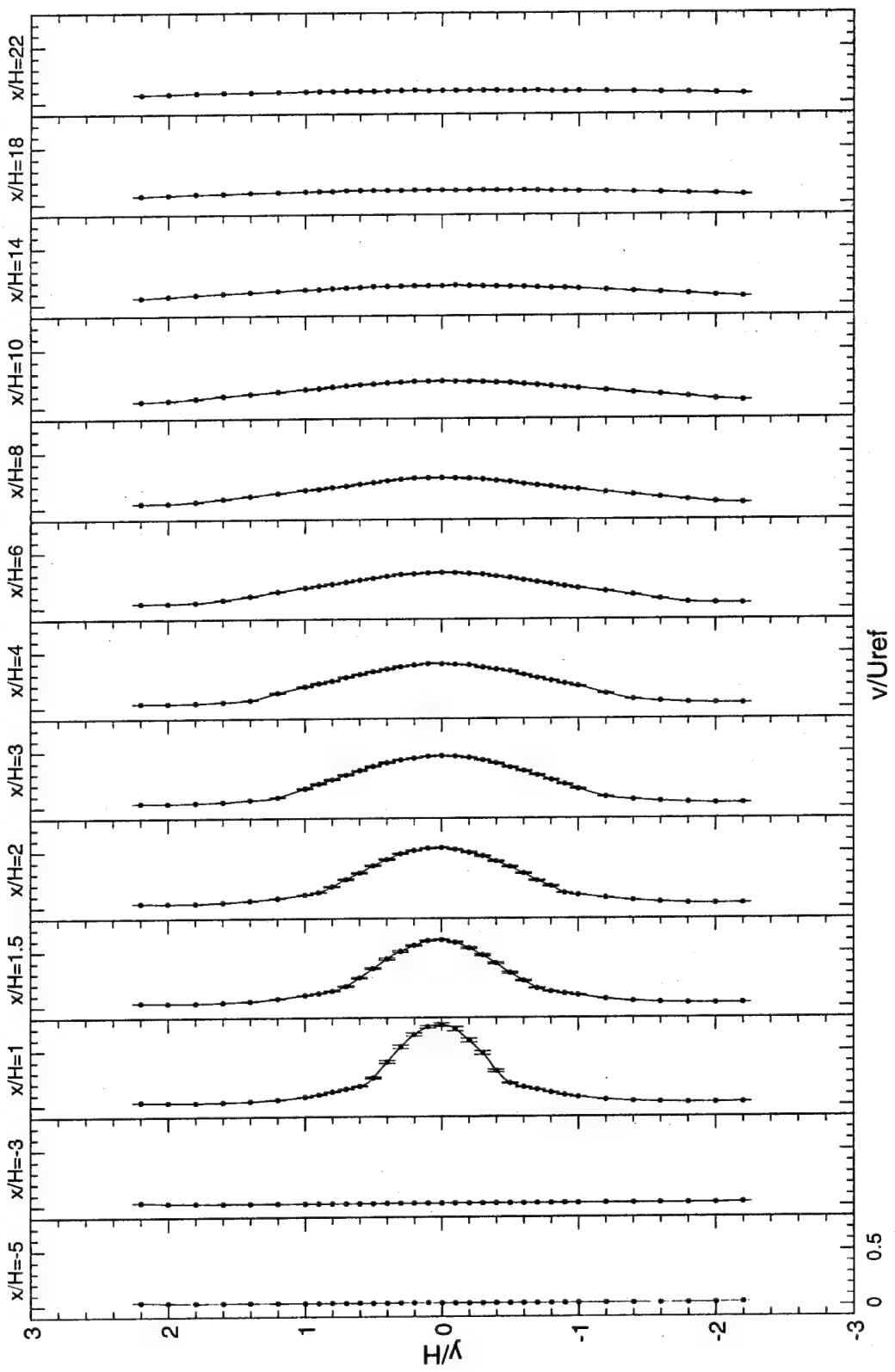


Figure 19. Normalized transverse turbulence intensity profiles; 3-d LDV.

shear layers. Comparisons of Figures 16 and 18 show that flow recovery is much faster in the transverse direction than in the axial direction with essentially zero mean transverse velocity downstream of $x/H=3$. In contrast, the axial velocity distribution shows a wake region characterized by a velocity deficit that continues to station $x/H=22$.

The measurements showed virtually no spanwise mean velocity as shown in Figure 20, except for a small peak at $x/H=1$. However, the normalized spanwise turbulence intensities shown in Figure 21 exhibit a maximum of 30% at station $x/H=1$. These turbulent fluctuations were still noticeable in the wake and remained until station $x/H=18$. More about this will be discussed in the near-field section.

5.3 Vortex Shedding Frequency

In an attempt to find the vortex shedding frequency, several single component measurements with large sample populations at high seeding rates were taken. Since LDV data do not provide a uniform time interval between velocity realizations, direct transformation of the velocity data from the time domain to the frequency domain is not easily accomplished. In order to convert the non-uniformly spaced velocity data into uniform time intervals, an averaging technique was employed. Essentially, a time interval, Δt , was selected and the data falling within each time interval were averaged. This averaging technique (time history method; see TSI manual, 1992) was applied to the complete data set to achieve an approximate velocity vs. equidistant time between samples. A Fast Fourier Transform (FFT) routine was then used for direct computation of the frequency spectrum. Figure 22 shows the power spectrum associated with velocity samples collected at $x/H=-5$ and $x/H=2$ at the indicated y-locations. A distinct frequency peak is noted at roughly $f=454$

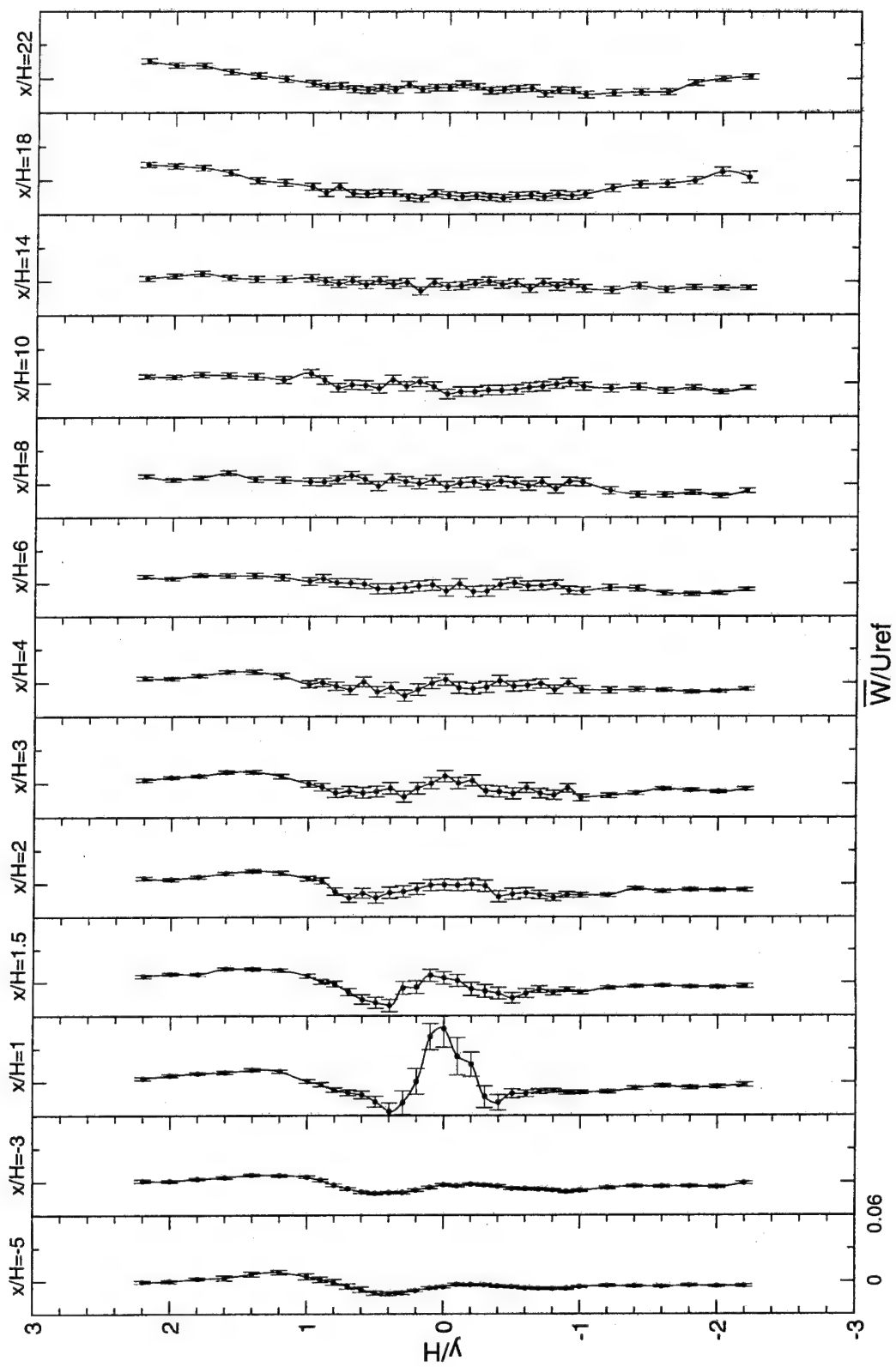


Figure 20. Normalized mean spanwise velocity profiles; 3-d LDV.

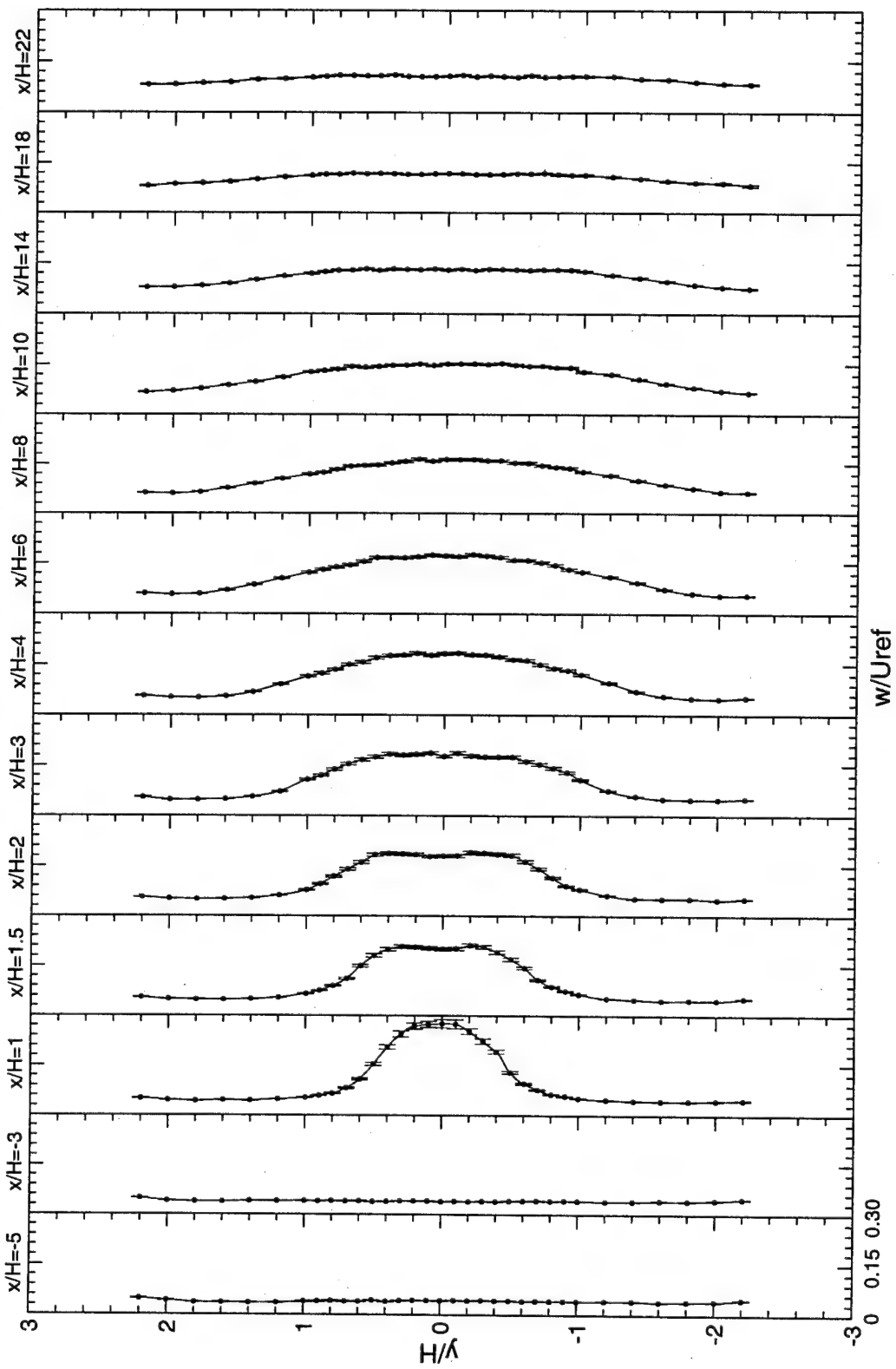


Figure 21. Normalized spanwise turbulence intensity profiles; 3-d LDV.

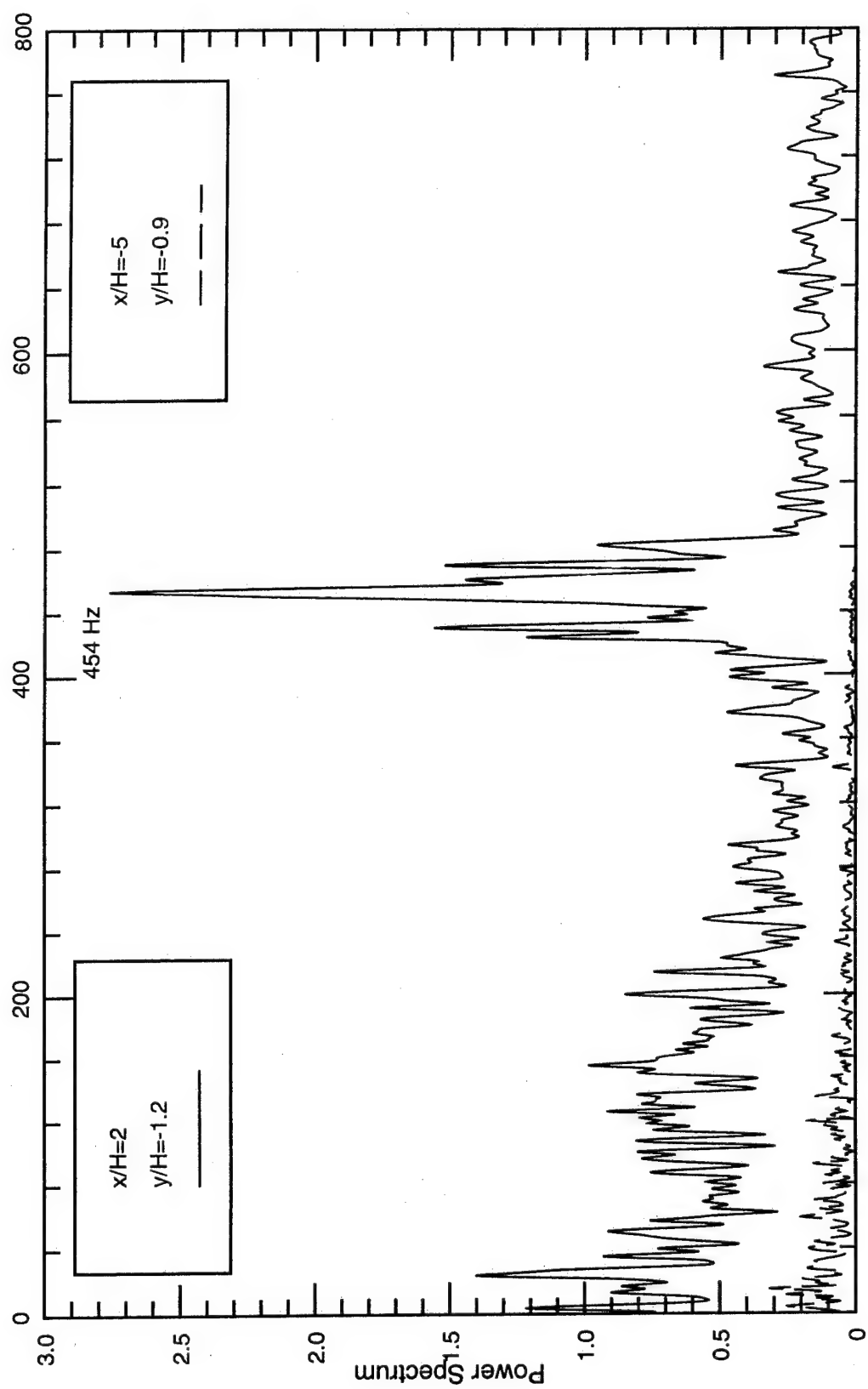


Figure 22. Frequency Spectra at $x/H = -5$ & $x/H = 2$.

Hz at the $x/H=2$ location. Power spectra of measurements at other downstream locations repeatedly identified this frequency, except at $x/H=22$, which did not show a dominant frequency. This shedding frequency corresponds to a Strouhal number, $St=0.24$, where;

$$St = fH / U_{ref} \quad (5.1)$$

Power spectra of the upstream velocity measurements did not identify a high energy peak at any particular frequency.

5.4 Turbulent Normal and Shear Stresses

Figures 23, 24 and 25 show profiles of the three measured normalized turbulent normal stresses (\bar{uu} , \bar{vv} , \bar{ww}). Once again, the bars in these figures denote 95% confidence intervals. The axial, transverse and spanwise turbulent normal stresses are clearly different in value and profile shapes. The different shapes indicate that the structure in and near the recirculation zone is quite anisotropic and remains so until $x/H=8$. The normalized transverse turbulent normal stresses exhibit the highest peak values (0.6), approximately five times the value of the peak axial turbulent normal stresses (0.12). This is due primarily to estimate average velocities which include both large scale periodic structures and the smaller scale more random like turbulence. The measured normalized turbulent shear stresses (\bar{uv} , \bar{uw} , \bar{vw}) are shown in Figures 26, 27 and 28. These measurements indicate that the \bar{uv} -shear stress is the only significant one of the three with peak normalized values of ± 0.12 , occurring at $x/H=1$.

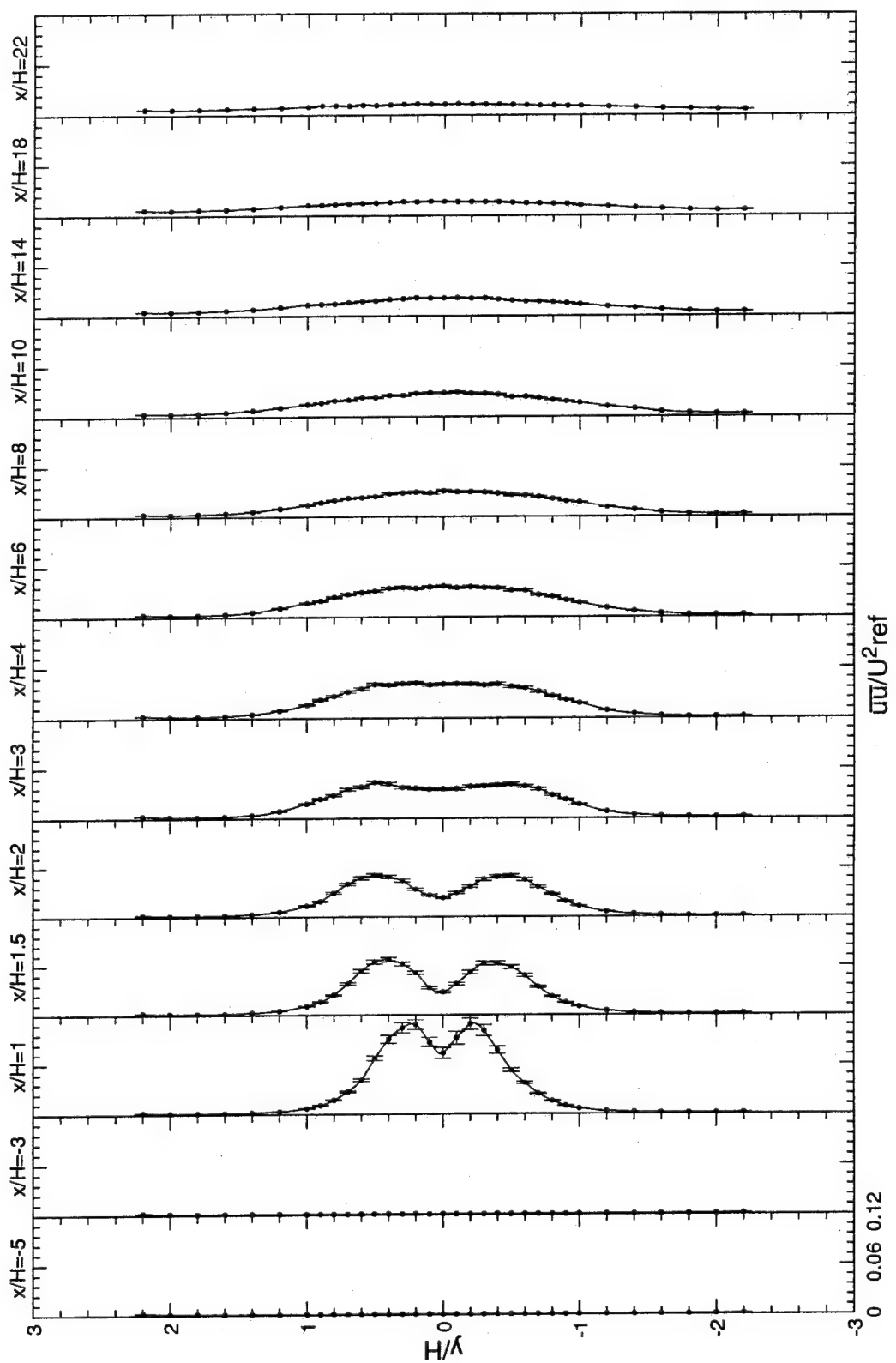


Figure 23. Normalized axial turbulent normal stresses.

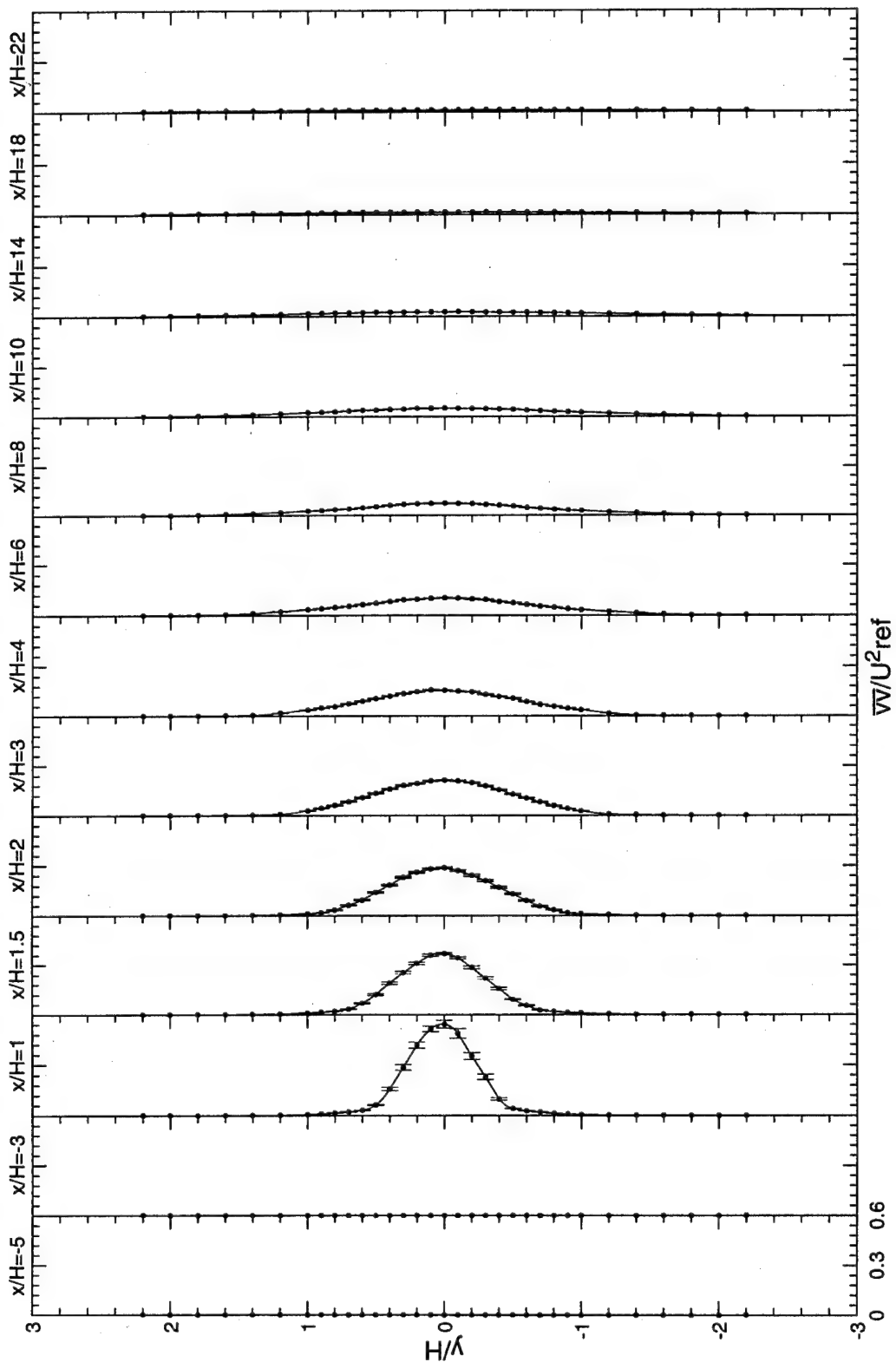


Figure 24. Normalized transverse turbulent normal stresses.

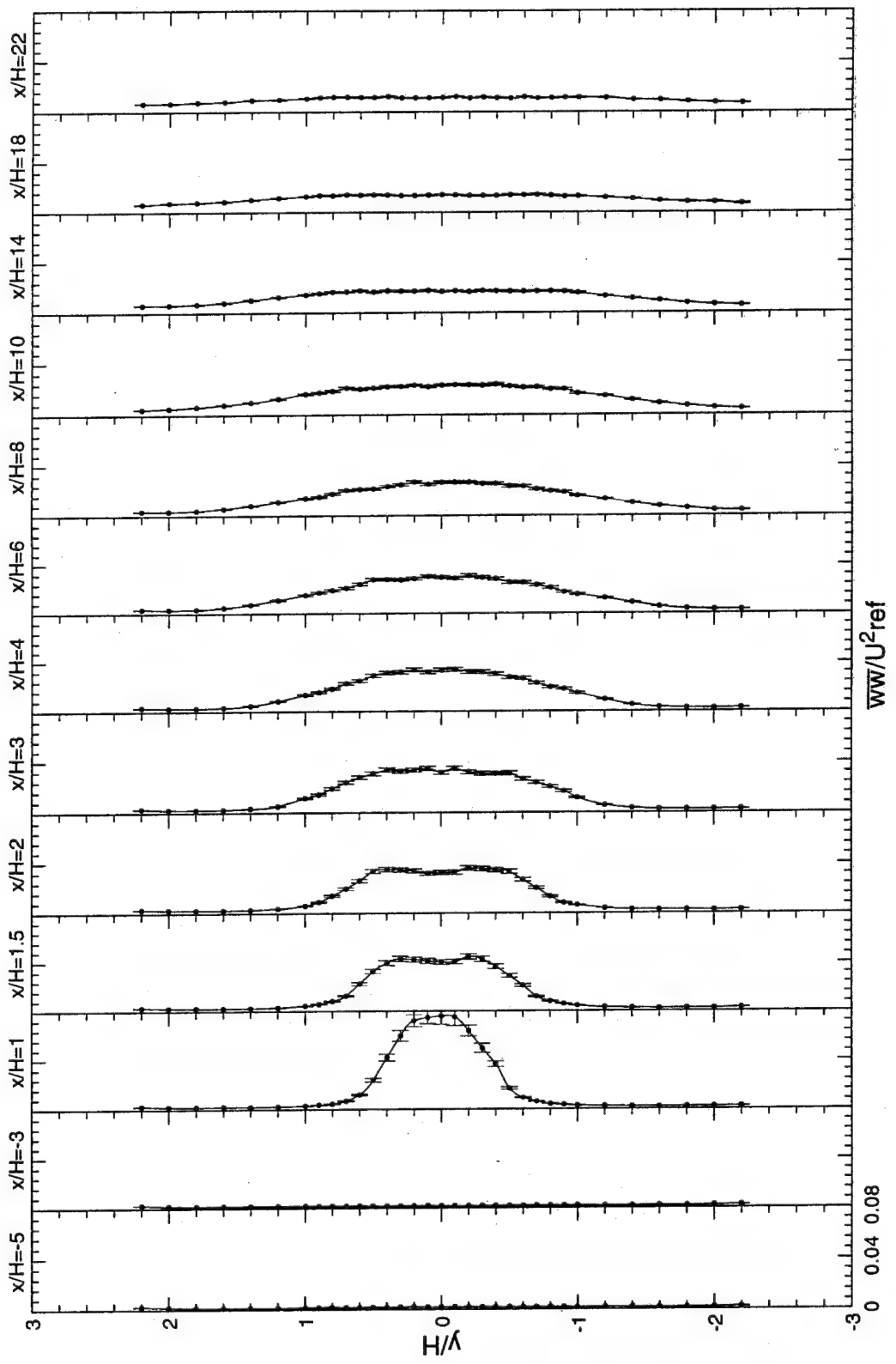


Figure 25. Normalized spanwise turbulent normal stresses.

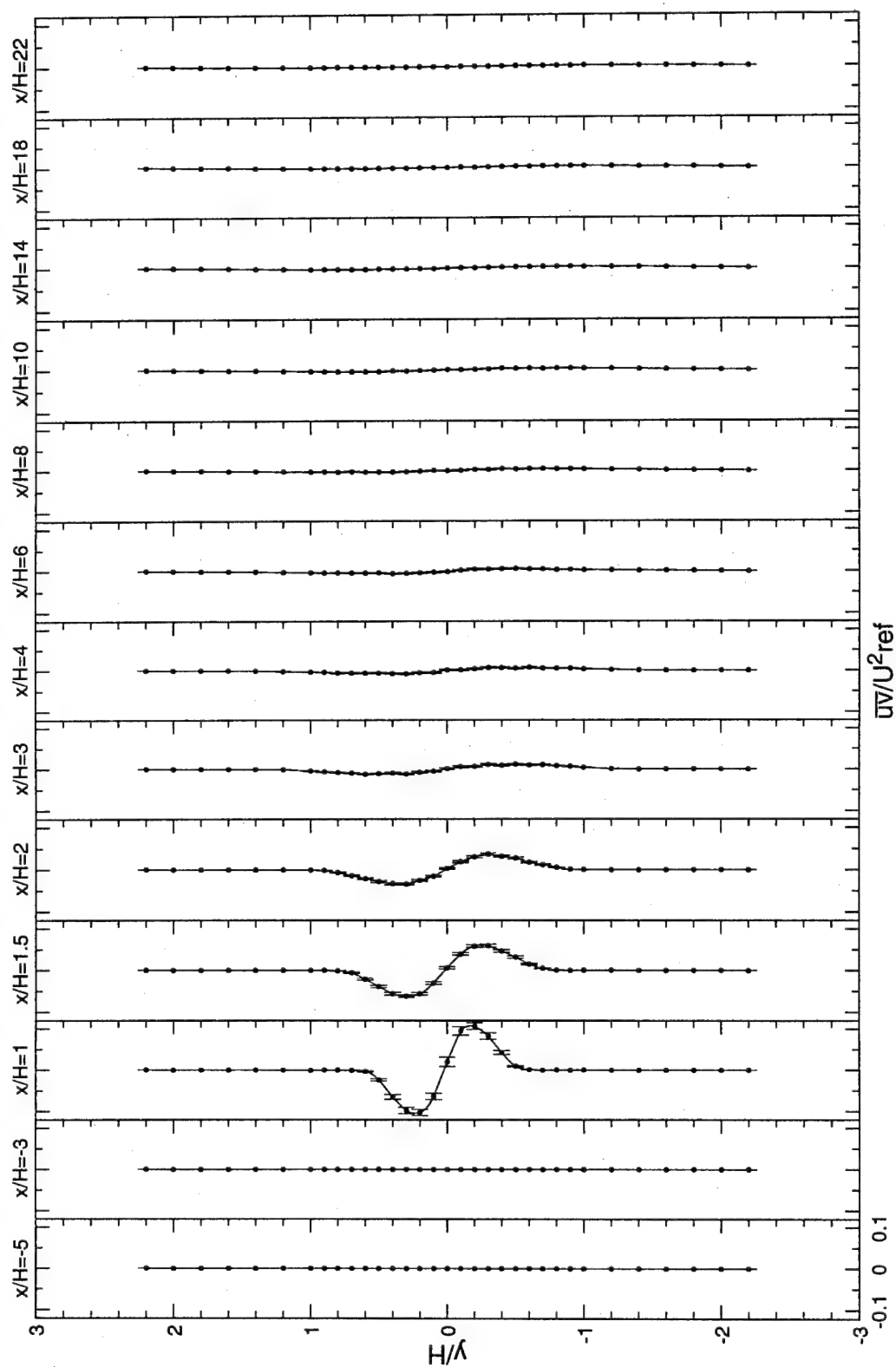


Figure 26. Normalized $\bar{u}\bar{v}$ turbulent shear stresses.

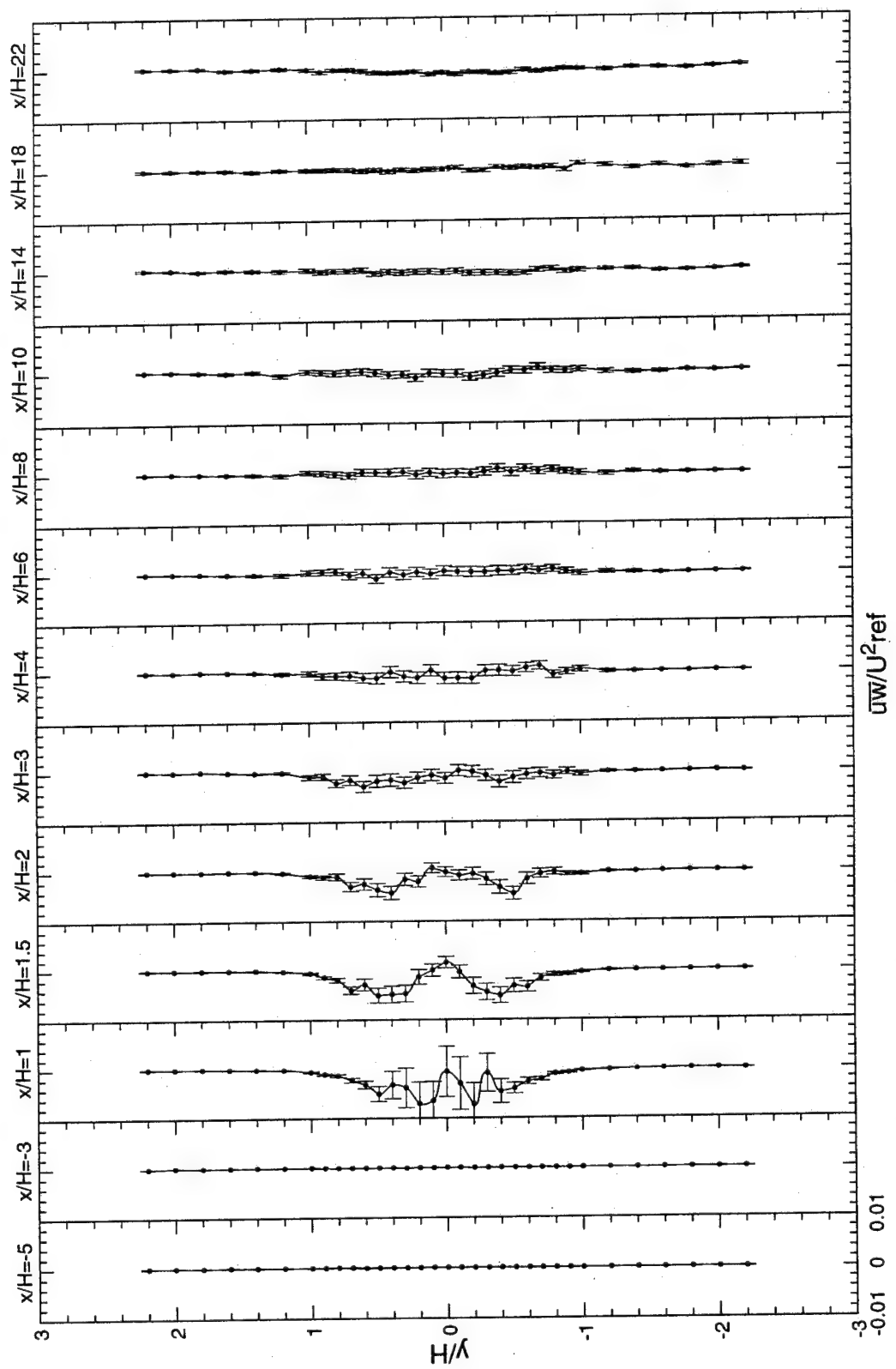


Figure 27. Normalized $\bar{u}w$ turbulent shear stresses.

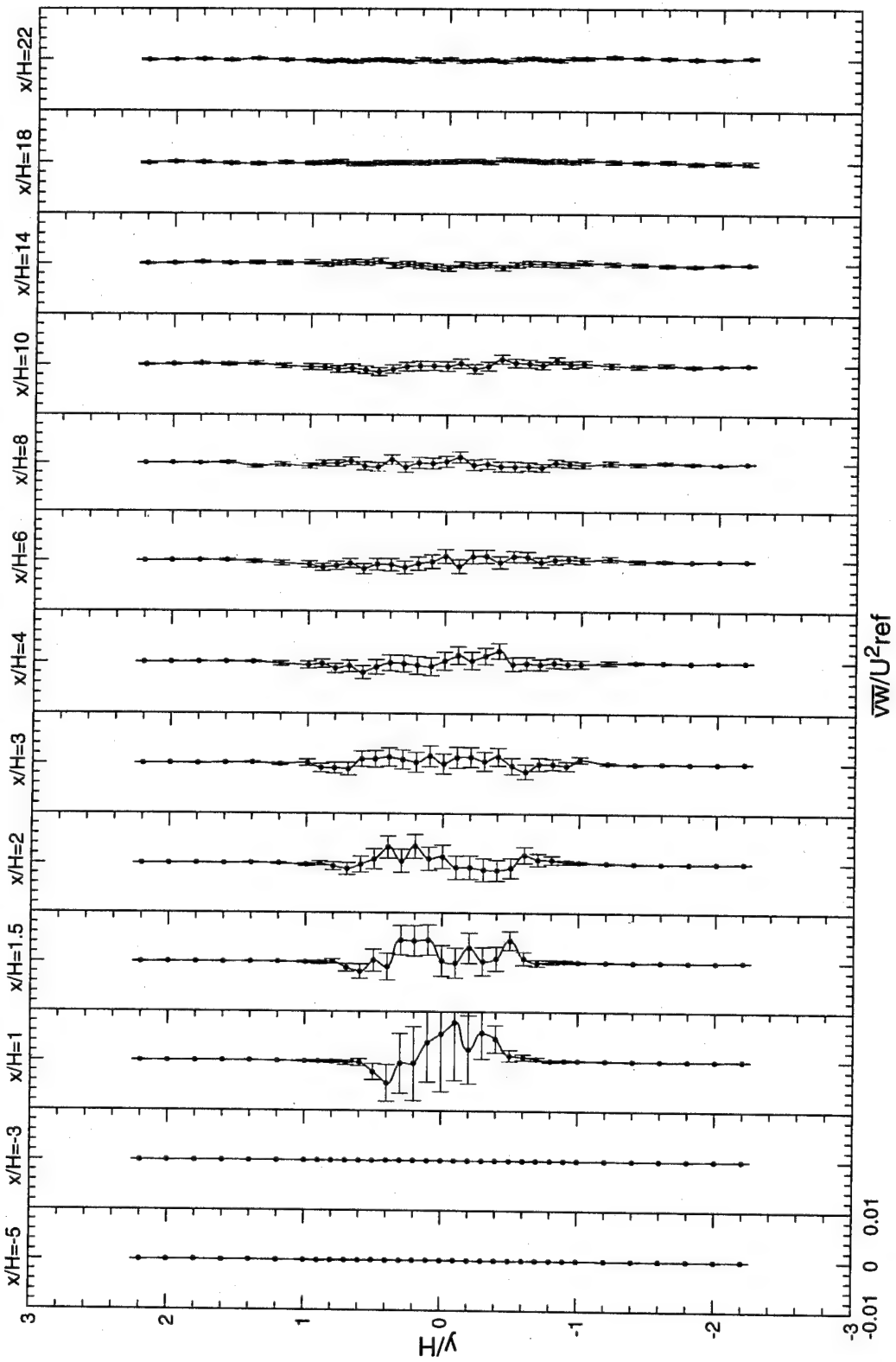


Figure 28. Normalized $\bar{v}w$ turbulent shear stresses.

5.5 Turbulent Triple Products

The turbulent triple products determined from the measurements made in this study are \overline{uuu} , \overline{uuv} , \overline{uvv} , \overline{uuw} , \overline{vww} , \overline{uvw} , \overline{vvv} , \overline{www} , and \overline{vwv} ; and are shown in their normalized form in Figures 29 through 37. The turbulent triple products represent the transport of the turbulence (TKE) by the fluctuating velocities. The maximum normalized (absolute) values in their order of magnitude are $\overline{vvv}/U_{ref}^3=0.28$, $\overline{uvv}/U_{ref}^3=0.05$, $\overline{uuv}/U_{ref}^3=0.03$, $\overline{uuu}/U_{ref}^3=0.028$, $\overline{vww}/U_{ref}^3=0.018$, $\overline{uvw}/U_{ref}^3=0.01$, $\overline{vvw}/U_{ref}^3=0.005$, $\overline{uuw}/U_{ref}^3=0.003$, and $\overline{www}/U_{ref}^3=0.0028$. The bi-modal hump-like feature of \overline{uuu} -triple product is due to the upper and lower shear layers. The value of \overline{vvv} was the largest (≈ 10 times that of \overline{uuu}). For the same reason described earlier when comparing \overline{uv} and \overline{uu} . It is worth noting that all terms containing an odd power of v such as \overline{uv} , \overline{vvv} , etc. are anti-symmetric, while those containing an even power of v such as \overline{vvv} , etc. are symmetric about the centerline. This is mainly due to the dominant antisymmetric nature of the transverse velocity component (Figure 18).

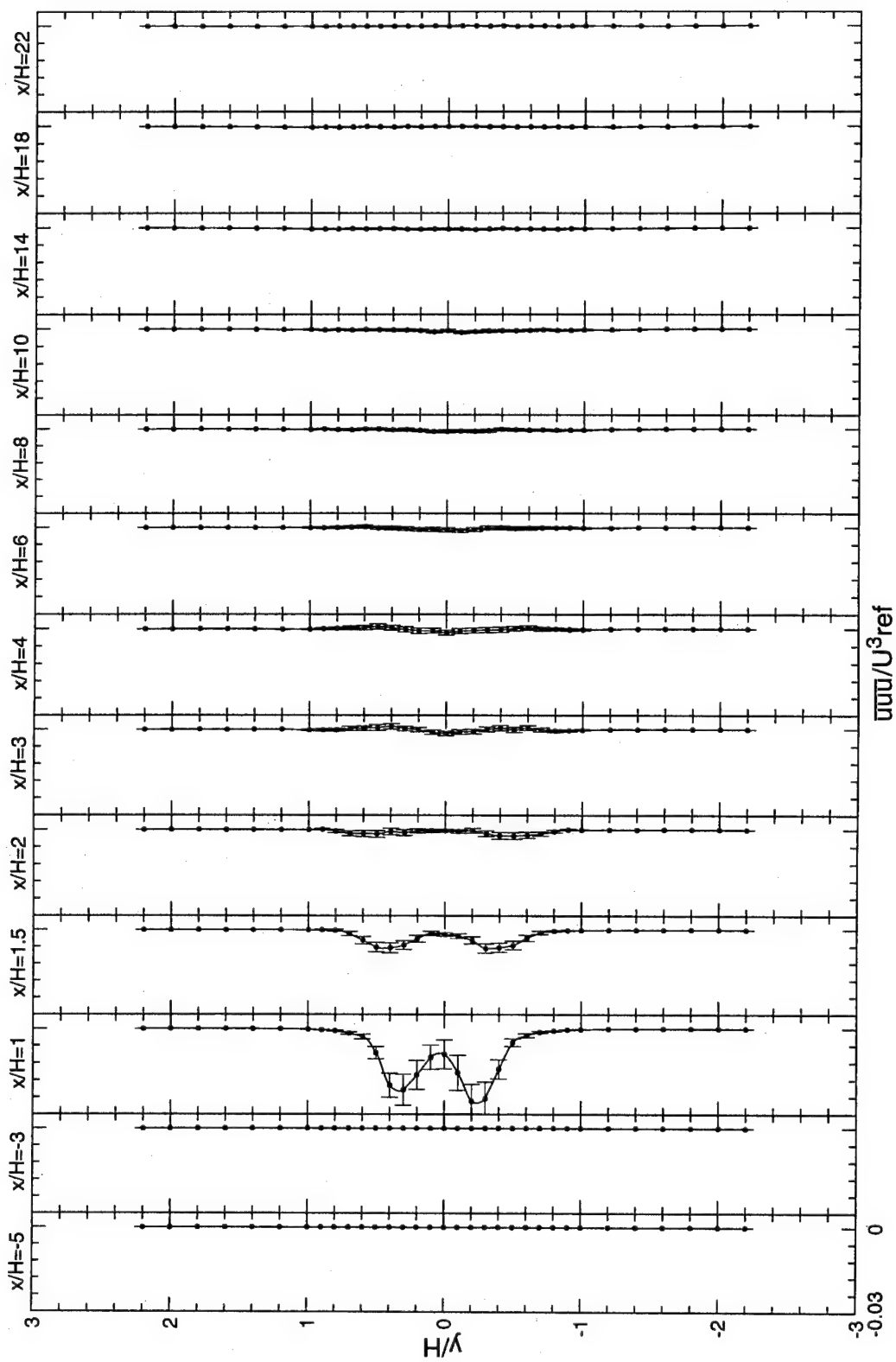


Figure 29. Normalized \overline{UUU} triple correlations.

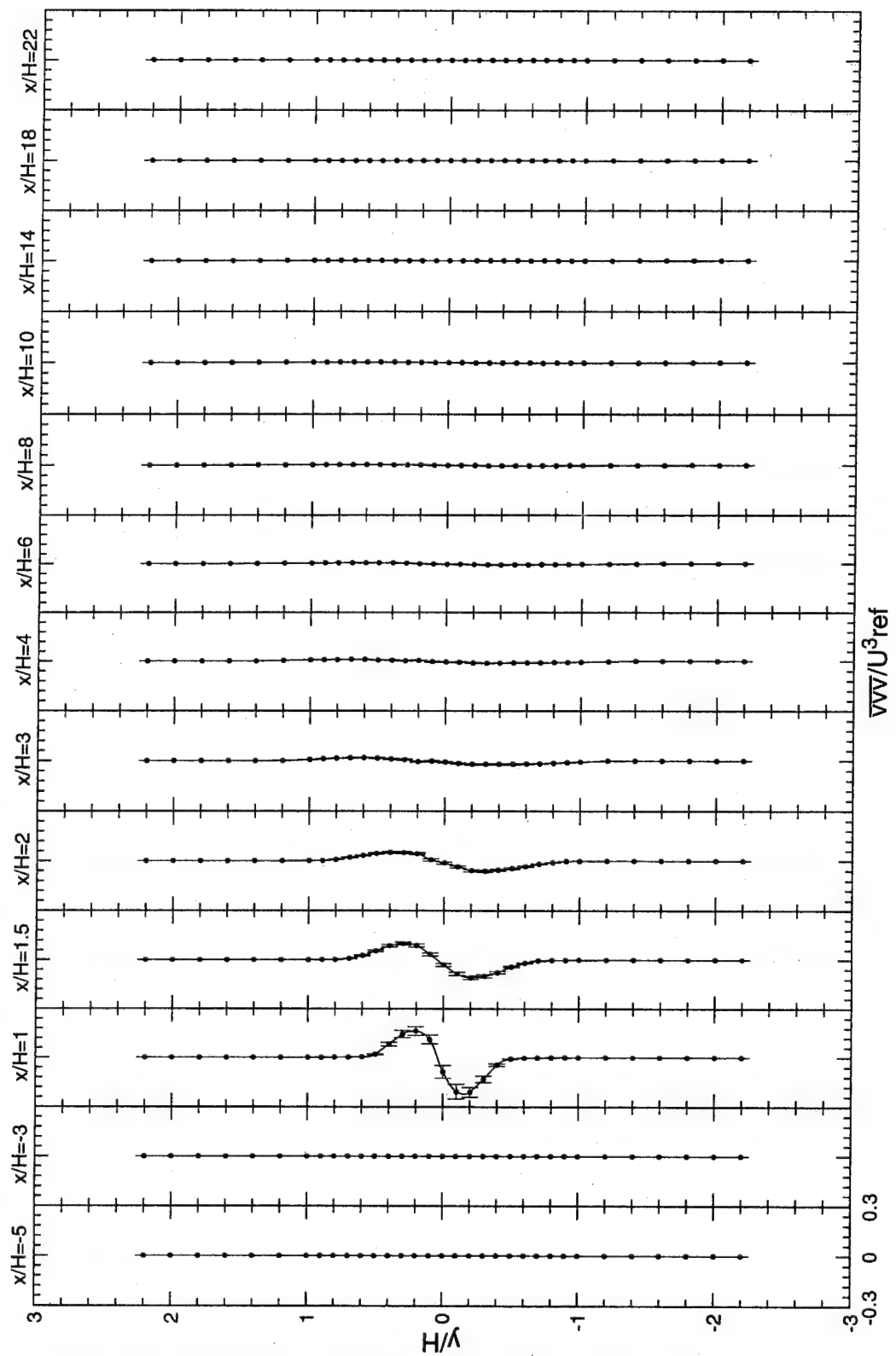


Figure 30. Normalized $\bar{V}\bar{V}\bar{V}$ triple correlations.

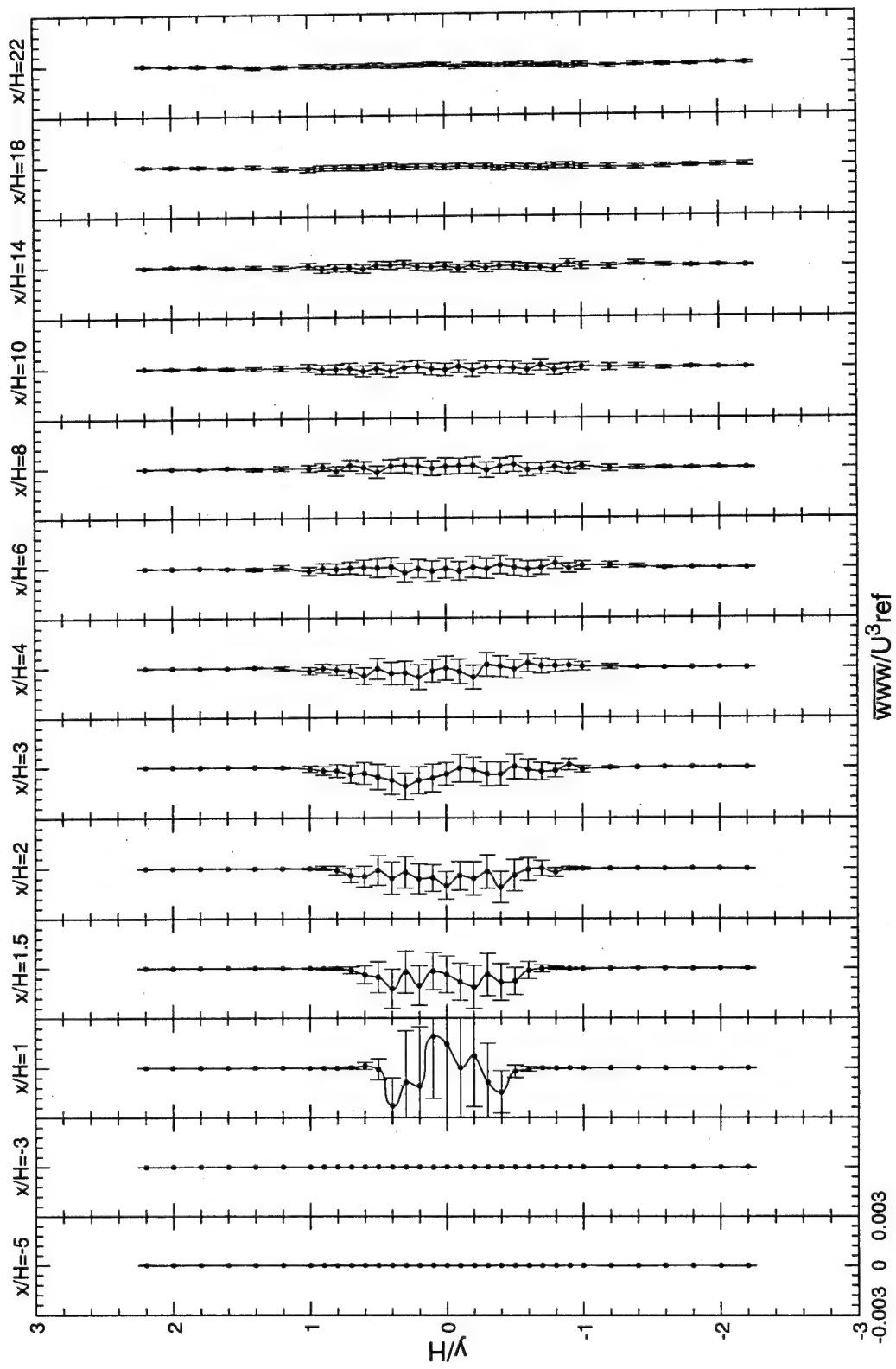


Figure 31. Normalized \overline{www} triple correlations.

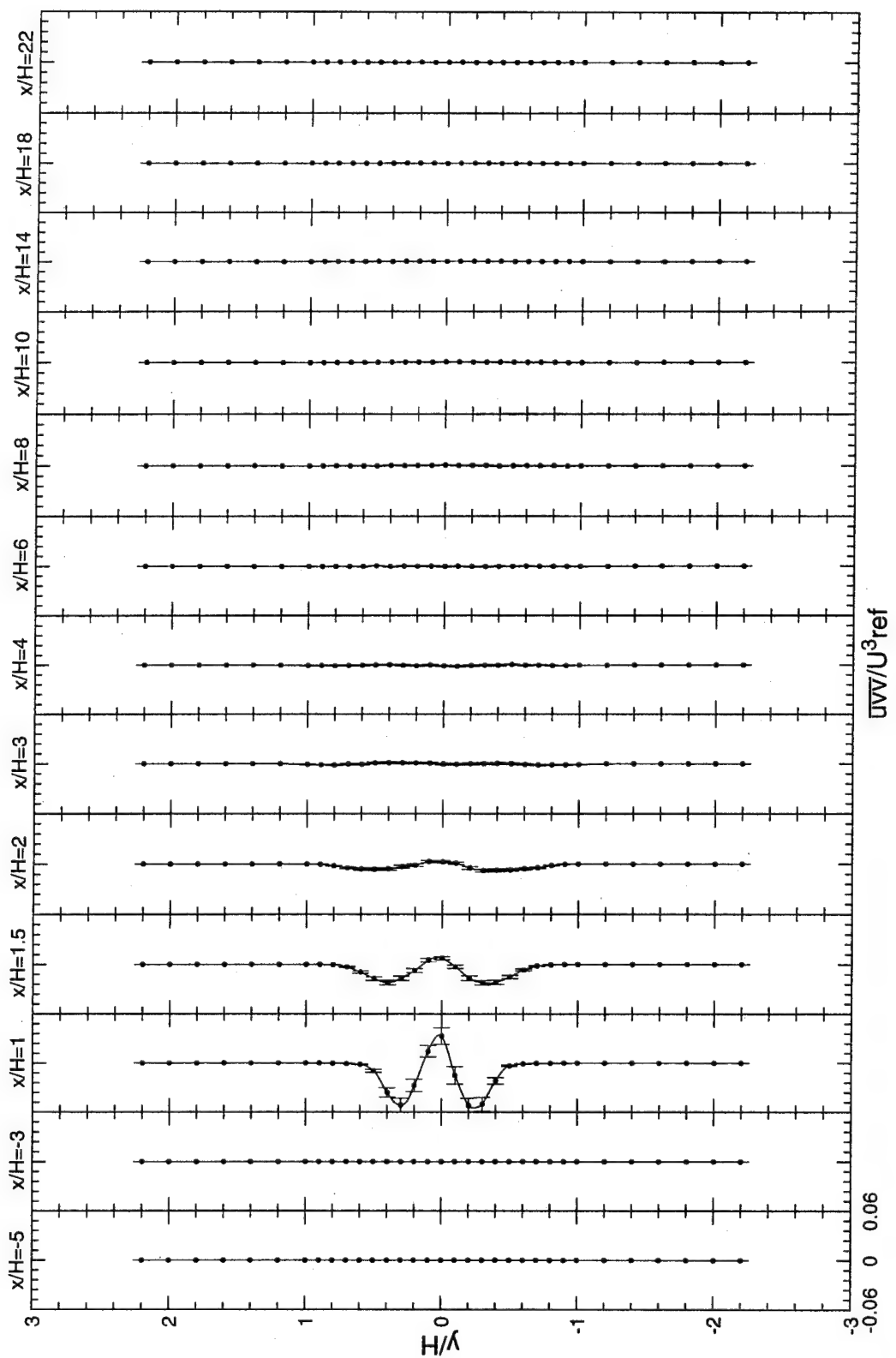


Figure 32. Normalized $\bar{U}VW$ triple correlations.

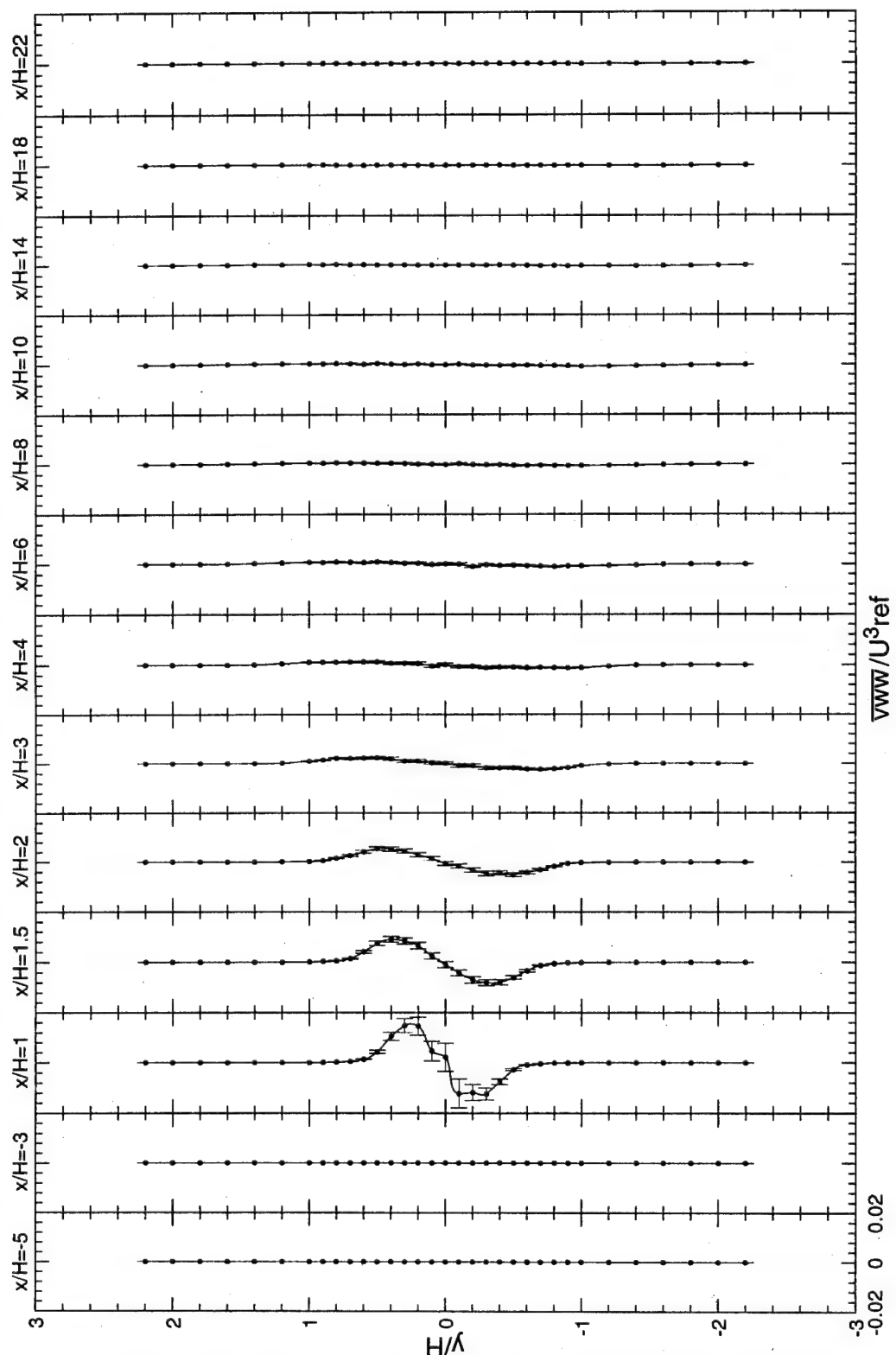


Figure 33. Normalized \overline{www} triple correlations.

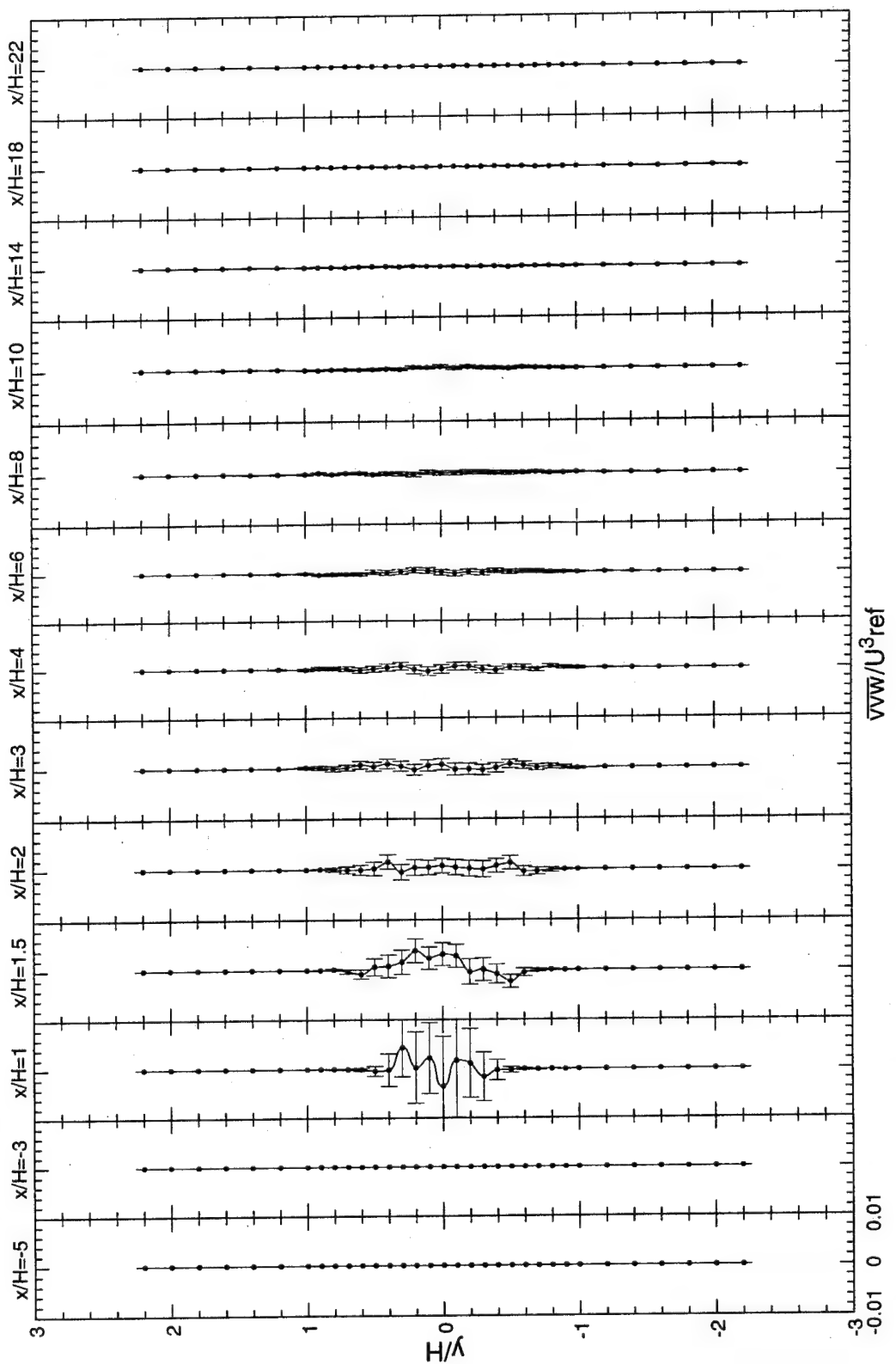


Figure 34. Normalized $\bar{v}vw$ triple correlations.

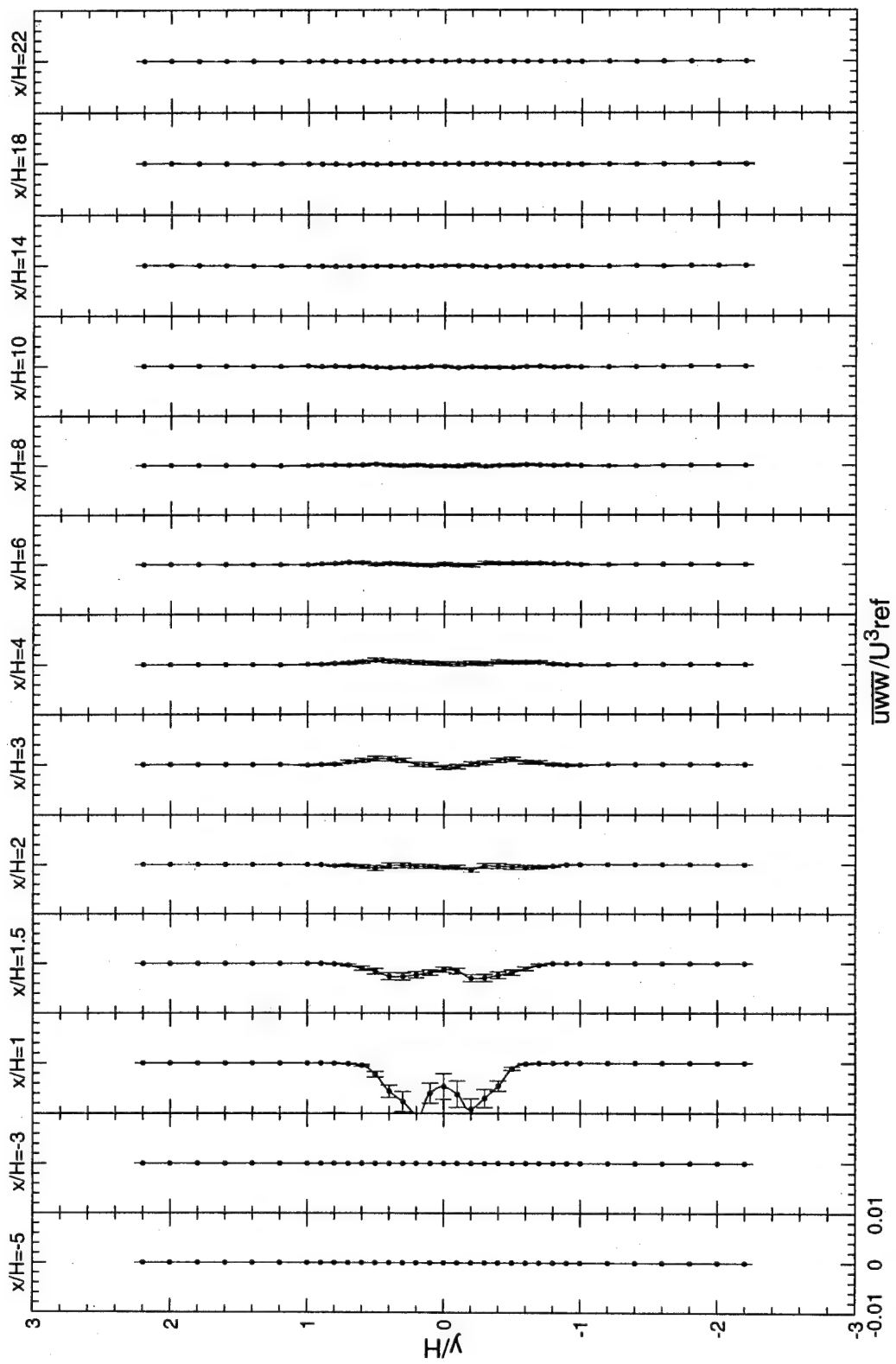


Figure 35. Normalized www triple correlations.

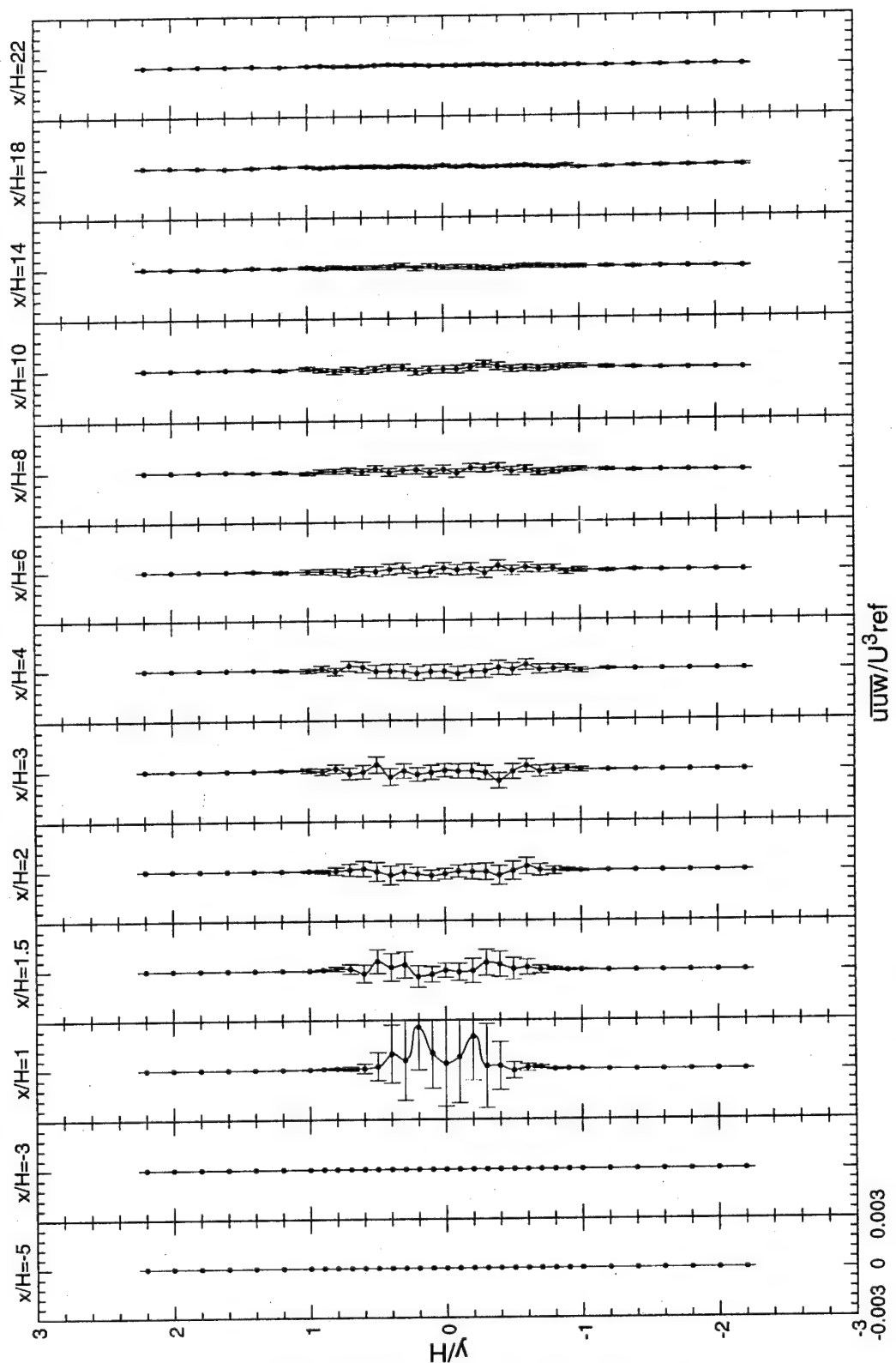


Figure 36. Normalized uuw triple correlations.

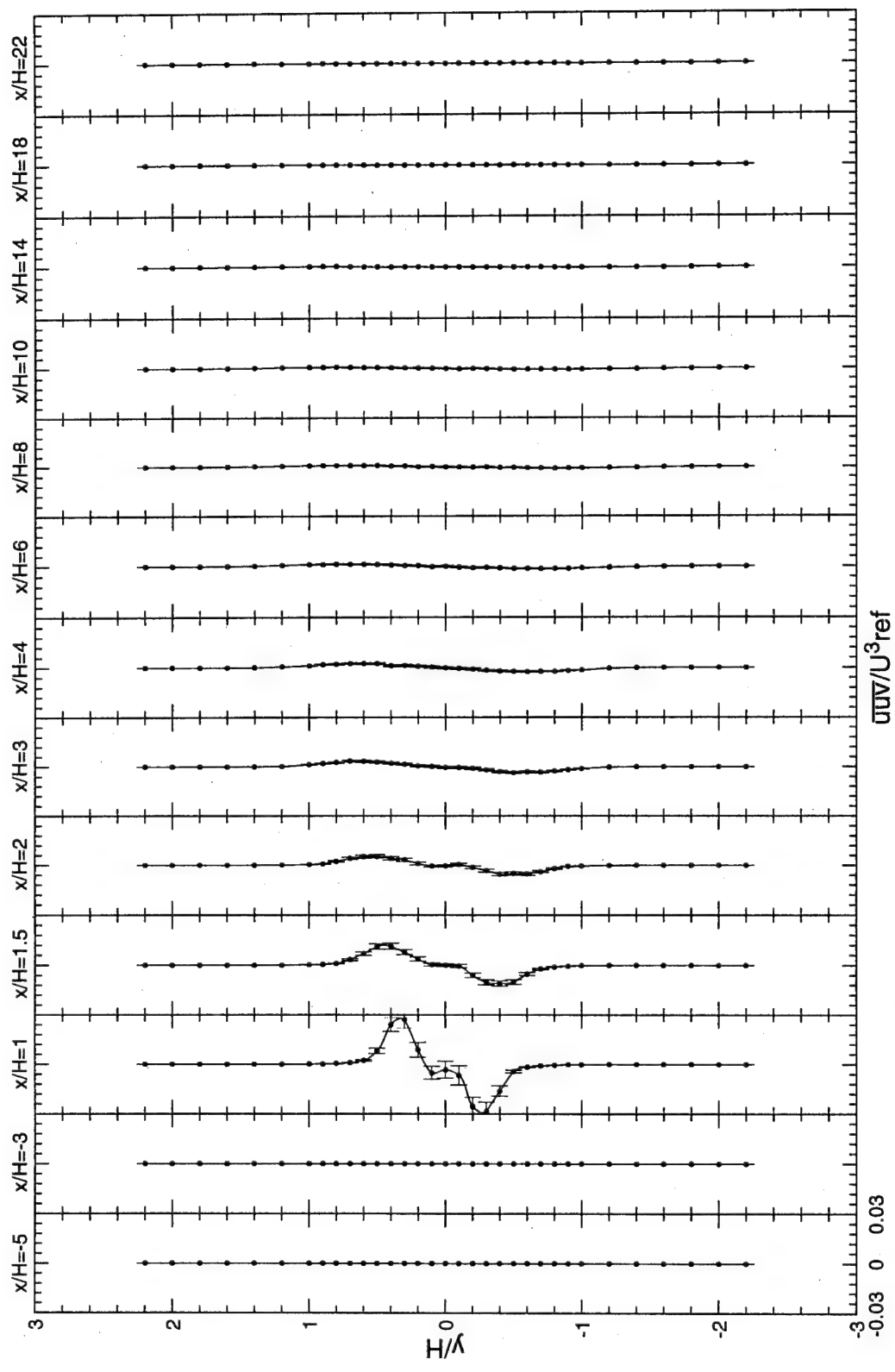


Figure 37. Normalized $\bar{U}U\bar{V}$ triple correlations.

5.6 Turbulent Kinetic Energy

The turbulent kinetic energy (TKE) is defined by Equation (5.2), where;

$$k \equiv \frac{\overline{uu} + \overline{vv} + \overline{ww}}{2} \quad (5.2)$$

Figure 38 shows the normalized turbulent kinetic energy profiles at the measured stations. Appendix H shows how the statistical uncertainty for k is calculated. The TKE peaked at station $x/H=1$ at the centerline to a normalized value of 0.38. The three normal stresses normalized with k are shown in Figures 39, 40 and 41. These figures clearly show that the turbulence downstream of the bluff body is not isotropic and thus care must be taken when one is attempting to numerically simulate these types of flow using simple turbulence models. Vortex shedding from the upper and lower separation points is believed to be the main cause of this phenomenon. The isotropic normalized values for \overline{uu} , \overline{vv} and \overline{ww} should be equal to $2k/3$. However, such a value was found only in the freestream or at further downstream positions behind the bluff body. The value for \overline{vv}/k was found to be the highest with a maximum value of 1.7, while that of \overline{ww}/k was the lowest with a maximum value of 1.1.

It is obvious from the measurements shown in the above figure that there is much more to be investigated in the very near-field just downstream of the bluff body. This will be the subject of the next Chapter.

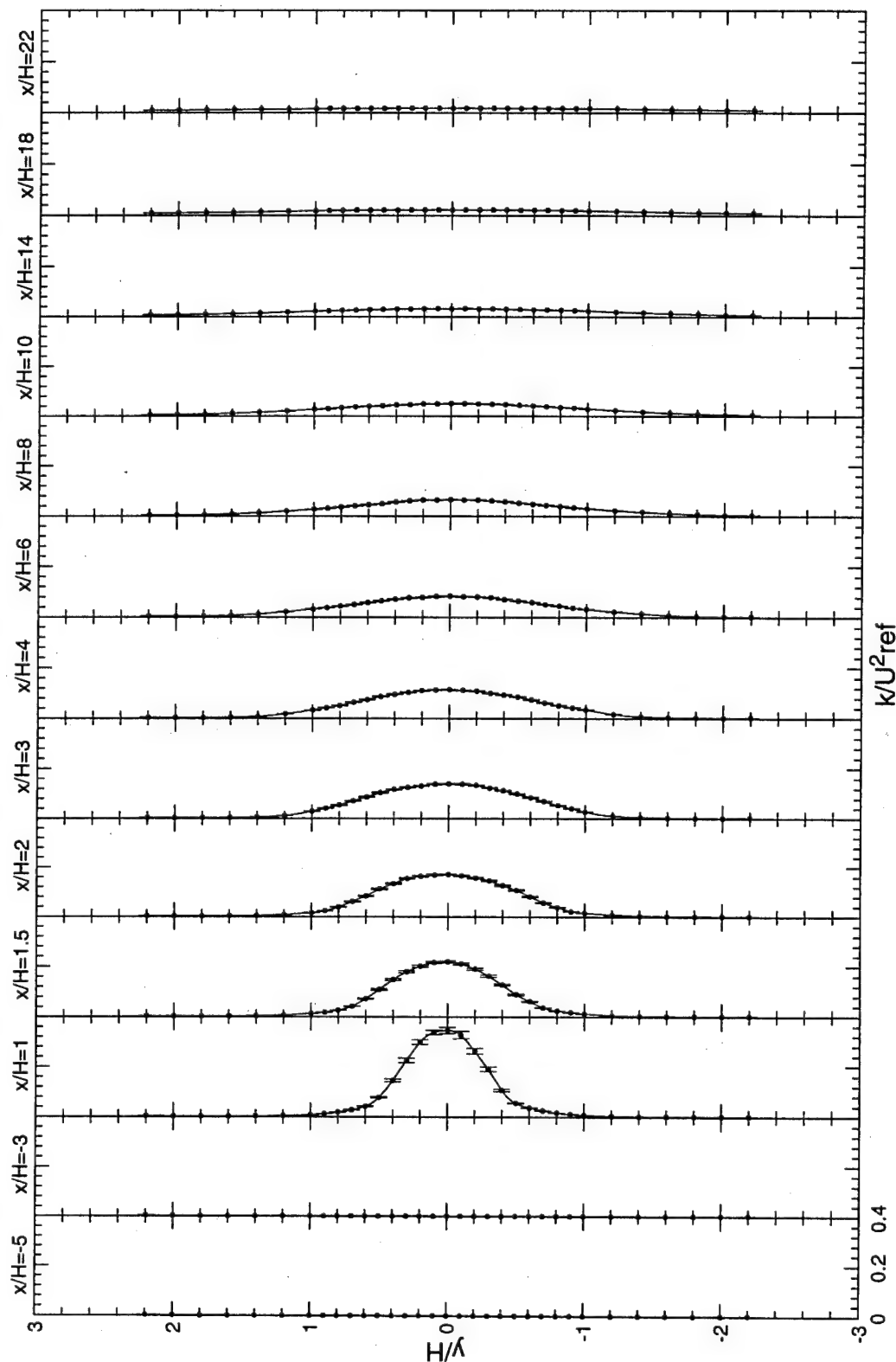


Figure 38. Normalized turbulent kinetic energy.

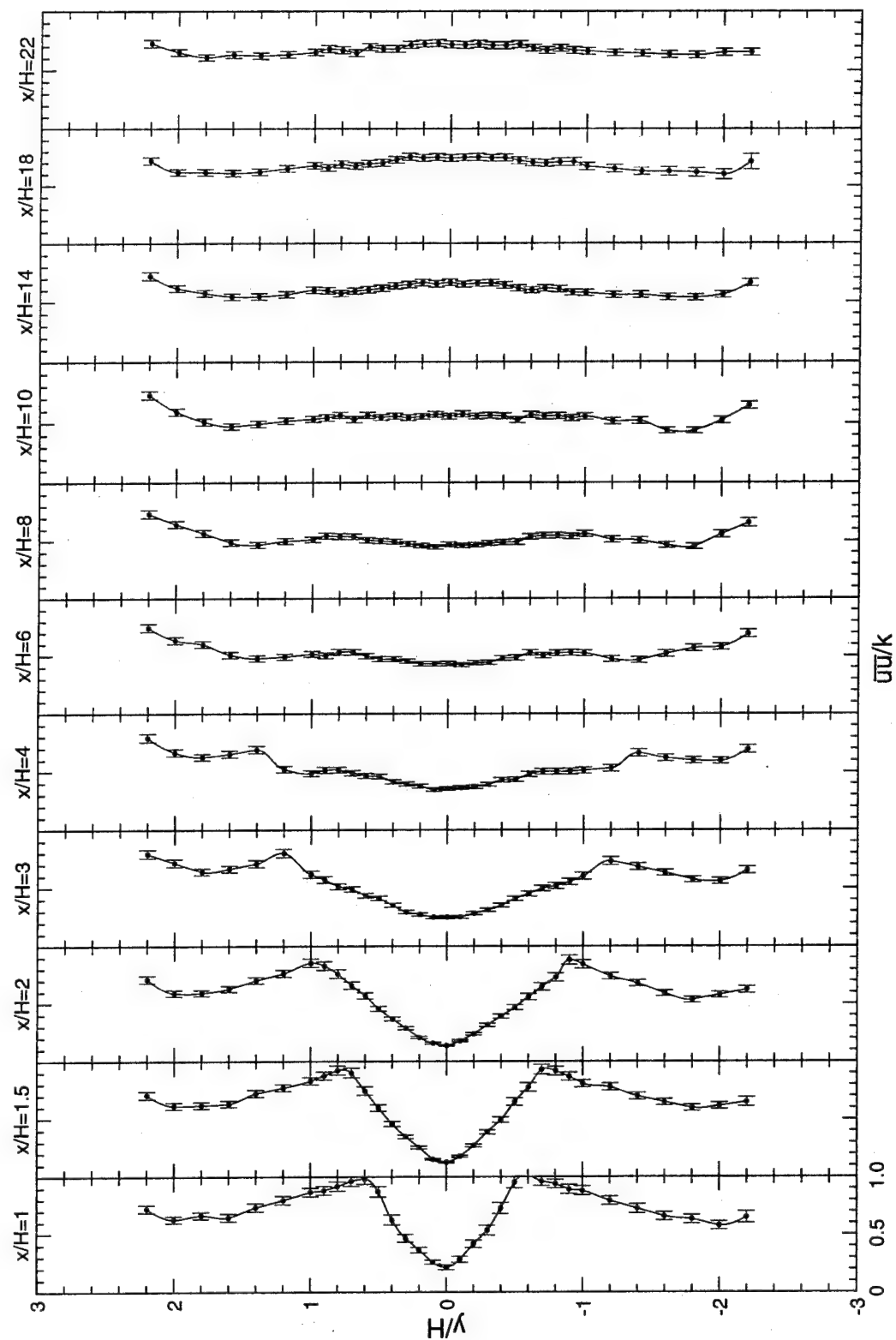


Figure 39. Axial mean normal stresses- Isotropy check.

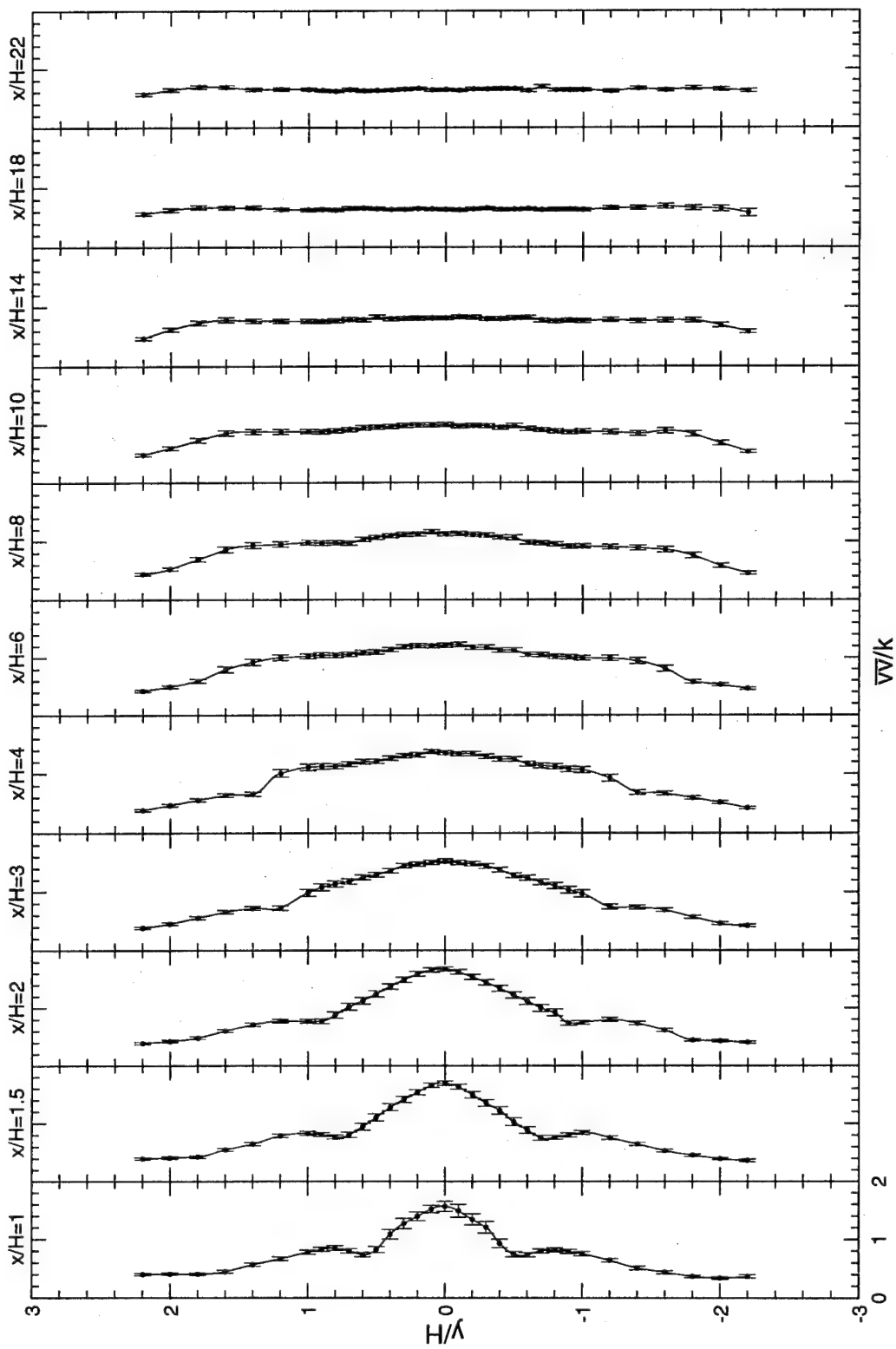


Figure 40. Transverse mean normal stresses- Isotropy check.

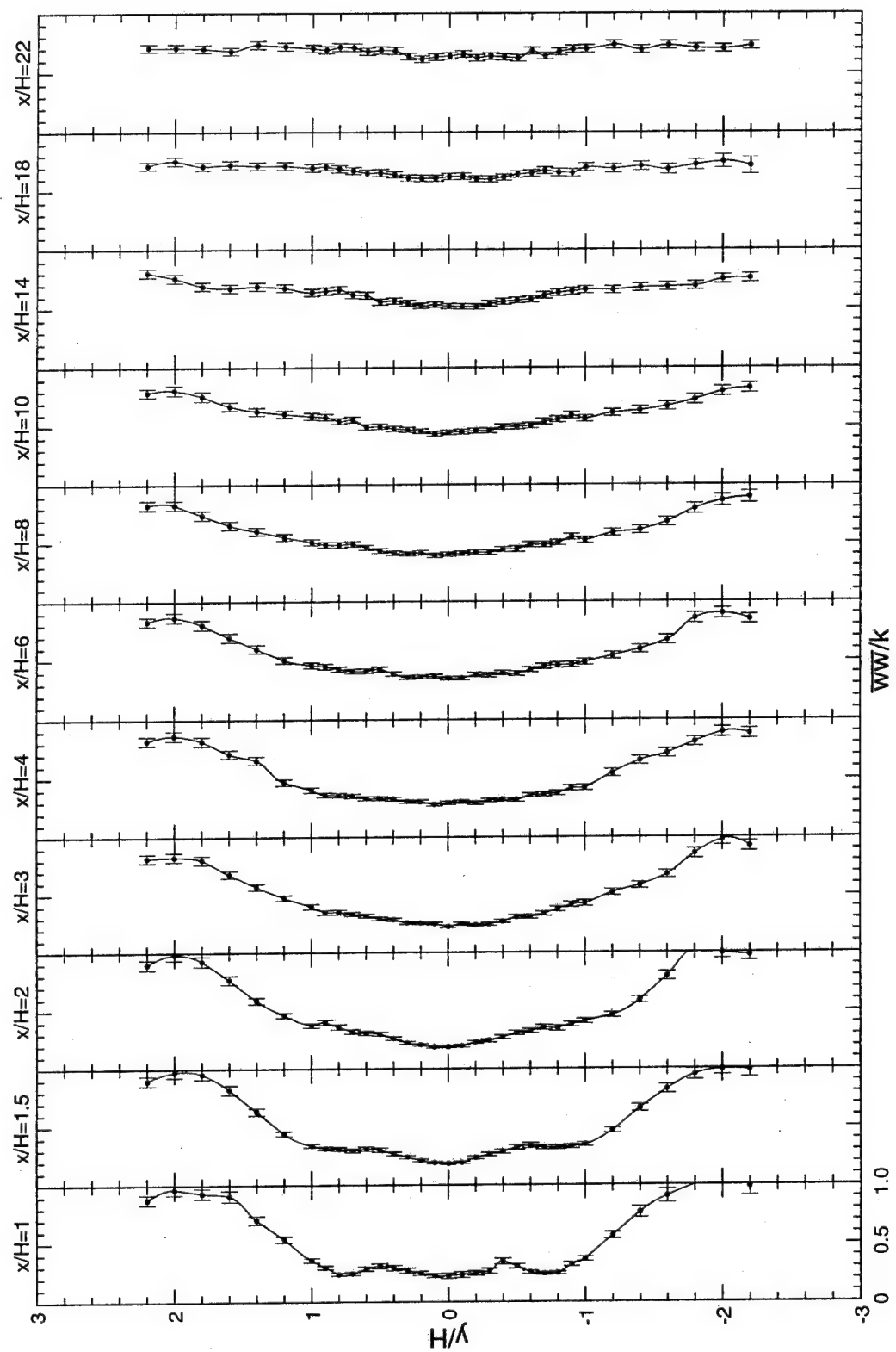


Figure 41. Spanwise mean normal stresses- Isotropy check.

CHAPTER 6

NEAR-FIELD EXPERIMENTAL RESULTS AND DISCUSSIONS

6.1 Introduction

In this section, the results of laser Doppler velocimeter (LDV) velocity measurements in the “near-field” are presented. Measurements of the axial, transverse and spanwise mean velocities, turbulent normal stresses as well as Reynolds stresses and turbulent triple products are included here. The turbulent kinetic energy (TKE) as well as the turbulence dissipation rate were also calculated. In this part of the study, the blue and green laser beams were rotated to $\pm 45^\circ$ relative to the tunnel bottom wall in order to gain access to the closest possible location, near the trailing edge of the bluff body, without beam interference. The following locations were investigated in the near-field, within and near the recirculation zone; $x/H=0.5, 0.6, 0.7, 0.8, 0.9, 1.0, 1.1, 1.2$. The smoothness of the profiles indicate that the data rate and the sample size ($N=5120$) are quite sufficient to obtain smooth data, even for the higher order moments. The mean spanwise velocities along the z -axis at $y/H=0$ at various x/H stations are also shown in this Chapter. Comparisons between commonly used assumptions for \overline{ww} , \overline{uww} , and \overline{vww} (when third component data is not available) and the experimental measurements of these quantities are made and presented. Newly derived expressions for these turbulence parameters are suggested using the data.

6.2 Mean Velocity Data

Simultaneous three-component measurements of mean velocity distributions are obtained by traversing the flowfield with the LDV probe volume in the vertical (y) direction at various axial positions. The measurements were made only out to $y/H=\pm 1.2$ as the velocities and higher order moments were nearly uniform in the freestream away from the centerline region, as depicted by the previously presented far-field measurements.

Non-dimensional mean axial velocity profiles are shown in Figure 42. All velocity measurements are normalized with the reference velocity, as obtained point-by-point, and all dimensions are normalized with the bluff-body height, $H=12.7$ mm (0.5 in.). Measurements gave virtually identical results when compared to those obtained with the previous LDV setups (i.e., see 1-d and 3-d measurements with 0° and 90° beam orientation at $x/H=1$). At all stations, the presence of the wake behind the bluff body can clearly be seen in the center of the flow, as well as the presence of two shear layers. Downstream of the bluff body, a time-averaged recirculation zone is present with associated reverse mean velocities. The first station, located one-half of the bluff-body height downstream ($x/H=0.5$), shows a maximum normalized velocity deficit of -0.35 (35% of the reference velocity). Although, the recirculation zone is often called the "dead air zone," in this study it contained unsteady flow. The length of this ellipsoidal-shaped, time-averaged recirculation zone, behind the bluff body, defined where $\bar{U} = 0$ at $y/H=0$, was found to be $x/H=0.9$. The width of the time-averaged recirculation zone was nearly one bluff-body thick, which is relatively small, when compared to the recirculation region behind a backward-facing step. These dimensions are in agreement with Raghunathan (1994). The shorter length of the recirculation zone is

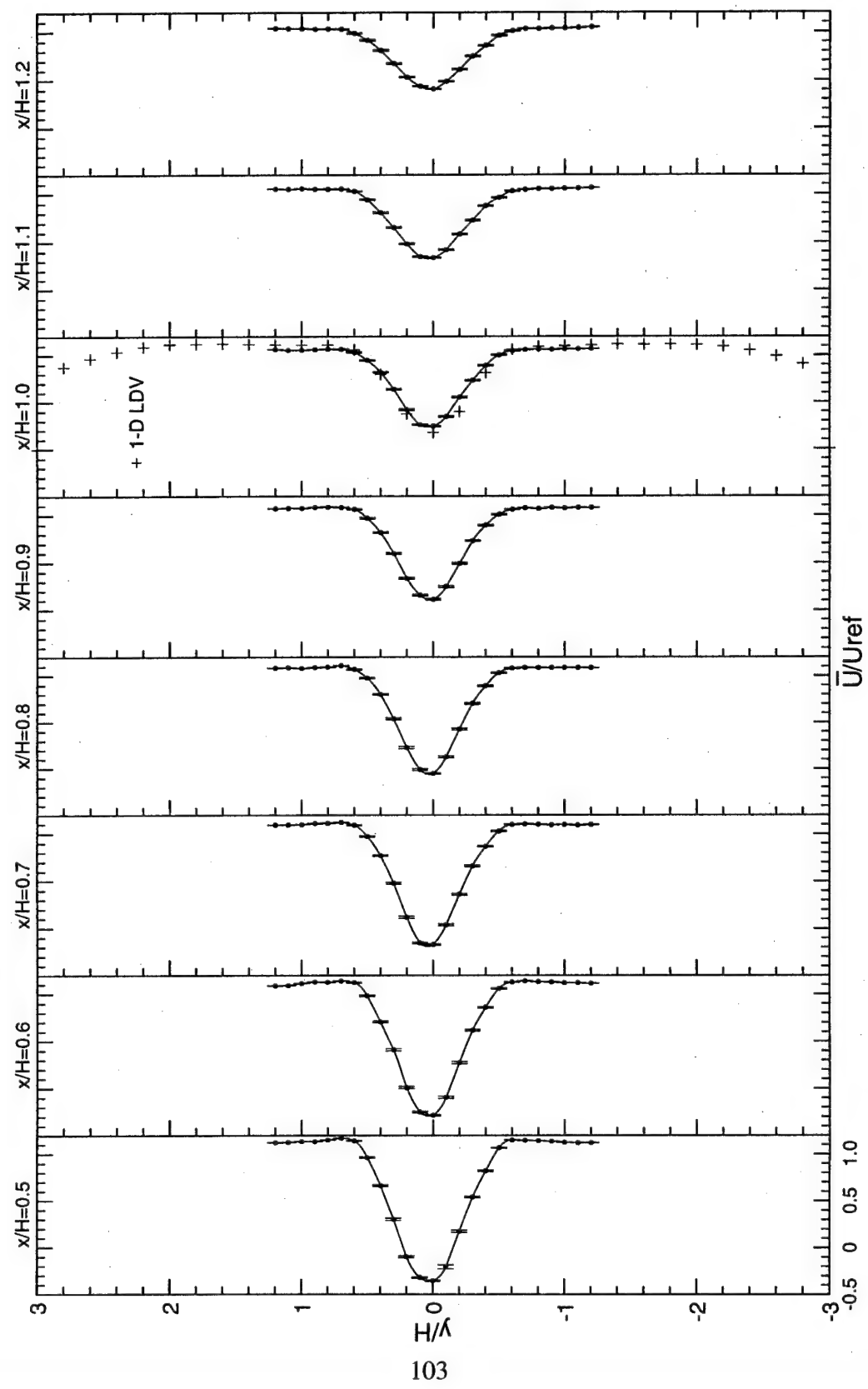


Figure 42. Normalized mean axial velocity profiles; 3-d LDV.

attributed to the inverse relationship that exists between blockage and the size of the recirculation zone. Davies and Beer (1970) indicated that the ratio of the pressure forces to inertia forces in the wake of the bluff body increases with the blockage ratio, resulting in a shorter distance to the stagnation point. However, the magnitude of the reverse flow is high in this region which results in rather intense vortex role-up. The width of the unsteady wake extended from $-0.6 < y/H < 0.6$ for all eight near-field stations, which is slightly larger than the bluff-body thickness. The normalized mean axial velocities at $y/H=0$ increased in the downstream direction from a value of -0.35 at $x/H=0.5$ to 0.6 at $x/H=1.2$ (Figure 42).

Figure 43 shows the normalized transverse mean velocity distributions. The mean transverse velocity profiles are anti-symmetric at all stations, since the transverse velocity is directed towards the centerline in this near-field region. Unlike the axial velocity, the magnitudes of the transverse velocities were relatively unchanged from axial station to station due to transverse direction oscillating shed vortices which span the entire length of the time-averaged recirculation zone. This is a result of the vortex roll-up process, which acts both upward and downward during the sampling time. In the axial direction, the vortex contribution to the U-velocity decreases as the convective freestream flow begins to dominate the weakening recirculating flow with increasing downstream distance.

Figure 44 shows the normalized mean spanwise velocity (\bar{W}) measurements at $z/H=0$ in the transverse direction. The data show that there exists a w-velocity component at the centerline station which diminishes in magnitude as the flow progresses further downstream, away from the bluff body. In a perfectly symmetric flow, one would not expect such behavior; \bar{W} would be zero in this case. These measurements may indicate that the probe

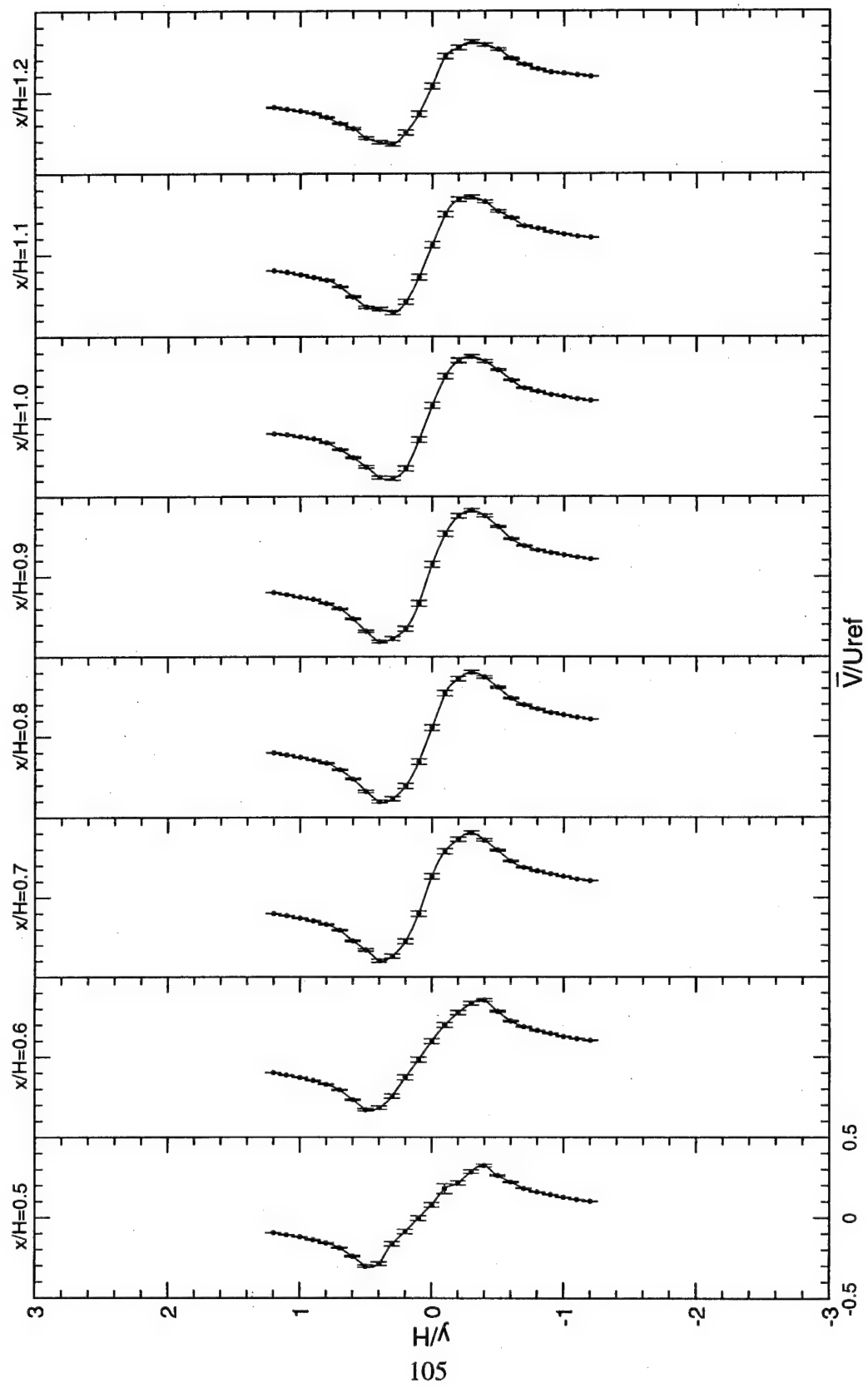


Figure 43. Normalized mean transverse velocity profiles; 3-d LDV.

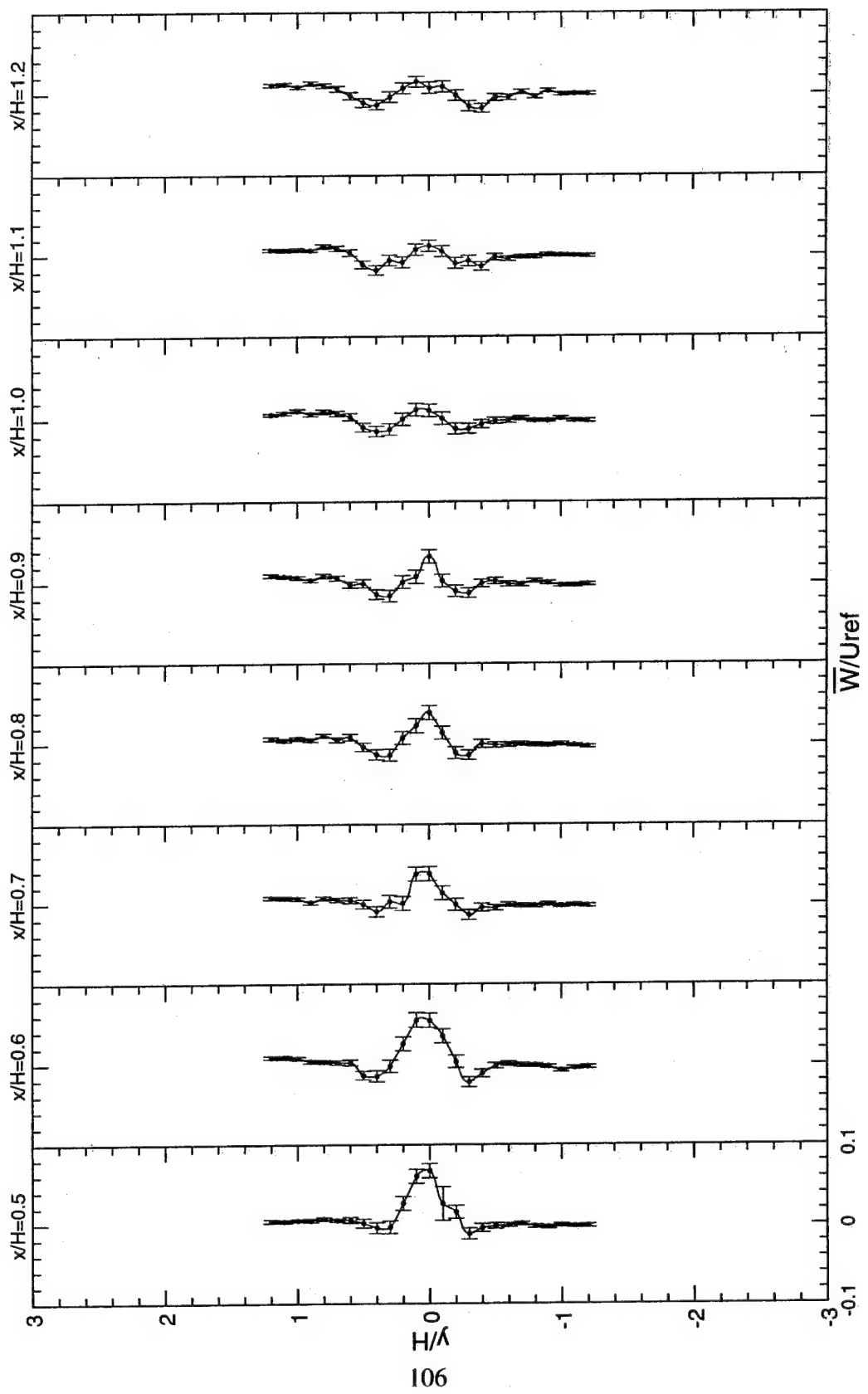


Figure 44. Normalized mean spanwise velocity profiles at $z/H=0$; 3-d LDV.

volume was not centered properly with respect to the fluid flow centerline in the spanwise direction. It is also speculated that non-symmetric boundary layer growth on the side walls could lead to a slight shift in the flow centerline in the spanwise direction.

Figure 45 shows the normalized mean spanwise velocity measurements along the z-axis at $y/H=0$ in the near-field. This figure clearly shows the three-dimensional nature of the flow behind the bluff body. However, this w-component is not symmetric with respect to the $z/H=0$ axis but shows a positive value for \bar{W} as was shown in Figure 44. In addition, Figure 45 suggests that there exists four counter-rotating (in the x-z plane) recirculating bubbles directly behind the bluff body that were slightly non-symmetric and thus did not cancel at $z=0$. This non-symmetric behavior could be attributed to many factors, such as, imperfect walls, a slight shift in bluff-body geometry, non-symmetric boundary layers as mentioned earlier, and possibly other factors. Three-dimensional flow characteristics were also reported by Armaly, et al. (1983) in the recirculation region behind a backward-facing step.

In an effort to define the recirculation zone location in the spanwise direction, separate 1-d LDV measurements were made at fifteen closely spaced axial locations along the z-axis. As shown in Figure 46 the incoming spanwise flow profile is flat as depicted by the two upstream stations. Also, downstream of the bluff body, a similar general profile shape as that obtained when using the 3-d LDV (i.e., Figure 45) is noticed. One difference however, is that the sign of the \bar{W} -velocity trend is reversed in the two very near stations; $x/H=0.02$, and $x/H=0.1$, when compared with the trend of the other downstream stations. This indicates that a vortex exists downstream of the bluff-body trailing edge with its center located very near the bluff body.

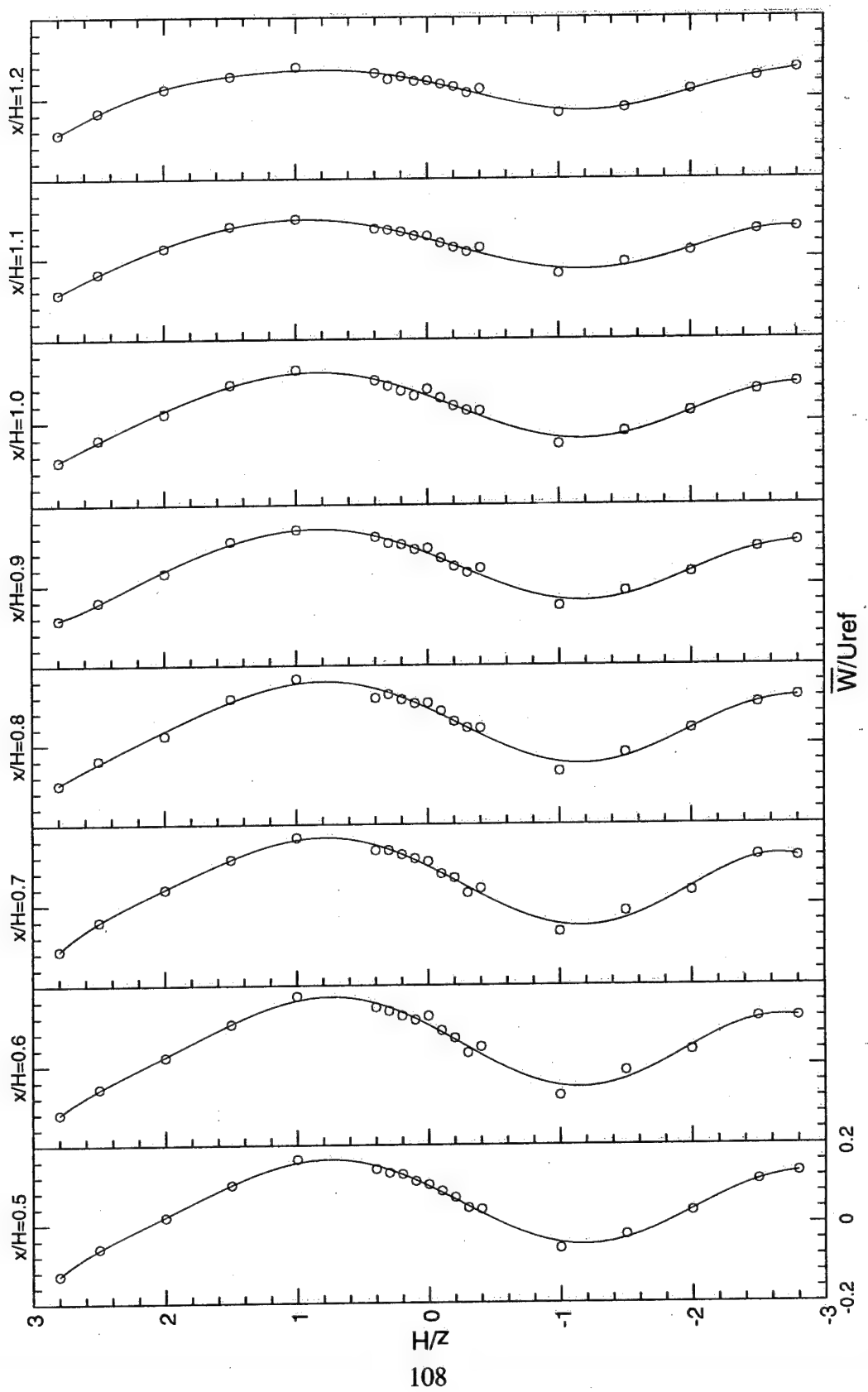


Figure 45. Normalized mean spanwise velocity profiles at $y/H=0$; 3-d LDV.

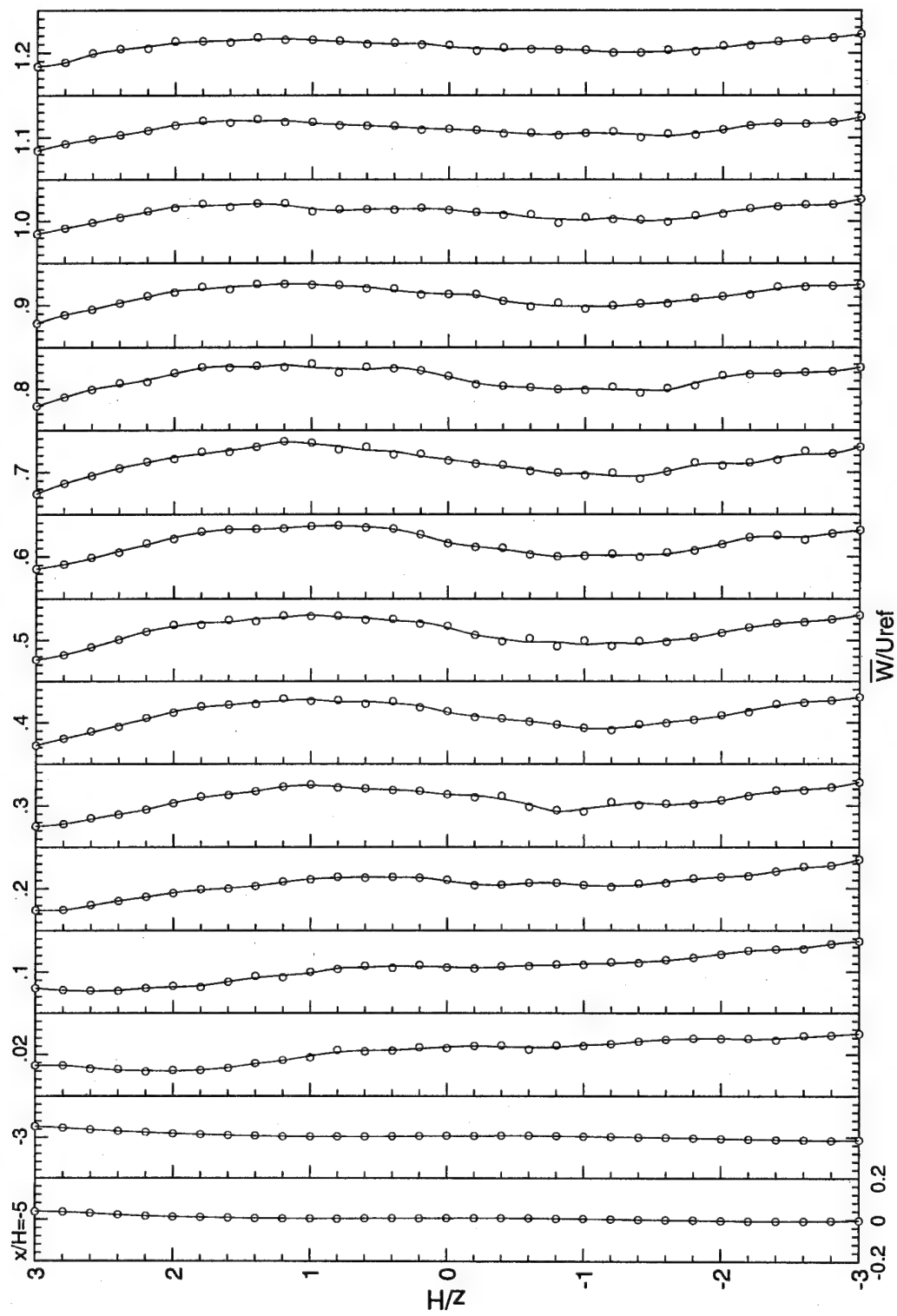


Figure 46. Normalized "1-d LDV" mean spanwise velocity profiles at $y/H=0$; 1-d LDV.

6.3 Turbulent Stresses

6.3.1 Reynolds Stresses

The normalized turbulent shear stresses (\bar{uv} , \bar{uw} , \bar{vw}) have also been obtained in the near-field region. These measurements indicate that the \bar{uv} shear stress (Figure 47) is the most significant one of the three, and its maximum value is five times larger than the maximum value of the other two shear stresses (Figures 48 & 49). The values of \bar{uv} were found to be rather small at $x/H=0.5$, the closest measurement station downstream of the bluff body. In the separated region, the shear stress increases to an absolute maximum of about $0.1xU_{ref}^2$ occurring at $x/H=0.9$, $y/H=\pm 0.2$, which is the locus of the time-averaged separating streamlines between the recirculation bubble and the surrounding flow.

6.3.2 Normal Stresses

Figures 50 through 52 show the normalized turbulent normal stresses at the eight near-field axial stations. It should be noted that local peak intensities occur at locations where the mean-velocity gradients are high, indicating that gradient transport turbulence models may work well. As expected, the axial normal stresses (Figure 50) show the double hump behavior due to the presence of shear layers near the top and bottom edge of the bluff body. Peak values of normalized axial turbulent stress occur at $x/H=0.5$, in the shear layers, and reached a value of 0.18, which corresponds to a maximum normalized axial turbulence intensity of 42.5%. The normalized value (31%), at $x/H=1$, compares well with that obtained behind a backward-facing step (25%), as reported by Gould, et al. (1990). It is noteworthy that the peak normalized transverse normal stress occurs on the centerline of the flow at

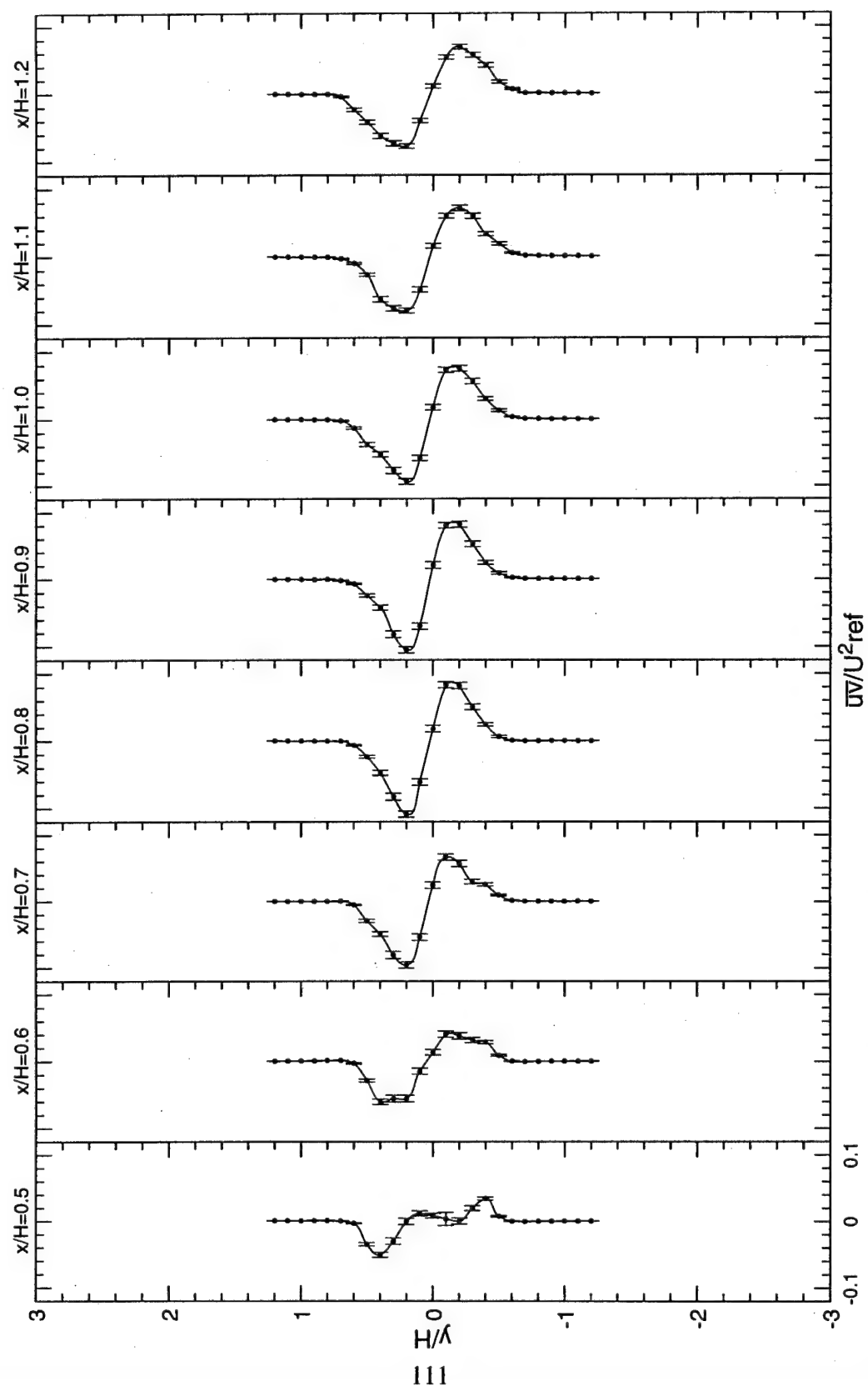


Figure 47. Normalized uv turbulent stress distributions.

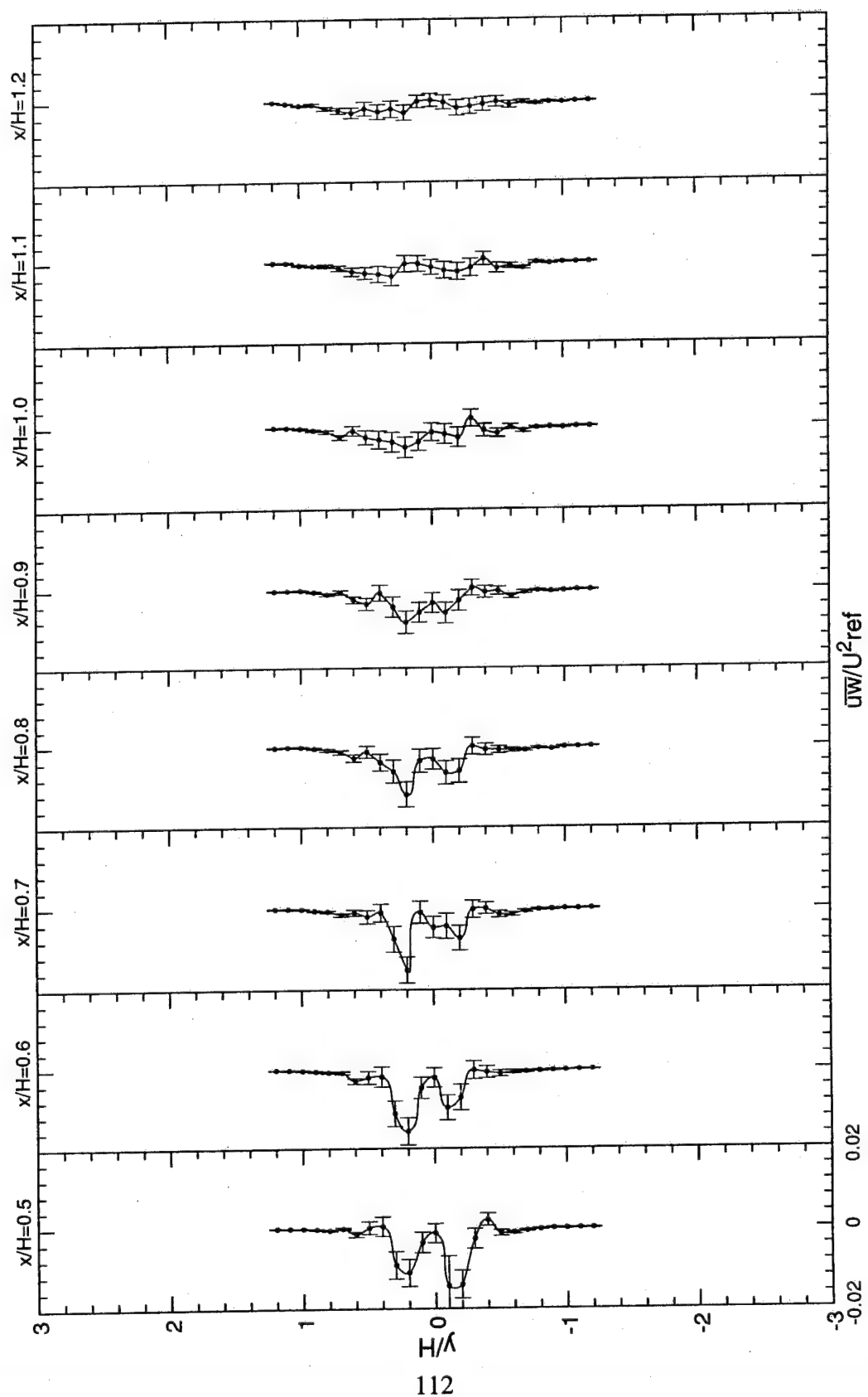


Figure 48. Normalized uw turbulent stress distributions.

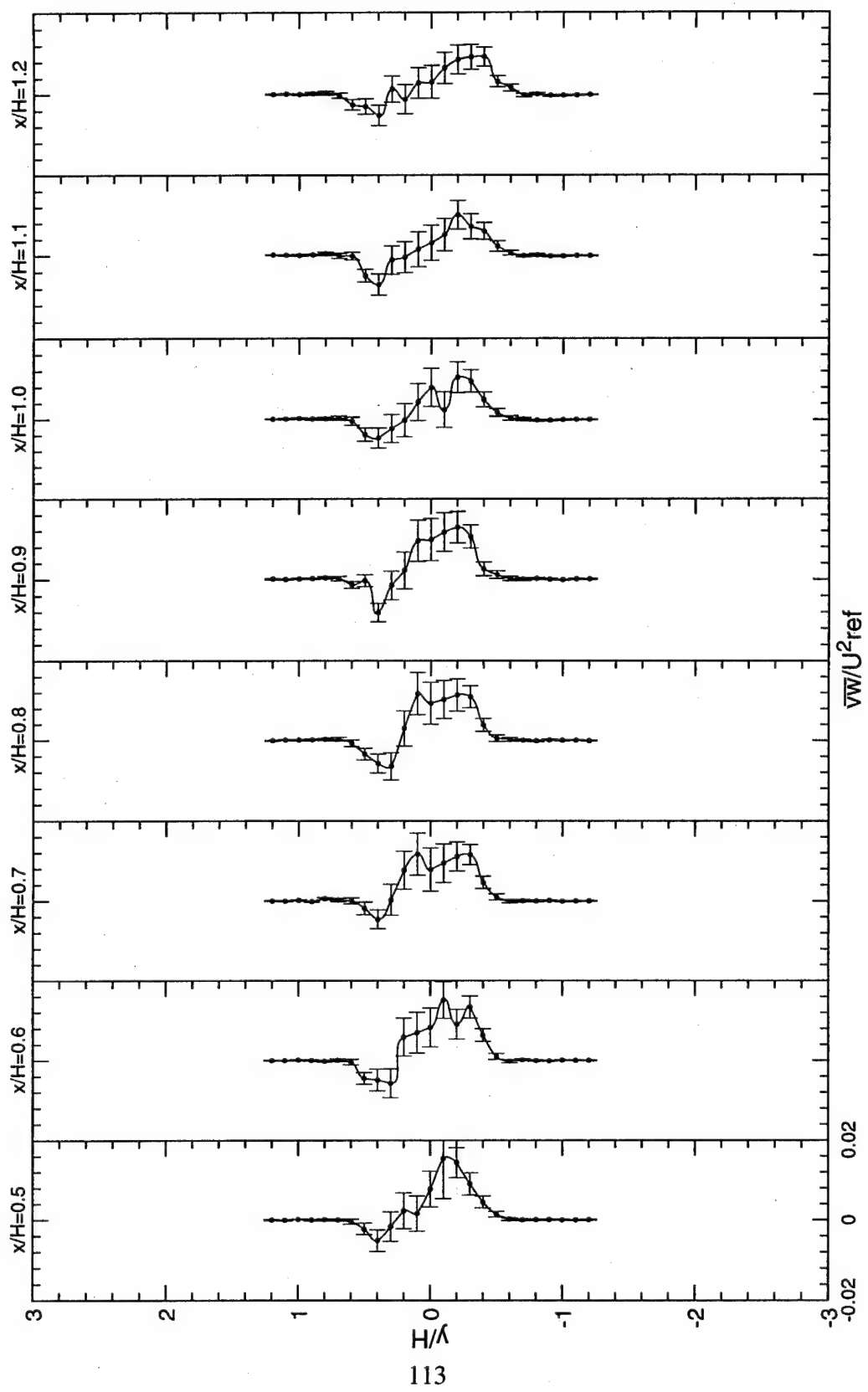


Figure 49. Normalized \overline{vw} turbulent stress distributions.

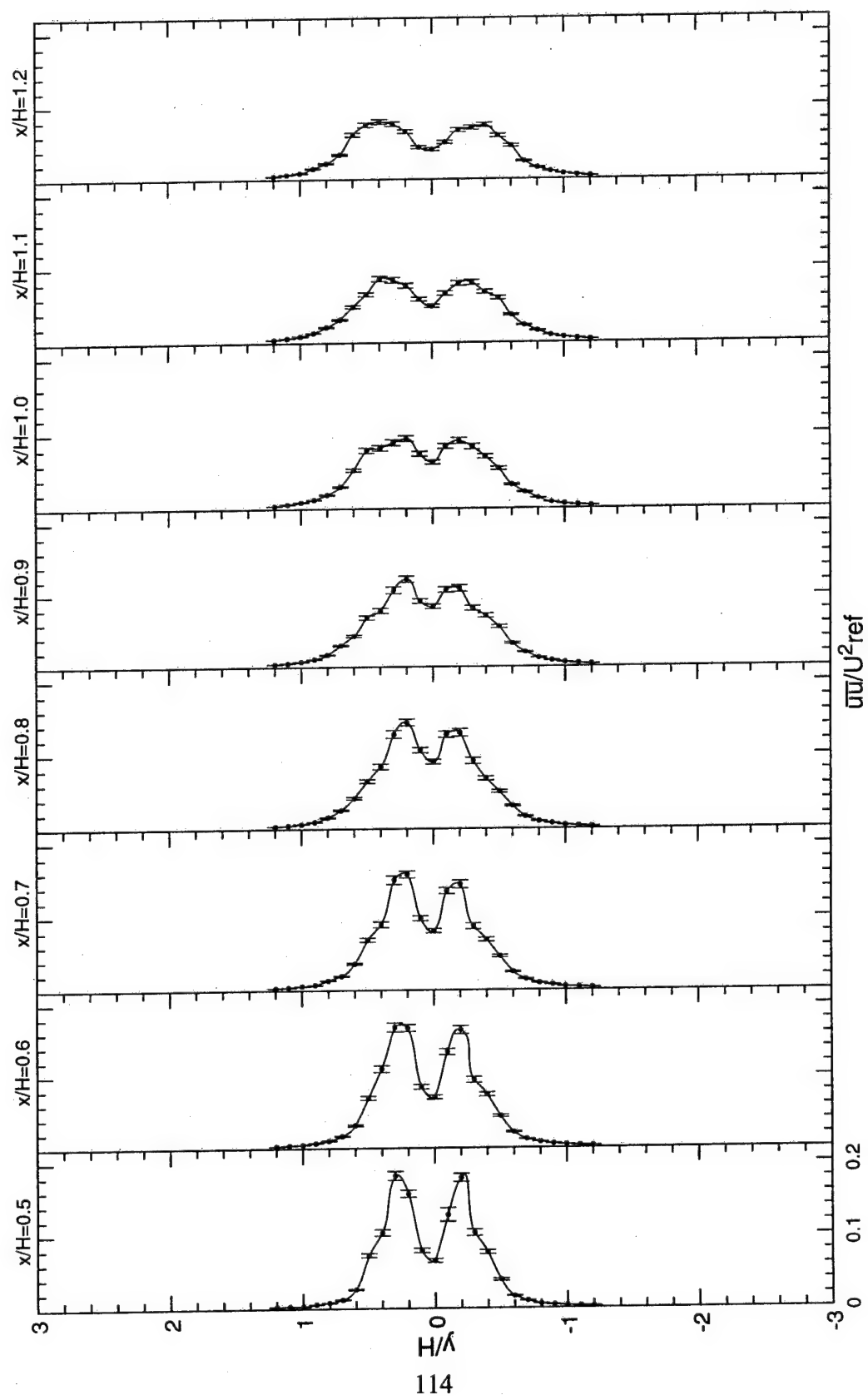


Figure 50. Normalized \overline{uu} turbulent stress distributions.

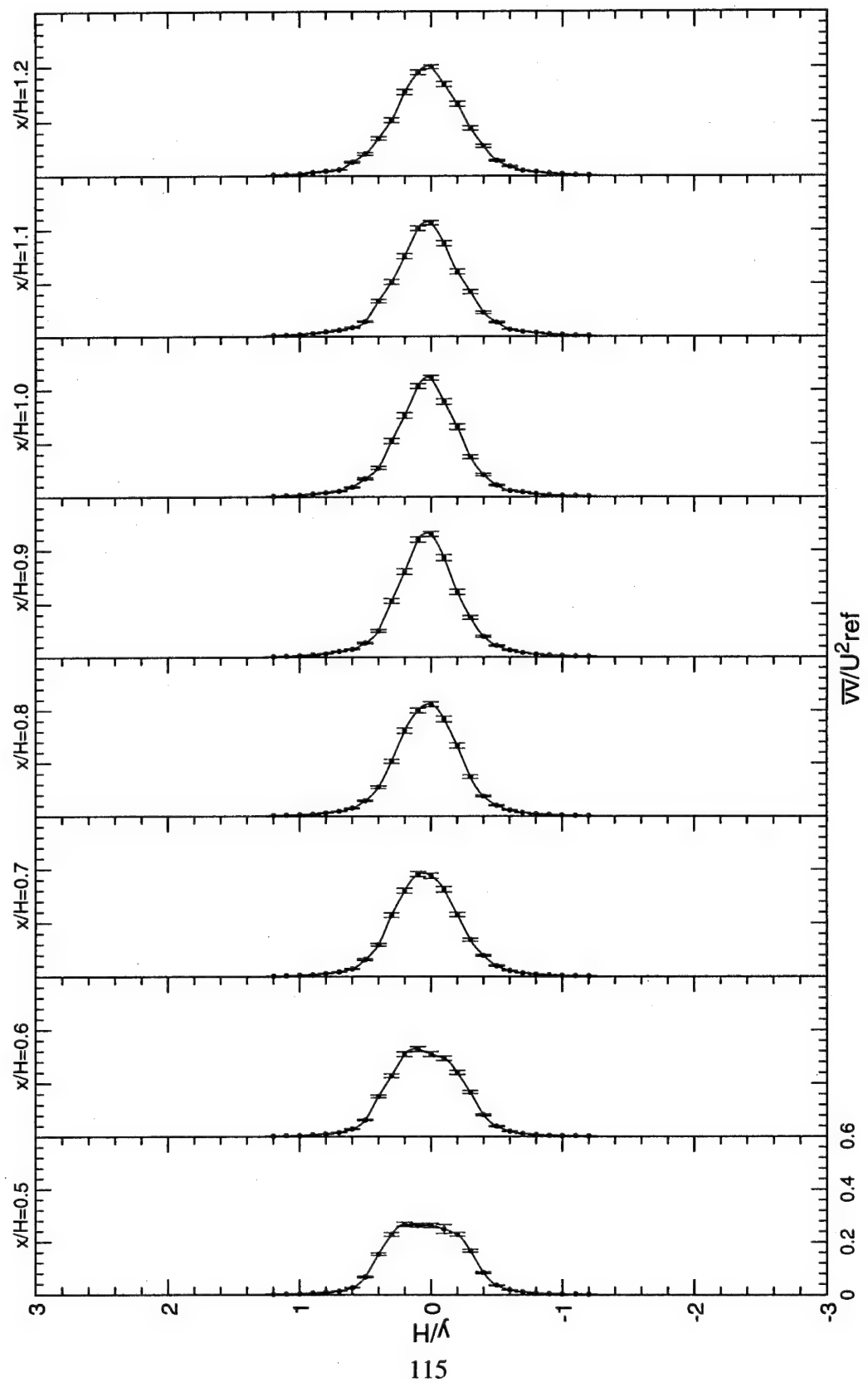


Figure 51. Normalized $\nabla \nabla$ turbulent stress distributions.

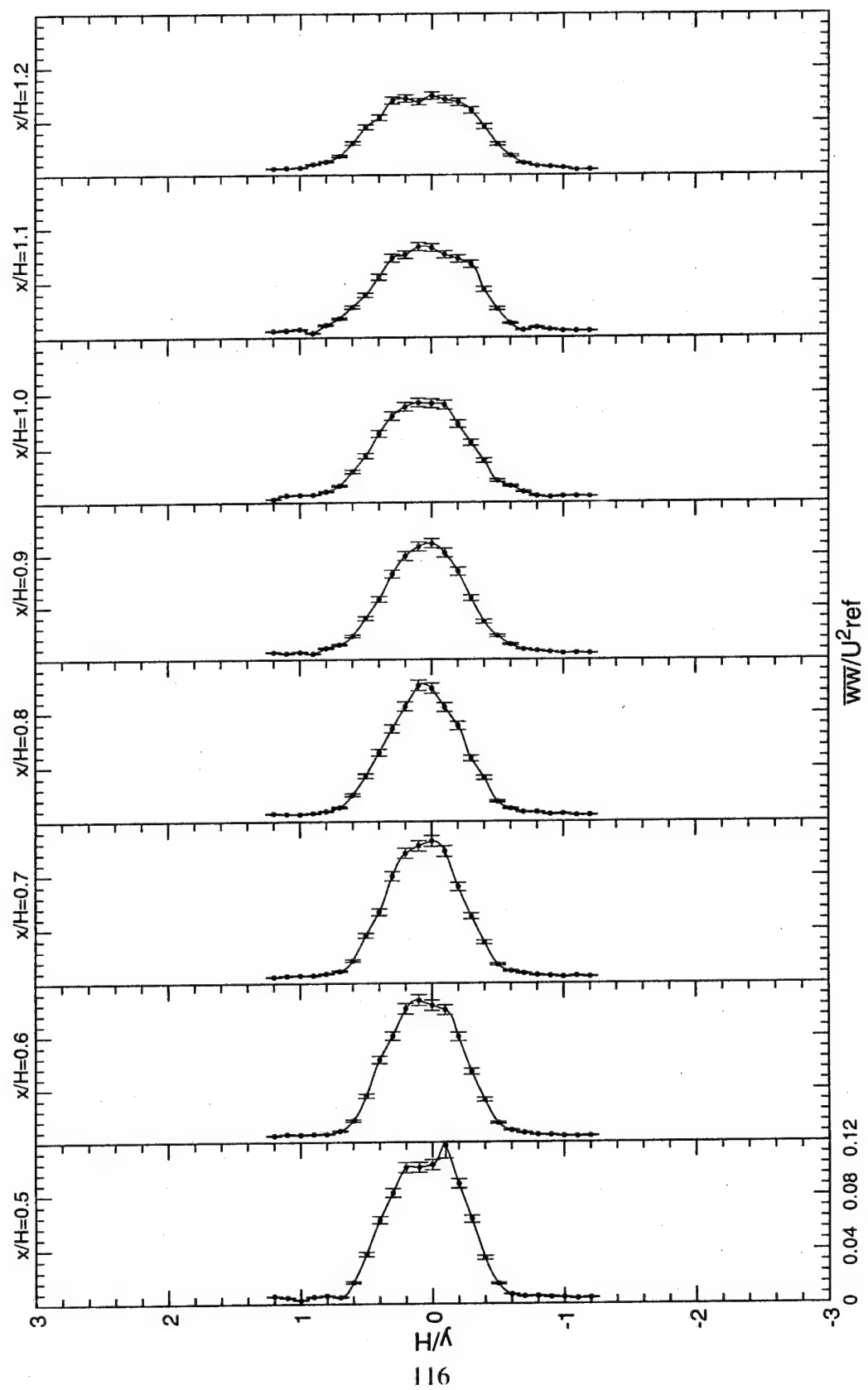


Figure 52. Normalized $\overline{w}w$ turbulent stress distributions.

$x/H=0.9$, and is roughly 0.49 (Figure 51). In addition, the peak value of the normalized spanwise normal turbulent stress (Figure 52) was found to be 0.12; at station $x/H=0.5$.

Durao, et al. (1988) made two-component LDV measurements behind a square cross-section cylinder in a water tunnel. A comparison of their results reveals that their flow is more isotropic than this bluff-body flow, but larger values of turbulent normal stresses are found in their flow as compared with the ones presented here. This may be due to the sharp corners at the leading edge of the square cross-section cylinder. In particular, on the centerline at $x/H=1$, $\overline{vv} = 2.4\overline{uu}$ in their flow; while, $\overline{vv} = 5.3\overline{uu}$ at the same location in this flow. The maximum value of normalized axial turbulent stress on the centerline, at $x/H=1$, was 0.22 in Durao, et al.'s study and 0.075 in this flow. Similarly, the maximum value of normalized transverse turbulent stress on the centerline, at $x/H=1$, was 0.68 in their study and 0.56 in this study.

With these comparisons in mind, one must note that the flow behind a bluff body is unsteady and somewhat periodic as vortex pairs are shed from the separation points. As mentioned in Chapter 5, a dominant frequency of 454 Hz ($St=0.24$) was found for this flow. In addition, the bi-modal PDF presented earlier (Figure 13) gives further proof that the flow contains large periodic structures. This vortex passage is responsible for the large peak values of transverse turbulent normal stress as simple ensemble averaging was used to obtain the turbulence statistics. It is believed that if Durao, et al.'s velocity decomposition method, which separates the large scale turbulence from the random turbulence, was applied to this data, this flow would appear more isotropic, as resulted in Durao, et al.'s study. It is noteworthy that the dominant frequency behind the square cross-section cylinders

corresponds to a Strouhal number of 0.13. Again, this may be due to the upstream corners, which may produce a larger recirculation zone thickness than the actual case.

As shown by the far-field measurements, the axial, transverse and spanwise turbulent normal stresses in the near-field are also clearly different in value and profile shapes. Again, the different shapes indicate that the structure of turbulence in and near the recirculation zone is quite anisotropic, at least for the case of ensemble averaging. This anisotropy implies the existence of multiple length scales in the turbulence structure.

6.4 Turbulent Kinetic Energy (TKE)

Figure 53 shows the measured normalized turbulent kinetic energy (TKE) profiles at the near-field stations. The error bars denote the 95% statistical uncertainty limits (see Appendix H). A center peak is noticed at the station $x/H=0.9$, which corresponds to the stagnation location. This maximum TKE occurs on the centerline behind the bluff body and has a normalized value of 32 percent. Downstream of $x/H=0.9$, this single peak decreases in magnitude, while two off-centerline peaks are depicted in the recirculation zone upstream of $x/H=0.8$. This center deficit region has a maximum normalized value of 16% and is due mainly to the influence of the axial normal stresses that possess a double hump behavior in the recirculation zone.

6.5 Isotropy

An isotropic flow is defined as one with no average shear stress and therefore, all three normal stresses must be equal. A check for isotropy was performed by normalizing the axial, transverse, and spanwise normal stresses with the turbulent kinetic energy, and are shown in Figures 54 through 56. As was mentioned in the previous chapter, isotropic

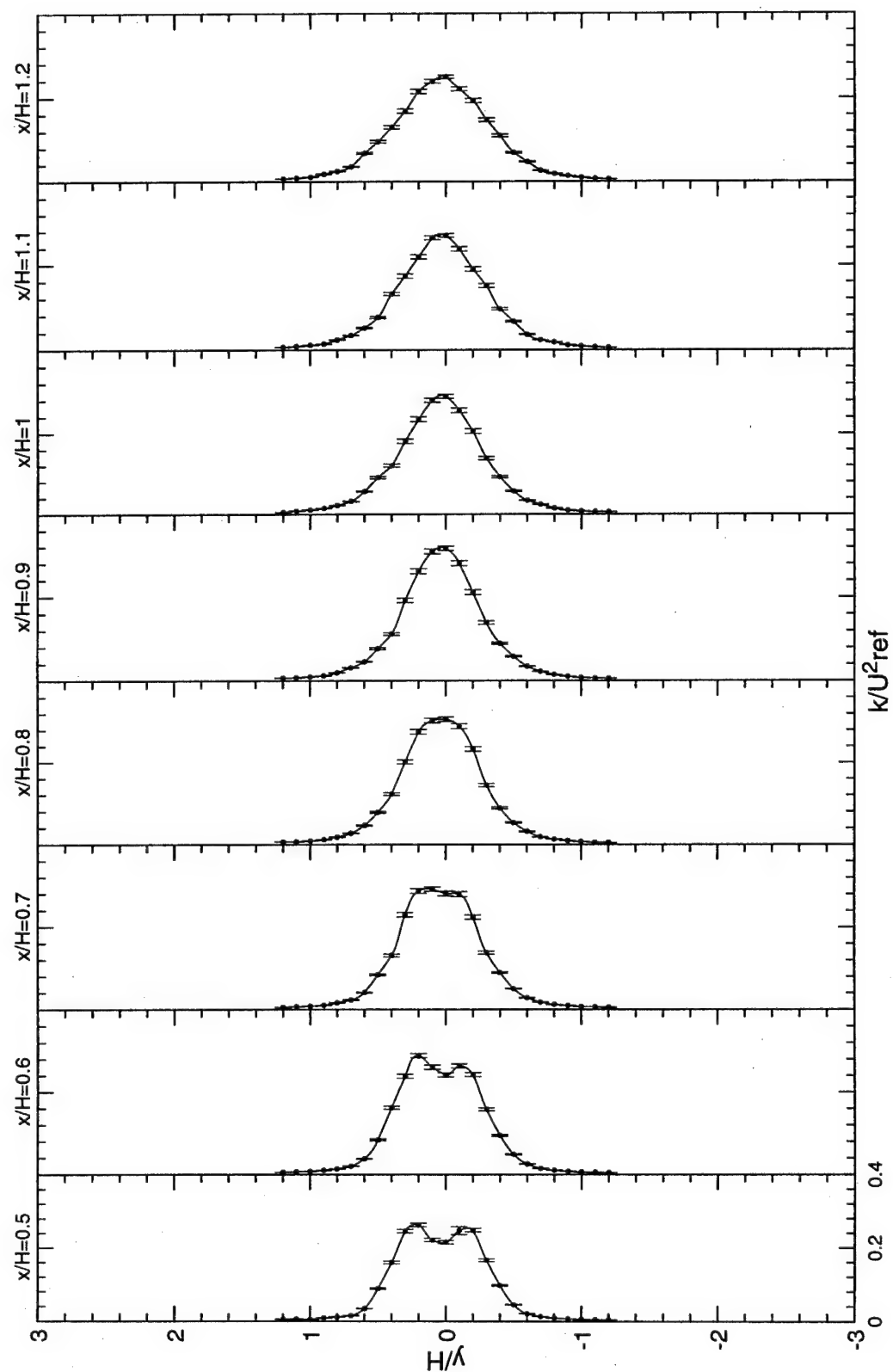


Figure 53. Normalized turbulent kinetic energy.

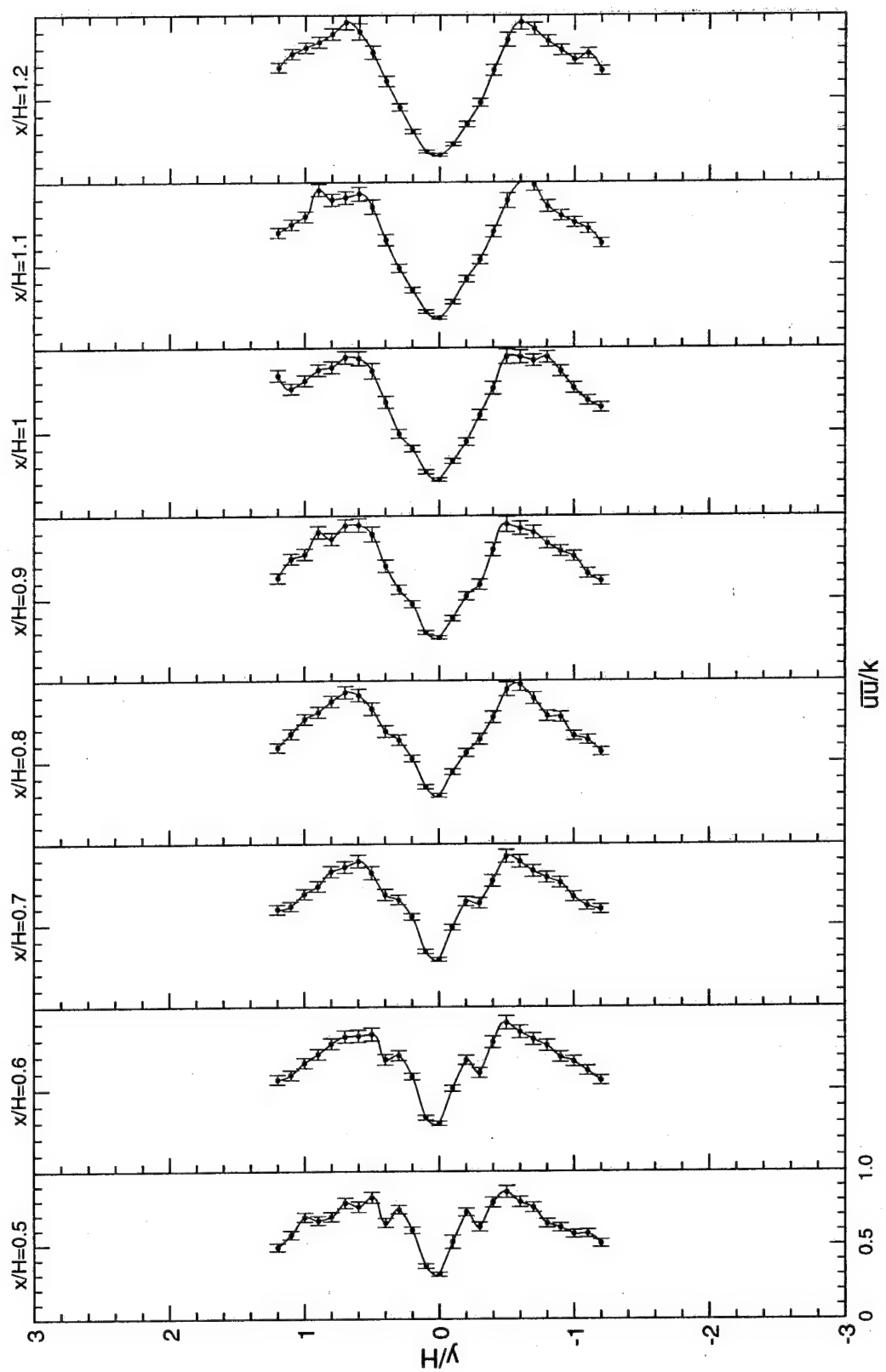


Figure 54. Axial mean normal stresses- Isotropy check.

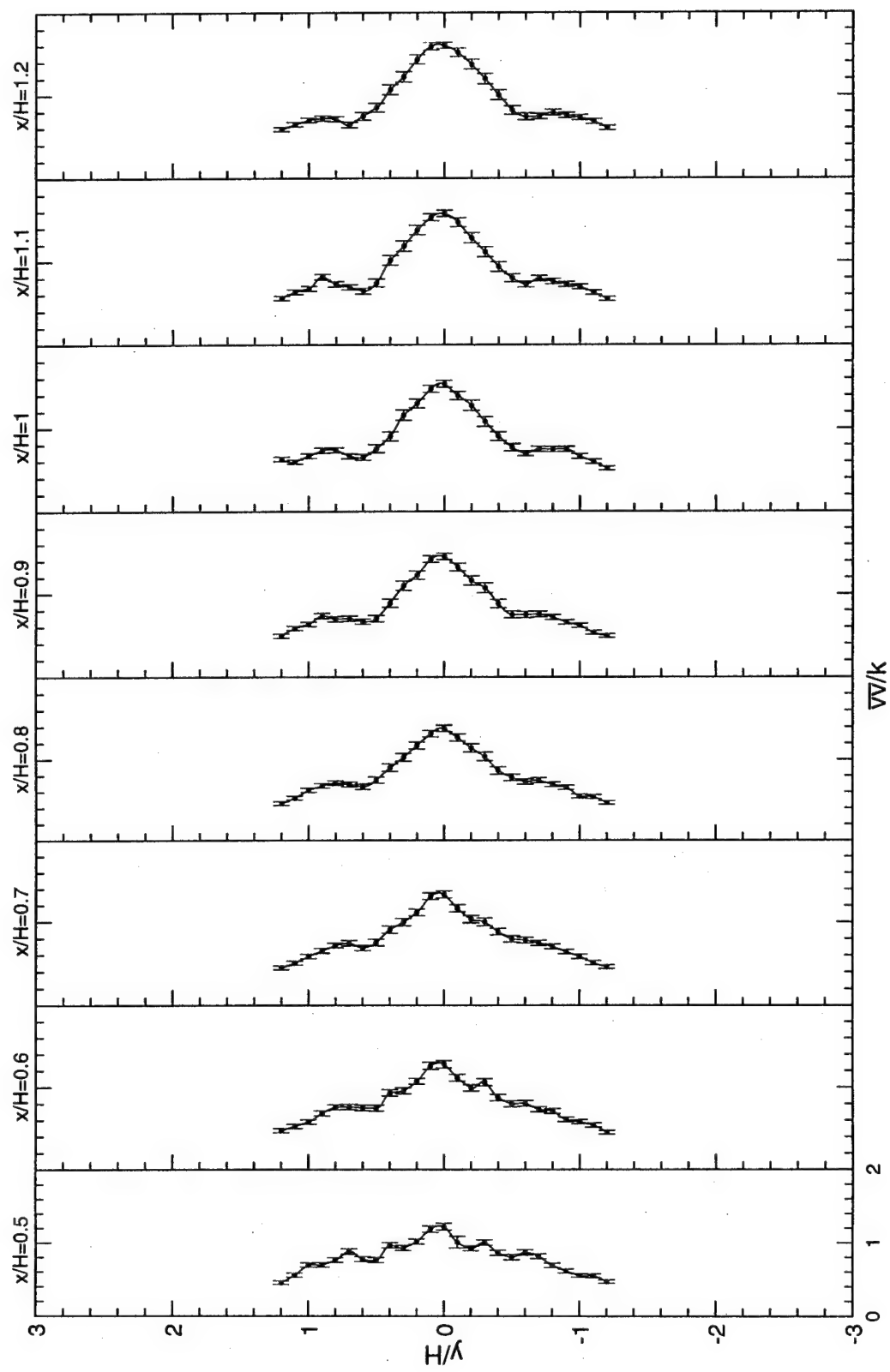


Figure 55. Transverse mean normal stresses- Isotropy check.

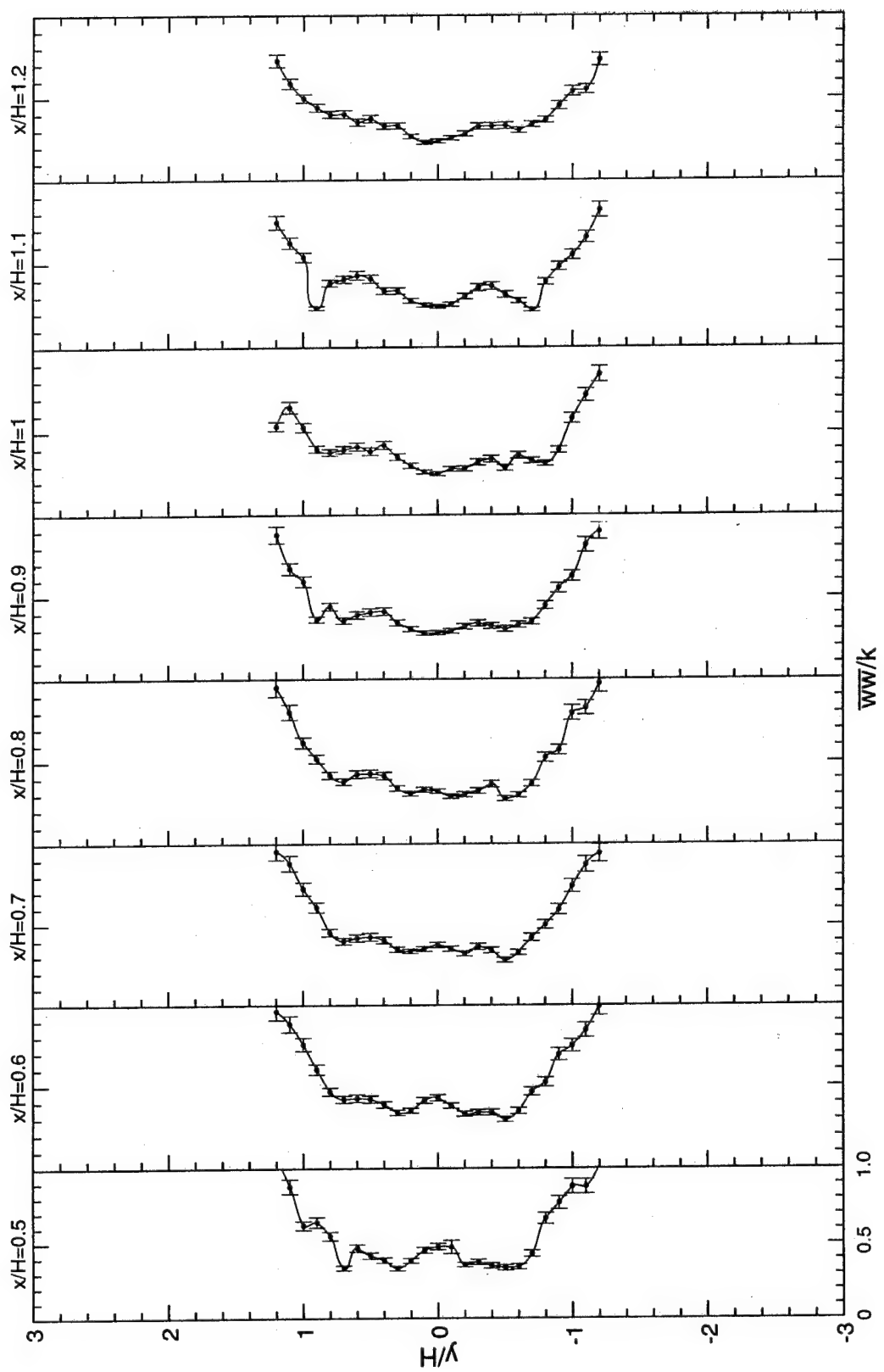


Figure 56. Spanwise mean normal stresses- Isotropy check.

behavior is found only in the freestream region and far downstream of the wake region in this flow. In the near-field, anisotropy is clearly evident by the ratios of \overline{uu}/k which varied between 0.2 at the centerline to 1.0 in the shear layers. The ratios of \overline{vv}/k showed a peak value of 1.6 on the centerline, while \overline{ww}/k showed a relatively flat value of 0.3.

6.6 WW Approximation

When the third component velocity measurements are not available, researchers rely on assumptions to approximate the values of the missing terms. For \overline{ww} , the following relationship is usually used, $\overline{ww} = C_1(\overline{uu} + \overline{vv})$ where $C_1=0.5$ is used in a backward-facing step geometry (see Driver & Seegmiller, 1985; Fuji & Gomi, 1976). The turbulent kinetic energy (TKE) defined as $k = (\overline{uu} + \overline{vv} + \overline{ww})/2$ is then approximated by $k = C_2(\overline{uu} + \overline{vv})$ where $C_2=0.75$ (see Chandrsuda & Bradshaw, 1981; and Etheridge & Kemp, 1978). It should be noted that for the case of isotropic turbulence, this approximation is exact. In the present study, the spanwise velocity terms were obtained from direct measurements. Validation of the estimation of \overline{ww} was performed by direct comparison to the measured data. Figure 57 shows the measured and estimated normalized turbulent kinetic energy using this simple approximation. The dotted lines show that the isotropic approximation clearly overestimates the actual value of \overline{ww} , especially in the recirculation zone. An approximation constant of $C_1=0.2$ (or $C_2=0.6$) was found to fit the data of this study much better than the value derived from isotropic assumptions. This is shown in Figure 57 by the continuous solid lines. It is noteworthy that a single constant works well even in the high velocity gradient regions of the shear layers. Azad, et al. (1987) suggested other values for C_1 which varied from 0.35 to 0.41 for fully developed pipe flow, from 0.33 to 0.48 for flow in a diffuser, and 0.4 for boundary

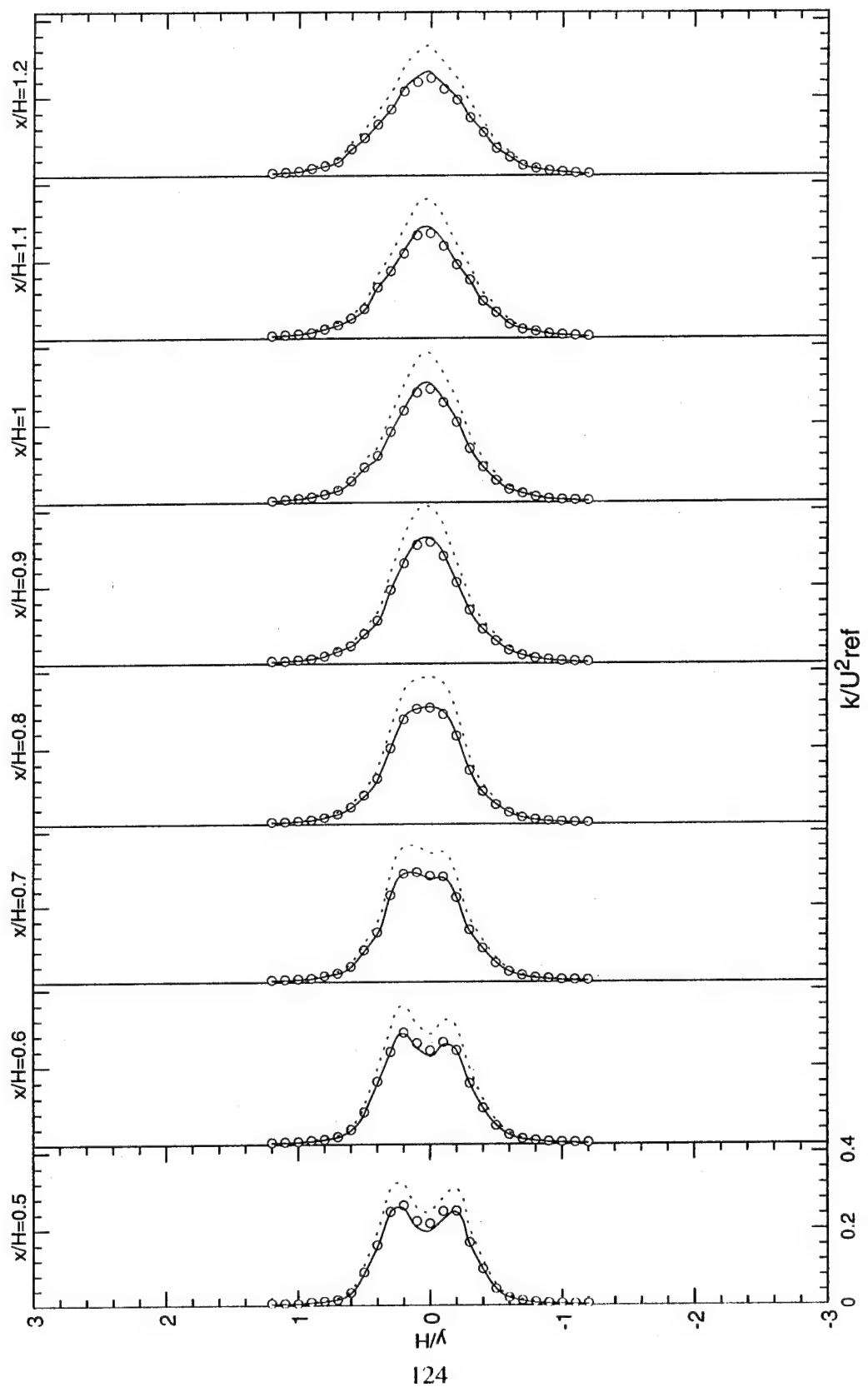


Figure 57. Normalized Turbulent Kinetic Energy (○ data k approximated by: ——— $0.6(\bar{u}u + \bar{v}v)$ ······ $0.75(\bar{u}u + \bar{v}v)$).

layer flow. Values for C_1 of 0.37 and 0.63 are inferred in Table 5.2 from Townsend (1980) for a laboratory equilibrium boundary layer and an atmospheric equilibrium boundary layer, respectively. Andreopoulos and Wood (1982) found that a constant of $C_1=0.5$ did not match their measured constant value (as reported in Figure 9) in the turbulent boundary layer with surface roughness. The reason that a small value for C_1 ($=0.2$) better matched the experimental data of this study was the high anisotropy encountered in this flow. In order to offset the high values of \overline{vv} , which were approximately a factor of 2.5 greater than the \overline{uu} values, a smaller coefficient is needed.

6.7 Turbulent Triple Products

The triple velocity correlations, $\overline{u_i u_j u_k}$, represent the diffusion of turbulent stresses due to turbulent velocity fluctuations and are called the turbulent diffusion flux of Reynolds stresses. Their gradients constitute the diffusion terms of the turbulent kinetic energy balance equation. To the author's knowledge, no direct measurement of these terms has ever been made in bluff-body flows. Researchers have proposed various models to simulate these terms. A good summary of current models is given by Cormack, et al. (1978) where a comparison of their model with four other techniques is presented. In the present study, all nine turbulent triple products (\overline{uuu} , \overline{uvv} , \overline{uvw} , \overline{vuu} , \overline{vvv} , \overline{vww} , \overline{wuu} , \overline{vww} , and \overline{www}) were determined and are presented as their normalized values in Figures 58 through 66. The error bars denote the 95% statistical uncertainty limits. These uncertainties are proportional to $N^{-1/2}$. This effect can be seen by comparing the uncertainties at $x/h=0.5$, $y/h=-0.1$ (Figures 58-66) and other neighboring locations. The sample size at this one location was erroneously set to 1024 samples instead of 5120 samples. The profiles of \overline{uuu} had a double hump feature

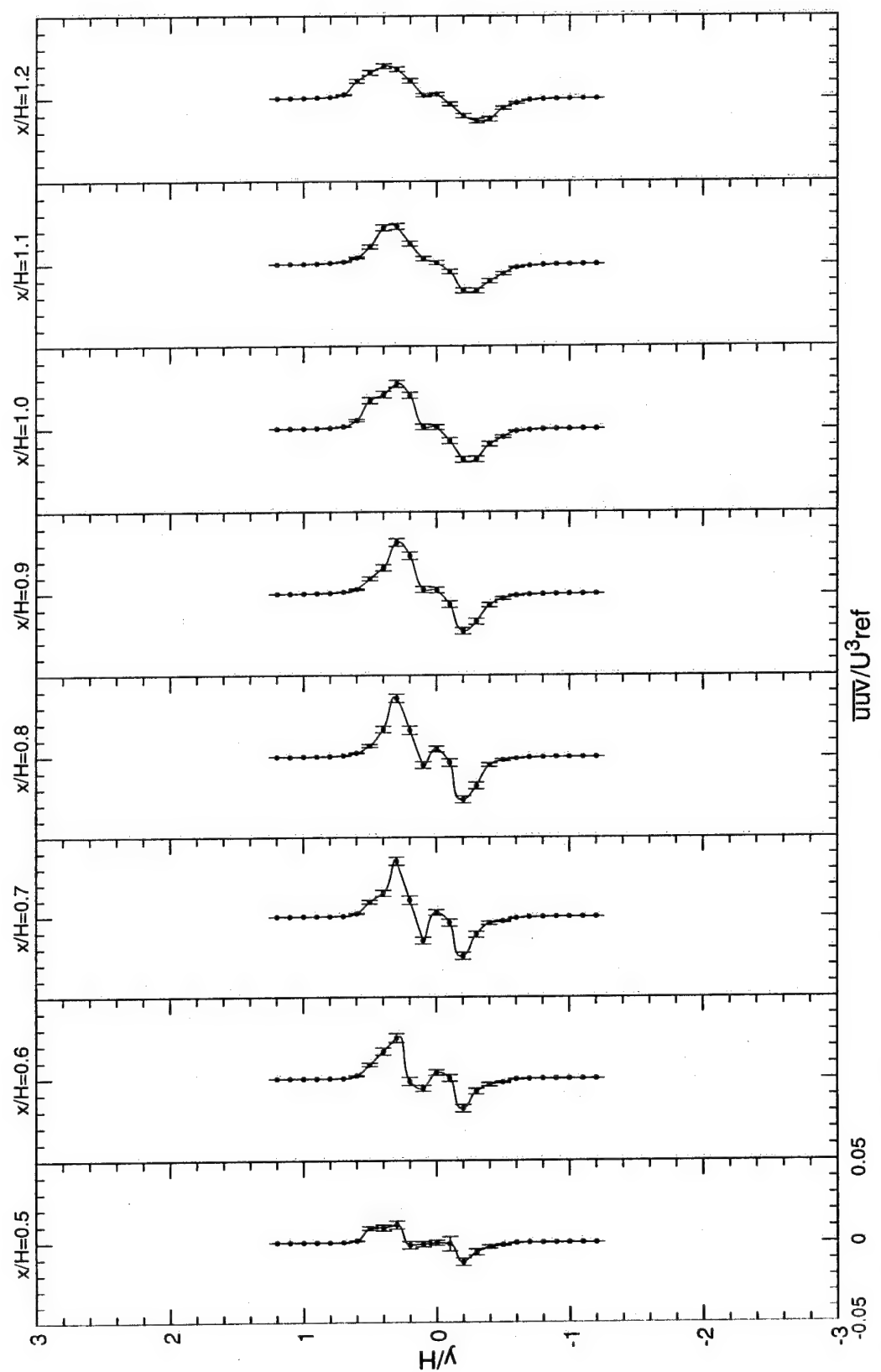


Figure 58. Normalized uuV turbulent triple product distributions.

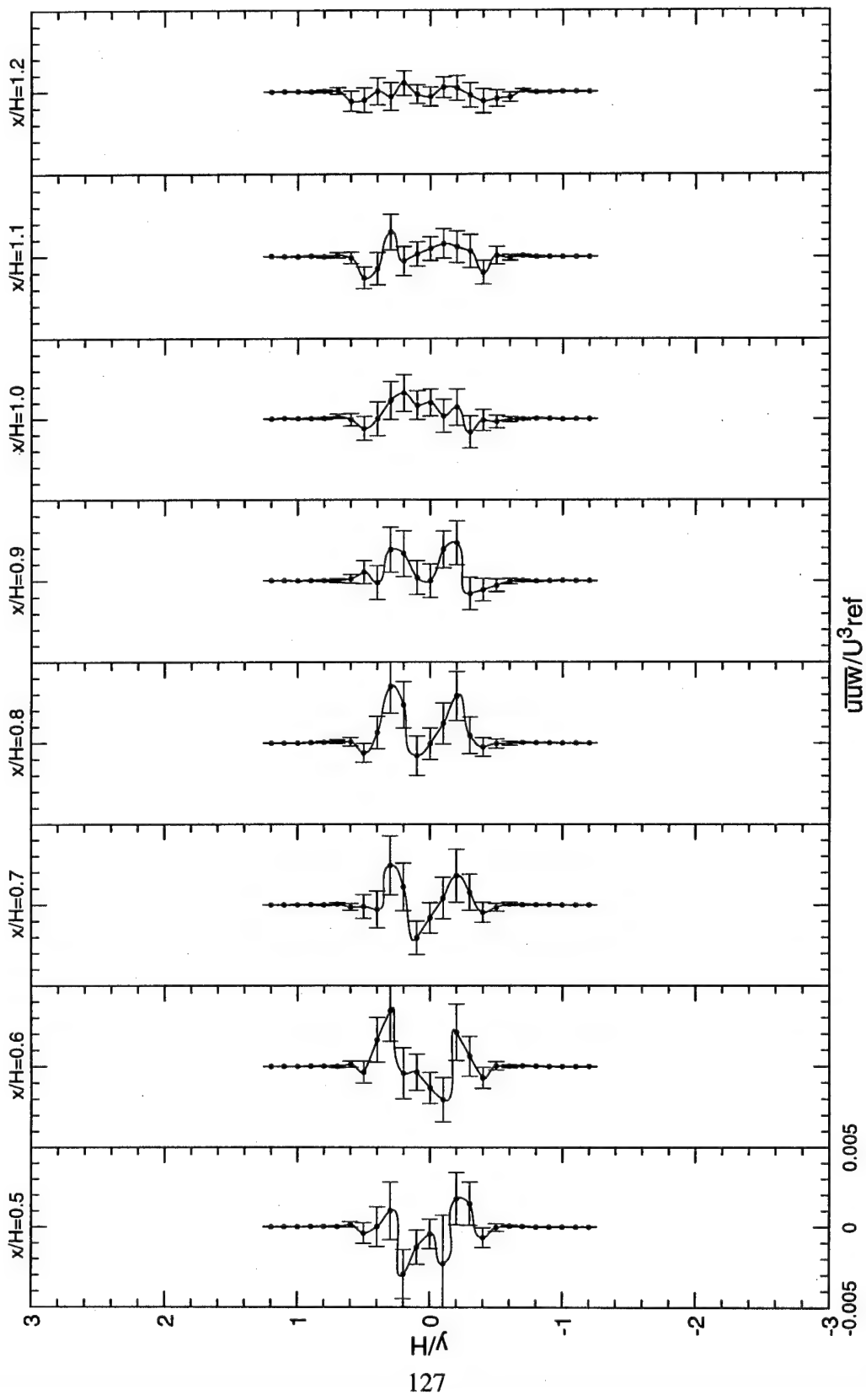


Figure 59. Normalized $u'vw$ turbulent triple product distributions.

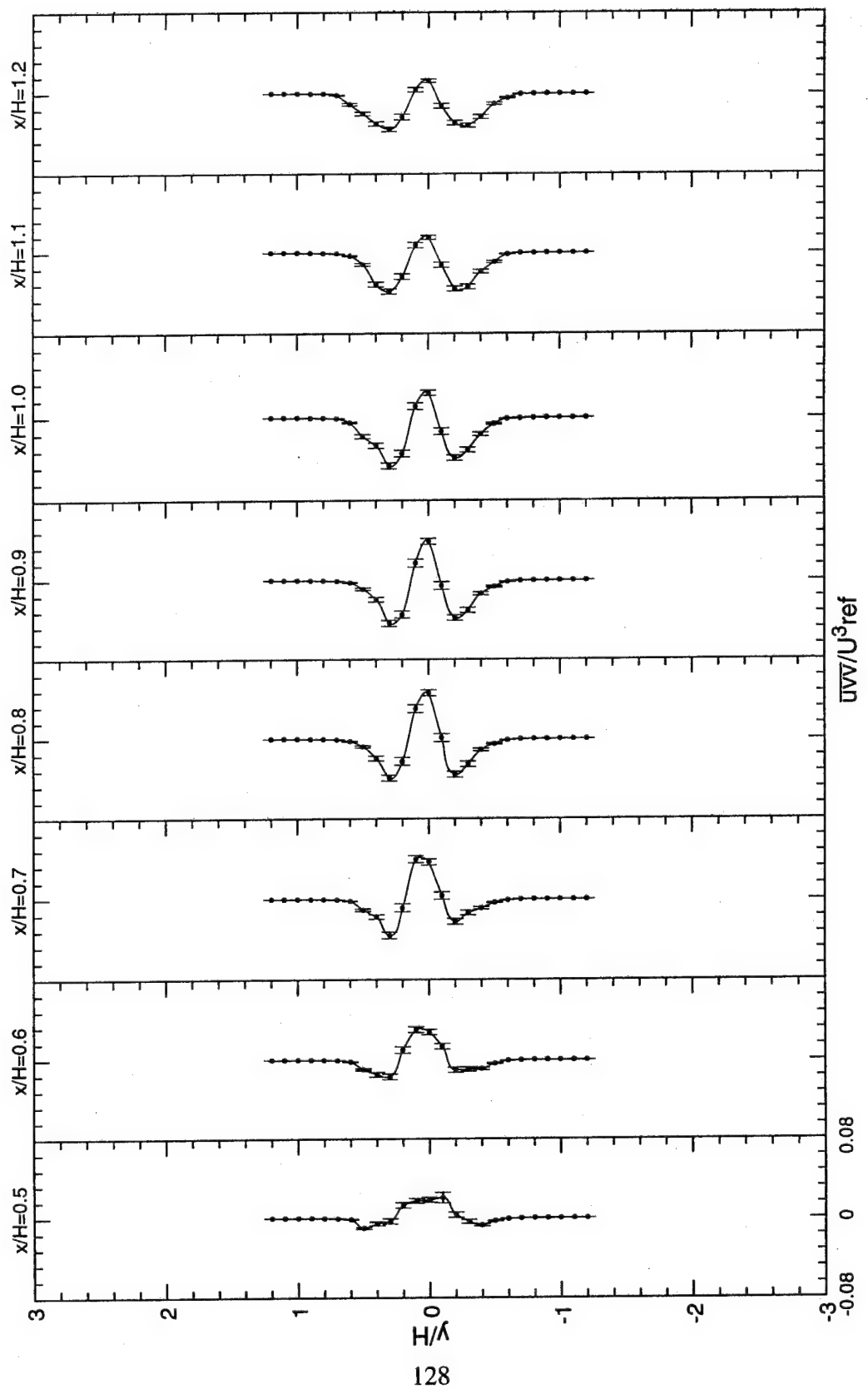


Figure 60. Normalized UVV turbulent triple product distributions.

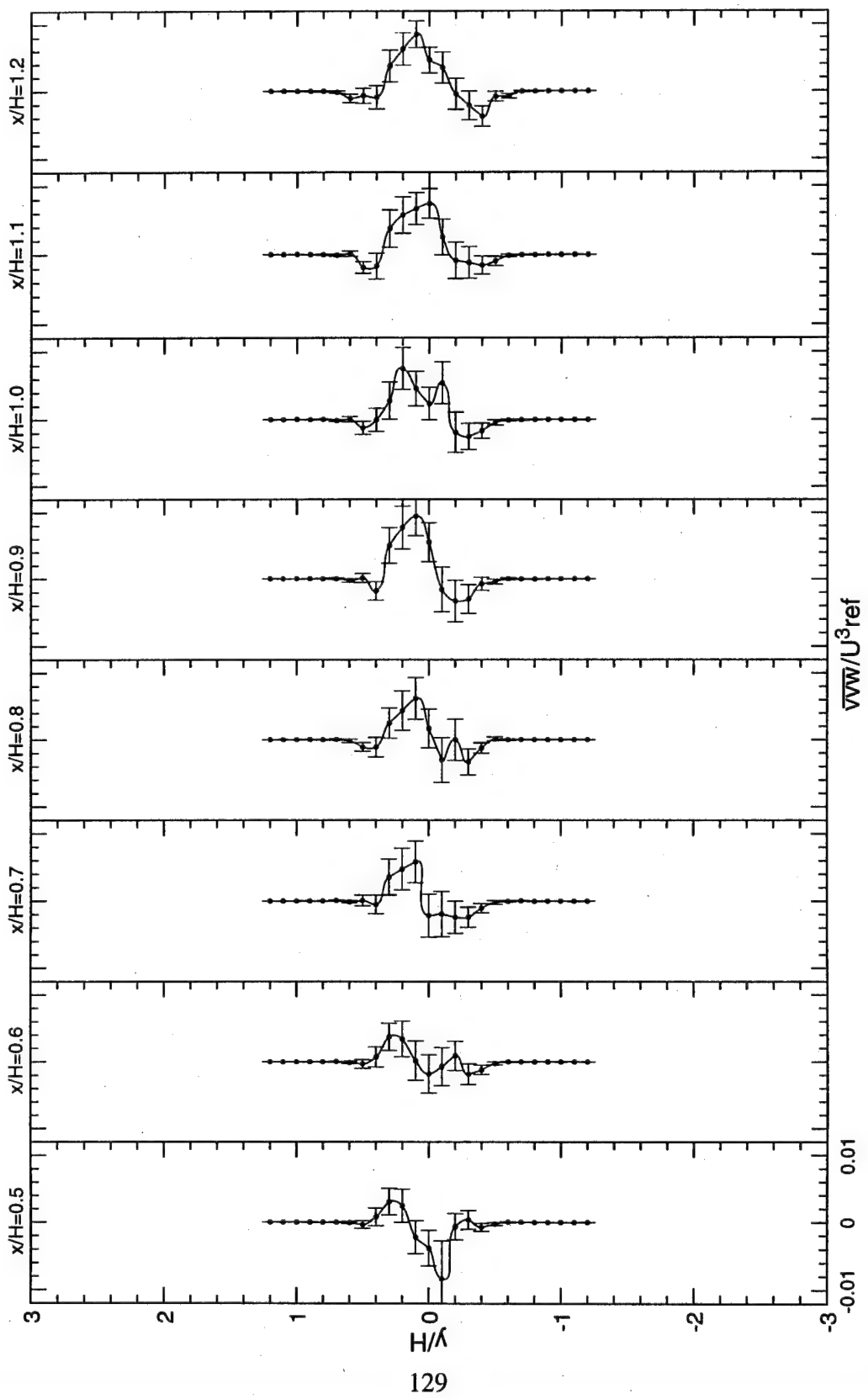


Figure 61. Normalized $\bar{v'w'w'}$ turbulent triple product distributions.

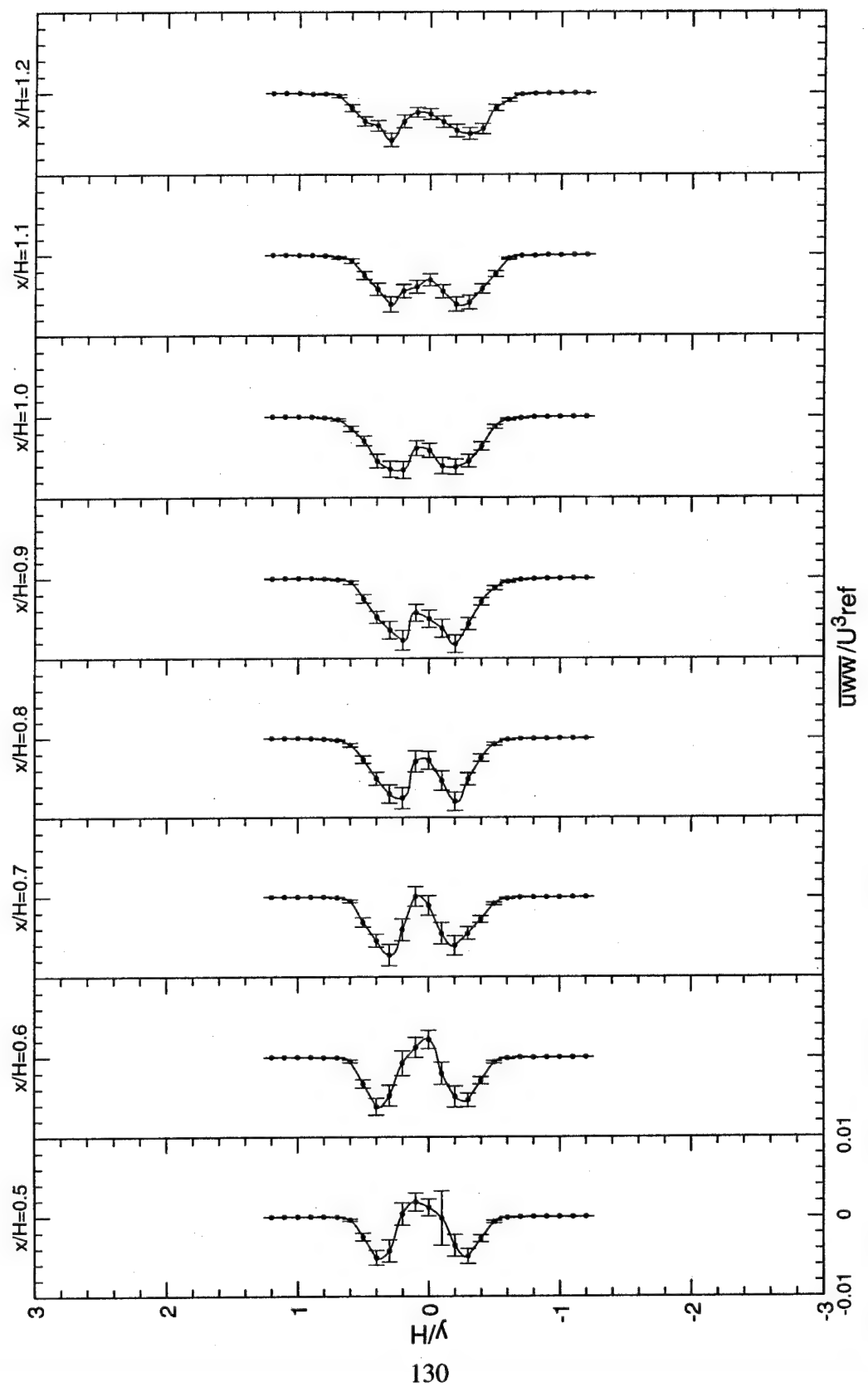


Figure 62. Normalized \bar{UWW} turbulent triple product distributions.

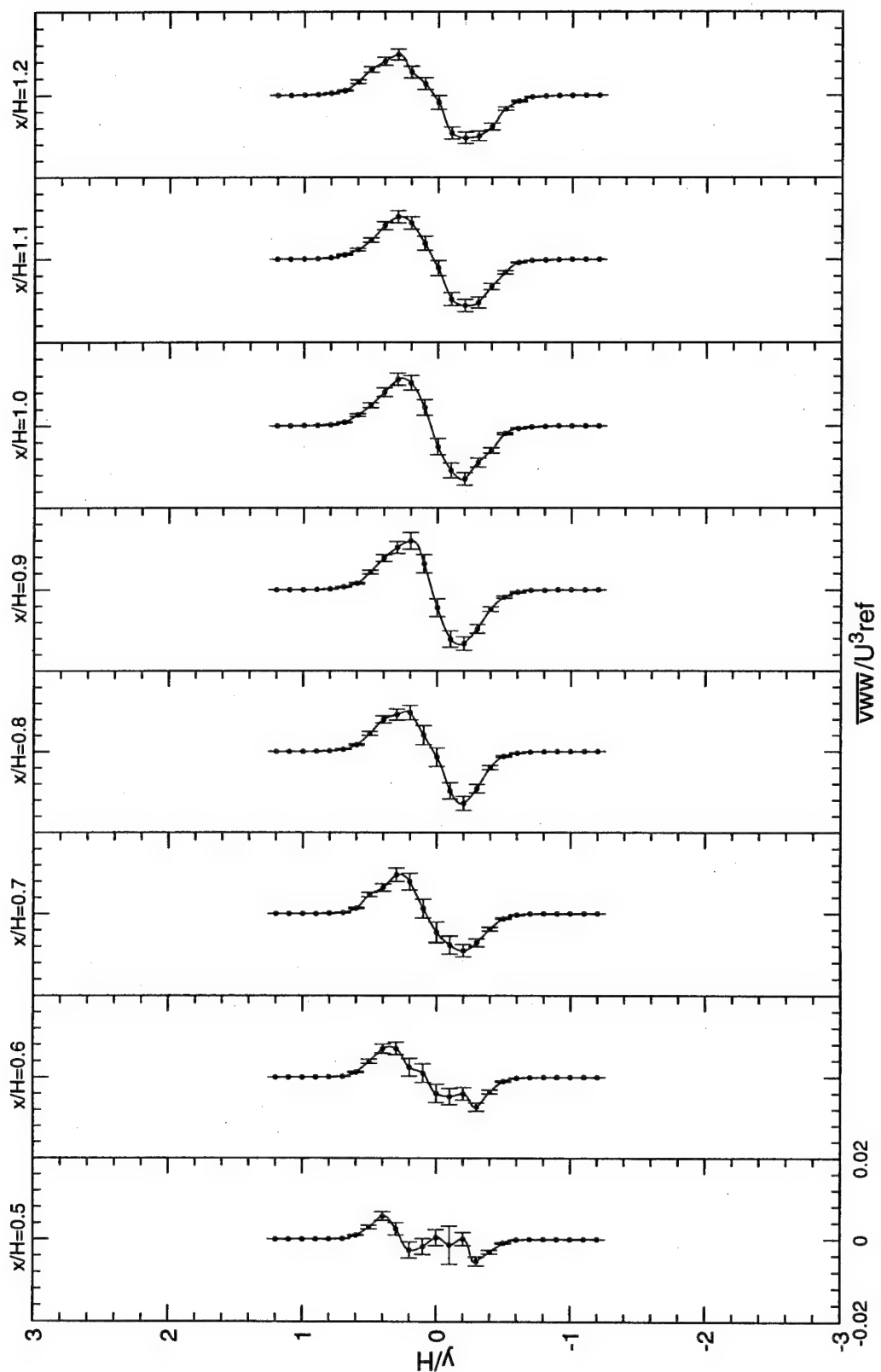


Figure 63. Normalized vww turbulent triple product distributions.

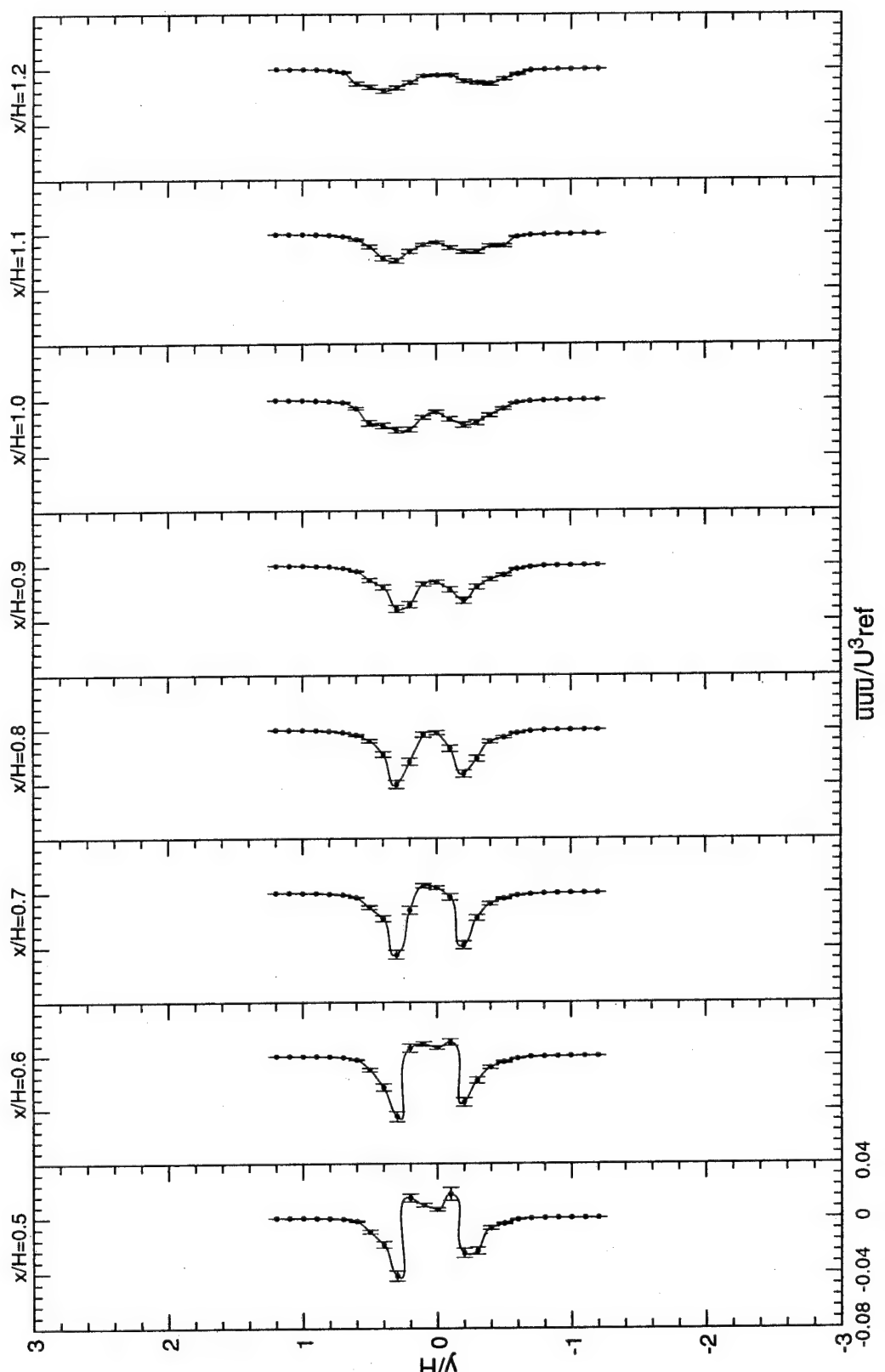


Figure 64. Normalized UUU turbulent triple product distributions.

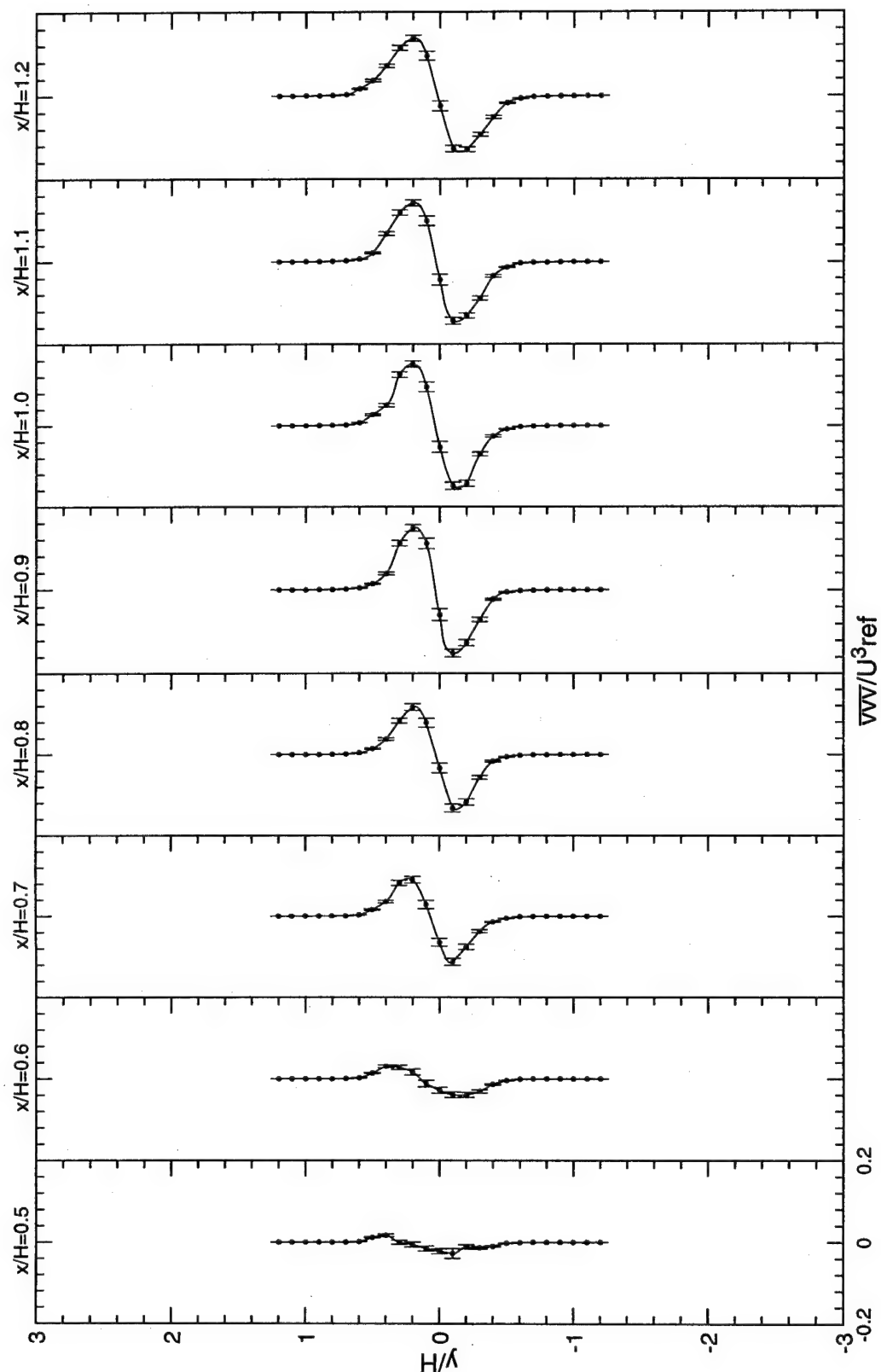


Figure 65. Normalized $\bar{v}v\bar{v}$ turbulent triple product distributions.

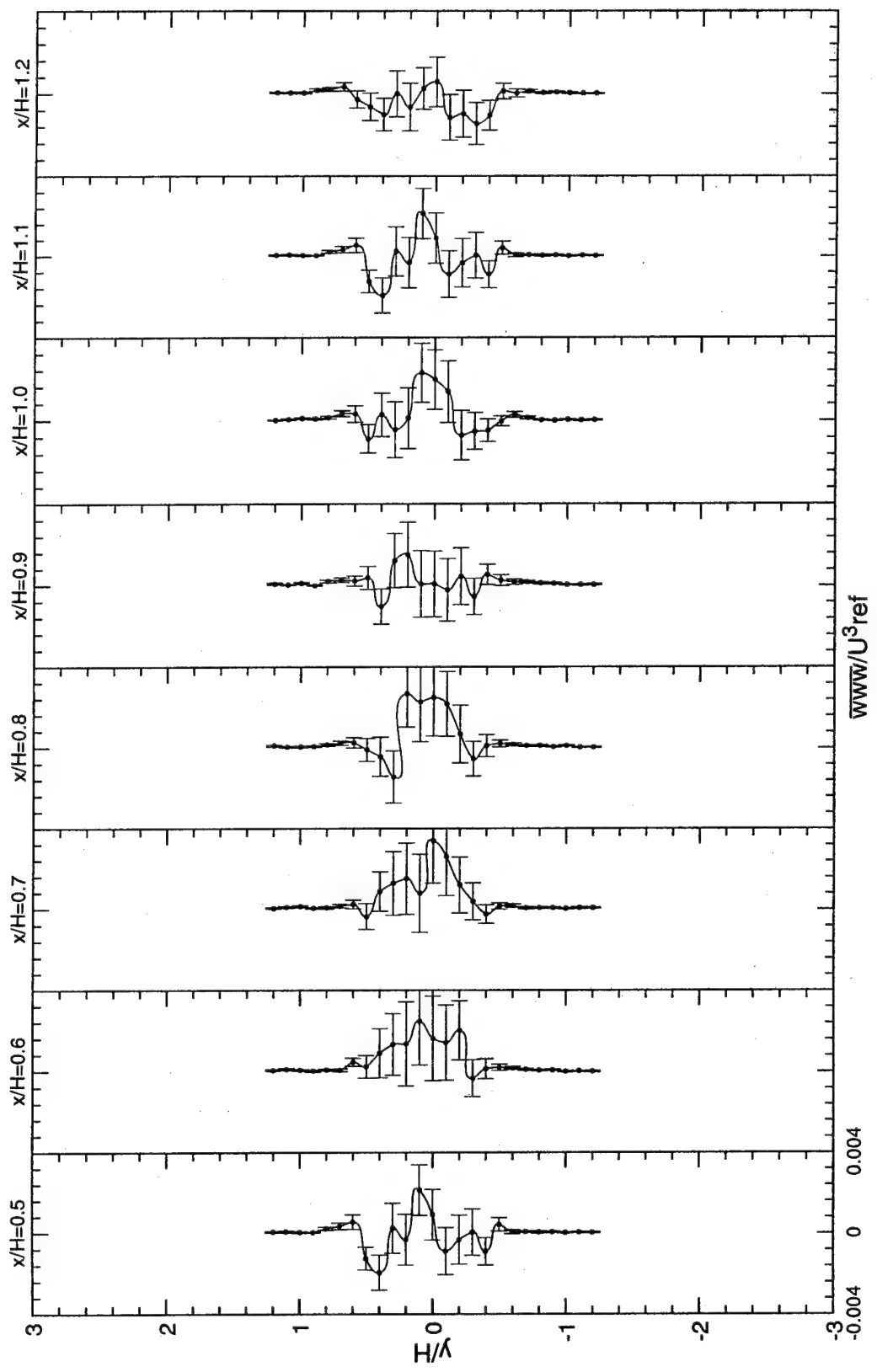


Figure 66. Normalized \overline{www}/U^3_{ref} turbulent triple product distributions.

with negative minimum values, in contrast to the \overline{uu} profiles. This double hump feature of \overline{uuu} is the result of the top and bottom shear layers as was the case with the axial turbulent normal stress distributions shown in Figure 50. The profiles of \overline{vvv} were antisymmetric, similar to the \overline{V} -profiles, but inverted. The \overline{www} profiles were wavy with large relative uncertainty, and no particular shape could be detected. It is noteworthy that the absolute uncertainty is approximately 5 times larger for \overline{vvv} ($0.016 U_{ref}^3$) than for \overline{www} ($0.0035 U_{ref}^3$). The maximum normalized values of $\overline{uuu} / U_{ref}^3$ and $\overline{vvv} / U_{ref}^3$ had factors of 5 and 3, less than the normalized values of $\overline{uu} / U_{ref}^2$ and $\overline{vv} / U_{ref}^2$, respectively. The maximum value of \overline{vvv} was found to be the largest of all the turbulent triple products (≈ 5 times that of \overline{uuu}) and peaks at the shear layer locations ($y/H=\pm 0.2$) and at the stagnation point ($x/H=0.9$) to a normalized maximum absolute value of 0.2 (Figure 65). All transverse component containing triple products terms showed rather small values in the recirculation zone and increased to maximum values at the stagnation point; otherwise the opposite was true.

Once again, maximum values of turbulent triple products in this flow were found to be up to 30 times larger than those reported for axisymmetric sudden expansion (Gould et al., 1990) and the backward-facing step flows (Driver and Seegmiller, 1985). This implies that the ensemble averaged diffusion of turbulent kinetic energy (which includes the periodic vortex shedding) is much higher in this flow than in the axisymmetric sudden expansion and backward-facing step flows. It is commonly known (Chandrsuda and Bradshaw, 1981) that large eddies are responsible for the significance of the triple products. The maximum normalized absolute values of the nine triple products in order of decreasing magnitude are:

$$\overline{vvv} / U_{ref}^3 = 0.18, \quad \overline{uvv} / U_{ref}^3 = 0.06, \quad \overline{uuu} / U_{ref}^3 = 0.05, \quad \overline{uuv} / U_{ref}^3 = 0.048, \quad \overline{vww} / U_{ref}^3 = 0.016,$$

$\overline{vww}/U_{ref}^3 = 0.01$, $\overline{uww}/U_{ref}^3 = 0.008$, $\overline{uuw}/U_{ref}^3 = 0.004$, $\overline{www}/U_{ref}^3 = 0.003$. Again this indicates that the \overline{vvv} triple correlation term dominates this type of flowfield, and that mixing (or turbulent diffusion) is highest in the transverse direction, a condition highly desirable because it allows for shorter length combustors.

6.8 uww and vww Approximations

When the spanwise velocity component cannot be measured, the following assumptions are generally made about the turbulent triple products \overline{uww} and \overline{vww} : $\overline{uww} = C_3(\overline{uvv} + \overline{uuu})$ and $\overline{vww} = C_4(\overline{uuv} + \overline{vvv})$, where $C_3 = C_4 = 0.50$ (see Driver & Seegmiller, (1985)). Wood and Bradshaw (1982) obtained a value of $C_4 = 0.20$ across an entire turbulent mixing layer constrained by a solid surface. Lawn (1971) deduced from Laufer's (1954) fully developed pipe flow results that $\overline{vww} \cong 0.5\overline{vvv} \cong 0.5\overline{uuv}$ and in turn, used $\overline{vww} = 0.25(\overline{uuv} + \overline{vvv})$. Nakagawa, et al. (1975) used the approximation, $\overline{vww} = \overline{vvv}$. Azad, et al. (1987) deduced that values for \overline{ww} and \overline{vww} vary with location in turbulent flows and that generalization is very risky. These approximations for \overline{uww} and \overline{vww} may have a large effect on the turbulent transport of the turbulent kinetic energy. Since all nine turbulent triple products have been calculated in this flow, it is of interest to determine how well these suggested approximations predict the actual values. Figure 67 shows a comparison between the experimentally determined values of \overline{uww} and some of the approximations mentioned above. As shown by the dotted lines, a value of $C_3 = 0.50$ clearly overpredicts the measured values. There is a great mismatch between the experimentally determined values of \overline{uww} and the suggestions of Lawn (1971) and Nakagawa (1975). No single value for C_3 could be

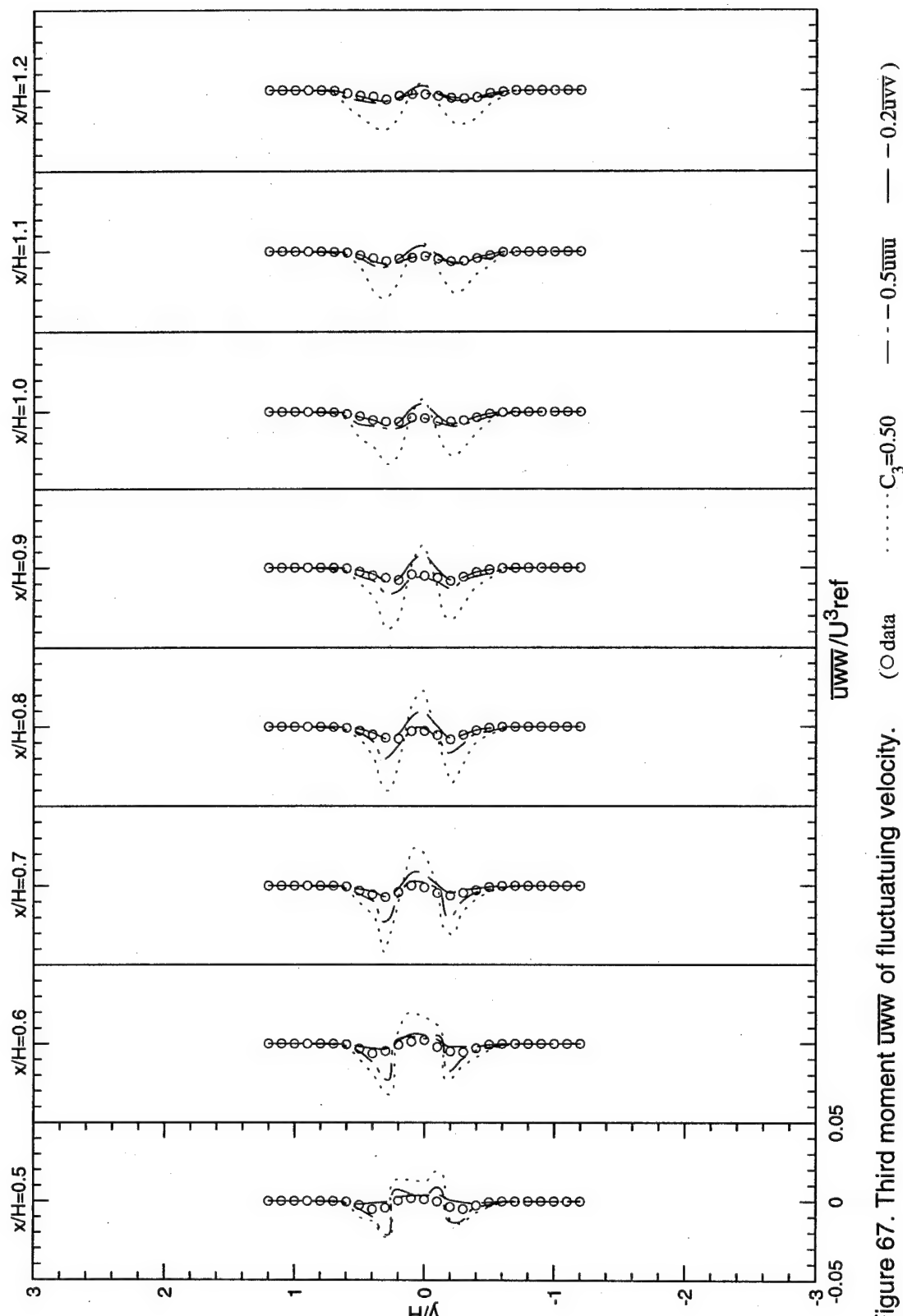


Figure 67. Third moment \overline{uww} of fluctuating velocity.

(○ data ······ $C_3=0.50$ —····· $-0.5\overline{u}\overline{u}\overline{u}$ —····· $-0.2\overline{u}\overline{v}\overline{v}$)

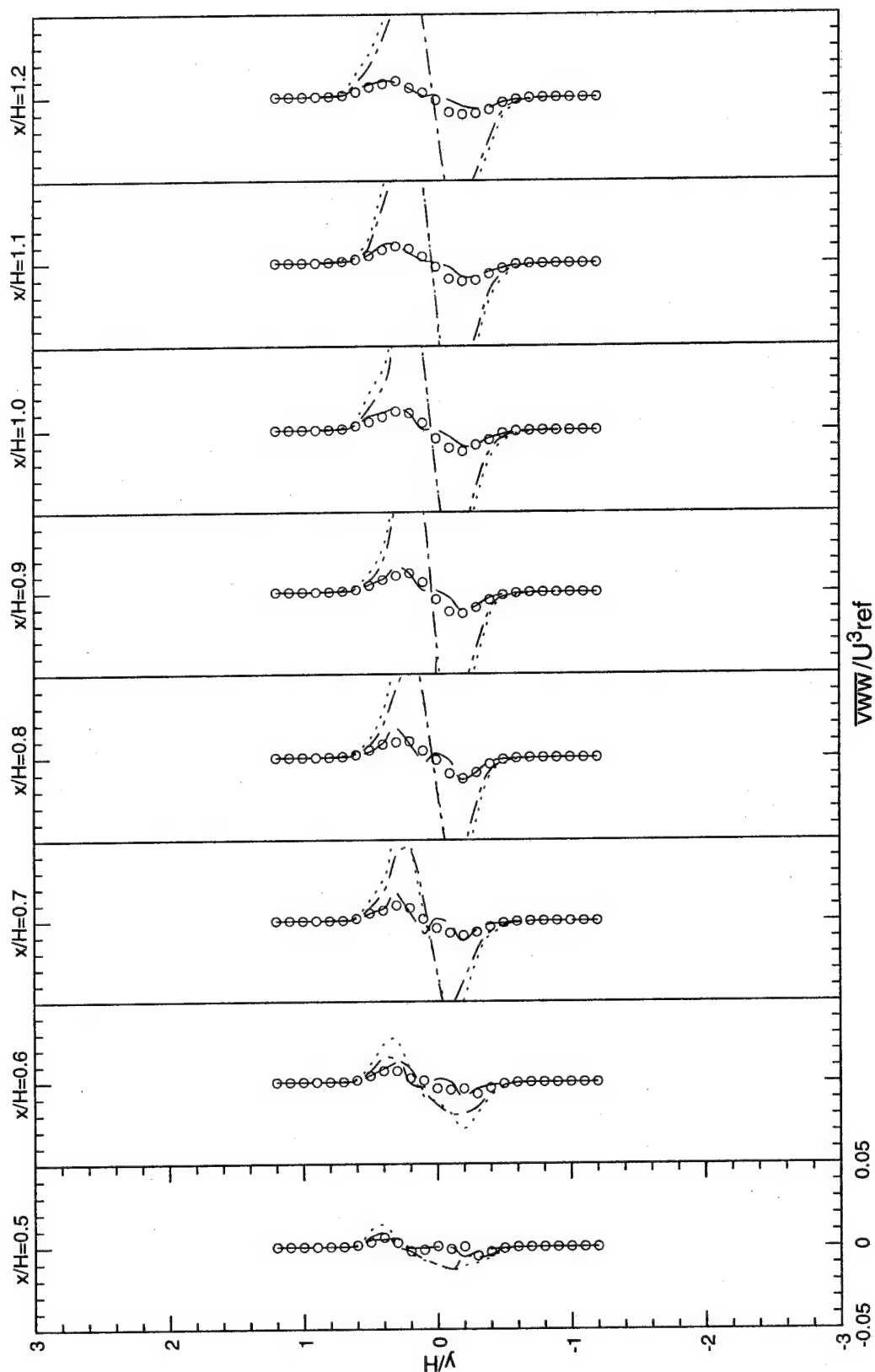


Figure 68. Third moment $\overline{v_{ww}}$ of fluctuating velocity. (○ data $\cdots \cdots$ $C_3 = 0.50$ $- - -$ $C_3 = 0.500$ $- \cdot -$ $C_3 = 0.5000$)

found for this flow, but as shown by the dashed lines, the simple relationship $\overline{uvw} \approx 0.2\overline{uvv}$ was found to best model the measured values. Figure 68 shows a comparison between the experimentally measured values of \overline{uvw} and the commonly used approximations. Again, the modeled approximations greatly overpredict the experimental data for \overline{uvw} , and a best fit to the measured values, as indicated by the dashed lines in Figure 68, would be $\overline{uvw} \approx 0.5\overline{uuv}$. No reasonable value for C_4 could be defined for this flow.

6.9 Turbulent Kinetic Energy (TKE) Balance

The approximate equation for the transport of TKE for steady, incompressible flow in Cartesian coordinates is given by Equation (6.1), (also, see Appendix F):

$$\overline{U} \frac{\partial k}{\partial x} + \overline{V} \frac{\partial k}{\partial y} + \overline{W} \frac{\partial k}{\partial z} = \quad \text{(convection)} \quad (6.1)$$

$$- \frac{1}{2} \left[\frac{\partial \overline{uuu}}{\partial x} + \frac{\partial \overline{vvv}}{\partial x} + \frac{\partial \overline{www}}{\partial x} + \frac{\partial \overline{vuu}}{\partial y} + \frac{\partial \overline{vvv}}{\partial y} + \frac{\partial \overline{vwv}}{\partial y} + \frac{\partial \overline{wuu}}{\partial z} + \frac{\partial \overline{wvv}}{\partial z} + \frac{\partial \overline{wwv}}{\partial z} \right] \quad (6.1)$$

(diffusion)

$$\left[\overline{uu} \frac{\partial \overline{U}}{\partial x} + \overline{vv} \frac{\partial \overline{V}}{\partial y} + \overline{ww} \frac{\partial \overline{W}}{\partial z} + \overline{uv} \frac{\partial \overline{U}}{\partial y} + \overline{uv} \frac{\partial \overline{V}}{\partial x} + \overline{uw} \frac{\partial \overline{U}}{\partial z} + \overline{uw} \frac{\partial \overline{W}}{\partial x} + \overline{vw} \frac{\partial \overline{V}}{\partial z} + \overline{vw} \frac{\partial \overline{W}}{\partial y} \right]$$

(production)

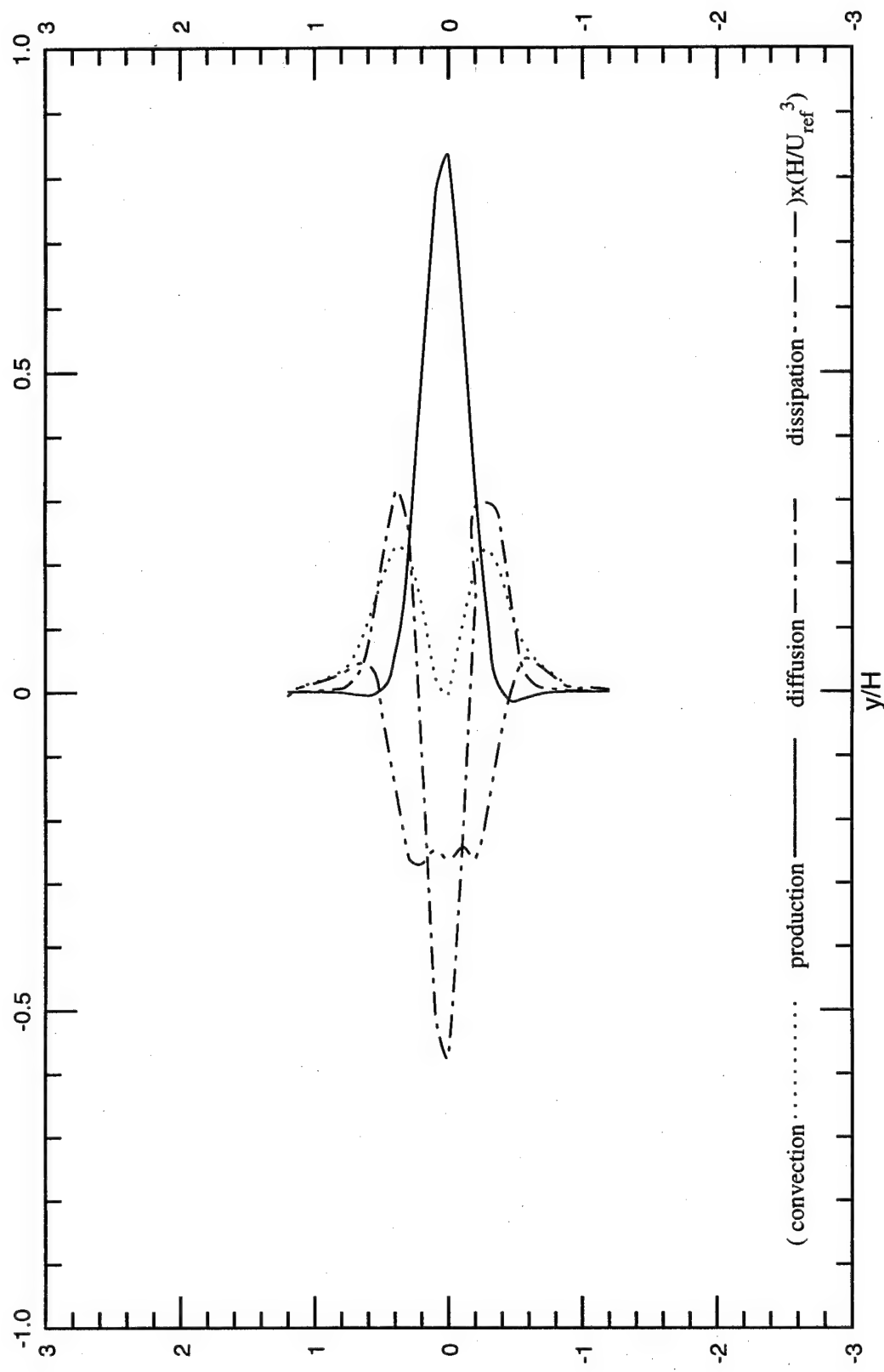
$$+ \epsilon \quad \text{(dissipation)}$$

Where the mean axial, transverse and spanwise velocities are denoted by \overline{U} , \overline{V} , and \overline{W} respectively. Equation (6.1) is composed of the following terms: 1) convection, 2) turbulent diffusion, 3) production, and 4) viscous dissipation of turbulent kinetic energy; where $k \equiv (\overline{uu} + \overline{vv} + \overline{ww})/2$. The exact transport equation for TKE has additional unknown terms which are not included in Equation (6.1). These include the three pressure-diffusion terms

which were assumed to be negligible in this study (see Appendix F), a commonly accepted assumption at locations away from solid walls. The viscous dissipation terms are represented by ε (where ε is a negative value), the turbulence dissipation rate (see Appendix F). Since most of the terms given in Equation (6.1) were measured except for ε , this equation can be used to estimate the turbulence dissipation rate by balance. Therefore, these values of dissipation rely heavily on the accuracy of the other terms in Equation (6.1).

Each term in Equation (6.1) was estimated by numerically differentiating the data using second order accurate finite difference algorithms (central differencing for interior points and forward differencing for end points). Since it is well known that numerical differentiation is a noisy process, these first derivatives of the data were then smoothed or least squares curve fitted to produce smooth profiles of each term. The smoothing technique developed by Gould (1994) was used. The selection of either an n^{th} order least squares polynomial curve fit or the Savitzky and Golay (1964) smoothing algorithm, which applies a convolution kernel to the original data, depended on the shape of each differentiated data profile. The choice of smoothing technique was based on how well each worked; the best method was selected for each individual profile of each variable in Equation (6.1).

Finally, regions in the flow where turbulent transport mechanisms of TKE are dominant, are identified. Figure 69a shows the profiles of the TKE terms at the bubble station, $x/H=0.9$. The individual terms are presented, with their associated statistical uncertainties (see Appendix H) in Figures 69b through 69e, at this most critical station. Statistical uncertainty calculations at all other stations were also made, but all uncertainties were smaller than those at the presented station, and thus are not shown. Because of the large



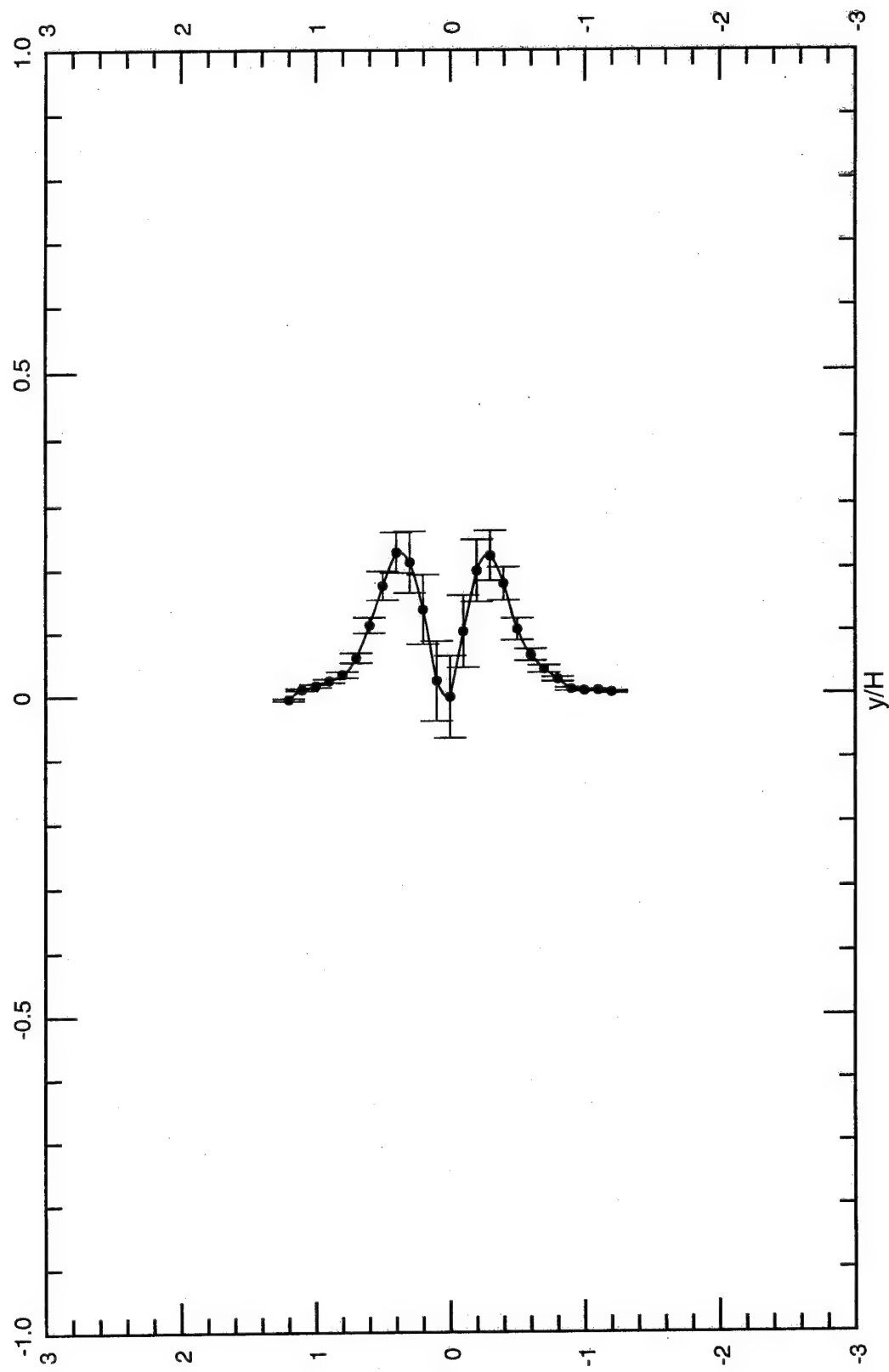


Figure 69b. Convection term with error bars at station $x/H=0.9$ (Bubble Location):

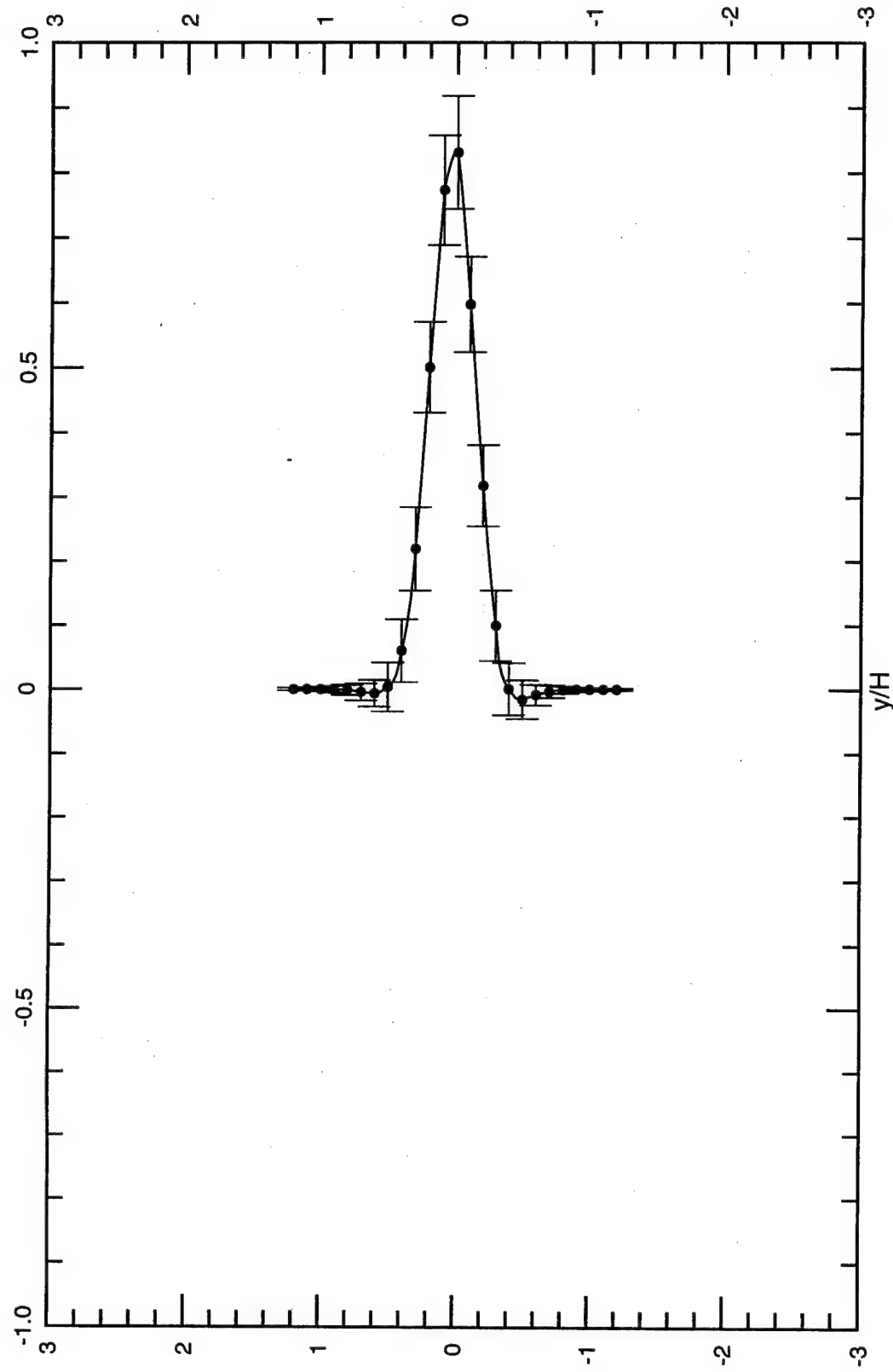


Figure 69c. Production term with error bars at station $x/H=0.9$ (Bubble Location).

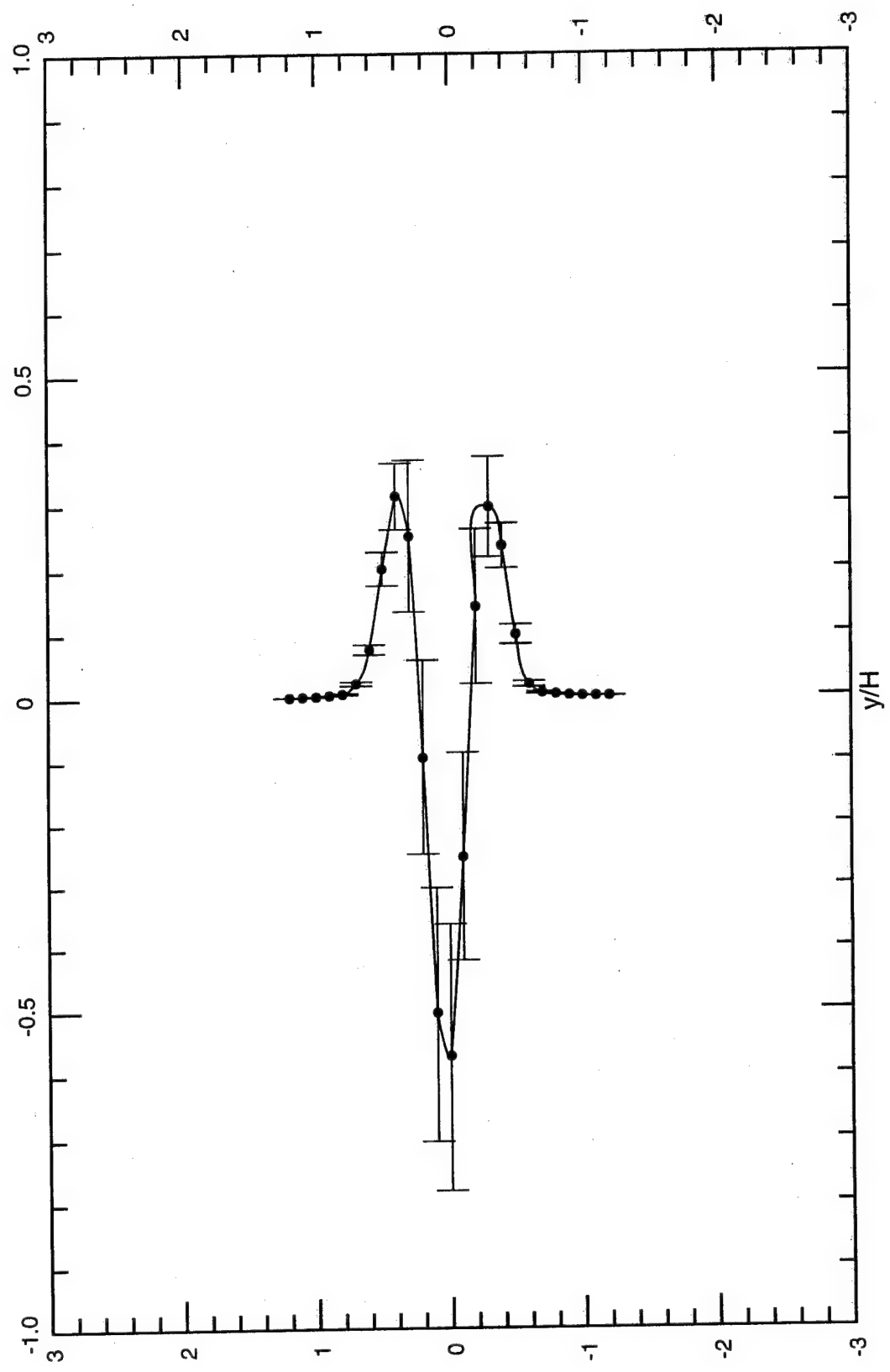


Figure 69d. Diffusion term with error bars at station $x/H=0.9$ (Bubble Location).

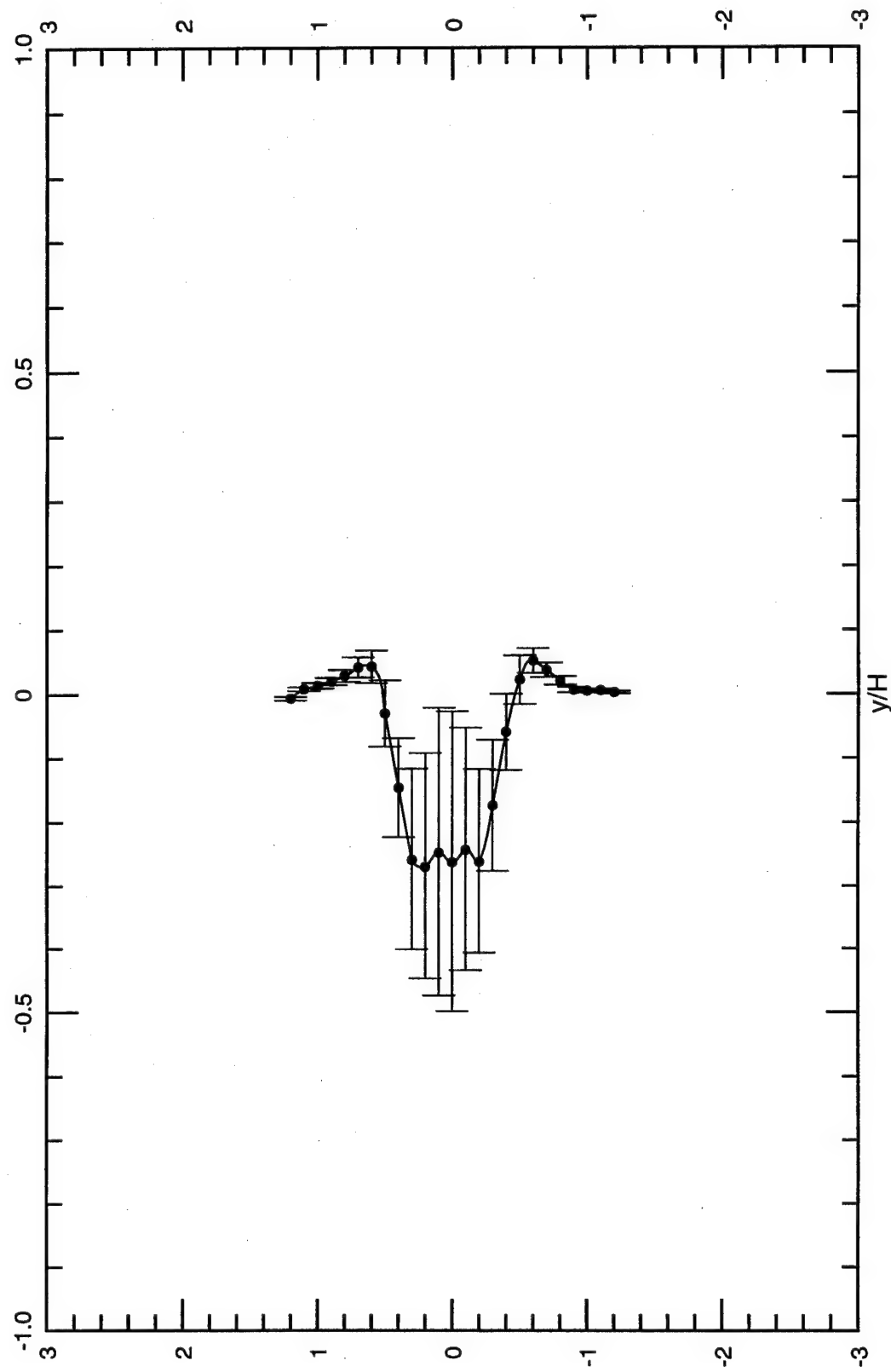


Figure 69e. Dissipation term with error bars at station $x/H=0.9$ (Bubble Location).

errors in the triple products caused by the relatively low number of samples (5120), the diffusion term shows the highest uncertainty, which in turn gives high uncertainty of the dissipation term, since this last term is obtained by balance.

6.9.1 TKE Terms

Figure 70 shows the measured values of the total convection, production, diffusion, and dissipation of TKE as defined by Equation (6.1) at various axial stations. Statistical uncertainty bars are not included in these figures for clarity sake as mentioned earlier. Also, note that "+" denotes Gain and "-" denotes Loss. These profiles show that the TKE is first produced in the shear layer where both \bar{uv} and the axial mean velocity gradient, $\partial\bar{U}/\partial y$, are large. This gives the double hump profile shown in this Figure at $x/H=0.5$. At downstream locations, however, the $\bar{vv}\partial\bar{V}/\partial y$ and $\bar{uu}\partial\bar{U}/\partial x$ terms contribute to the production of TKE and cause the profile shape to change from the double hump shape to the single peak shape shown in Figure 69a and Figure 70. Turbulent diffusion, which is difficult to model, shows a double hump feature with two small positive peaks at the shear layers, and a large deficit in the center. This deficit reaches a maximum normalized value of -0.062 at the stagnation point (Figure 69a). Convection of TKE shows a double hump behavior which is positive with peaks towards the outside of the shear layers, and is near zero in the recirculation zone behind the bluff body near the centerline. The convection profiles seem to maintain constant values and shape throughout the whole near-field region. In general, the data show that production and diffusion significantly contribute to the turbulent kinetic energy, with absolute peaks at $y/H=0$. Convection remained relatively low, while diffusion reached a minimum at the stagnation point (Figure 69a), where the triple products are high indicating

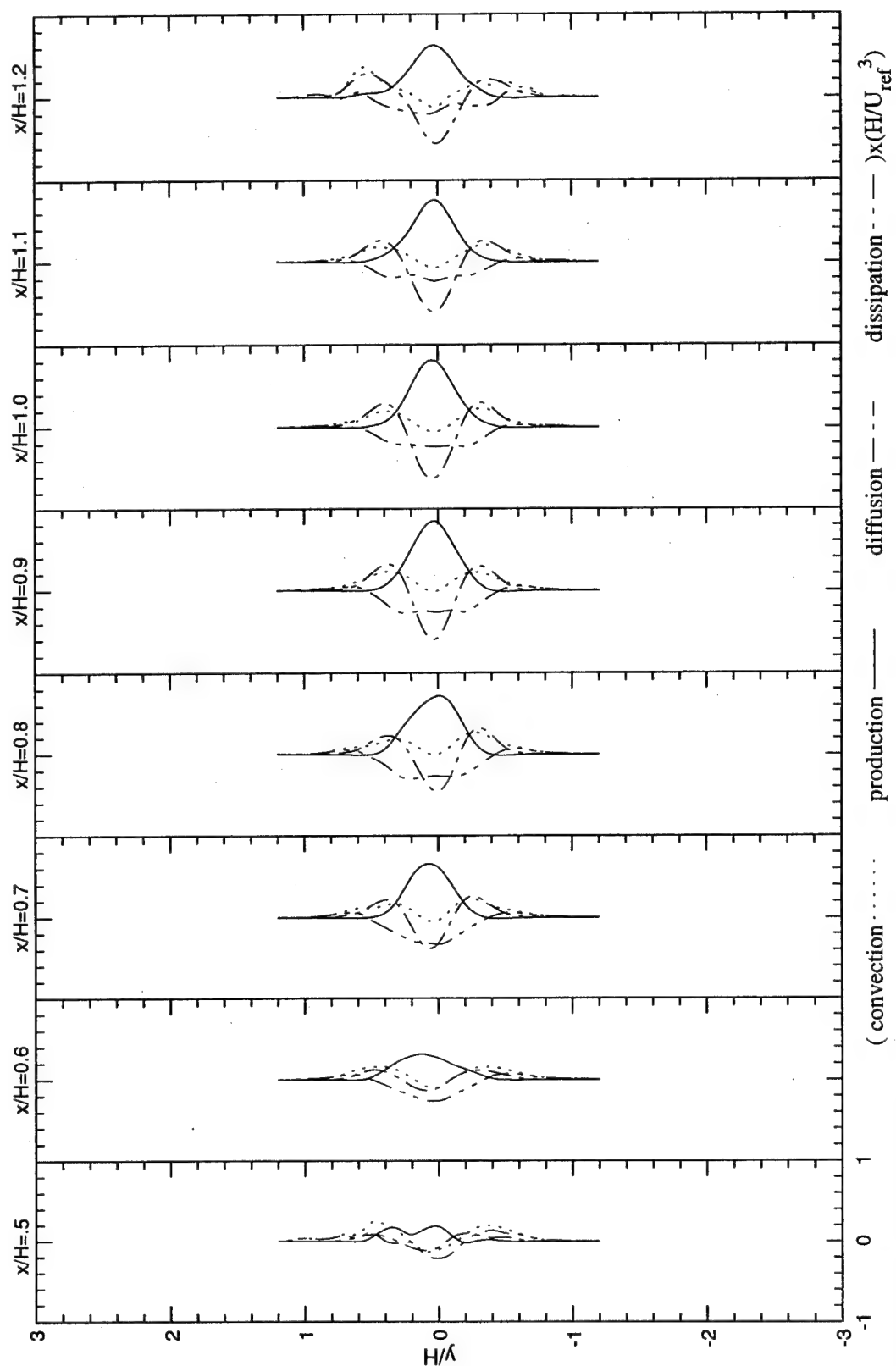


Figure 70. TKE Balance.

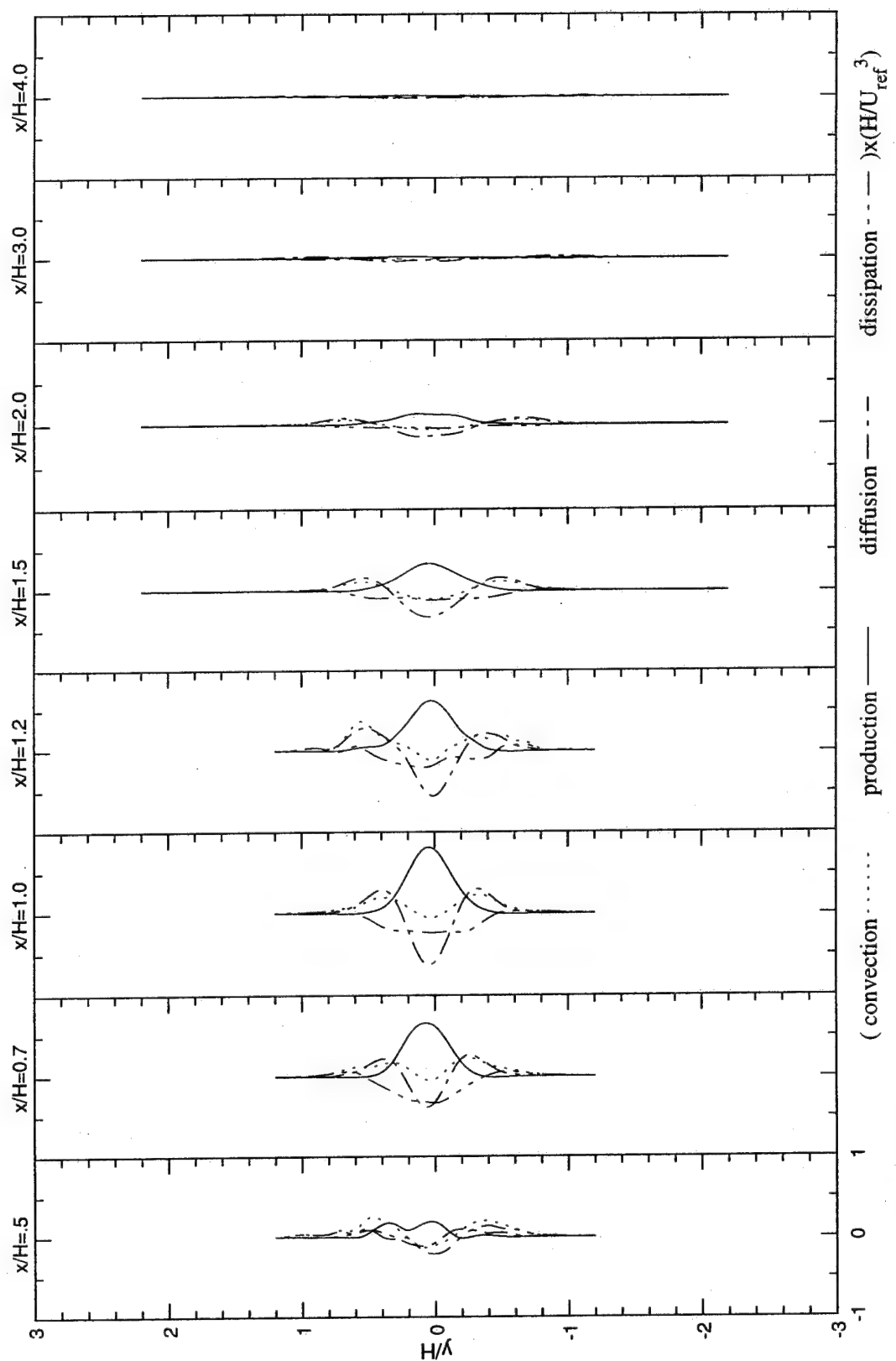


Figure 71. TKE Balance.

the presence of large eddies or at least very periodic flow. As for the dissipation, the values remained relatively constant and were of the same size as the diffusion at the first three stations. Finally, the levels of convection, diffusion, production and dissipation of TKE diminished relatively quickly in this flow and are near zero for $x/H > 3$ as shown in Figure 71. This may explain why the profiles of TKE (Figure 53) relax slower in the axial direction than does the velocity field; TKE is not diffusing very rapidly at these downstream locations.

Figures 72 through 74 show the contributing terms to each of the production, convection, and diffusion terms. For instance, $\bar{v}\bar{v}\partial\bar{V}/\partial y$ was the dominating term in the production of TKE (Figure 72) and peaked to a maximum normalized value of 1, at the stagnation station, $x/H=0.9$. The $\bar{V}dk/dy$ term was the only one that had a significant value in the convection of TKE, with a maximum double peaks of normalized value of 0.25 at the shear layers. In the diffusion of TKE, the term $\partial\bar{v}\bar{v}\bar{v}/\partial y$ shows a double hump behavior with maximum absolute normalized values of 0.6 at the stagnation station.

6.9.2 Derivatives

In addition, the raw measurements were numerically differentiated using second order accurate finite difference algorithms (central differencing for interior points and forward differencing for end points) and plotted in Figures 75 through 81. Note that no smoothing was performed to create these figures. The relative smoothness shown, particularly for the 1st derivative profiles, give additional confidence in the accuracy of the test condition and the measurement data. Additional points of measured data (i.e., \bar{U} , $\bar{u}\bar{u}$, $\bar{u}\bar{u}\bar{u}$, ...) and first derivatives of these parameters were interpolated so that smaller Δx , could be used, giving smaller numerical errors.

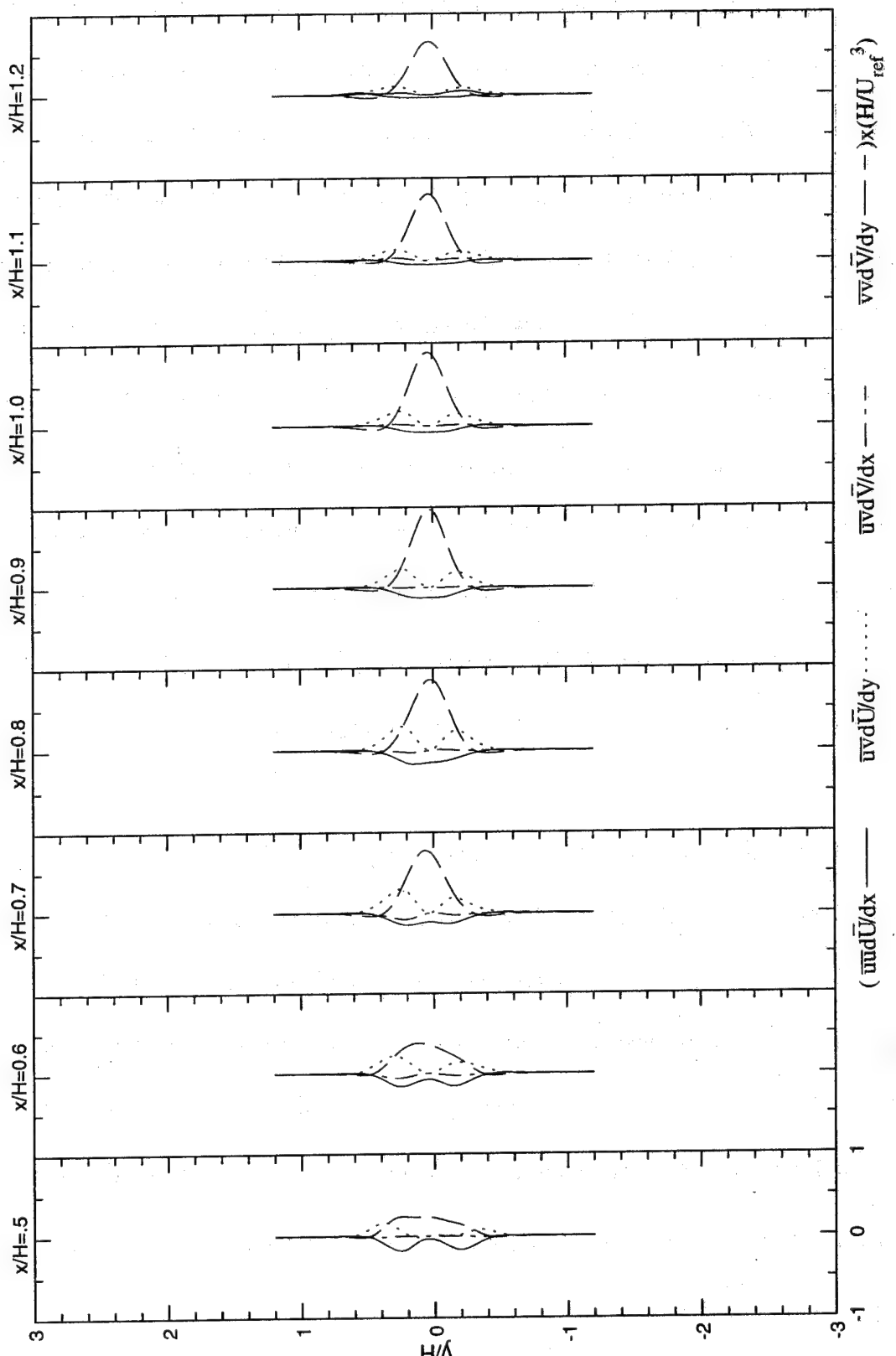


Figure 72. Production of TKE.

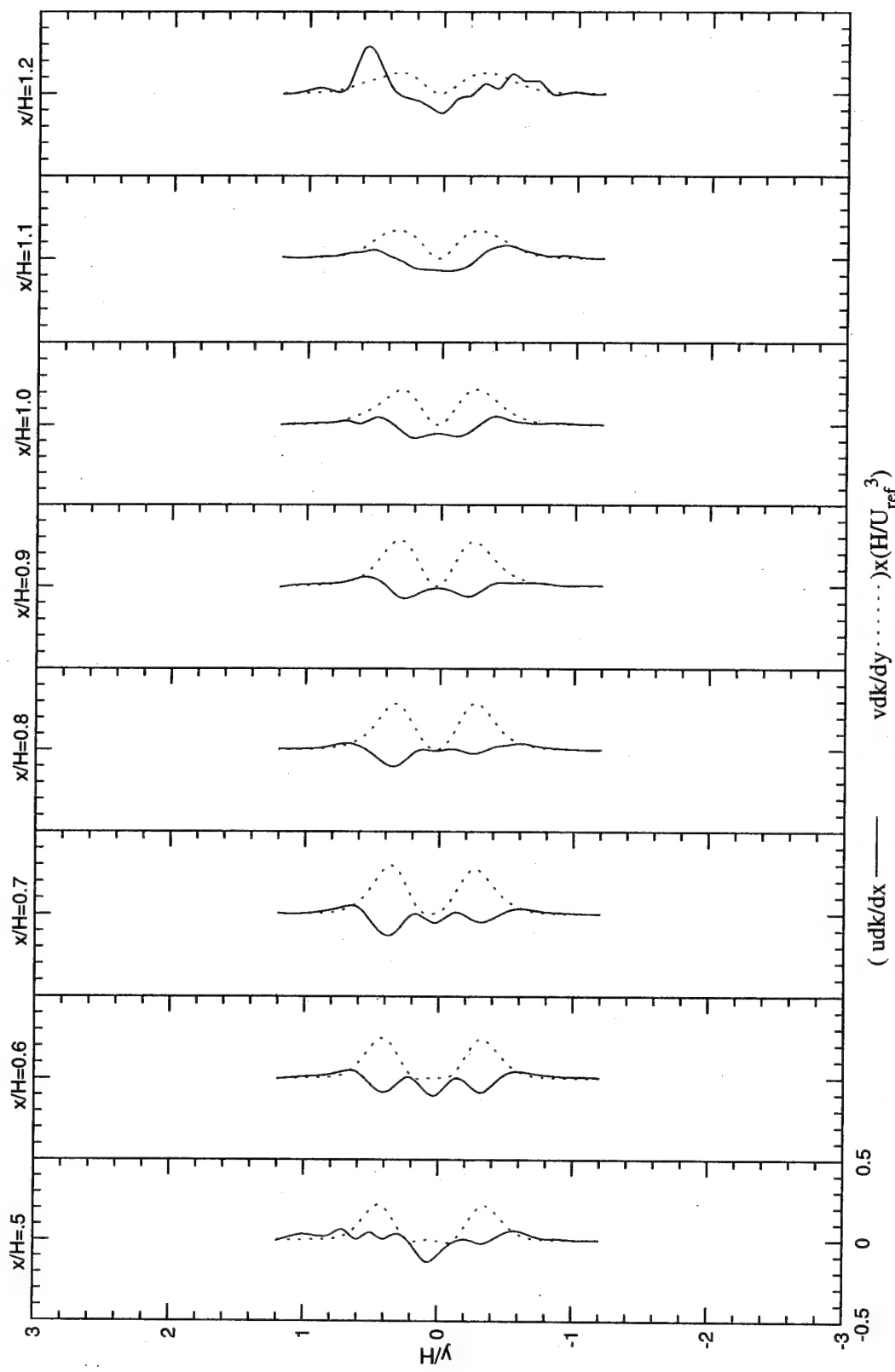


Figure 73. Convection of TKE.

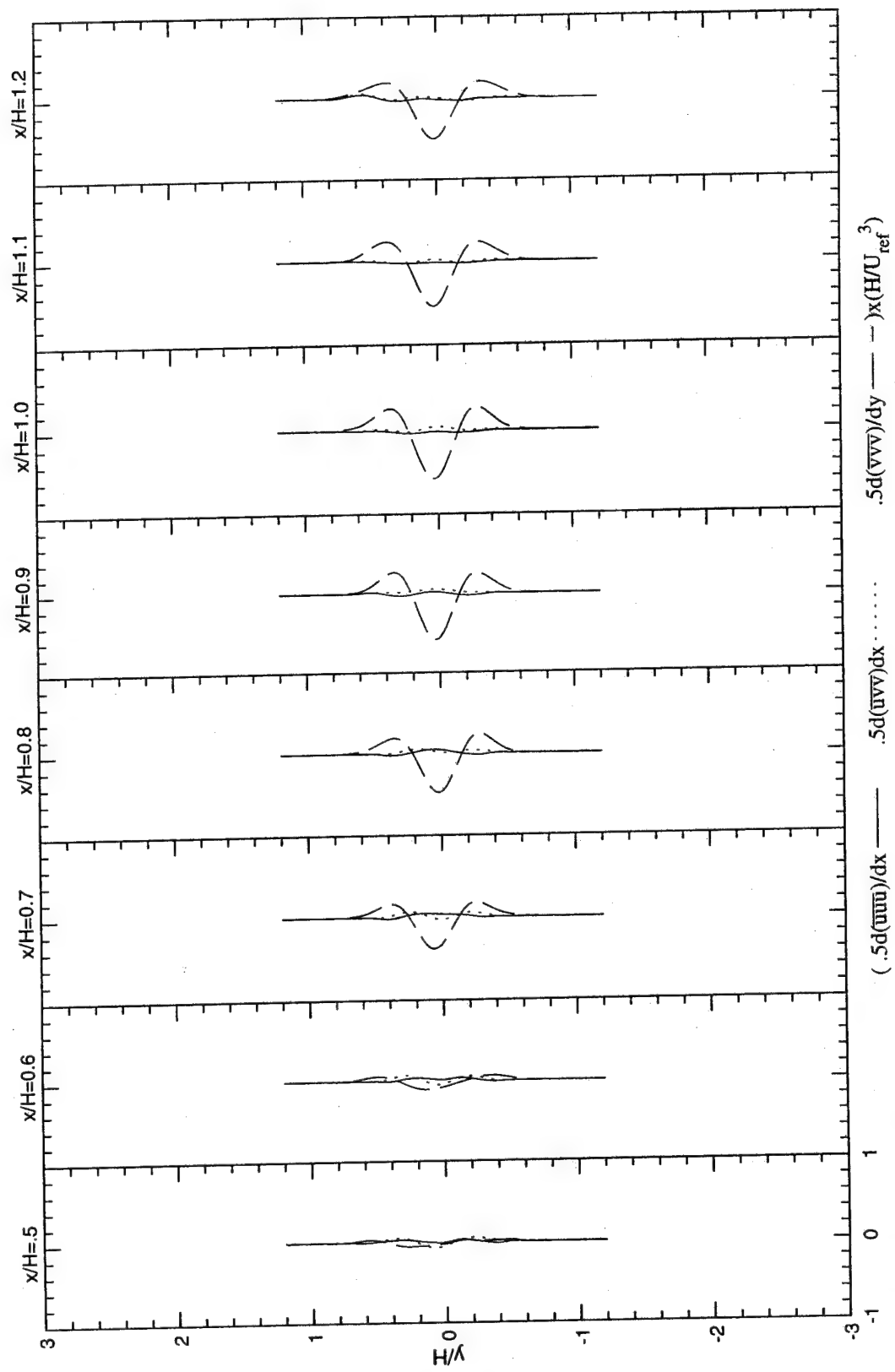


Figure 74. Diffusion of TKE.

The x- and y- derivatives of the mean axial velocity followed the same decreasing trend as the velocities themselves (Figure 75). The y-derivatives showed positive and negative peaks at the shear layers while the x-derivatives showed a maximum peak at the centerline, with the exception of the two first stations where a slight dip was noticed. The reverse is observed in the case of the transverse derivatives (Figure 76). It is noteworthy that the x-transverse derivatives decreased from station $x/H=0.5$ to $x/H=0.9$ and reversed slope direction as they began to increase again (Figure 76). The y-spanwise derivatives (Figure 77) showed an antisymmetric behavior, while the x-derivatives reversed direction with respect to the velocity profiles.

The y-derivatives of the \bar{uv} -shear stress (Figure 78) showed minimum centerline values which reached a maximum at the stagnation point. The first station was the only one with a double hump. The x-derivatives showed a minimum and a maximum at the shear layers, which decreased to almost zero at the stagnation point and began to increase again. The \bar{uu} -derivatives (Figure 79) showed a decreasing trend away from the bluff body. The transverse y-derivatives showed a maximum and a minimum, while the x-derivatives showed a double hump. The transverse normal stress (\bar{vv}) x-derivatives (Figure 80) showed a minimum and a maximum which decreased away from the bluff body, while the x-derivatives showed a centerline maximum which flipped at the stagnation point and thereafter. The spanwise normal stress x-derivatives (Figure 81) showed an anti-symmetric behavior, while the y-derivatives showed a reverse direction with respect to the velocity profiles.

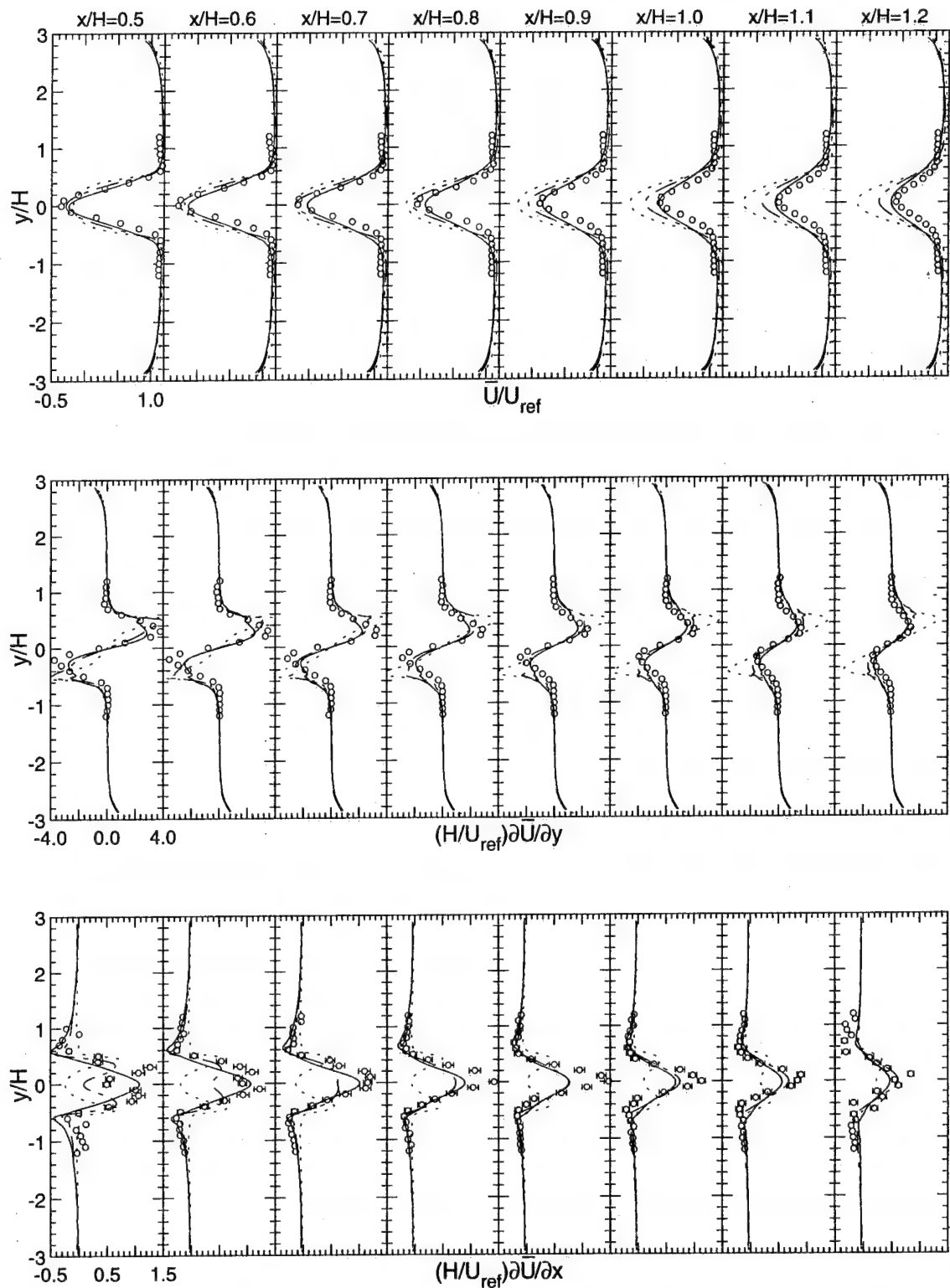


Figure 75. Normalized mean axial velocity and velocity gradient distributions.

(○ data, - - - steady state $k-\epsilon$, - - unsteady $k-\epsilon$, — unsteady RNG)

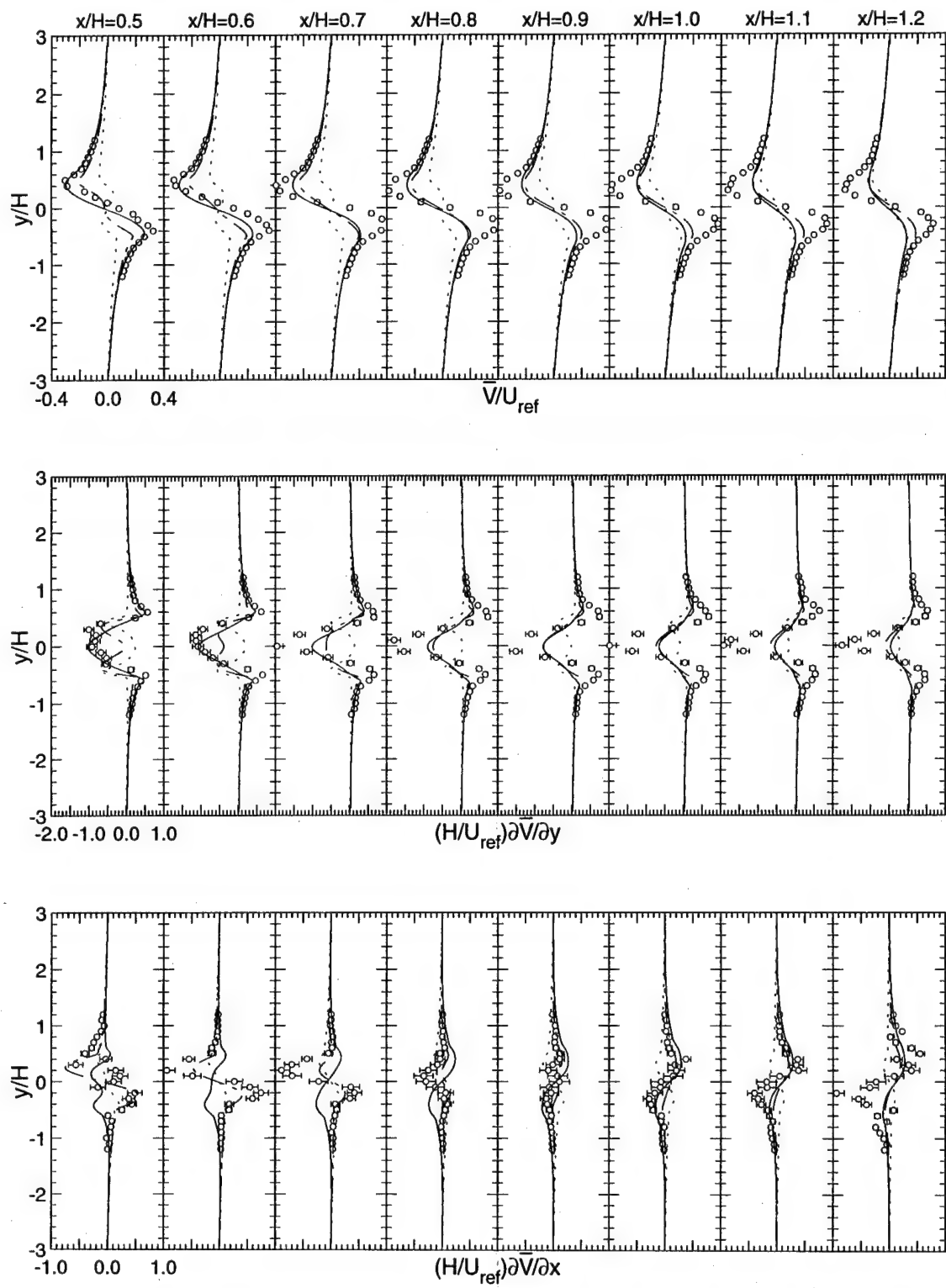


Figure 76. Normalized mean transverse velocity and velocity gradient distributions.

(○ data, - - - steady state $k-\epsilon$, - - unsteady $k-\epsilon$, — unsteady RNG)

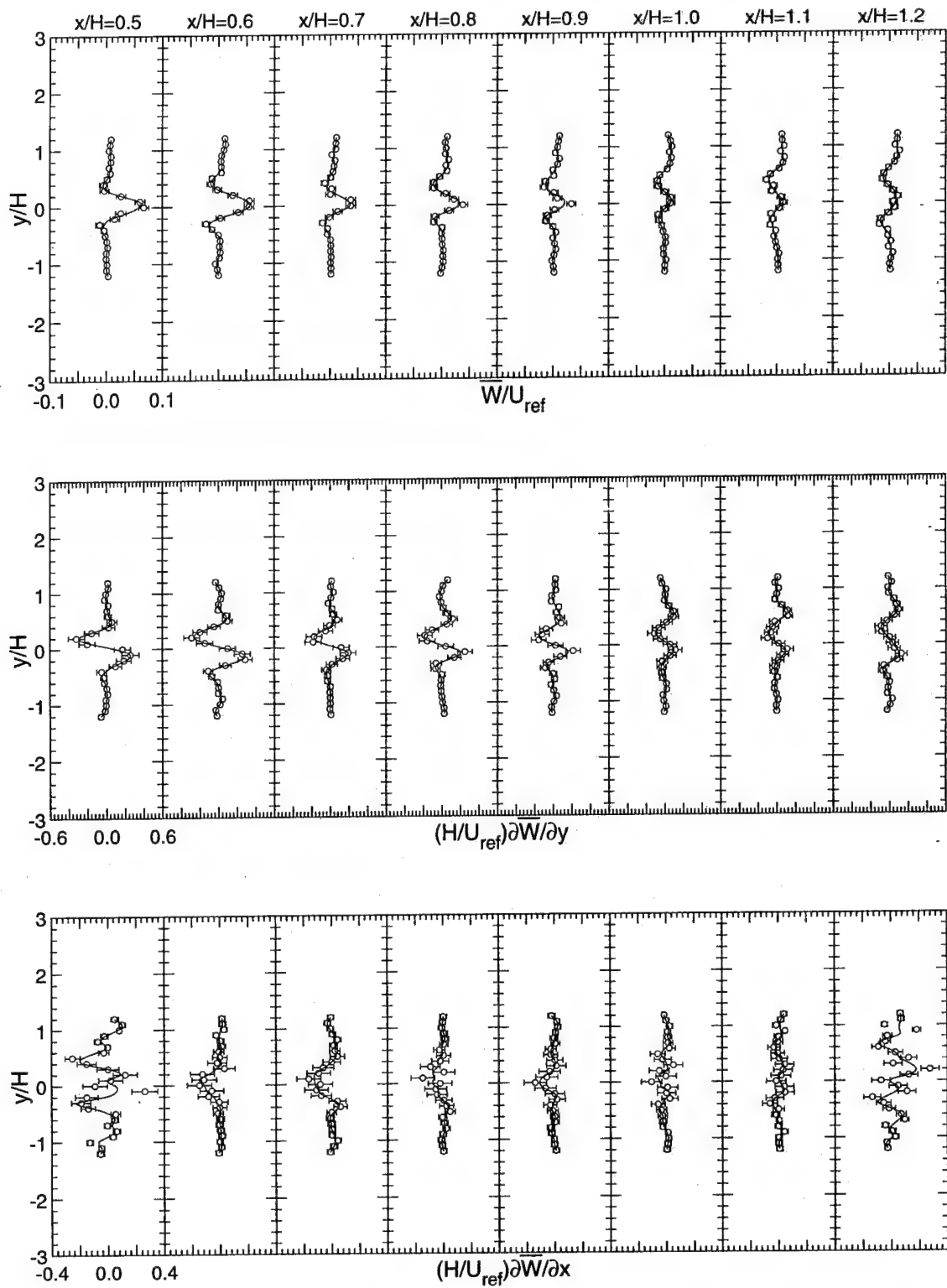


Figure 77. Normalized mean spanwise velocity and velocity gradient distributions.

(○ data, — smoothed curve-fit)

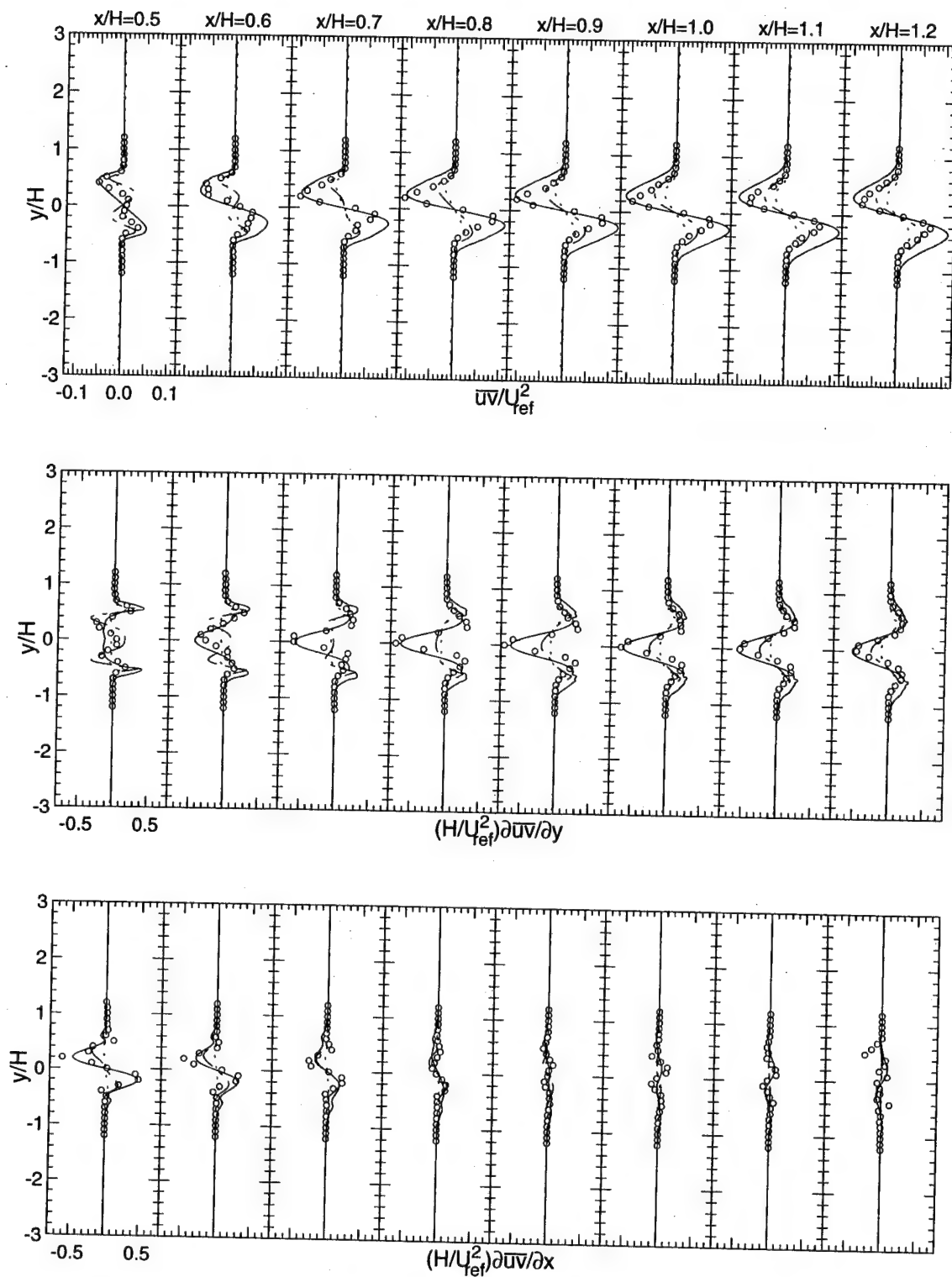


Figure 78. Normalized $\bar{u}v$ turbulent stress and stress gradient distributions.

(○ data, - - - steady state k-ε, - - - unsteady k-ε, — unsteady RNG)

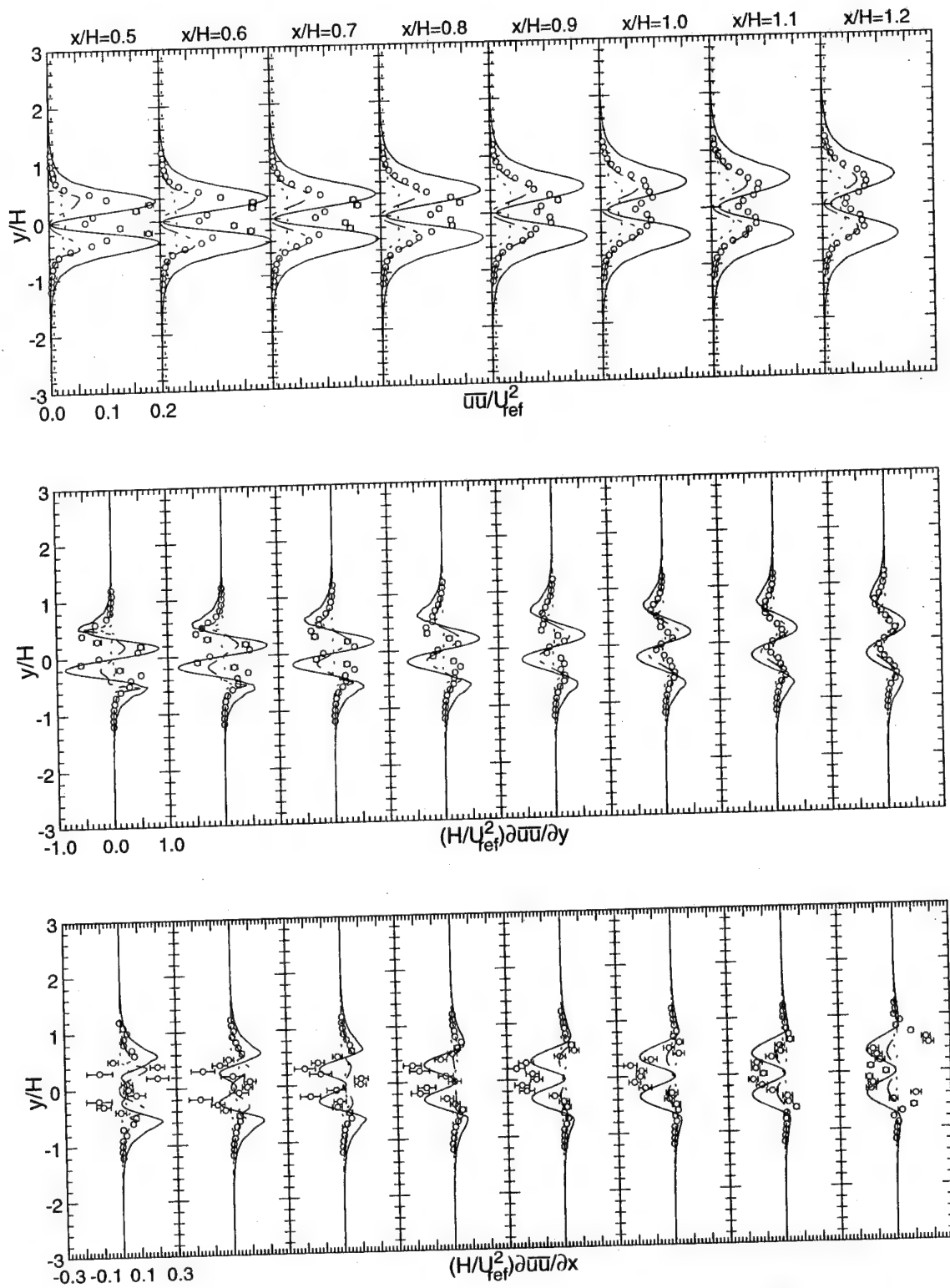


Figure 79. Normalized $\bar{u}\bar{u}$ turbulent stress and stress gradient distributions.
 (○ data, - - - steady state k- ϵ , - - unsteady k- ϵ , — unsteady RNG)

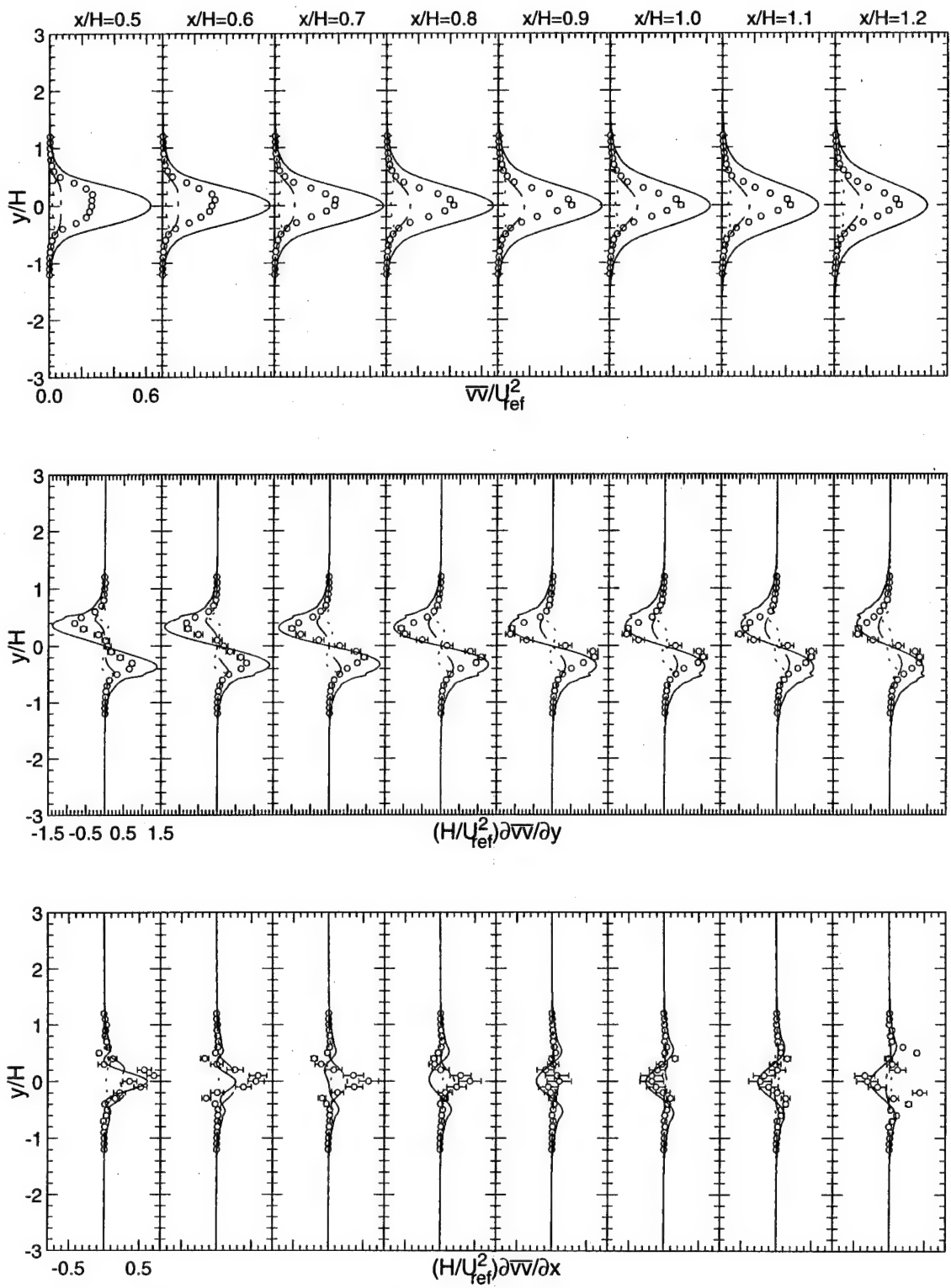


Figure 80. Normalized $\bar{v}v$ turbulent stress and stress gradient distributions.

(○ data, - - - steady state $k-\epsilon$, - - - unsteady $k-\epsilon$, — unsteady RNG)

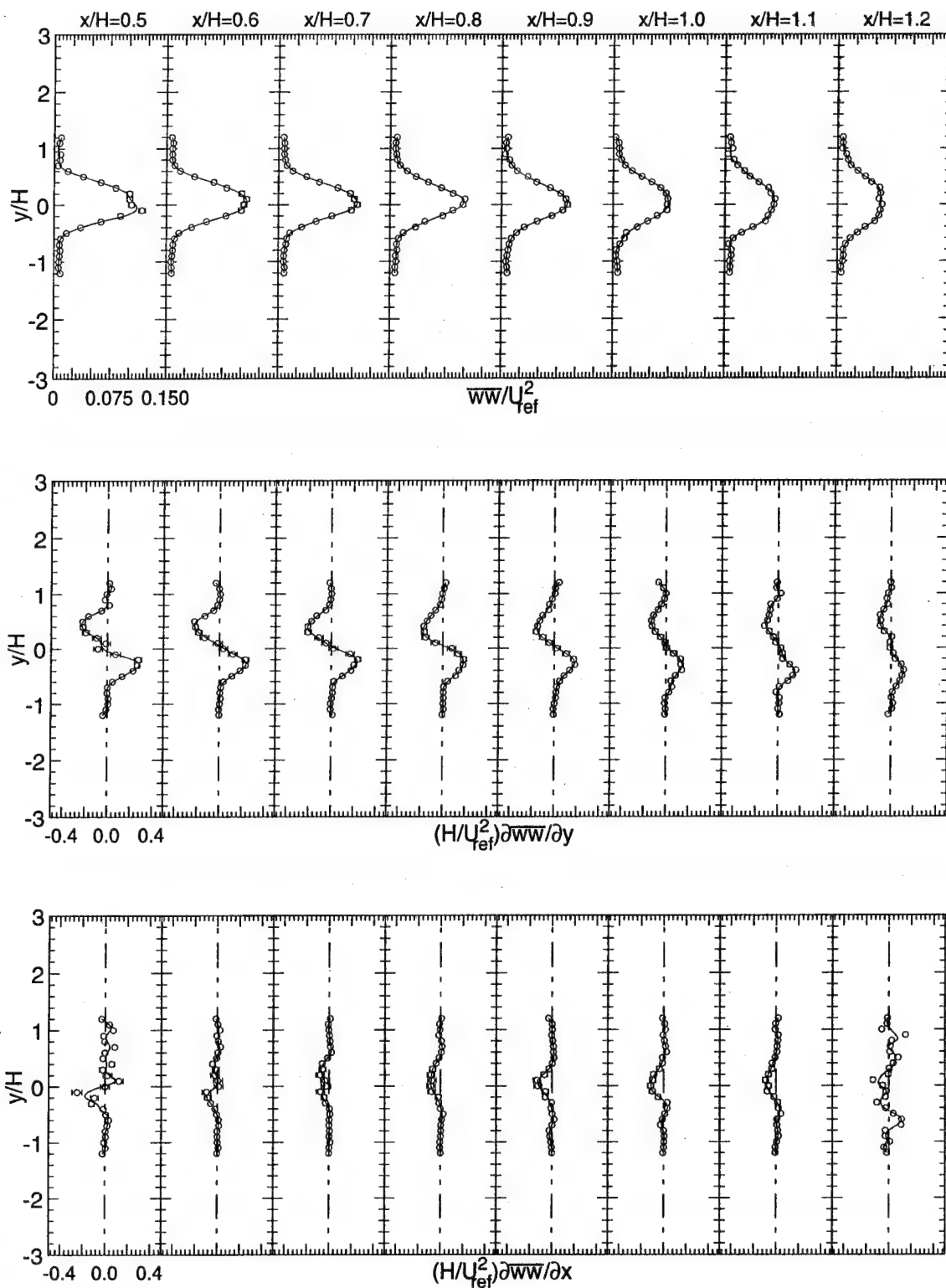


Figure 81. Normalized $\overline{w}w$ turbulent stress and stress gradient distributions.

(○ data, — smoothed curve-fit)

For a truly two-dimensional flow, $\partial \bar{U} / \partial x = -\partial \bar{V} / \partial y$ (Etheridge & Kemp, 1977); however, as Figure 82 indicates, this flow shows a departure from two-dimensionality, that extends even beyond station $x/H=1.2$, downstream of the stagnation point.

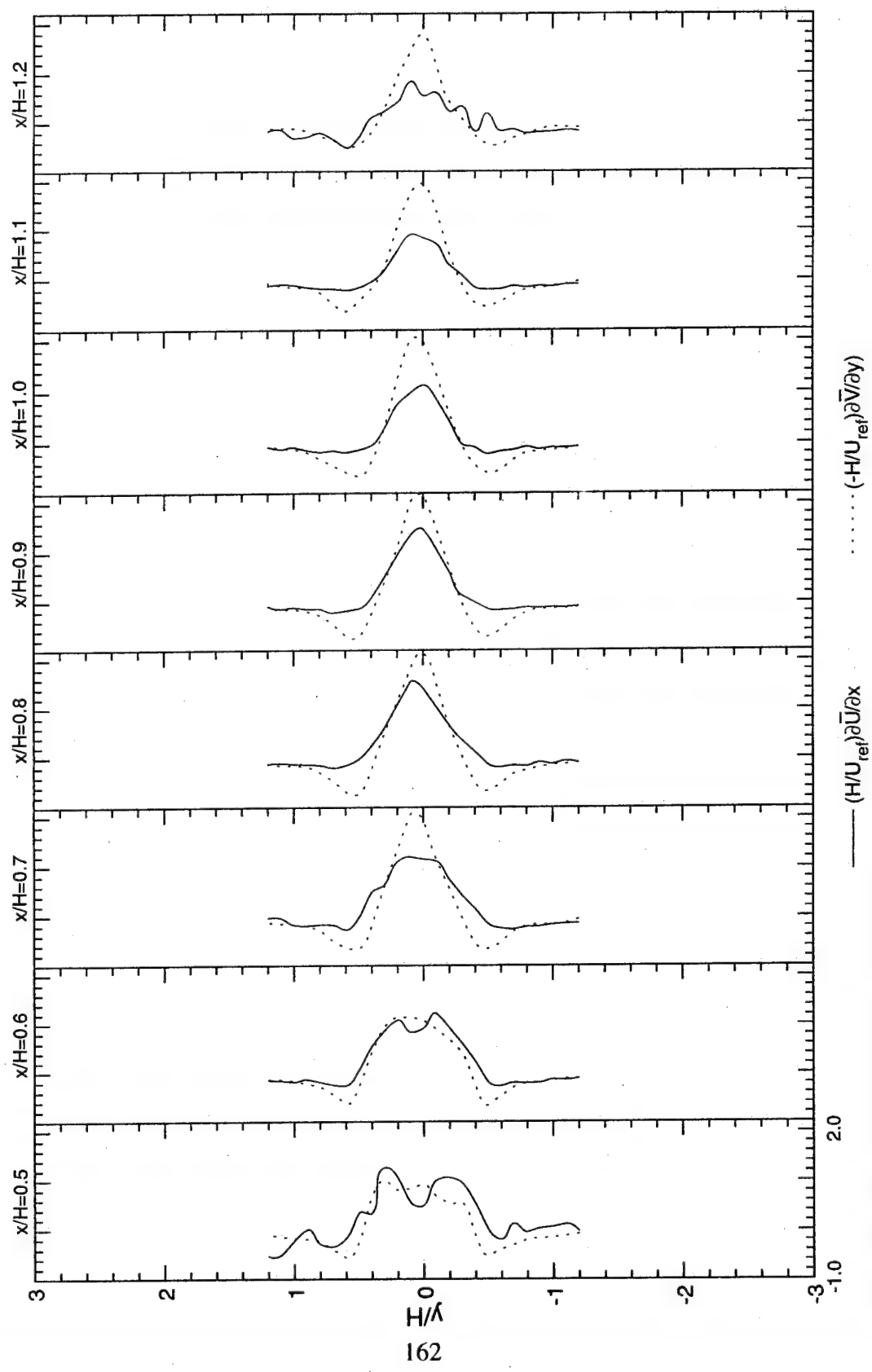


Figure 82. Two-dimensionality verification.

CHAPTER 7

NUMERICAL RESULTS AND DISCUSSION

7.1 Introduction

Like the experimental studies, many CFD researchers have conducted numerical studies on simple bluff-body geometries. These studies have produced solutions using techniques varying in sophistication from the steady-state algebraic stress model of Kodali and Amano (1986) to the dynamic subgrid-scale Large-Eddy Simulations (LES) of Yang and Ferziger (1993). Some early solutions modeled only half of the symmetric geometry, thus imposing symmetry on the flow. However, detailed studies such as the current study, have shown that the instantaneous flowfield consists of a structured pattern of alternating large scale vortices. A symmetry plane enforced by the numerical model precludes the formation of the shed vortices, and thus requires the turbulence model to account for this physical mechanism. Comparisons to experimental measurements have shown such predictions to be inadequate for bluff-body flowfields. Researchers have been able to improve the numerical modeling by including the entire flowfield. When solved with time-accurate algorithms, the flow is free to oscillate about the geometric symmetry plane. Such oscillations add significantly to both the time-averaged turbulent normal and shear stresses in the wake of the bluff body.

7.2 Numerical Technique

The numerical analysis for the current study was executed by CFD Research Corporation (CFDRC) of Huntsville, Alabama. A full report of the numerical technique and

results can be found in Raffoul, et al. (1995). The numerical analysis was accomplished using a commercially available CFD code, CFD-ACE (Avva, 1993). CFD-ACE is a pressure based finite-volume code designed for the analysis of incompressible and compressible flowfields, using a modified SIMPLEC algorithm. All solutions used 2nd order accurate central differencing, stabilized with upwind biasing to solve the 2-d incompressible Navier-Stokes equations. The computational domain extended 63.5 mm (2.5 in) upstream of the bluff body ($x/H=-5$) and 508 mm (20 in) downstream ($x/H=40$). All solutions used a constant inflow profile matched to the experimental data (see Figure 6), and a fixed pressure exit condition. The current study presents results from three solutions: 1) a symmetric, steady-state, 2-d, $k-\epsilon$ solution; 2) a standard 2-d, $k-\epsilon$, time-accurate solution; and 3) an RNG, 2-d, $k-\epsilon$, time-accurate solution.

The first solution enforced symmetry by modeling only half of the geometry. The solution was converged to steady state on a 102x38-grid (partially shown in Figure 83), using the standard $k-\epsilon$ model with wall functions.

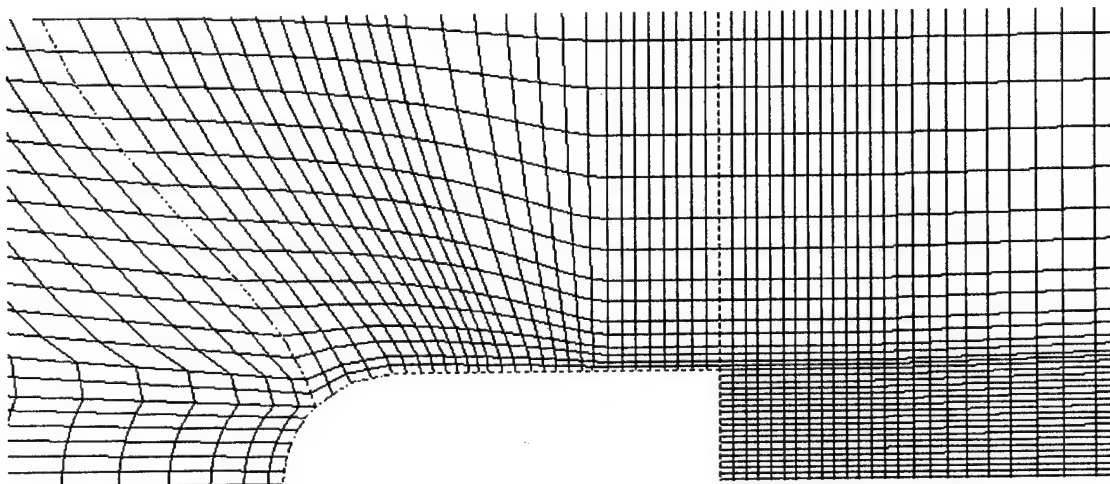


Figure 83. Grid near bluff body used for CFD analyses.

The Reynolds stresses for the steady-state solution were calculated from the Boussinesq equation;

$$\overline{u_i u_j} = \frac{\mu_r}{\rho} \left(\frac{\partial \bar{U}_i}{\partial x_j} + \frac{\partial \bar{U}_j}{\partial x_i} \right) - \frac{2}{3} k \delta_{ij} \quad (7.1)$$

where;

$$\mu_r = 0.09 \rho \frac{k^2}{\epsilon} \quad (7.2)$$

The second solution modeled the entire flowfield on a 102x77-grid (mirror of symmetric grid) and required a time-accurate solver. Again, the standard $k-\epsilon$ model was used with wall functions. The solution was first advanced 200 iterations in a steady-state mode to establish the flowfield, and also to allow an asymmetric velocity field to develop. The solution was then restarted in a time-accurate mode and advanced 4500 time-steps at 5.0×10^{-6} sec per time-step. Finally the solution was advanced ~ 2500 time-steps to collect the turbulence statistics. Care was taken to ensure that the statistics were collected over a whole period of the vortex shedding cycle. Turbulence statistics were calculated in a fashion similar to the experimental procedure, with each time-step producing one sample.

The third solution was obtained in a similar manner except the RNG $k-\epsilon$ model was employed. The reader is referred to Yakhot, et al. (1992) for more information on the RNG theory. One of the major differences between the standard $k-\epsilon$ model and the RNG $k-\epsilon$ model, is that many of the constants are derived from the RNG theory, removing much of the ad-hoc nature of the standard $k-\epsilon$ model. The RNG $k-\epsilon$ model was found by Speziale and Thangam (1992) to give good results for the backward-facing step flow of Kim, et al. (1978).

7.3 Results and Discussion

The mean velocities, \bar{U} , and \bar{V} , and three of the Reynolds stresses, \bar{uu} , \bar{uv} , and \bar{vw} for all three solutions are shown with the experimental measurements in Figures 75, 76, and 78 through 80. Predictions using the three-component schemes listed above are also included in these figures. The predicted mean velocities, using the symmetric steady-state method, indicate that the numerical predicted recirculation bubble extends to $x/H=2$, much further downstream than the experimentally determined bubble position. The numerical prediction gives a bubble length of four half bluff body heights, similar to a backward-facing step. This is to be expected since the bluff-body model resembles a backward-facing step with a slip wall at the centerline for the symmetric case method. The predicted Reynolds stresses are also comparable to those measured in a backward-facing step flows. However, the experimentally measured Reynolds stresses for the bluff-body flow were found to be ~ 5 times higher than those found in backward-facing step flows. The underprediction of the Reynolds stresses by the steady-state solution leads to the incorrect bubble length in the recirculation zone. For the purpose of fuel injection and mixing studies, such an analysis is not sufficient.

The time-accurate solutions were able to predict the vortex shedding behind the bluff body. The standard $k-\epsilon$, time-accurate, solution predicted a Strouhal number, $St=0.240$, which compared well to the experimental value of 0.243. The predicted time-averaged velocities and Reynolds stresses are also shown in Figures 75, 76, and 78 through 80 by the dot-dash lines. The separation bubble calculated with the time-accurate solution method was considerably shorter than that predicted using the steady-state solution method, extending

only to $x/H=1.0$. However, the predicted length of the bubble was still longer than the measurements indicated, and the predicted wake spread slightly slower than the experimentally determined wake size. While the magnitudes of the predicted Reynolds stresses were higher when using this time-accurate scheme than those predicted using the steady-state method, they remained lower than the experimental results.

To improve the time-accurate results, the RNG $k-\epsilon$ turbulence model developed by Yakhot, et al. (1992) was tested. The Strouhal number predicted by the time-accurate RNG model method was 0.25, slightly higher than that obtained from the experimental data. However, the mean velocity predictions were significantly improved, as shown in Figures 75 and 76 by the solid lines. The predicted separation bubble was shorter with this scheme and ended slightly ahead of the experimental measurements ($x/H=0.7$). In addition, the overall mean velocity field was predicted fairly well, except for the transverse velocity just downstream of the stagnation point. This deficiency in accurately predicting the transverse velocities may be a result of 3-d effects near the bluff body.

Comparisons of the predicted Reynolds stresses to the measurements are also improved with the time-accurate RNG model method (Figure 78). However, the normal stresses are overpredicted (Figures 79, 80), leading to the shorter separation bubble. The largest discrepancy occurs with the transverse normal stress, the values of which are overpredicted by a factor of three. Martensson, et al. (1991) obtained similar results using LES, and found that the transverse normal stresses were reduced significantly when simulated with a 3-d analysis.

CHAPTER 8

CONCLUSIONS

A three-component laser Doppler velocimeter was used to measure the three components of the velocity vector, normal and shear stresses, and all nine turbulent triple products in the isothermal and incompressible turbulent flowfield downstream of a 2-d bluff body mounted at mid-stream in a rectangular test section. A benchmark quality database is established for future reference and for computational fluid dynamics code development and validation. The three-component measurements were validated using separate one-component LDV measurements by showing excellent agreement of the axial mean velocity throughout the tunnel. A mass flow balance was performed by numerically integrating the 1-d data acquired from top to bottom of the tunnel. The agreement for all measured stations was within 2% of the most upstream station. Negative axial velocities were found in the recirculation zone. Spanwise velocity measurements in the near-field indicated that the flow is three-dimensional just downstream of the bluff body. The measured turbulent triple products are unique in that no similar work has been reported previously. Validation of some commonly used normal stresses, and turbulent triple product approximations was made and found to greatly overpredict the experimental values. Newly derived models for \overline{ww} , \overline{uww} , and \overline{vww} in this flow were found using the direct measurements. A balance of the turbulent kinetic energy in this flow was also performed. The production, convection, and diffusion of turbulent kinetic energy were computed directly from the experimental data using numerical differencing. Turbulence dissipation rate was obtained by balance. Regions in the flowfield

where turbulent kinetic energy is produced, convected, and diffused were also identified.

The measurements also revealed that the flowfield was dominated by strong, periodic vortex shedding in the wake, yielding a symmetric vortex pair in the mean flow. The mean spanwise velocity component was measured in the wake. Significant spanwise flow was found at axial stations less than $x/H=1.2$, however the source for this spanwise component has not been clearly identified. The time-averaged recirculation bubble behind the bluff body ended at $x/H=0.9$, significantly shorter than the recirculation zone found in a backward-facing step flow. The dominant vortex-shedding frequency was found to be 454 Hz, corresponding to a Strouhal number of 0.243. The strong vortex shedding was responsible for the presence of high turbulence in the near field with a high degree of anisotropy.

A parallel Computational Fluid Dynamics (CFD) study was initiated to gauge the predictive accuracy of currently available CFD techniques. Three solutions were compared: a 2-d steady-state solution using the standard $k-\epsilon$ model, a standard $k-\epsilon$, time-accurate solution, and a 2-d time-accurate solution using a Renormalized-Group (RNG) $k-\epsilon$ turbulence model. The numerical simulations showed that the bluff-body flowfield cannot be accurately predicted using steady-state calculations, because no mechanism exists to predict the amplified time-averaged Reynolds stresses which result due to vortex shedding. The time-accurate standard $k-\epsilon$ model predicts the vortex-shedding frequency accurately, but underpredicts the Reynolds stresses and overpredicts the length of the recirculation zone by 10%. The RNG $k-\epsilon$ model predicts a higher vortex-shedding frequency, but offers a closer match to the mean velocities. However, the Reynolds stresses tend to be overpredicted. A 3-d analysis covering the entire spanwise domain should improve the results.

BIBLIOGRAPHY

Abolfadl, M. A., and Sehra, A. K., (1993), "Experimental Investigation of Exhaust System Mixers for a High Bypass Turbofan Engine," *AIAA 93-0022*, 31st Aerospace Sciences Meeting, Reno, NV, Jan. 11-14.

Absil, L. H. J., (1988), "Laser Doppler Measurements of Mean Turbulence Quantities, Time- and Spatial-Correlation Coefficients in the Wake of a Circular Cylinder," *Journal of Fluid Mechanics*, June 11-14.

Andreopoulos, J. and Wood, D. H., (1982), "The Response of a Turbulent Boundary Layer to a Short Length of Surface Roughness," *Journal of Fluid Mechanics*, **118**, pp. 143-164.

Armany, B. F., Durst, F., Pereira, J. C. F., and Schonung, B., (1983), "Experimental and Theoretical Investigation of Backward-Facing Step Flow," *Journal of Fluid Mechanics*, (1983), **127**, pp. 473-496.

Arnal, M., and Friedrich, R., (1991), "Large-Eddy Simulation of a Turbulent Flow with Separation," *Turbulent Shear Flows 8*, Springer-Verlag.

Avva, R., (1993), "CFD-ACE: Theory Manual," CFDRC Report GR-93-1.

Azad, R. S., Kassab, S. Z., and Dang T. H., (1987), "Experimental Evaluation of Approximations for w^2 and vw^2 ," *AIAA Journal*, **25**, 1, pp. 171-173.

Baker, R. J., Hutchinson, P., and Whitelaw, J. H., (1974), "Preliminary Measurements of Instantaneous Velocity in a 2m Square Furnace Using Laser Anemometry," *Journal of Heat Transfer*, Vol. **96**, pp. 410-420.

Barnett, D., and Bentley, H., (1974), "Statistical Bias of Individual Realization Laser Velocimeters," *Proceedings of the Second International Workshop on Laser Velocimetry*, Purdue University, p. 428.

Benedict, L. H., and Gould, R. D. (1996), "Towards Better Uncertainty Estimates for Turbulence Statistics," *Physics of Fluids*. Accepted for Publication.

Boussinesq, J., (1877), *Mem. Pres. par div. savant a l'acad sci. Paris*, **23**, 46.

Caron, S. D., and Gallagher, K. E., (1989), "High Speed Turboramjet Ramburner Component Test Program," *JANNAF Propulsion Meeting*, **IV**, pp. 161-170, Cleveland, OH.

Castro, I. P., (1977), "Numerical Difficulties in the Calculation of Complex Turbulent Flows," Turbulent Shear Flows I, Springer-Verlag, pp. 220-236.

Chandrsuda, C., and Bradshaw, P., (1981), "Turbulence Structure of a Reattaching Mixing Layer," *Journal of Fluid Mechanics*, **118**, pp. 171-194.

Chou, P. Y., (1945), "On Velocity Correlations and the Solution of the Equations of Turbulent Fluctuation," *Quart. Appl. Math.*, **3**, 38.

Choudhury, D., and Kim, S., (1993), "Calculation of Turbulent Separated Flows Using a Renormalization Group Based $k-\epsilon$ Turbulence Model," Fluids Engineering Division, **149**, Separated Flows, ASME.

Cormack, D. E., Leal, L. G., and Seinfeld, J. H., (1978), "An Evaluation of Mean Reynolds Stress Turbulence Models: The Triple Velocity Correlation," *Journal of Fluids Engineering*, **100**, pp. 47-54.

Craig, R. R., Nejad, A. S., Hahn, E. Y., and Schwartzkopf, K. G., (1986), "Approach for Obtaining Unbiased Laser Doppler Velocimetry Data in Highly Turbulent Flows," *Journal of Propulsion and Power*, **2**, 6, pp. 541-545, Nov.-Dec.

Davidou, B I., (1961), "On the Statistical Dynamics of an Incompressible Turbulent Fluid, Soviet Physics-Doklady, **6**, 10.

Davies, T. W., and Beer, (1971), 'Flow in the Wake of Bluff-Body Flame Stabilizers," 13th International Symposium on Combustion, pp. 631-638, Salt Lake City, Ut.

Dougherty, E. R., (1990), "Probability and Statistics for Engineering, Computing, and Physical Sciences," Prentice-Hall, Inc., pp. 329 - 331.

Driver, D. M., and Seegmiller L. H., (1985), "Features of a Reattaching Turbulent Shear Layer in Divergent Channel Flow," *AIAA Journal*, **23**, 2, pp. 163-171.

Durao, D. F. G., Heitor, M. V., and Pereira, J. C. F., (1988), "Measurements of turbulent and Periodic Flows Around a Square Cross-Section Cylinder," *Experiments in Fluids*, **6**, pp. 298 - 304.

Durst, F., and Rastogi, A. K., (1977), "Theoretical and Experimental Investigations of Turbulent Flows with Separation," Turbulent Shear Flows I, Springer-Verlag, pp. 208-219.

Durst, F., Melling, A., and Whitelaw, J. H., (1976), "Principles and Practice of Laser-Doppler Anemometry," Academic Press Inc., New York, New York.

Elliott, J. K., Manning, T. A., Qiu, Y. J., Greitzer, E. M., and Tan, C. S., (1992), "Computational and Experimental Studies of Flow in Multi-Lobed Forced Mixers," *AIAA 92-3568*, 28th Joint Propulsion Conference and Exhibit, Nashville, TN, July 6-8.

Etheridge, D. W., and Kemp, P. H., (1978), "Measurements of Turbulent Flow Downstream of a Rearward-Facing Step," *Journal of Fluid Mechanics*, **86**, 3, pp. 545-566.

Fox, R. W., and McDonald, A. T., (1978), "Introduction to Fluid Mechanics," John Wiley & Sons, p. 428.

Franke, R., and Rodi, W., (1991), "Calculation of Vortex Shedding Past a Square Cylinder with Various Turbulence Models," Turbulent Shear Flows 8, Springer-Verlag.

Fuji, S., and Gomi, M., (1976), "A Note on the Two-Dimensional Cylinder Wake," *Journal of Fluids Engineering*, **98**, pp. 318-320.

Fuji, S., Gomi, M., and Eguchi, K., (1978), "Cold Flow Tests of a Bluff-Body Flame Stabilizer," *Journal of Fluids Engineering*, **100**, pp. 323-332.

Geropp, D., and Leder A., (1985), "Turbulent Separated Flow Structures Behind Bodies with Various Shapes," International Conference on Laser Anemometry - Advances and Application, Manchester, UK.

Gould, R. D., Stevenson W. H., and Thompson, H. D., (1986), "A Parametric Study of Statistical Velocity Bias," Proceedings of the Fifth International Congress on Applications of Laser and Electro-Optics, Arlington, VA, November 10-13.

Gould, R. D., Stevenson W. H., and Thompson, H. D., (1988), "Turbulence Characteristics of an Axisymmetric Reacting Flow," NASA Contractor Report 4110.

Gould, R. D., Stevenson, W. H., and Thompson, H. D., (1990), "Investigation of Turbulent Transport in an Axisymmetric Sudden Expansion," *AIAA Journal*, **28**, 2, pp. 276-283.

Gould, R. D., (1994), "Analysis of Laser Doppler Velocimetry Data," Final Report RDL-22, Summer Research Program, Wright Laboratory; AFOSR.

Gould, R. D., (1995), "Data Reduction and Analysis for Laser Doppler Velocimetry," Final Report, Summer Research Extension Program, Wright Laboratory; AFOSR.

Harlow, F. H., and Nakayama, P. I., (1967), "Turbulent Transport Equations," *Phys. Fluids*, **10**, 11, p. 2323.

Hautman, D. J., and Rosfjord, T. J., (1989), "Inlet Flow Documentation and Combustion Measurements in a Ramjet Test Combustor," 26th JANNAF Combustion Meeting, **IV**, pp. 13-28, Pasadena, CA.

Hautman, D. J., Pfau, D. J., and Anderson, T. J., (1990), "Combustion Tests in a Ramjet Test Combustor," 27th JANNAF Combustion Meeting, **II**, pp. 421-434, Cheyenne WY.

Hinze, J. O., (1975), "Turbulence," 2nd Edition, McGraw-Hill Book Co., New York.

Hogg, S., I., (1988), "Second-Moment-Closure Calculations of Strongly-Swirling Confined Flows with and without Density Variations," Ph.D. Thesis, Department of Mechanical Engineering, University of Manchester, England.

Hosokawa, S., Ikeda, Y., Minato, M., and Nakajima, T., (1993), "Flow Measurements Behind V-Gutter Under Non-Combusting Condition," *AIAA 93-0020*.

Jones, W. P., and Lunder, B. E., (1972), "The Prediction of Laminarization with a Two-Equation Model of Turbulence," *Int. J. Heat and mass transfer*, **15**, 301.

Jones, G. S., Kamemoto, D. Y., and Gartrell, L. R., (1990), "An Investigation of the Effects of Seeding in Laser Velocimetry Systems," *AIAA 90-0502*, 20th Aerospace Sciences Meeting, Reno, NV.

Kendall, M. G., (1969). The Advanced Theory of Statistics, Vol.1, 3rd ed., Hafner Publishing Co., Ny, p.243.

Kim, J., Kline, S., and Johnston, J., (1978), "Investigation of Separation and Reattachment of a Turbulent Shear Layer: Flow Over a Backward-Facing Step," Report MD-37, Thermo Sciences Division, Dept. of Mechanical Engineering, Stanford University.

Kodali, V., and Amano, R., (1986), "Prediction of Turbulent Flows Behind Bluff Bodies by Using an Algebraic-Stress Model," *AIAA-86-1061*.

Larousse, A., Martinuzzi, R., and Tropea, C., (1991), "Flow Around Surface-Mounted, Three-Dimensional Obstacles," Turbulent Shear Flows 8, Springer-Verleg, pp. 127-139.

Laufer, J., (1954), NACA Rep. 1174.

Launder, B. E., and Sharma, B. I., (1974), "Application of the Energy Dissipation Model of Turbulence to the Calculation of Flow Near a Spinning Disc," *Letters in Heat and Mass Transfer*, **1**, 2, pp. 131-138.

Lawn, C. J., (1971), "The Determination of the Rate of Dissipation in Turbulent Pipe Flow," *Journal of Fluid Mechanics*, **48**, pp. 477-505.

Lefebvre, A. H. (1983), Gas Turbine Combustion, McGraw-Hill, p.128, 131, 134 & 137.

Lyn, D. A., (1989), "Phase-Averaged Turbulence Measurements in the Separated Shear-Layer region of Flow Around a Square Cylinder. Proc. 23rd Congress of the Int. Association for Hydraulic Research, Ottawa, Canada, Aug. 21-25, A85 - A92.

Malecki, R., and Lord, W., (1990), "Navier-Stokes Analysis of a Lobed Mixer and Nozzle," *AIAA 93-0453*, 28th Aerospace Sciences Meeting, Reno, NV, Jan. 8-11.

Mansingh, V., and Oosthuizen, P., (1990), "Effects of Splitter Plates on the Wake Flow Behind a Bluff Body," *AIAA Journal*, May, pp. 778-783.

Martensson, H., Eriksson, L., and Albraten, P., (1991), "Numerical Simulations of Unsteady Wakeflow," 10th International Symposium on Air-Breathing Engines (ISABE), 2, Nottingham, England.

Maurice, M., (1992), "An Investigation of Laser Velocimetry Measurements Within High Speed, Complex Flows," Ph.D. Thesis, University of Dayton, Ohio.

McCormick, D. C., and Bennet, J. C., (1993), "Vortical and Turbulent Structure of a Lobed Mixer Free-Shear Layer," *AIAA 93-0219*, 31st Aerospace Sciences Meeting, Reno, NV, Jan. 11-14.

McLaughlin, D. K., and Tiederman, W. G., (1973), "Bias Correction for Individual Realization Laser Anemometry Measurements in Turbulent Flows," *Physics of Fluids*, **16**, 12, pp. 2082-2088.

Mehta, R. D. (1990), "Verification of Three-Dimensional Laser Doppler Velocimeter Measurements," *Experiments in Fluids*, **8**, pp. 354-356.

Meyers, J. F., (1985), "The elusive third component," Proc. ASME Symposium on Laser Anemometry, Winter Annual Meeting, Miami, FL, Nov. 17-21.

Moss, W. D., Baker, S., and Bradbury, L. J. S., (1977), "Measurements of Mean Velocity and Reynolds Stresses in Some Regions of Recirculating Flow," *Turbulent Shear Flows I*, Springer-Verlag, pp. 198-207.

Nakagawa, H., Nezu, I., and Ueda, H., (1975), "Turbulence of Open Channel Flow Over Smooth and Rough Beds," *Proceedings of the Japanese Society of Civil Engineers*, **241**, pp. 155-168.

Okamoto, S., (1981), "Turbulent Shear Flow Behind Hemisphere-Cylinder Placed on Ground Plane," *Turbulent Shear Flows 3*, Springer-Verlag, pp. 171-185.

Owens, S. F., (1992), "CFD-ACE: Command Language Reference Manual," CFDRC Report GR-92-6, August.

Pearce, J., Qasim, A., Maxwell, T., and Paramesawaran, S., (1992), "A Computational Study of Coherent Wake Structures Behind 2-D Bluff Bodies," *J. of Wind Engineering and Industrial Aerodynamics*, 41-44, pp. 2853-2861.

Perry, A., and Steiner, T., (1987), "Large-Scale Vortex Structures in Turbulent Wakes behind Bluff Bodies: Part 1. Vortex Formation Processes," *Journal of Fluid Mechanics*, 174, pp. 233-270.

Prandtl, L., (1925), "Z. Andew. Math. U. Mech.," 5, p. 136. Also, Goldstein, S., (1938), "Modern Developments in Fluid Dynamics," 1, p. 205, Oxford University Press, New York.

Prandtl, L., (1945), "Über ein neues formelsystem fur die ausgebildete turbulenz," Nachrichten Von der Akad der Wissenschaft in Gottingen.

Przulj, V., and Younis, B., (1993), "Some Aspects of the Prediction of Turbulent Vortex Shedding," *Fluids Engineering Division*, 149, Separated Flows, ASME, pp. 75-81.

Rabe, D., and Sabroske, K., (1994), "Laskin Nozzle Performance for Laser Flow Measurement Seeding," *AIAA 94-0044*, 32nd Aerospace Sciences Meeting & Exhibit, Reno, NV, Jan.10-13.

Raffoul, C., Nejad, A., Gould, R., and Spring, S., (1995), "An Experimental and Numerical Study of the Isothermal Flowfield Behind a Bluff Body Flameholder," accepted for presentation at the *ASME Turbo Expo '95*, Houston, Texas, June 5-8.

Raghunathan, S. and Said B. (1994), "Flow Around a Circular Cylinder With Cooling," *AIAA 94-0665*, 32nd Aerospace Sciences Meeting & Exhibit, Reno, NV, Jan.10-13.

Reynolds, O., (1895), "Philosophical Transactions," 186, 123.

Rodi, W., (1972), "The Prediction of free Turbulent Boundary Layers by Use of a Two-Equation Model of Turbulence," Ph.D. Thesis, Univ. of London.

Roesler, T., Stevenson, W. H., and Thompson, H. D., (1980), "Investigation of Bias Errors in Laser Doppler Velocimeter Measurements," AFWAL-TR-80-2108, December.

Rotta, J. C., (1968), "Über eine Methode zur Berechnung Turbulenter Scherstromungen, Aerodynamische Versuchsanstalt Gottingen Rept. 69/A/14.

Ryden, R., Eriksson, L., and Olovsson, S., (1993), "Large-Eddy Simulation of Bluff Body Stabilised Turbulent Premixed Flames," ASME 93-GT-157.

Savitzky, A. and Golay, J., (1964), "Smoothing and Differentiation of Data by Simplified Least Squares Subroutine," *Analytical Chemistry*, **36**, p.1627.

Sjunnesson, A., Olovsson, S., and Sjöblom, B., (1991), "Validation Rig - A Tool for Flame Studies," 10th International Symposium on Air Breathing Engines (ISABE), Nottingham, England.

Snyder, P. K., Orloff, K. L. and Reinath, M. S., (1984), "Reduction of Flow Measurement Uncertainties in Laser Velocimeters with Non-orthogonal Channels," *AIAA Journal*, **22**, pp. 1115 -1123.

Speziale, C., and Thangam, S. (1992), "Analysis of an RNG Based Turbulence Model for Separated Flows," NASA CR 189600.

Spring, S. A., and Smith, C. E., (1992), "CFD Analysis of Fuel Injection/Flameholder Concepts for Ramburners," JANNAF Propulsion Meeting, Indianapolis, IN, Feb. 24-27.

Stevenson, W. H., Thompson, H. D., and Roesler, T. C., (1982), "Laser Velocimeter Measurements and Analysis in Turbulent Flows with Combustion-Part I," Air Force Wright Aeronautical Labs, AFWAL-TR-2076, September.

Taylor, G. I., (1915), "Eddy Motion in the Atmosphere," Philosophical Transactions of the Royal Society of London, Series A, **215**, pp. 1-26.

Tennekes, H., and Lumley, J. L., (1972), A First Course in Turbulence, The MIT Press, p.2.

Townsend, A. A., (1980), "The Structure of Turbulent Shear Flow," Cambridge University Press, New York.

TSI, Incorporated, (1992), "Model IFA 750 Digital Burst Correlator," P.O. Box 64394, St. Paul, MN 55164 USA (Ph: 612-483-4711).

Werner, H., and Wengle, H., (1991), "Large-Eddy Simulation of Turbulent Flow Over and Around a Cube in a Plate Channel," Turbulent Shear Flows 8, Springer-Verlag.

Wilcox, D., C., (1993), "Turbulence Modeling for CFD," DCW Industries, Inc., La Canada, Ca. 91011.

Williamson, C. H. K., (1989), "Three-Dimensional Aspects and Transition of the Wake of a Circular Cylinder," Turbulent Shear Flows 7, Springer-Verlag, pp. 173-194.

Wood, D. H. and Bradshaw, P., (1982), "A Turbulent Mixing Layer Constrained by a Solid Surface, Part 1. Measurements Before Reaching the Surface," *Journal of Fluid Mechanics*, **122**, pp. 57-89.

Yakhot, V., Orszag, S., (1986), "Renormalization Group Analysis of Turbulence. I. Basic Theory," *J. Sci. Comput.* **1**, 3.

Yakhot, V., Orszag, S., Thangan, S., Gatski, T., and Speziale, C., (1992), "Development of Turbulence Models for Shear Flows by a Double Expansion Technique," *Phys. Fluids*, **A4** (7).

Yang, K., and Ferziger, J., (1993), "Large-Eddy Simulation of Turbulent Obstacle Flow Using a Dynamic Subgrid-Scale Model," *AIAA Journal*, **31**, 8.

Yanta, W. J., and Smith, R. A., (1973), "Measurements of Turbulence-Transport Properties with a Laser Doppler Velocimeter," *AIAA Paper 73-169*.

APPENDIX A

LDV Data Reduction Equations

Velocity Calculation

The fringe spacing, d_f , depends only on the wavelength of light, λ , and the full angle ϕ , according to the following equation;

$$d_f = \frac{\lambda}{2 \sin(\phi / 2)}$$

The velocity is then obtained from;

$$U_x = f_D d_f$$

where;

λ = wavelength of incident light (different for each color) in meters,

f_D = frequency detected at photodetector (measured frequency of particle) in Hz,

U_x = velocity of flow perpendicular to fringes, in m/sec,

d_f = distance between fringes, in meters, and

ϕ = angle of beam intersection (measured prior to data acquisition), in degrees.

For the case with frequency shifting, the following equation is used;

$$U_x = (f_D - f_s) d_f$$

where;

f_s = shifted frequency (operator preset) = 40 MHz.

Beam Diameter

The probe volume diameter equation, based on $1/e^2$, is;

$$d_m = \frac{4\lambda f}{\pi D_{e^2} E}$$

where;

λ = laser beam wavelength, in meter,

f = lens focal length, in meter,

D_{e-2} = light beam diameter entering lens and defined as region where intensity is greater than $1/e^2$ (~ 0.135) of centerline intensity; 1.5E-3 for green; 1.36E-3 for blue, in meter, and

E = beam expansion ratio, in this case: $150/40=3.75$.

Probe Volume Length

The probe volume length, l_m , is obtained by;

$$l_m = \frac{d_m}{\tan(\phi / 2)}$$

Number of Fringes

The number of fringes, N_{fr} , is obtained by;

$$N_{fr} = \frac{d_m}{d_f}$$

where, d_m , and d_f are obtained as shown above.

APPENDIX B

Mean Velocity Equations & Coordinate Transformation

In order to allow for implementation of nonperfectly orthogonal angles as shown in illustration B.1, modification of the equations derived for orthogonal system was necessary.

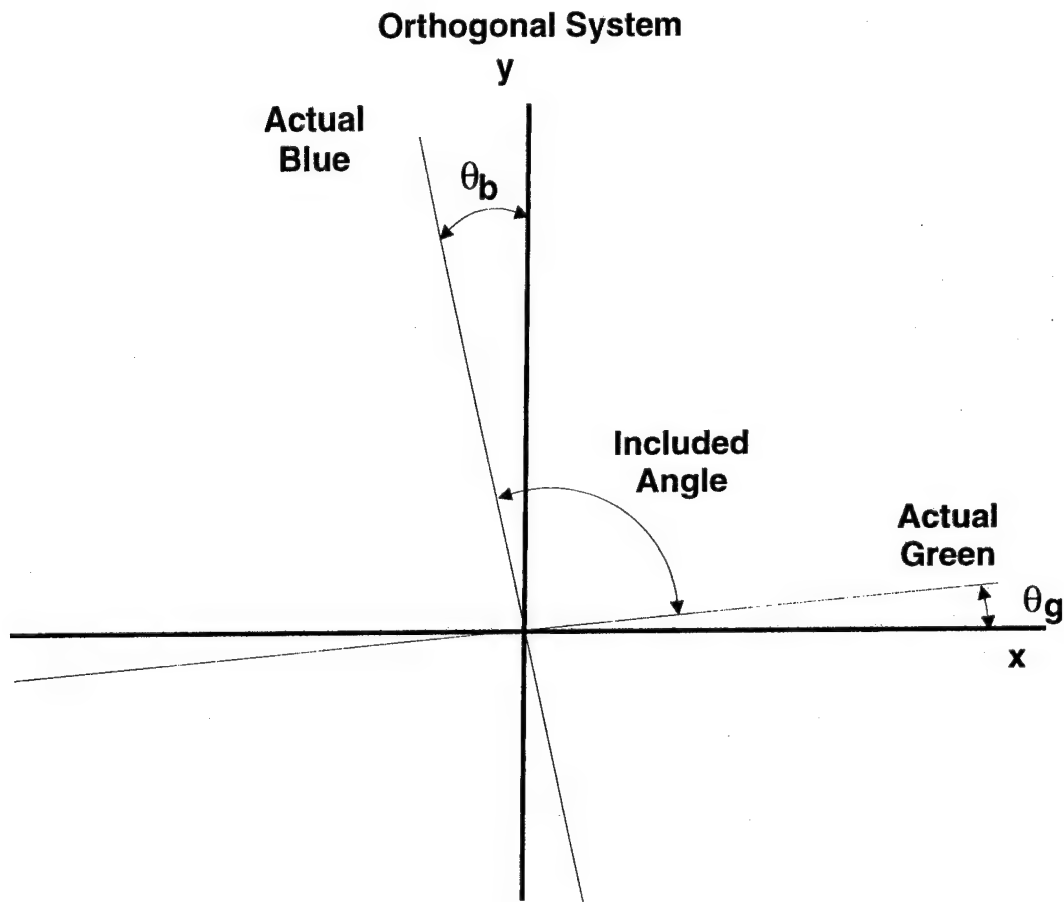


Illustration B.1. Departure from orthogonal system.

Where, θ_b , θ_g are the deviation angles of the blue and the green beams from being orthogonal. The included angle = $90^\circ + \theta_b - \theta_g$. There is an infinite number of combinations for θ_b and θ_g for any configuration, and the values chosen may effect δ . A typical use would be to input $\theta_b = \theta_b$ - θ_g and $\theta_g = 0$; δ would then be the angle between the green beam and the reference axis.

The following equations were used to perform a coordinate transformation for an LDV system where, the x & y-coordinates may vary from being at 90 degrees to each other.

For a three-component system, the following equations are used:

$$U_1 = \frac{U_b \sin \theta_g - U_g \sin \theta_b}{\sin(\theta_g - \theta_b)}$$

$$U_2 = \frac{U_b \cos \theta_g - U_g \cos \theta_b}{\sin(\theta_b - \theta_g)}$$

$$U_3 = U_v \cos \theta_v$$

where;

U_g , U_b , and U_v are the velocities measured by the tilted system,

U_1 , U_2 , and U_3 are the results of the transformed velocities,

g , b , and v are related to processors 1, 2, and 3 respectively, and

where;

θ_g = the tilted angle in the x-direction, and

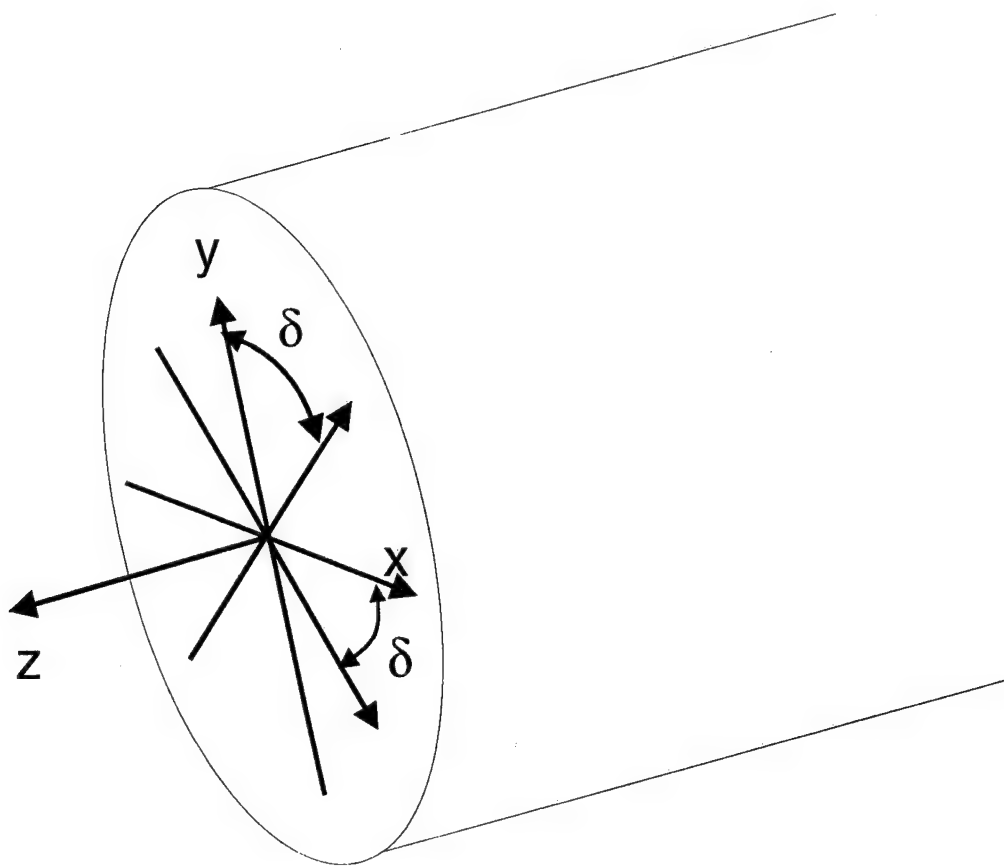
θ_b = the tilted angle in the y-direction, and

θ_v = the tilted angle in the z-direction.

For a perfectly orthogonal system, each component would measure directly the pertaining velocity. But, at times, even when great effort was made in order to obtain a perfectly orthogonal system, it was found that this was very difficult to accomplish. Therefore, these equations allow for this type of correction.

Now, if the xy-axis is rotated as was the case here (rotation is 45 degrees), corrections are needed that would allow for correct measurement of all three components (see Illustrations B:2), where;

δ = the rotation of the system in the xy-plane or about the z-axis where positive rotation is counterclockwise (looking from the left). $\delta=0$ defines an LDV system whose x-axis is parallel to the experiment x-direction.



Positive rotation defined by Right-Hand Rule

Illustration B.2. Rotation about the z-axis, or in the xy-plane.

The next set of equations were used to perform a coordinate transformation for rotating a system about the z-axis (rotating the system in the xy plane) and rotation of a system about the x-axis (tilting out of the xy-plane, see Illustration B.3).

$$U = U_1 \cos \delta - U_2 \sin \delta$$

$$V = U_1 \cos \epsilon \sin \delta + U_2 \cos \epsilon \cos \delta - U_3 \sin \epsilon$$

$$W = U_1 \sin \epsilon \sin \delta + U_2 \sin \epsilon \cos \delta + U_3 \cos \epsilon$$

where;

ϵ = the tilt of the system out of the xz-plane or about the x-axis where positive ϵ is a tilt above the xz-plane and negative ϵ is below the xz-plane. $\epsilon = 0$ defines an LDV system whose axis is in the xz-plane (in this study, ϵ was set = 0).

U, V, and W are the results of the transformed velocities.

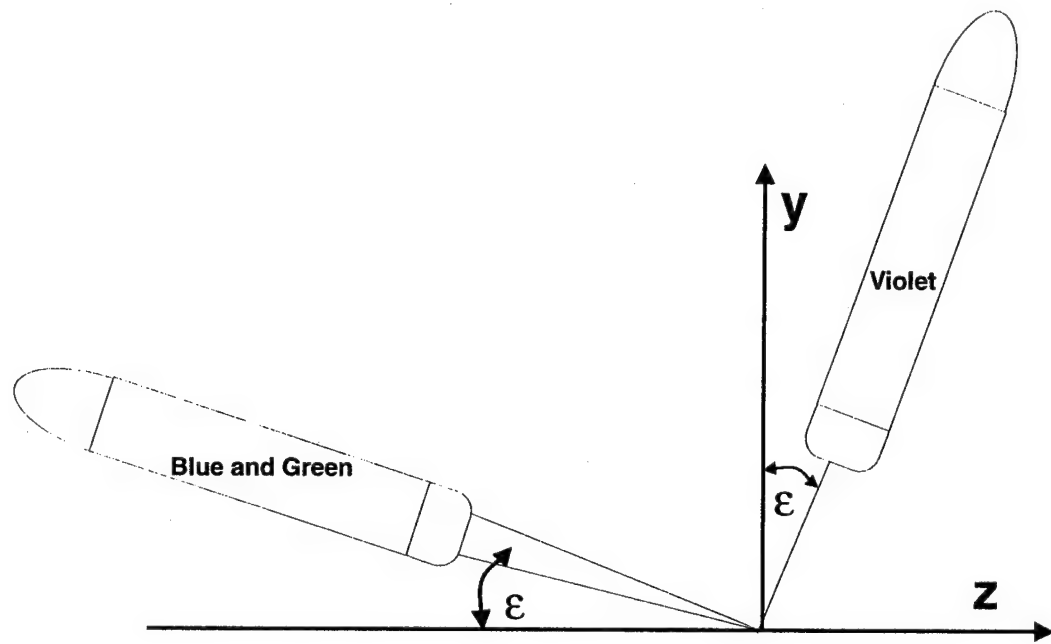


Illustration B.3. Tilt of the system about the x-axis.

APPENDIX C

LDV Definitions and Description of Components

Definitions

Laser Doppler velocimetry (LDV) is a technique for measuring fluid flow velocity by tagging the fluid and measuring the velocity of the tagged material.

The laser is a device for transforming incoherent light of various frequencies of vibrations into a very narrow intense beam of coherent light. The name is derived from the initial letters of "Light Amplification by Stimulated Emission of Radiation." In the emission of ordinary light the molecules or the atoms of the source emit their radiation independently of each other, and consequently there is no definite phase relationship among the vibrations in the resultant beam. The light is therefore incoherent. The laser, by means of an optical resonator, forces the atoms of the material of the resonator to radiate in phase. The emitted radiation is stimulated by the excitation of the atoms to a higher energy level by means supplied to the device.

Most lasers consist of three components, a resonator structure, a plasma tube, and a power supply. The resonator holds the two reflective mirrors in precise alignment, thus forming a resonant optical cavity. One of these mirrors is partially transmissive and will allow a fraction of the light beam to escape as light output power. The plasma tube provides optical gain within the resonator causing it to act as an oscillator. The power supply provides d.c. voltage across the plasma tube to sustain a controlled arc discharge through the fill-gas of the plasma tube (i.e., to excite gas atoms to a higher energy level which in turn radiate to a lower state).

Johann Doppler first predicted that the measured frequency and wave length of the scattered light depends on the relative motion of the scattering source and the observer. Now, in LDV the particles in the fluid are illuminated by the incident focused laser beams and become sources of scattered light. The change in frequency (Doppler shift) of the scattered light due to the motion of the particles when observed by a stationary observer (photomultiplier tube) allows the particle velocity to be determined. The minimum system requirements are:

- Light source (laser)
- Transmitting optics
- Receiving optics
- Photodetector (converts light energy to electrical signal)
- Signal processor (converts frequency to voltage)

- Data processor (computer etc.): to calculate moments, store data, etc.

Description of Components

Laser

The light source is usually an Argon-ion laser which emits strongly at 476.5, 488, 514.5 nm. For most four-beam two-color systems, the 488 (blue) and 514.5 (green) nm lines are used.

Transmitting Optics

1. Beam collimator - is usually mounted directly on the laser output port. This component ensures minimum beam divergence and locates the beam waist at the focal point of the final focusing lens.
2. Color separator - This component separates the output laser beam into individual colors by means of a dispersion prism assembly.
3. Plane mirrors - These serve to align the individual beams with the previously defined optical axis.
4. Polarization rotators - These components ensure correct orientation of the incident beam polarity.
5. Beam splitters - These components split the incident beam into two beams of equal intensity.
6. Bragg cells - These components are acousto-optic devices which are used to frequency shift one of the beams from the beam splitter. The other beam is passed through an optical block to maintain coherence.
7. Beam steering modules - These are small prisms which are used to steer the beams for proper alignment and ensuring the beams cross at the same point.
8. Beam spacers - These components serve to reduce the spacing between the parallel beams before entering the beam expander.
9. Beam expander - This component serves to increase the beam diameter and spacing, thereby resulting in a finer probe volume.
10. Focusing lens - This component focuses the beams from the beam expander to form the probe (measurement) volumes.

Receiving Optics

1. In the back-scatter mode the focusing lens acts as the collector of the scattered light from the probe volume.
2. Field stop system - This is used to optimize the focal depth of the collecting optics, i.e. it serves as an optical filter for the elimination of extraneous background light.
3. Color separator - In a two color system, this component separates and directs the scattered light by means of a dichroic mirror.
4. Receiving modules - These components consist of a lens and mirror assembly which focuses the scattered light on to the photomultiplier tube.

APPENDIX D

Data Reduction Notes

Mean:	$\bar{U} = \frac{1}{n} \sum_{i=1}^n U_i$	or	$\frac{1}{n} (U_1 + U_2 + U_3 + \dots + U_n)$
RMS:	$U_{rms} = \sqrt{\frac{\sum_{i=1}^n U_i^2}{n}}$	or	$\sqrt{\frac{U_1^2 + U_2^2 + U_3^2 + \dots + U_n^2}{n}}$
SIGMA:	$U_\sigma = \sqrt{\frac{\sum_{i=1}^n U_i^2}{n} - \left(\frac{\sum_{i=1}^n U_i}{n} \right)^2}$	or	$\sqrt{U_{rms}^2 - \bar{U}^2}$

where n is the number of samples in the data set.

Turbulence intensity(%): $100 U_\sigma / U_{ref}$

Second Moments:

$$\begin{aligned}
 \bar{uv} &= \frac{1}{n} \sum_{i=1}^n ((U_i - \bar{U})(V_i - \bar{V})) \\
 &= \frac{1}{n} \sum_{i=1}^n (U_i V_i - U_i \bar{V} - \bar{U} V_i + \bar{U} \bar{V}) \\
 &= \left(\frac{1}{n} \sum_{i=1}^n U_i V_i \right) - \left(\bar{V} \sum_{i=1}^n \frac{U_i}{n} \right) - \left(\bar{U} \sum_{i=1}^n \frac{V_i}{n} \right) + (\bar{U} \bar{V}) \\
 &= \left(\frac{1}{n} \sum_{i=1}^n U_i V_i \right) - (\bar{V} \bar{U}) - (\bar{U} \bar{V}) + (\bar{U} \bar{V}) \\
 &= \left(\frac{1}{n} \sum_{i=1}^n U_i V_i \right) - (\bar{V} \bar{U}) = \bar{U} \bar{V} - \bar{U} \bar{V} \\
 &= \left(\sum_{i=1}^n \frac{U_i V_i}{n} \right) - \left(\sum_{i=1}^n \frac{U_i}{n} \right) \left(\sum_{i=1}^n \frac{V_i}{n} \right)
 \end{aligned}$$

Similarly,

$$\bar{uu} = \left(\sum_{i=1}^n \frac{U_i U_i}{n} \right) - \left(\sum_{i=1}^n \frac{U_i}{n} \right) \left(\sum_{i=1}^n \frac{U_i}{n} \right) = U_\sigma^2$$

Triple Products:

$$\begin{aligned}
 \bar{uvw} &= \frac{1}{n} \left(\sum_{i=1}^n (U_i - \bar{U})(V_i - \bar{V})(W_i - \bar{W}) \right) \\
 &= \frac{1}{n} \left(\sum_{i=1}^n (U_i V_i - U_i \bar{V} - \bar{U} V_i + \bar{U} \bar{V})(W_i - \bar{W}) \right)
 \end{aligned}$$

$$= \frac{1}{n} \left(\sum_{i=1}^n (U_i V_i W_i - U_i \bar{V} W_i - \bar{U} V_i W_i + \bar{U} \bar{V} W_i - U_i V_i \bar{W} + U_i \bar{V} \bar{W} + \bar{U} V_i \bar{W} - \bar{U} \bar{V} \bar{W}) \right)$$

$$= \left(\frac{1}{n} \sum_{i=1}^n U_i V_i W_i \right) - \left(\bar{V} \frac{1}{n} \sum_{i=1}^n U_i W_i \right) - \left(\bar{U} \frac{1}{n} \sum_{i=1}^n V_i W_i \right) + \left(\bar{U} \bar{V} \sum_{i=1}^n \frac{W_i}{n} \right) -$$

$$\left(\bar{W} \frac{1}{n} \sum_{i=1}^n U_i V_i \right) + \left(\bar{V} \bar{W} \sum_{i=1}^n \frac{U_i}{n} \right) + \left(\bar{U} \bar{W} \sum_{i=1}^n \frac{V_i}{n} \right) - (\bar{U} \bar{V} \bar{W})$$

$$\frac{1}{n} \sum_{i=1}^n U_i V_i W_i = \sum_{i=1}^n \frac{U_i V_i W_i}{n}; \quad \bar{V} \frac{1}{n} \sum_{i=1}^n U_i W_i = \bar{V} \sum_{i=1}^n \frac{U_i W_i}{n}$$

$$\bar{U} \frac{1}{n} \sum_{i=1}^n V_i W_i = \bar{U} \sum_{i=1}^n \frac{V_i W_i}{n}; \quad \bar{U} \bar{V} \sum_{i=1}^n \frac{W_i}{n} = \bar{U} \bar{V} \bar{W}; \quad \bar{W} \frac{1}{n} \sum_{i=1}^n U_i V_i = \bar{W} \sum_{i=1}^n \frac{U_i V_i}{n}$$

$$\bar{V} \bar{W} \sum_{i=1}^n \frac{U_i}{n} = \bar{V} \bar{W} \bar{U}; \quad \bar{U} \bar{W} \sum_{i=1}^n \frac{V_i}{n} = \bar{U} \bar{W} \bar{V}$$

$$= \sum_{i=1}^n \frac{U_i V_i W_i}{n} - \bar{V} \sum_{i=1}^n \frac{U_i W_i}{n} - \bar{U} \sum_{i=1}^n \frac{V_i W_i}{n} + \bar{U} \bar{V} \bar{W} - \bar{W} \sum_{i=1}^n \frac{U_i V_i}{n} + \bar{V} \bar{W} \bar{U} + \bar{U} \bar{W} \bar{V} - \bar{U} \bar{V} \bar{W}$$

$$= \sum_{i=1}^n \frac{U_i V_i W_i}{n} - \bar{V} \sum_{i=1}^n \frac{U_i W_i}{n} - \bar{U} \sum_{i=1}^n \frac{V_i W_i}{n} + 2(\bar{U} \bar{V} \bar{W}) - \bar{W} \sum_{i=1}^n \frac{U_i V_i}{n}$$

Similarly: $\bar{u} \bar{u} \bar{v} = \frac{1}{n} \left(\sum_{i=1}^n (U_i - \bar{U})^2 (V_i - \bar{V}) \right)$

$$= \frac{1}{n} \left(\sum_{i=1}^n (U_i U_i - 2U_i \bar{U} + \bar{U} \bar{U}) (V_i - \bar{V}) \right)$$

$$= \frac{1}{n} \left(\sum_{i=1}^n (U_i U_i V_i - U_i U_i \bar{V} - 2U_i \bar{U} V_i + 2U_i \bar{U} \bar{V} + \bar{U} \bar{U} V_i - \bar{U} \bar{U} \bar{V}) \right)$$

$$= \sum_{i=1}^n \frac{U_i U_i V_i}{n} - \bar{V} \sum_{i=1}^n \frac{U_i U_i}{n} - 2\bar{U} \sum_{i=1}^n \frac{U_i V_i}{n} + 2(\bar{U} \bar{U} \bar{V})$$

Similarly: $\bar{u} \bar{u} \bar{w} = \sum_{i=1}^n \frac{U_i U_i W_i}{n} - \bar{W} \sum_{i=1}^n \frac{U_i U_i}{n} - 2\bar{U} \sum_{i=1}^n \frac{U_i W_i}{n} + 2(\bar{U} \bar{U} \bar{W})$

$$\bar{u} \bar{v} \bar{v} = \sum_{i=1}^n \frac{U_i V_i V_i}{n} - \bar{V} \sum_{i=1}^n \frac{V_i V_i}{n} - 2\bar{V} \sum_{i=1}^n \frac{U_i V_i}{n} + 2(\bar{U} \bar{V} \bar{V})$$

$$\bar{v} \bar{v} \bar{w} = \sum_{i=1}^n \frac{V_i V_i W_i}{n} - \bar{W} \sum_{i=1}^n \frac{V_i V_i}{n} - 2\bar{V} \sum_{i=1}^n \frac{V_i W_i}{n} + 2(\bar{V} \bar{V} \bar{W})$$

$$\overline{uvw} = \sum_{i=1}^n \frac{U_i W_i V_i}{n} - \bar{U} \sum_{i=1}^n \frac{W_i V_i}{n} - 2\bar{W} \sum_{i=1}^n \frac{U_i V_i}{n} + 2(\bar{U} \bar{W} \bar{V})$$

$$\overline{vww} = \sum_{i=1}^n \frac{V_i W_i W_i}{n} - \bar{V} \sum_{i=1}^n \frac{W_i W_i}{n} - 2\bar{W} \sum_{i=1}^n \frac{V_i W_i}{n} + 2(\bar{V} \bar{W} \bar{W})$$

$$\overline{uuu} = \sum_{i=1}^n \frac{U_i^3}{n} - 3\bar{U} \sum_{i=1}^n \frac{U_i U_i}{n} + 2\bar{U}^3$$

$$\overline{vvv} = \sum_{i=1}^n \frac{V_i^3}{n} - 3\bar{V} \sum_{i=1}^n \frac{V_i V_i}{n} + 2\bar{V}^3$$

$$\overline{www} = \sum_{i=1}^n \frac{W_i^3}{n} - 3\bar{W} \sum_{i=1}^n \frac{W_i W_i}{n} + 2\bar{W}^3$$

Skewness Coefficient; $3^{\text{rd}} \text{ Moment}/2\sigma_u^3$

$$4^{\text{th}} \text{ Moment (U)} \dots \sum_{i=1}^n \frac{U_i^4}{n} - 4\bar{U} \sum_{i=1}^n \frac{U_i^3}{n} + 6\bar{U}^2 \sum_{i=1}^n U_i^2 - 3\bar{U}^4$$

$$4^{\text{th}} \text{ Moment (V)} \dots \sum_{i=1}^n \frac{V_i^4}{n} - 4\bar{V} \sum_{i=1}^n \frac{V_i^3}{n} + 6\bar{V}^2 \sum_{i=1}^n V_i^2 - 3\bar{V}^4$$

$$4^{\text{th}} \text{ Moment (W)} \dots \sum_{i=1}^n \frac{W_i^4}{n} - 4\bar{W} \sum_{i=1}^n \frac{W_i^3}{n} + 6\bar{W}^2 \sum_{i=1}^n W_i^2 - 3\bar{W}^4$$

Flatness Coefficient (Kurtosis); $4^{\text{th}} \text{ Moment}/\sigma_u^4$

Note:

The 3^{rd} Moments are also called Skewness; and the 4^{th} Moments are called Flatness.

APPENDIX E

Software File Output Format

X(in)	Y(in)	Z(in)	Uref(m/s)		
\bar{U} / U_{ref}	\bar{V} / U_{ref}	\bar{W} / U_{ref}	Usig/Uref	Vsig/Uref	Wsig/Uref
$\bar{uu} / U^2 ref$	$\bar{vv} / U^2 ref$	$\bar{ww} / U^2 ref$	$\bar{uv} / U^2 ref$	$\bar{uw} / U^2 ref$	$\bar{vw} / U^2 ref$
$\bar{uuu} / U^3 ref$	$\bar{uuv} / U^3 ref$	$\bar{uvw} / U^3 ref$	$\bar{vuu} / U^3 ref$	$\bar{vvv} / U^3 ref$	$\bar{vww} / U^3 ref$
$\bar{wuu} / U^3 ref$	$\bar{vww} / U^3 ref$	$\bar{www} / U^3 ref$			

APPENDIX F

Turbulent Kinetic Energy Equation

Starting with the Navier Stokes Equation in tensor notations, without the time-dependent term;

$$\rho U_j \frac{\partial U_i}{\partial x_j} = - \frac{\partial P}{\partial x_i} + \mu \frac{\partial^2 (U_i)}{\partial x_j^2} \quad (F.1)$$

Substitute;

$$U_i = \bar{U}_i + u_i \quad \& \quad P = \bar{P} + p \quad (F.2)$$

to get;

$$\rho(\bar{U}_j + u_j) \frac{\partial(\bar{U}_i + u_i)}{\partial x_j} = - \frac{\partial(\bar{P} + p)}{\partial x_i} + \mu \frac{\partial^2(\bar{U}_i + u_i)}{\partial x_j^2} \quad (F.3)$$

Now multiply each term by u_i and take the mean of this scalar equation, realizing that the product of a mean and a fluctuating quantity has zero mean; and the mean of a fluctuating quantity is zero as well.

$$\begin{aligned} \overline{\rho u_i \bar{U}_j \frac{\partial \bar{U}_i}{\partial x_j}} + \overline{\rho u_i u_j \frac{\partial \bar{U}_i}{\partial x_j}} + \overline{\rho u_i \bar{U}_j \frac{\partial u_i}{\partial x_j}} + \overline{\rho u_i u_j \frac{\partial u_i}{\partial x_j}} = \\ - \overline{u_i \frac{\partial \bar{P}}{\partial x_i}} - \overline{u_i \frac{\partial p}{\partial x_i}} + \overline{\mu u_i \frac{\partial^2 \bar{U}_i}{\partial x_j^2}} + \overline{\mu u_i \frac{\partial^2 u_i}{\partial x_j^2}} \end{aligned} \quad (F.4)$$

Note that;

$$\overline{u_i \bar{U}_i \frac{\partial \bar{U}_i}{\partial x_i}}, \overline{u_i \frac{\partial \bar{P}}{\partial x_i}}, \text{ and } \overline{v u_i \frac{\partial^2 \bar{U}_i}{\partial x_j^2}} \text{ have zero mean.}$$

Therefore; the equation reduces to;

$$\overline{\rho u_i u_j \frac{\partial \bar{U}_i}{\partial x_j}} + \overline{\rho u_i \bar{U}_j \frac{\partial u_i}{\partial x_j}} + \overline{\rho u_i u_j \frac{\partial u_i}{\partial x_j}} = - \overline{u_i \frac{\partial p}{\partial x_i}} + \overline{\mu u_i \frac{\partial^2 u_i}{\partial x_j^2}} \quad (F.5)$$

Also, the following modifications may be made;

$$u_i \bar{U}_j \frac{\partial u_i}{\partial x_j} = \bar{U}_j \frac{\partial}{\partial x_j} \left(\frac{u_i u_i}{2} \right) \quad (F.6)$$

$$\overline{u_i u_j} \frac{\partial u_i}{\partial x_j} = u_j \frac{\partial}{\partial x_j} \left(\frac{\overline{u_i u_i}}{2} \right) \quad (\text{F.7})$$

$$\overline{u_i u_j} \frac{\partial \overline{U_i}}{\partial x_j} = \overline{u_i u_i} \frac{\partial \overline{U_i}}{\partial x_j} \quad (\text{F.8})$$

$$\overline{u_i} \frac{\partial p}{\partial x_i} = \frac{\partial (\overline{u_i p})}{\partial x_i} - p \frac{\partial \overline{u_i}}{\partial x_i} = \frac{\partial (\overline{u_i p})}{\partial x_i} \quad (\text{F.9})$$

$$\text{and, } \overline{u_j} \frac{\partial}{\partial x_j} \left(\frac{\overline{u_i u_i}}{2} \right) = \frac{\partial}{\partial x_j} \left(\overline{u_j} \frac{\overline{u_i u_i}}{2} \right) - \frac{\overline{u_i u_i}}{2} \frac{\partial \overline{u_j}}{\partial x_j} = \frac{\partial}{\partial x_j} \left(\overline{u_j} \frac{\overline{u_i u_i}}{2} \right) \quad (\text{F.10})$$

since; $\frac{\partial u_i}{\partial x_i} = \frac{\partial u_j}{\partial x_j} = 0$, from the continuity equation.

After these substitutions are made, and letting $k = \frac{1}{2}(\overline{u_i u_i})$, we get;

$$\overline{\rho u_i u_j} \frac{\partial \overline{U_i}}{\partial x_j} + \rho \overline{U_j} \frac{\partial k}{\partial x_j} + \frac{1}{2} \frac{\partial}{\partial x_j} \left(\rho \overline{u_j} \frac{\overline{u_i u_i}}{2} \right) = - \frac{\partial (\overline{u_i p})}{\partial x_i} + \mu \overline{u_i} \frac{\partial^2 \overline{u_i}}{\partial x_j^2} \quad (\text{F.11})$$

or in another form;

$$\overline{\rho U_j} \frac{\partial k}{\partial x_j} = - \frac{1}{2} \frac{\partial}{\partial x_j} \left(\rho \overline{u_j u_i u_i} \right) - \overline{\rho u_i u_j} \frac{\partial \overline{U_i}}{\partial x_j} - \frac{\partial (\overline{u_i p})}{\partial x_i} + \mu \overline{u_i} \frac{\partial^2 \overline{u_i}}{\partial x_j^2} \quad (\text{F.12})$$

Where;

$$\overline{\rho U_j} \frac{\partial k}{\partial x_j} = \text{Convection terms} \quad (\text{F.13})$$

$$- \frac{1}{2} \frac{\partial}{\partial x_j} \left(\rho \overline{u_j u_i u_i} \right) - \frac{\partial (\overline{u_i p})}{\partial x_i} = \text{Diffusion terms} \quad (\text{F.14})$$

$$- \overline{u_i u_j} \frac{\partial \overline{U_i}}{\partial x_j} = \text{Production terms} \quad (\text{F.15})$$

$$+ \mu \overline{u_i} \frac{\partial^2 \overline{u_i}}{\partial x_j^2} = \text{Dissipation terms} \quad (\text{F.16})$$

Of this equation, the following terms were estimated using experimental measurements;

1. All convection terms
2. All production terms
3. All gradients of triple products

Dissipation was calculated by balance assuming the terms involving pressure are negligible. However, dissipation (per unit mass) is defined as (Wilcox, C. 1993);

$$\varepsilon = -v \frac{\overline{\partial u_i \partial u_i}}{\partial x_k \partial x_k} \quad (F.17)$$

where, this term is obtained from;

$$v \overline{u_i \frac{\partial^2 u_i}{\partial x_j^2}} = -v \frac{\overline{\partial u_i \partial u_i}}{\partial x_k \partial x_k} + \frac{\partial}{\partial x_j} [v \frac{\partial}{\partial x_j} (\frac{\overline{u_i u_i}}{2})] = -v \frac{\overline{\partial u_i \partial u_i}}{\partial x_k \partial x_k} + \frac{\partial}{\partial x_j} (v \frac{\partial k}{\partial x_j}) \quad (F.18)$$

$$\frac{\partial}{\partial x_j} (v \frac{\partial k}{\partial x_j}) = \text{Molecular Diffusion}$$

If molecular diffusion is negligible, than ε is equivalent to the dissipation terms shown above.

The turbulent kinetic energy equation is similar to the Reynolds-stress equation (shown in the next page) with the exception of the missing Pressure-Strain interaction term. The reason for this may be deduced from Equation (9) above;

$$\overline{u_i \frac{\partial p}{\partial x_i}} = \frac{\partial (\overline{u_i p})}{\partial x_i} - \overline{p \frac{\partial u_i}{\partial x_i}} = \frac{\partial (\overline{u_i p})}{\partial x_i} \quad (F. 9)$$

which shows that;

$$\overline{p \frac{\partial u_i}{\partial x_i}} = 0 \quad (F.19)$$

to satisfy mass continuity.

Therefore, the Pressure-Strain interaction terms make no contribution to the overall level of turbulence activity.

Reynolds Stress Transport Equation

$$\rho \bar{U}_k \frac{\partial \bar{u}_i \bar{u}_j}{\partial x_k} = \quad \text{(Convection)}$$

$$- \left[\rho \bar{u}_i \bar{u}_k \frac{\partial \bar{U}_i}{\partial x_k} + \rho \bar{u}_i \bar{u}_k \frac{\partial \bar{U}_j}{\partial x_k} \right] \quad \text{(Production)}$$

$$- \frac{\partial}{\partial x_k} \left[\frac{\partial \bar{u}_i \bar{u}_j}{\partial x_k} - \mu \left[\frac{\partial \bar{u}_i \bar{u}_j}{\partial x_k} + \bar{u}_j \frac{\partial \bar{u}_k}{\partial x_i} + \bar{u}_i \frac{\partial \bar{u}_k}{\partial x_j} \right] \right] - \frac{\partial \bar{P} \bar{u}_j}{\partial x_i} - \frac{\partial \bar{P} \bar{u}_i}{\partial x_j} \quad \text{(Diffusion)}$$

$$+ P \left[\frac{\partial \bar{u}_i}{\partial x_j} + \frac{\partial \bar{u}_j}{\partial x_i} \right] \quad \text{(Pressure-Strain Interaction)}$$

$$- 2\mu \frac{\partial \bar{u}_i \bar{u}_j}{\partial x_k \partial x_k} - \mu \left[\frac{\partial \bar{u}_i \partial \bar{u}_k}{\partial x_k \partial x_i} + \frac{\partial \bar{u}_j \partial \bar{u}_k}{\partial x_k \partial x_j} \right] \quad \text{(Dissipation)}$$

Of this equation, the following terms may be experimentally estimated using experimental measurements:

1. All convection of Reynolds stresses terms
2. All production of Reynolds stresses terms
3. All gradients of triple products

The pressure-diffusion terms are very difficult if not impossible to measure at this point and are usually assumed negligible. This assumption is reasonable for fully turbulent flows at locations away from the wall, such as is the case here. The pressure-strain interaction terms are also referred to as the 'redistribution' terms because they do not contribute in the generation or the destruction of turbulence, but they simply smooth the distribution of the stresses throughout the flow. This term vanishes for constant density flows because of the mass continuity constraint (Hogg, S., 1988):

$$\bar{P} \frac{\partial \bar{u}_i}{\partial x_i} = 0$$

The viscous dissipation terms contain the dissipation of the Reynolds stresses due to small scale molecular motion and interaction.

APPENDIX G

U_{ref} Uncertainty Calculation

$$\text{Bernoulli's equation: } \Delta P = \frac{1}{2} \rho U^2$$

$$\text{Density } (\rho) = \frac{P}{RT}$$

$$\text{Velocity } (U) = \sqrt{\frac{2\Delta P}{\frac{P_s}{RT}}}$$

$$U_{ref} (\text{max}) = \sqrt{\frac{2\Delta P_s^+}{\frac{P_s^-}{RT_s^+}}}$$

$$U_{ref} (\text{min}) = \sqrt{\frac{2\Delta P_s^-}{\frac{P_s^+}{RT_s^-}}}$$

Humidity Correction Error to U_{ref}

Since the one-component data were taken in winter, while the 3-component data in the summer, the reference velocity error due to the changes in the relative humidity would be computed as follows;

$$R = \bar{R} / \text{M.W.}$$

where; M.W. = M.W. (air) + M.W. (air) $\times \varpi$

M.W. = molecular weight

ϖ = humidity ratio = 0.622 \times Pv/Pa

$$Pv = \Phi Pg$$

Pg = saturation pressure at P

Φ = relative humidity

$$Pa = P - Pv$$

P = atmospheric pressure

Uncertainty in the Means

$$\Delta \bar{U} = \pm 1.96 \sigma_u / \sqrt{N}$$

$$\Delta \bar{V} = \pm 1.96 \sigma_v / \sqrt{N}$$

$$\Delta \bar{W} = \pm 1.96 \sigma_w / \sqrt{N}$$

where; the constant 1.96 corresponds to a confidence interval of 95%, and σ_u , σ_v , and σ_w are the estimators of the largest standard of deviation values of the U, V, and W-components.

N is the number of samples.

To obtain the percent error, $\Delta \bar{U}$ is then divided by U_{ref} , the upstream reference velocity, the result is subtracted from 1; and the outcome is multiplied by 100.

(Note: for a 99% confidence interval, the constant to be used is 2.576 (instead of 1.96).

APPENDIX H

Uncertainties in TKE (k) and TKE Terms

The turbulent kinetic energy “ k ” is the sum of three terms and is written as such;

$$k \equiv \frac{1}{2} (\overline{uu} + \overline{vv} + \overline{ww}) \quad (H.1)$$

In order to obtain the statistical uncertainty for “ k ”, the “Sum” rule needs to be applied.

First, recall that the basic measure of uncertainty is the variance (the actual values to be used are those of the uncertainty errors obtained with the “jackknife” method described by Benedict & Gould (1995) and are listed after each parameter in the computer output). There are basic rules for linear combinations of random variables. For instance:

If a and b are constants, and X and Y are random variables, then;

$$\sigma_{aX+bY}^2 = a^2 \sigma_X^2 \quad (H.2)$$

$$\sigma_{aX+bY}^2 = a^2 \sigma_X^2 + b^2 \sigma_Y^2 + 2ab \sigma_{XY} \quad (H.3)$$

If X and Y are independent, than the last term drops out;

$$\sigma_{aX+bY}^2 = a^2 \sigma_X^2 + b^2 \sigma_Y^2 \quad (H.4)$$

The variance for a difference (when X and Y are independent) is the same as the sum;

$$\sigma_{aX-bY}^2 = a^2 \sigma_X^2 + b^2 \sigma_Y^2 \quad (H.5)$$

To get the uncertainty in any of these terms, the square root needs to be calculated.

As an example of a “Sum” term, the uncertainty for “ k ” is evaluated as such;

$$\sigma_k^2 = \frac{1}{4} \sigma_{uu}^2 + \frac{1}{4} \sigma_{vv}^2 + \frac{1}{4} \sigma_{ww}^2 = \frac{1}{4} (\sigma_{uu}^2 + \sigma_{vv}^2 + \sigma_{ww}^2) \quad (H.6)$$

and;

$$\sigma_k = \sqrt{\frac{1}{4} (\sigma_{uu}^2 + \sigma_{vv}^2 + \sigma_{ww}^2)} = \frac{1}{2} \sqrt{\sigma_{uu}^2 + \sigma_{vv}^2 + \sigma_{ww}^2} \quad (H.7)$$

Therefore, the uncertainty in “ k ”, is the square root of the sum of the square of the associated uncertainties of each term.

Note: there is also another method to calculate the uncertainty in a "Sum". The error equation is;

$$\sigma^2 = \sum_{i=1}^n (\theta_i \sigma_i)^2 \quad (H.8)$$

where, θ_i are the partial derivatives, and σ_i are the variances. Using this equation to find the uncertainty in "k" gives:

$$\theta_1 = \frac{\partial k}{\partial uu} = \frac{1}{2} ; \quad \theta_2 = \frac{\partial k}{\partial vv} = \frac{1}{2} ; \quad \theta_3 = \frac{\partial k}{\partial ww} = \frac{1}{2} \quad (H.9)$$

$$\sigma_k^2 = \left(\left(\frac{1}{2} \sigma_{uu} \right)^2 + \left(\frac{1}{2} \sigma_{vv} \right)^2 + \left(\frac{1}{2} \sigma_{ww} \right)^2 \right) \quad (H.10)$$

and,

$$\sigma_k = \sqrt{\frac{1}{4} \sigma_{uu}^2 + \frac{1}{4} \sigma_{vv}^2 + \frac{1}{4} \sigma_{ww}^2} = \frac{1}{2} \sqrt{\sigma_{uu}^2 + \sigma_{vv}^2 + \sigma_{ww}^2} \quad (\text{same as H.7}) \quad (H.11)$$

Now, for the uncertainty in a "Product" term, equation H.8 still applies. For instance, the uncertainty in the " \overline{uu} / k " term is calculated as such;

$$\text{let: } P = \frac{\overline{uu}}{k} \quad (H.12)$$

then:

$$\frac{\partial P}{\partial \overline{uu}} = \frac{1}{k} \quad (H.13)$$

$$\frac{\partial P}{\partial k} = -\frac{\overline{uu}}{k^2} \quad (H.14)$$

$$\sigma_{\overline{uu}/k} = \sqrt{\left(\frac{1}{k} \sigma_{\overline{uu}} \right)^2 + \left(-\frac{\overline{uu}}{k^2} \sigma_k \right)^2} \quad (H.15)$$

For the "TKE" terms, the same technique is used. However, now one has to deal with "k" in addition. For instance, in the "Convection" of TKE term, $\overline{U} \partial k / \partial x$, the following is used;

$$\sigma_{\bar{U} \partial k / \partial x} = \sqrt{\left[\frac{\partial k}{\partial x} \right]^2 \sigma_{\bar{U}}^2 + (\bar{U})^2 \sigma_{\partial k / \partial x}^2} \quad (H.16)$$

The first term on the left of (H.16) is obtained from the experimental data, using central differencing. The second term is the uncertainty in the mean axial velocity, and is available. The third term is the mean axial velocity. The last term in (H.16) is dealt with as follows;

$$\sigma_{\partial k / \partial x}^2 = \frac{(\sigma_{k_{i+1}}^2 + \sigma_{k_{i-1}}^2)}{(x_{i+1} - x_{i-1})^2} \quad (H.17)$$

and the terms in the numerator are calculated according to;

$$\sigma_{k_{i+1}}^2 = \frac{1}{4} (\sigma_{uu_{i+1}}^2 + \sigma_{vv_{i+1}}^2 + \sigma_{ww_{i+1}}^2) \quad (H.18)$$

and,

$$\sigma_{k_{i-1}}^2 = \frac{1}{4} (\sigma_{uu_{i-1}}^2 + \sigma_{vv_{i-1}}^2 + \sigma_{ww_{i-1}}^2) \quad (H.19)$$

Similar calculations need to be done for $\bar{V} \partial k / \partial y$, and for all other TKE terms.